Understanding the controls on the extension and the timing of the Patagonian Ice Sheet during the last glacial cycle

MARIA PAZ VERONICA LIRA BAHAMONDE

LIRA BAHAMONDE, MARIA PAZ VERONICA (2024) Understanding the controls on the extension and the timing of the Patagonian Ice Sheet during the last glacial cycle. Doctoral thesis, Durham University.

Understanding the controls on the extension and the timing of the Patagonian Ice Sheet during the last glacial cycle

María Paz Verónica Lira Bahamonde

A Thesis presented for the degree of Doctor of Philosophy

Department of Geography
Durham University

June 2024

Understanding the controls on the extension and the timing of the Patagonian Ice Sheet during the last glacial cycle

María Paz Verónica Lira Bahamonde

Abstract

Patagonia is an interesting site to research the past climatic conditions upon glacier studies, because it hosts the larger ice body outside Antarctica in the Southern Hemisphere. This is important in the present and past context of regional climate and global sea level. Moreover, it is the only land of mass that straddles the core of the Southern Westerly Winds (SWWs), which are a critical climatic control in the higher latitudes of the Southern Hemisphere and are directly linked to the precipitations in the area. Several works focused on reconstructing the timings of past glaciations of the former Patagonian Ice Sheet (PIS). However, the geochronology shows an asynchrony in the timings of the ice maxima along the last glacial cycle. Reasons for this are still unclear, but most of them are centred around differences in the past configurations of the SWWs.

This thesis combines different approaches to tackle the asynchrony problem. It studies the glacial geomorphology and geochronology of the Seno Skyring ice lobe, which was previously under-studied. Additionally, through transient ice sheet modelling, it explores the climatic conditions required to simulate the growth and decay of the whole PIS through the last glacial cycle by constraining the model ice extent with geomorphological and chronological records (published and from this work).

The modelling suggests that the asynchrony along Patagonia is likely related to the interaction of climatic and topographic controls. Where the SWWs' core expanded northwards with respect to today's position, bringing wetter conditions towards central and northern Patagonia with an oscillating northern extent through the last glacial cycle. Moreover, topographic differences within the northern, central, and southern PIS are also crucial in the evolution of mass balance change and local ice glacier response, producing differences in the resilience of the deglaciation, thus more advantageous positions during a glacial readvance.

Contents

List of Figures

List of Tables

List of Abbreviations

SWWs	Southern Westerly Winds
PIS	Patagonian Ice Sheet
LGM	Last Glacial Maximum
MIS	Marine Isotopic Stage
PISM	Parallel Ice Sheet Model
ACR	Antarctic Cold Reversal
YD	Younger Dryas
LB	Laguna Blanca
RV	Río Verde
OSL	optically stimulated luminescence
SST	Sea Surface Temperature
ELA	Equilibrium-line Altitude
GEBCO	General Bathymetric Chart of the Oceans
NPI	Northern Patagonian Icefield
SPI	Southern Patagonian Icefield
CDI	Cordillera Darwin Icefield
SIA	shallow ice approximation
SSA	shallow shelf approximation
SIA_e	SIA enhancements
SSA_e	SSA enhancements
PDD	Positive Degree Day
SD	standard deviation
PMIP3	Paleoclimate Modelling Intercomparison Project Phase III
EPICA	European Project for Ice Coring in Antarctica
T	Temperature
Pp	Precipitation

Declaration and statement of copyright

This thesis is based on research conducted at the Department of Geography, Durham University, United Kingdom. I confirm that no part of this work has been submitted for any other degree at this or any other university, and all content is my own work unless otherwise referenced in the text.

María Paz Verónica Lira Bahamonde

Department of Geography
Durham University
Submitted June 2024
Final version November 2024

Acknowledgements

I am immensely grateful to my supervisors, Mike Bentley and Stewart Jamieson, for their guidance, patience and unhesitating support throughout this whole process. I am also very grateful for the support of my external supervisor from Chile, Juan Luis García, who always encouraged me to have in-depth discussions about Patagonia. I learnt infinity from all of you.

To many Durham Geography staff, who were always willing to help with a smile, thanks.

To all my friends from Geography and Durham who made this international journey feel like home. I can say now that I have an extended family all over the world.

To people outside the university who helped and gave me valuable advice through my PhD. To Andy Hein and Ángel Rodés for their help and discussions in the cosmogenic data analysis. To Julien Seguinot, whose help was crucial to solving a big modelling issue and months of stagnation. To Bob McCulloch for the useful discussions and feedback about the palaeoclimate.

I am grateful to my friends Consuelo Antezana, Gabriel Gómez and Hans Fernández, who spent weeks with me in the field. Thank you, and let's hope for more field trips in the southern latitudes.

I am always grateful to my family - my parents, my brother and Pedro - who have always supported and encouraged me to pursue and fulfil my dreams.

This thesis would not have been possible without the PhD studentship from ANID PFCHA/Doctorado Becas Chile/2018—72190469.

The fieldwork campaigns were funded by the Chilean Grant FONDECYT #1161110 (awarded by JL García), Gilchrist Educational Fund, Geography Department-Durham University and Norman Richardson Award-Ustinov College. The cosmogenic samples to constrain the moraine deposition were funded with the Chilean Grant FONDECYT #1161110. The ^{10}Be depth profile sample process was funded with NERC Cosmogenic Isotope Analysis Support grants 9199/1019 (awarded by M. Bentley and MP. Lira) and 9140/1013 (awarded by M. Bentley and C. Darvill).

The modelling part was undertaken in the Hamilton High Performance Computer Service of Durham University.

A mi Patagonia …

Chapter 1. Introduction

Laguna del Desierto and Monte Fitz Roy, central Patagonia

1.1. The Importance of Understanding the Last Patagonian Ice Sheet

Understanding the mechanisms of present and future climate change and its consequences, such as the melting of glaciers, is dependent on our ability to reconstruct past changes in the climate system and their interaction with the landscape. The Patagonian region represents an important site to research the effect of the last ice age climate upon glaciers for at least two reasons. Firstly, the preservation of the glacial landforms is unusually conspicuous, due to the dry conditions that occurred in the lee side of the Andes Range (Coronato et al., 2004) and the reducing ice extent through time (Clapperton, 1993). Secondly, its unique position in the mid-to-high southern latitudes, makes it the only continental mass that straddles the core of the Southern Westerly Winds (SWWs) belt (Garreaud et al., 2013), and makes it a suitable place to observe the behaviour of this climate feature which drives much of the climate in the mid-latitudes of the Southern Hemisphere. During the last glacial cycle in Patagonia, the Patagonian Ice Sheet (PIS) developed for nearly ~2000 km along the Andean Range, extending continuously from 38°S to 55°S, reaching the southern tip of the continent (Glasser & Jansson, 2008; Rabassa, 2008; Figure 1.1A).

Numerous efforts have been made to reconstruct the extent and timing of past glaciations in this area. The Last Glacial Maximum (LGM) between 26.5 and 19 ka, sensu stricto (Clark et al., 2009) and its termination embrace one of the biggest climate changes of the last 100 kyr, but the response of the PIS is not yet robustly quantified. This is because the geochronological constraints remain restricted to only a few localities, and it shows that there is an asynchrony in the occurrence of the maximum ice extent or local LGM within ice lobes. For instance, most outlets in northern and southern Patagonia show an earlier maximum during the Marine Isotopic Stage (MIS) 3 (Darvill et al., 2015; Denton et al., 1999; García et al., 2018; García et al., 2021; Zech et al., 2011). While in central Patagonia, most of the geochronology shows ice maxima during early MIS 2 (Douglass et al., 2006; Hein et al., 2010; Kaplan et al., 2004; Leger et al., 2021). A key question, therefore, is what is the pattern and cause of this asynchrony? Varied works have focussed on reconstructing these glacial-deglacial trends during the last glaciation in order to understand this asynchrony, and these have been linked to local, regional and interhemispheric connections (Anderson et al., 2009; Denton et al., 2010; Jouzel et al., 2007; Toggweiler et al., 2006). For example, one explanation for the difference in timing of the glacial advances along Patagonia is that they may have fluctuated out of phase and would therefore have been affected by different forcing. Darvill et al. (2016) suggest that the primary factors that drive the glacial activity during the last glacial cycle are the feedback between atmospheric and oceanic current systems (Figure 1.1B). For instance, the increase in the Antarctic sea ice could produce the migration of the oceanic fronts (Sub- Tropical and Sub-Antarctic), and this may have altered the sea surface temperature around Patagonia. Therefore, this would change the position and/or intensity of the Antarctic Circumpolar Current, as well as the SWWs, which have been proposed to significantly influence the precipitation amount on the

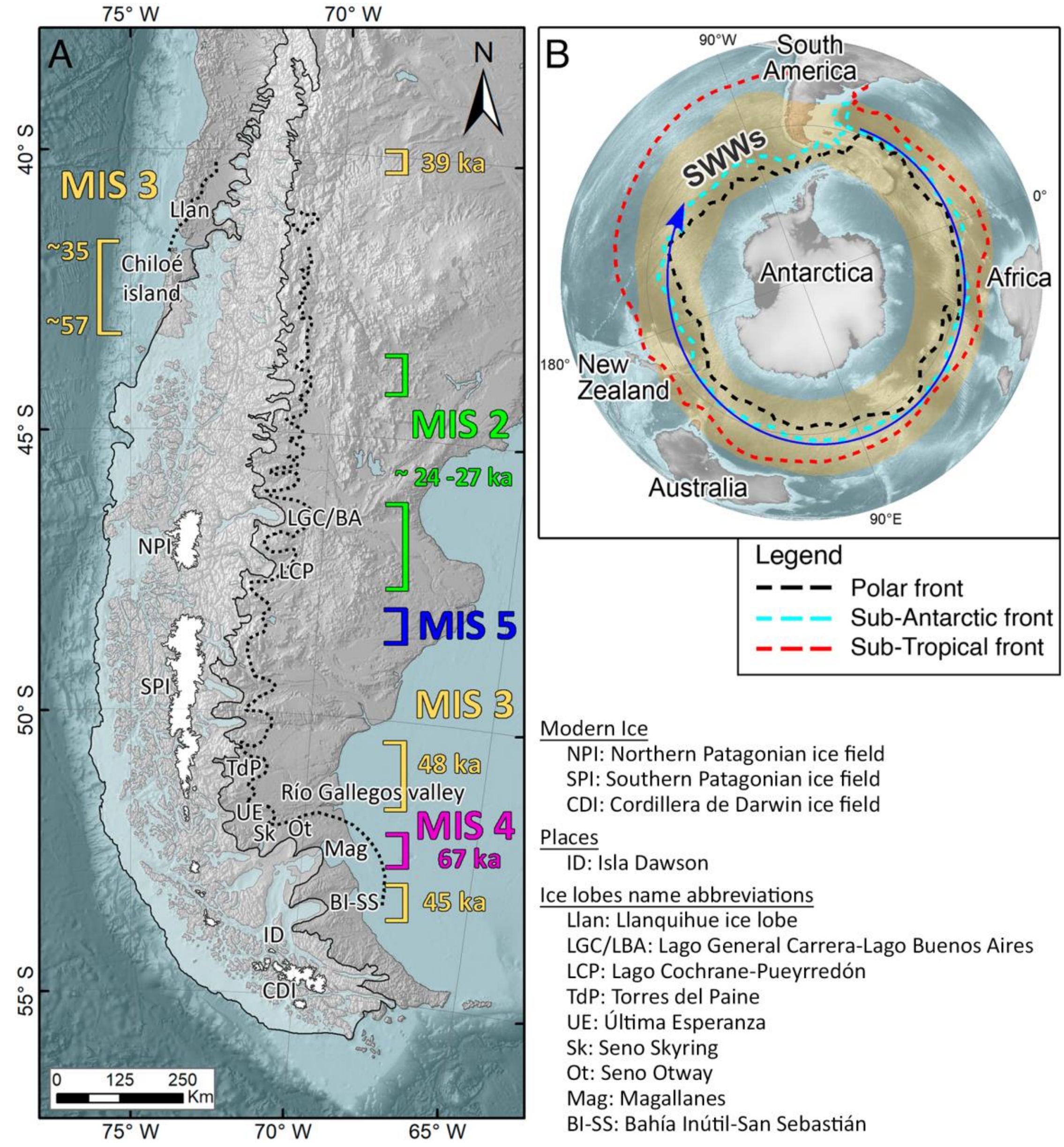

Figure 1.1. Maps showing the location and context of the study area of Patagonia. (A) Map of Patagonia. Modern ice is shown by white polygons. The black continuous line indicates the former Ice Sheet extension during the Last Glacial Maximum according to Davies et al., (2020). Black dashed line shows the inferred extension of the Great Patagonia Glaciation (Singer et al., 2004). The timings for the ice maxima of the dated ice lobes during the last glacial period are shown by brackets, they indicate the latitudinal extent of the ice maxima for a certain period. The brackets are opened towards the dated ice lobes, either on the western or eastern side of the Andes. (B) Polar stereographic projection of the Southern Hemisphere, showing the unique position of the southernmost South America as the only land mass south of 47°S besides Antarctica. The yellow shaded area corresponds to the Southern Westerly Winds domain, and the blue arrow indicates the position of the modern core located ~51°S (Lamy et al., 2010). The oceanic fronts around Antarctica are shown as well, after Kohfeld et al. (2013).

Andes in Patagonia (Anderson et al., 2009; Denton et al., 2010). However, the evolution of the movement of SWWs remains under debate. This may be crucial for the mass balance of the PIS and, thus, for the fluctuations of its outlets (Lamy et al., 2010), with the potential for significantly different responses of outlet lobes depending on their relative position to the SWWs.

Comprehending the behaviour and the timings of the PIS is crucial to understanding the drivers that controlled the glaciations, and by implication likely to help constrain past changes in key drivers such as SWWs. One way to explore the forcing mechanisms is to use precise glacial chronologies tied to numerical modelling of former fluctuations of the PIS. There have been surprisingly few attempts to use ice sheet modelling along the whole of Patagonia (Hulton et al., 1994; 2002; Wolff et al., 2023; Yan et al., 2022). Recently, more data has become available for Patagonia, such as an increase in the geochronological constraints of the glacial fluctuations (Davies et al., 2020) and improvements in datasets of bed elevation, which considers the fjord bathymetries and free ice topography on the present ice fields (Fürst et al., 2024; Millan et al., 2019). This combination of improvements in quality of numerical models, boundary condition data, and in availability of constraints for models provides a timely opportunity to improve the quality and usefulness of the modelling simulations.

This project seeks to understand the controls on the glacier extent and retreat in Patagonia in response to a rapidly changing climate and potential shifts in atmospheric circulation during the last glacial cycle. Through an integrated approach, the project combines geomorphological mapping, geochronology and numerical modelling. The glacial geomorphology and geochronology will be investigated in the Seno Skyring ice lobe, which is located in southeastern Patagonia (Figure 1.1). This is a key outlet, with no chronology of glaciation, but yet lying in a critical location between the well-studied records in the Magellan Strait and in Torres del Paine – Última Esperanza region. The new understanding of this lobe will then feed into the available constraints for the third approach: to perform a set of numerical modelling experiments that will consider different palaeoclimatic scenarios compared to a recent geochronology compilation (Davies et al., 2020) as a border condition to test the response of PIS.

1.2. Aim, Objectives and Research Questions:

The aim of this study is to understand the controls on ice growth and retreat during the last glacial period along Patagonia and particularly the regional asynchrony of the local LGM glacier extents.

A series of research questions and associated objectives are outlined below to address this research aim:

RQ1: *What were the glacial extent and retreat pattern of the Seno Skyring glacier: a key ice lobe that lacks geochronological constraints during the last glacial period? Is this pattern comparable to its neighbouring ice lobes*?

To answer this question this work proposes the following objectives:
Objective 1: To produce a detailed glacial geomorphological map of the Seno Skyring ice lobe in southern Patagonia, which has been previously mapped at a large scale, in order to understand its maximum extent, its pattern of retreat, and the evolution of glacier dynamics during the last glacial period.

Objective 2: To establish an accurate chronological record of the local LGM and subsequent retreat of the Seno Skyring Ice lobe in order to fill a key spatial gap in understanding the temporal evolution of the former Patagonian Ice Sheet.

RQ2: *How sensitive is the LGM ice sheet to non-climatic controls (e.g., changes in glaciology, subglacial conditions, topography)?*
RQ3: *Can we successfully simulate the LGM ice sheet extent along Patagonia?*
RQ4: *What climate conditions are needed to grow an LGM ice sheet for Patagonia?*

The following objective explores these questions.
Objective 3: To use numerical modelling, specifically the Parallel Ice Sheet Model (PISM), to test the sensitivity of a steady-state LGM ice sheet model to a range of possible glaciological conditions and to potential steady-state climatic conditions for the PIS at the LGM through.

The following research questions rely on the achievement of objective 3.
RQ5: *Can we simulate the PIS through the last glacial cycle?*
RQ6: *What controls the retreat pattern of the ice sheet?*
RQ7: *Can we understand what controls the asynchrony in the timings of the maximum ice extent in Patagonia?*

The following objectives investigate the answers to these questions.
Objective 4: To develop palaeoclimate scenarios for the last glacial cycle related to changes in the dynamics of the SWWs.

Objective 5: To conduct transient simulations of the growth, maximum extent and decay of the PIS to explore which climatic patterns and non-climatic factors were important for controlling the behaviour of the PIS during the last glacial period.

1.3. Study Area

The Ice Fields located in Patagonia are the largest body of ice after Antarctica in the Southern Hemisphere (Warren & Sugden, 1993), and thus they are important in the context of regional climate and global sea level, both now and in the past (Carrivick et al., 2016; Glasser et al., 2011). This work concentrates on the former Patagonian ice sheet, with a focus on the late Pleistocene ice extent, especially during the last glacial cycle, and localities where there is proxy or modern data on the main drivers that controlled the glaciations. The descriptions here are brief as this information is detailed, where needed, in the introductions to the chapters that follow.

1.3.1. Patagonian Ice Sheet Configuration

Today, Patagonia hosts three large ice fields: the Northern and Southern Patagonian Ice Field (46-47.5°S and 48-51°S, respectively) and the smaller Darwin Cordillera Ice Field, situated at 51°S, among several minor ice caps (Glasser & Jansson, 2008; Glasser et al., 2008). The late Pleistocene Patagonian Ice Sheet merged all of these ice masses and extended continuously for ~2000 km along the Andean mountains from 38°S to 55°S of latitude, with a previously modelled total volume of ~500,000 km^3 (Hulton et al., 2002; Wolff et al., 2023). In northern Patagonia (~38-43°S) the glaciers were confined to the mountain valleys, described as an alpine glaciation style, and at the western margin of the Andes, the ice reached the Pacific Ocean at ~43°S, southern Chiloé Island (García, 2012). South from there, the western margin formed a large set of marine-terminating outlets, eroding along pre-existing structural faults (Glasser & Ghiglione, 2009). In central and southern Patagonia (~43°-55°S), the ice behaved in a less confined Ice Sheet style (Bentley et al., 2005; Darvill et al., 2014; Lovell et al., 2011), extending broadly to the east of the southern Andes, generating widespread outlet glaciers, marked by well-preserved moraines with associated outwash plains and, in many cases, leaving proglacial lakes during its retreat (Glasser et al., 2008).

1.3.2. Late Pleistocene Glaciations in Patagonia

The best-preserved records of glacial geomorphology in the Patagonia area are located on the east side of the Andes, a result of its dry conditions and relatively stable tectonic context with no major uplift (Clapperton, 1993), and are particularly well exposed due to sparse vegetation. At least 19 different terminal moraines from the Pleistocene in the eastern part of Southern Patagonia have been registered; these deposits are well exposed and preserved at the Buenos Aires Lake lobe (46°S; Singer et al., 2004). The oldest and most extensive glaciation records have been well maintained due to the presence of till interbedded with lava flows, which have a maximum age of 1.1 Ma, dated with 40Ar/39Ar and K/Ar methods (Singer et al., 2004; Ton-That et al., 1999). In southernmost Patagonia some of the pre-LGM outlet lobes coalesced and reached the Atlantic coast south of Río Gallegos valley and north of Magellan Strait (Rabassa, 2008). Evidence of the last two previous glacial cycles (MIS 8 and MIS 6) have been dated in two outlets in central eastern Patagonia through cosmogenic nuclide sampling on moraine boulders (Peltier et al., 2023) and surface cobbles from the associated outwash plain (Leger et al., 2023).

Despite the extensive Pleistocene record in the region, the major focus of the chronological studies has tended to be on the last glacial period (between 110-10 ka). This is reviewed more extensively in Chapter 2 but in broad terms this period saw the PIS reach full-glacial conditions several times (García et al., 2021; Moreno et al., 2015; Smedley et al., 2016). However, the geochronology of the maximum ice extent shows differences in the timing of occurrence of these events along Patagonia, suggesting an asynchrony of the local LGM. Northern Patagonia outlets record ice maxima during early MIS 3. Cosmogenic methods constrain one outlet in northeastern Patagonia at ~39 ka (Zech et al., 2011), and at ~34 ka in northwestern Patagonia with radiocarbon methods (Denton et al., 1999; Moreno et al., 2015). Central eastern Patagonia shows ice maxima during MIS 2, between 27 – 25 ka (Douglass et al., 2006; Hein et al., 2010; Kaplan et al., 2004; Leger et al., 2021; Peltier et al., 2023), almost contemporaneous to the global LGM. One outlet, located east of the main axis of the Andean range, dates back to MIS 5a (Mendelová et al., 2020). The local LGM in southern latitudes precedes by ~20 kyrs the glacial advances in central Patagonia. For instance, Torres del Paine and Última Esperanza ice lobes have ice maxima at 48 ka (García et al., 2018; Sagredo et al., 2011), while in Bahía Inútil-San Sebastián a maximum advance dates back to 45 ka (Darvill et al., 2015; García et al., 2018; Sagredo et al., 2011), both during mid-early MIS 3. Moreover, the Magallanes ice lobe located also in Southern Patagonia, records the ice maxima during MIS 4 (Peltier et al., 2021). However, there are still many outlets that lack geochronological constraints during this period.

After the last glacial termination, ~18 ka (Denton et al., 2010; Moreno et al., 2015), a global cold event occurred, producing a glacier readvance. This event in Antarctica is denoted as the Antarctic Cold Reversal (ACR), which took place between 14.6-12.8 ka (Lemieux-Dudon et al., 2010), preceding the northern hemisphere event, that occurred between 12.9-11.7 ka (Blunier & Brook, 2001), and is called the Younger Dryas (YD). In a similar way to the LGM, the timing and cause of the cold reversal along Patagonia is not well understood and nor is the pattern of the PIS response. In some areas there is evidence of cooling at the same time as the YD chronozone in the Northern Hemisphere, particularly registered on the west (Moreno et al., 2001) and east side (Ariztegui et al.,

1997) of the Andes in the northern Patagonia at 41°S, while further south this signal is less clear (Sugden et al., 2005). On the other hand, some authors have reported earlier glacier advances in mid-southern Patagonia (47-53°S) coeval with the ACR (García, 2012; Moreno et al., 2001; Sagredo et al., 2018; Sugden et al., 2005). The data available for the cold reversal event at the end of the Pleistocene is not as extensive as the LGM data. At the Lago Buenos Aires ice lobe (46°S), a young moraine advance, dates to 14.4±0.9 ka (Douglass et al., 2006). However, in six inner tributary valleys of the Lago General Carrera/Buenos Aires and Purreydón ice lobes, there is evidence of late glacial advances, coincident with the European YD cold event (Glasser et al., 2012). Conversely, at Río Tranquilo Valley, located as well at the inner part of the Pueyrredón Lake lobe, an earlier advance is documented, with ages of 14.9±0.5 ka, coincident with the ACR event (Sagredo et al., 2018). At the Torres del Paine ice lobe, 400 km south, the ACR event is well documented at three different valleys, with ages ranging about 13.2±0.8 ka (Fogwill & Kubik, 2005), 14.8-12.6 ka (Moreno et al, 2001) and an average of 14 ka from three consecutive glacial advances (García et al., 2012). At Isla Dawson in the Magellan Strait (54°S), radiocarbon data constrain a young glacial advance, the moraine E, between 15.5-11.7 cal. ka (McCulloch et al., 2005b).

1.3.3. Asynchrony of the glacial fluctuations along Patagonia

Reasons for this asynchrony between different parts of the PIS are not clear. It has been suggested that the glacial fluctuations in the Southern Hemisphere responded either to a Northern Hemisphere or to a Southern (Antarctica) forcing, depending on the latitude and period (Sugden et al., 2005). For instance, Sugden et al. (2005) suggest a blend of both hemisphere climatic signals during the late glacial. A direct link between Antarctic proxies and these southern hemisphere land masses at millennial scales is inferred during MIS 3 and global LGM (Darvill et al., 2015; García et al., 2018), by comparing sea surface temperatures from western Patagonia (Kaiser et al., 2005; Mashiotta et al., 1999) to dust deposition records in the ocean and Antarctic cores (Sugden et al., 2009). However, the asynchrony of the local LGM could indicate that the regions in Patagonia were affected by different factors, such as topographic controls (Bentley, 1996; Mendelová et al., 2020; Sugden et al., 2002) and/or changes in the atmospheric and oceanic frontal systems (Darvill et al., 2016).

The understanding of the forcing mechanism(s) that drove the glaciations along the last glacial cycle is still unclear, and the evolution of the climatic system is still under debate. It has been proposed that the expansion of Antarctic sea ice alters the oceanic currents, producing a shifting of the Sub-Antarctic Front to the north, generating colder conditions on the coast of Patagonia (Bertrand et al., 2014; Lamy et al., 2004). This movement would also produce a migration of the atmospheric fronts, altering the position of the SWWs, which are directly linked to the precipitation in the area (Garreaud et al., 2013), and their maximum intensities are currently concentrated in a ‘core configuration’ between ~50-55°S (Lamy et al., 2010). Marine records obtained from the continental shelf on western Patagonia (Kaiser et al., 2005; Lamy et al., 2004), and a terrestrial core from a mire located on Chiloé Island (Heusser et al., 1999), indicates wetter conditions for northwestern Patagonia during the cold periods of the last glacial cycle, e.g. MIS 4 and early MIS 2. This suggests a northwards shift of the SWWs’ core (e.g. Bertrand et al., 2014; Kaiser et al., 2005; Lamy et al., 2004; Lamy et al., 2010), but the pattern of movement of the core during the last glacial cycle is still under debate; some authors mention a northern migration of the core (Hulton et al., 2002), which will suggest drier conditions for the South, while other authors refer to a northern expansion (Kaiser et al., 2005), which imply wetter conditions for the North but keeping quite similar conditions for the South. Furthermore, the core’s northern extent during this period is also unknown.

1.3.4. Numerical Modelling of the Patagonian Ice Sheet

There have been a few ice sheet model reconstructions for the whole of Patagonia during the last glacial cycle (Hulton et al., 1994; 2002; Wolff et al., 2023; Yan et al., 2022). It is notable that the early modelling attempts started nearly 30 years ago, and perhaps surprisingly in contrast to modelling of other ice sheets, they only re-commenced in the last few years.

Previous modelling is reviewed in more detail in Chapters 3 and 4 but briefly, most of the model reconstructions have aimed to have a better understanding of the climatic controls on past glaciation. Hulton et al. (1994) took an approach where they combined climatic factors into an ELA position which they modified to account for changes in the temperatures, winds and precipitation. Nonetheless, this approach does not distinguish between the behaviour of the isolated climatic factors, temperature and precipitation (Hulton et al., 2002). Hulton et al. (2002) performed a new approach which treated the temperature and the precipitation independently. They did this by decreasing the overall temperature by 6°C and modifying the distribution of the winds and precipitation along Patagonia, with the aim of simulating the expected climatic conditions according to the hypothesised changes of the SWWs positions. This approach resulted in a larger ice sheet in central Patagonia, with an underestimated extent in the northern and southern regions. Twenty years later and with more geochronological constraints, Yan et al. (2022) forced the PIS with a different palaeoclimate model from the PMIP project for the LGM. They experienced difficulties in achieving the ice extent constrained by the geochronology, especially in the northern area of the PIS. Recently, Wolff et al. (2023)

reconstructed the ice thickness and volume of the former PIS during the LGM through an inverse modelling approach, fitting geochronologically-constrained ice extents and trim lines.

Other numerical model reconstructions for specific regions have also been performed, with the aim of understanding the climatic conditions during the LGM, late glacial and deglaciation periods in those areas (Leger et al., 2021; Martin et al., 2022; Muir et al., 2023; Peltier et al., 2021). Their findings converge in suggesting that in northern and central Patagonia, past climatic conditions were wetter than today (Leger et al., 2021; Martin et al., 2022; Muir et al.,2023), while in the south, they were slightly drier (Peltier et al., 2021), all these accompanied by a decrease in the temperatures, the magnitude of which is dependent on the period that is modelled.

1.4. Thesis structure

A summary of the chapters is outlined below. Chapter 2 covers the development of glacial geomorphological mapping and a new geochronology for fluctuations of the Seno Skyring ice lobe. Chapters 3 and 4 are present the numerical modelling of the PIS with chapter 3 describing the modelling set-up and steady-state climatic sensitivity tests for Patagonia and Chapter 4 showing time-evolving modelling simulations forced by different palaeoclimatic scenarios. Every chapter has an extensive literature review focussing directly on the research topic; therefore, in Chapter 1, the review of the study area is brief. The conclusions are presented in Chapter 5, which brings the findings from the mapping, geochronology and modelling together to summarise the key advances of the thesis.

1.4.1. Chapter 2: The Last Glacial Maximum and Deglacial History of the Seno Skyring Ice lobe (52°S), Southern Patagonia (2022).

María-Paz Lira, Juan-Luis García, Michael J. Bentley, Stewart S. R. Jamieson, Christopher M. Darvill, Andrew S. Hein, Hans Fernández, Ángel Rodés, Derek Fabel, Rachel K. Smedley and Steven A. Binnie. Frontiers Earth Sciences, 10, 892316. Special issue: Glaciation and climate change in the Andean Cordillera.

This published paper seeks to fill a gap in the geomorphology and geochronology of the southern part of the PIS. It presents a new map of the glacial geomorphology of the lobe and outlines the history of the glacial advance and retreat of the Seno Skyring ice lobe during the last glacial period. The methods and results are based on detailed glacial geomorphological mapping from remote sensing and fieldwork, and geochronological analysis of different key events, which tackle objectives 1 and 2. The geomorphology shows that this outlet has two different moraine systems which are separated by a lake that formed during deglaciation. We constrain the glacial advances and deglaciation timings of this outlet and find that the outer moraine system reached close to ice maxima conditions during early MIS 2. These results suggest that the Seno Skyring ice lobe behaves asynchronously with respect to the neighbouring ice lobes which had ice maxima either during early MIS 3 and one during MIS 4. The paper then explores some of the potential explanations for asynchrony.

In this chapter, I undertook the computer-based mapping, the fieldwork, and did much of the laboratory analysis of the cosmogenic nuclides samples, with the exception of the samples from the depth profile. I analysed the geochronological data and drew all the figures. I drafted the manuscript in discussion with M Bentley, JL García and S Jamieson. JL García, M Bentley, H Fernández and A Hein attended to fieldwork. C. Darvill contributed samples to complement the collected data from the depth profile. A Hein, H Fernández, Á Rodés, D Fabel, R Smedley and S Binnie contributed to the laboratory sample dating process. All authors discussed the results and contributed to the final manuscript.

1.4.2. Chapter 3. Exploring Palaeo Climate along Patagonia during the last glacial cycle using Ice Sheet Modelling: Part I - Modelling set-up and climate parameter sensitivity.

This chapter details the ice sheet modelling setup for Patagonia using PISM. It describes the input data that the model requires and also explains the reasons for the model's physical and glaciological constraints. Moreover, it evaluates the influence of different temporal resolutions of the climatic input in the mass balance computation. Finally, it shows some climatic steady-state sensitivity tests for the LGM, conducted by scaling the modern configuration of the temperature and precipitation by different factors. The chapter therefore demonstrates that the palaeo PIS can successfully be simulated, and shows that for the LGM, a climate that is significantly different in pattern from the modern is required. These sensitivity tests meet objective 3 and form the foundation for the construction of the palaeoclimate scenarios in Chapter 4.

1.4.3. Chapter 4. Palaeoclimate along Patagonia during the last glacial cycle through Ice Sheet Modelling: Part II - transient simulations.

This chapter presents the construction of different palaeoclimate scenarios based on the available proxy data and on the climatic sensitivity tests performed in Chapter 3, and then use the PISM to test the time-evolving (transient) glaciation response of Patagonia to these scenarios, thus addressing objectives 4 and 5. The ice sheet simulations from these palaeoclimatic scenarios are compared in detail against geochronological constraints, integrating the data obtained from objectives 1 and 2 with previous publications. From the simulations, we suggest that the SWWs' core had an expanded configuration where the northern extent fluctuated along the last glacial cycle, demonstrating that previous inferences on northwards SWW migration appear to be robust. These past precipitation configurations played an important role in the asynchrony of the PIS during the last glacial cycle. However, this chapter also explains how the differences in the ice surface elevation and bed topography from the northern, central and southern PIS are crucial in the evolution of the mass balance changes.

1.4.4. Chapter 5: Discussion

This chapter draws together the discussion from Chapters 2, 3 and 4 and summarises the main findings. The chapter also summarises some suggested next steps to continue the investigations in this thesis.

Chapter 2. The Last Glacial Maximum and Deglacial History of the Seno Skyring Ice Lobe (52°S), Southern Patagonia

Lira, M. P., García, J. L., Bentley, M. J., Jamieson, S. S., Darvill, C. M., Hein, A. S., Fernández, H., Rodés, Á., Fabel, D., Smedley, R. K. & Binnie, S. A. (2022). The Last Glacial Maximum and Deglacial History of the Seno Skyring Ice Lobe (52° S), Southern Patagonia. *Frontiers in Earth Science*, *10*, 892316.

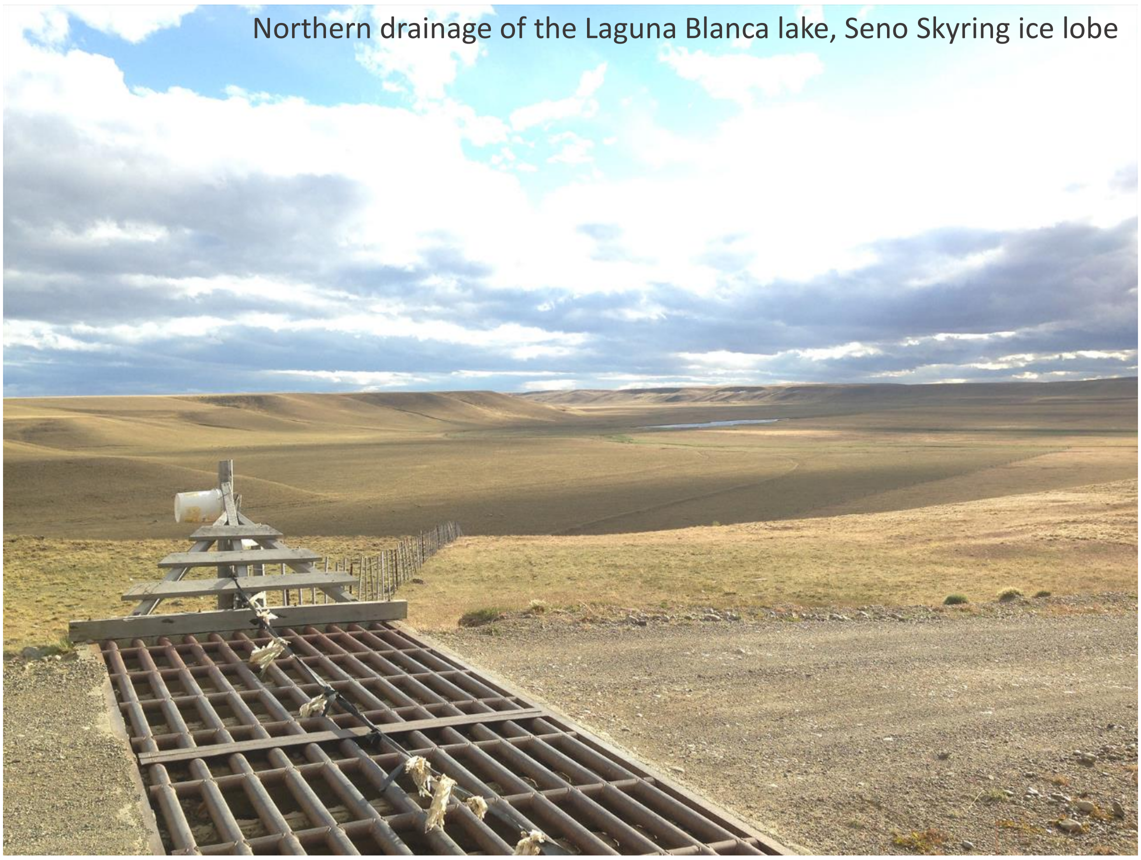

Northern drainage of the Laguna Blanca lake, Seno Skyring ice lobe

Abstract

There are still many uncertainties about the climatic forcing that drove the glacier fluctuations of the Patagonian Ice Sheet (PIS, 38–55°S) during the last glacial period. A key source of uncertainty is the asynchrony of ice lobe fluctuations between the northern, central, and southern PIS. To fully understand the regional trends requires careful mapping and extensive geochronological studies. This paper presents geomorphological and geochronological reconstructions of the glacial and deglacial landforms formed during the last glacial period at the Seno Skyring lobe, southernmost Patagonia (52°S, 71°W). We present a detailed geomorphological map, where we identify two moraine systems. The outer and older is named Laguna Blanca (LB) and the inner Río Verde (RV). The LB moraines were built subaerially, whereas parts of the RV were deposited subaqueously under the palaeo lake Laguna Blanca, which developed during deglaciation. We conducted surface exposure ^{10}Be dating methods on boulder samples collected from LB and RV glacial margins. The moraine LB III and LB IV formed at 26.3 ± 2.3 ka (n = 5) and 24.3 ± 0.9 ka (n = 3), respectively. For the inner RV moraine, we obtained an age of 18.7 ± 1.5 ka (n = 6). For the palaeo Laguna Blanca evolution, we performed ^{10}Be exposure ages on shoreline berms and optically stimulated luminesce dating to constrain the lake levels, and ^{10}Be depth profile dating on an outwash deposit formed by a partial lake drainage event, which occurred at 22 ± 3 ka. For the RV moraine deglaciation, we performed radiocarbon dating of basal sediments in a peat bog, which indicates that the glacier retreated from the terminal RV moraine by at least c. 16.4 cal kyr BP. Our moraine geochronology shows an asynchrony in the maximum extents and a different pattern of ice advances between neighbouring lobes in southern Patagonia. We speculate that this may be due, at least in part, to the interaction between topography and the precipitation carried by the southern westerly wind belt. However, we found broad synchrony of glacial readvances contemporaneous with the RV moraine.

2.1. Introduction

The location of Patagonia in the Southern Hemisphere makes it a good location to study paleoclimate of the Southern Hemisphere since it is the only continental region that straddles the core of the Southern Westerly Winds (SWWs; Figure 2.1A), which are directly linked with the precipitation and temperatures affecting the region (Garreaud, 2009). Moreover, its close position to Antarctica allows comparisons between the terrestrial and marine records from Patagonia with Antarctic climatic proxies (Darvill et al., 2016; García et al., 2020; Sugden et al., 2009). The last glacial cycle was marked by a number of cold intervals, according to Antarctic ice cores (Jouzel et al., 2007). However, these events are not consistently represented in the glacial geomorphology of the Patagonian Ice Sheet (PIS) margin (Davies et al., 2020). Terrestrial geochronologic records show that the maximum extents of the ice lobe fluctuations along the PIS occurred at different times during the last glacial period, suggesting an asynchrony between northern, central and southern Patagonia. Most moraine chronologies have recorded local ice maxima during MIS 2 and MIS 3, but also MIS 4 and MIS 5a (Darvill et al., 2015; Douglass et al., 2006; García et al., 2018; 2021; Hein et al., 2010; Kaplan et al., 2004; Leger et al., 2021; Mendelová et al., 2020; Peltier et al., 2021). This asynchrony of the glacial maximum extensions could be in response to the interaction of different factors, such as shifts of the atmospheric and oceanic frontal systems, Antarctic Sea-ice migration and Southern Ocean stratification (Darvill et al., 2016) and/or topographic controls (Sugden et al., 2002). However, the understanding of the forcing mechanisms that drove this difference in the timing of the glacial fluctuations is still incomplete. To fully understand the past climate that prevailed along the PIS during the last glacial cycle, it is necessary to perform careful mapping and extensive geochronological studies of different outlets. Here, we present glacial geomorphological observations paired with geochronology of the former Seno Skyring lobe (52°S, 71°W) to contribute to the understanding of the behaviour of the former PIS. The glacial geomorphology of this outlet has seen a range of geomorphological mapping at different scales (Caldenius, 1932; Darvill et al., 2014; Lovell et al., 2012; Meglioli, 1992) but the glacial landforms have not previously been dated. Using a combined approach of satellite images, aerial photographs stereoscopic analysis, and field mapping, we produced a more detailed geomorphological map of the study area than previous work and provide a detailed chronological framework using ^{10}Be exposure ages from boulders resting on moraine ridges, cobbles on beach berms and outwash plains, a ^{10}Be depth profile through outwash sediment, optically stimulated luminescence dating of lacustrine deposits, and radiocarbon dating of basal peat sediments. Our aim is to understand the behaviour of the Seno Skyring lobe during the last glacial period and termination.

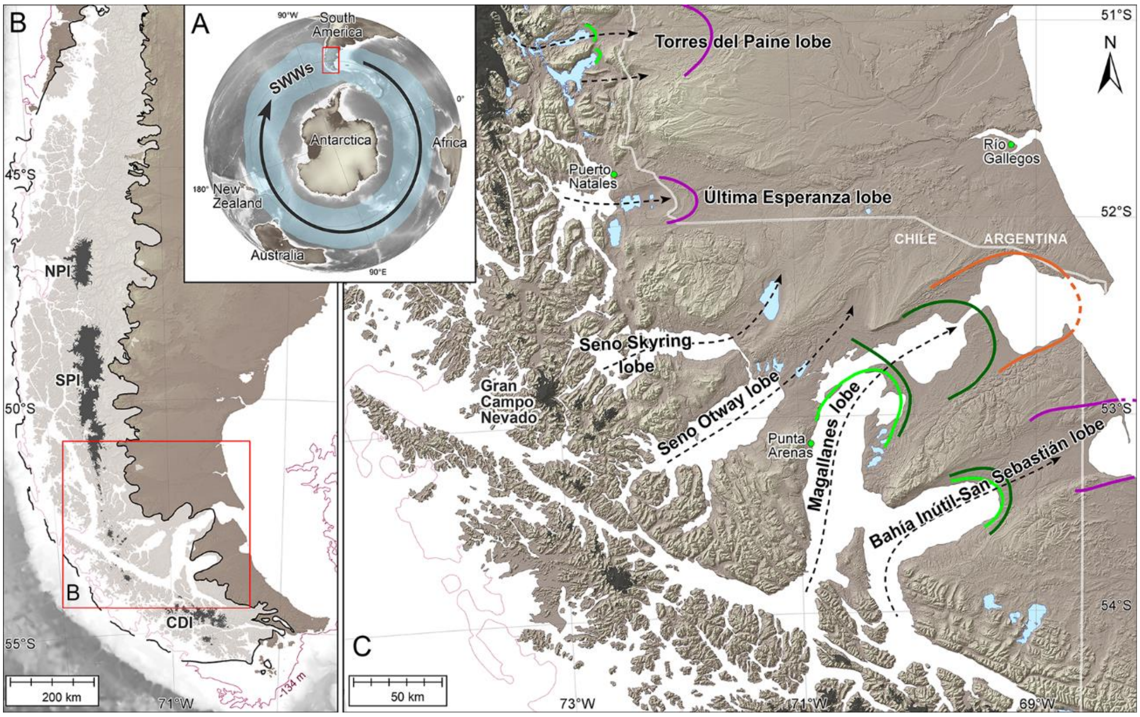

Figure 2.1. Location map. A). Location of Patagonia and the Southern Westerly Winds belt. B). Extension of the Patagonian Ice Sheet during the LGM at 25 ka (pale grey shading, PATICE, Davies et al., 2020). Modern ice is shown by dark grey shading; NPI: Northern Patagonian Icefield, SPI: Southern Patagonian Icefield, CDI: Cordillera de Darwin Icefield. Bathymetric contour of -134 m indicates approximate fall in eustatic sea level during the LGM (Lambeck et al., 2014). C). Location of Seno Skyring ice lobe in Southernmost Patagonia and adjacent ice lobes. Coloured arcs correspond to the age of dated moraine belts from the last glacial cycle: orange corresponds to MIS4, purple to MIS 3 and green to MIS 2 (Darvill et al., 2015; García et al., 2018; Peltier et al., 2021). Darker green indicates glacial margins during early MIS 2 (between 26-24 ka), while lighter green arcs indicate glacial margins from 24 ka to before the onset of the glacial termination (~18 ka; Denton et al., 2010). Black dashed lines are hypothesised flow lines of major outlet lobes. Background image is a Copernicus DEM (30 m resolution).

2. 2. General Setting and Study Area

2.2.1. Southern Patagonian Ice Sheet Setting

During the last glacial cycle in Patagonia, the PIS developed continuously along the Andean Cordillera from 38° to 55°S (Figure 2.1B), extending for about 2000 km (Glasser & Jansson, 2008; Rabassa, 2008; Davies et al., 2020). In southernmost Patagonia, the PIS extended to the west through tidewater-terminating outlets, calving into the Pacific Ocean. To the east, the outlets extended for 10–100 s of km across the Patagonian steppe (Figure 2.1C). The bed topography in this area is slightly unusual in the way the ice occupied reverse-bed slopes whose gradient varied between lobes (Anderson et al., 2012; Kaplan et al., 2009). The eastern area contains the best-preserved records of glacial geomorphology in the region as a result of its dry conditions and relatively stable tectonic context with no major uplift (Clapperton, 1993).

The climate in Patagonia is strongly influenced by SWWs, which impact the position of the Sub Tropical and Sub Antarctic Fronts. The SWWs are directly linked with precipitation (Garreaud et al., 2013), and their core is today located between ~50–55°S (Lamy et al., 2010). During the winter months the SWWs' core expands northwards and during the summer it contracts southwards, in response to seasonal changes in the Antarctic sea ice extent (Garreaud et al., 2013). The precipitation in western Patagonia ranges between 5,000–10,000 mm/year, decreasing abruptly towards the east to less than 300 mm/year (Garreaud, 2009), due to the orographic effect produced by the Andean Cordillera. This rain shadow effect strongly affects the vegetation in the area. Magellanic Moorland and evergreen forest are dominant in the west, and a few tens of kilometres east from the Andes Cordillera, the vegetation sharply changes to Patagonian steppe (Tuhkanen et al., 1989-1990).

We focus here on the southernmost part of the PIS, from the former lobe in Torres del Paine–derived from the southernmost tip of the present-day Southern Patagonia Icefield–south to the former Bahía Inútil-San Sebastián lobe that extended across Tierra del Fuego (Figure 2.1C). This region incorporates a range of different topographic settings from former outlets that terminated close to the mountains (10 s of km length) with a steep slope (such as Torres del Paine, and Última Esperanza), to low-gradient outlets terminations that extended 100 s of km east across the low elevation areas of Patagonia, such as Magallanes, and Bahía Inútil-San Sebastián lobes (Benn & Clapperton, 2000b).

2.2.2. Study Area and Previous Work

The Seno Skyring ice lobe originated at Gran Campo Nevado ice cap (52°40′S), a remnant of the continuous extension of the PIS along the Austral Andes, which has altitudes up to ~1,500 m a.s.l. From there, the ice lobe extended to the east of the Andes (Kilian et al., 2007), sculpting deep valleys that today form the fjord of Seno Skyring (Figure 2.1C). Caldenius (1932) was the first to identify four moraine systems deposited east of Seno Skyring (Figure 2.2); we follow Caldenius' nomenclature for the moraine systems. After Caldenius' (1932) map, Meglioli (1992), Lovell et al. (2012), and Darvill et al. (2014) improved the glacial geomorphological mapping at a regional scale. Later studies suggested that the two inner moraine systems, Laguna Blanca (LB) and Río Verde (RV)—older and younger respectively—were formed during the last glacial cycle, based on the outlet glacier's relationship with neighbouring dated glacial lobes (Darvill et al., 2017; Davies et al., 2020). A proglacial lake formed during the retreat between these two moraine systems (Caldenius, 1932). It has been hypothesised that a partial proglacial drainage may have occurred in front of the receding Seno Otway and Magallanes lobes (Benn & Clapperton, 2000b; Darvill et al., 2014; Lovell et al., 2012).

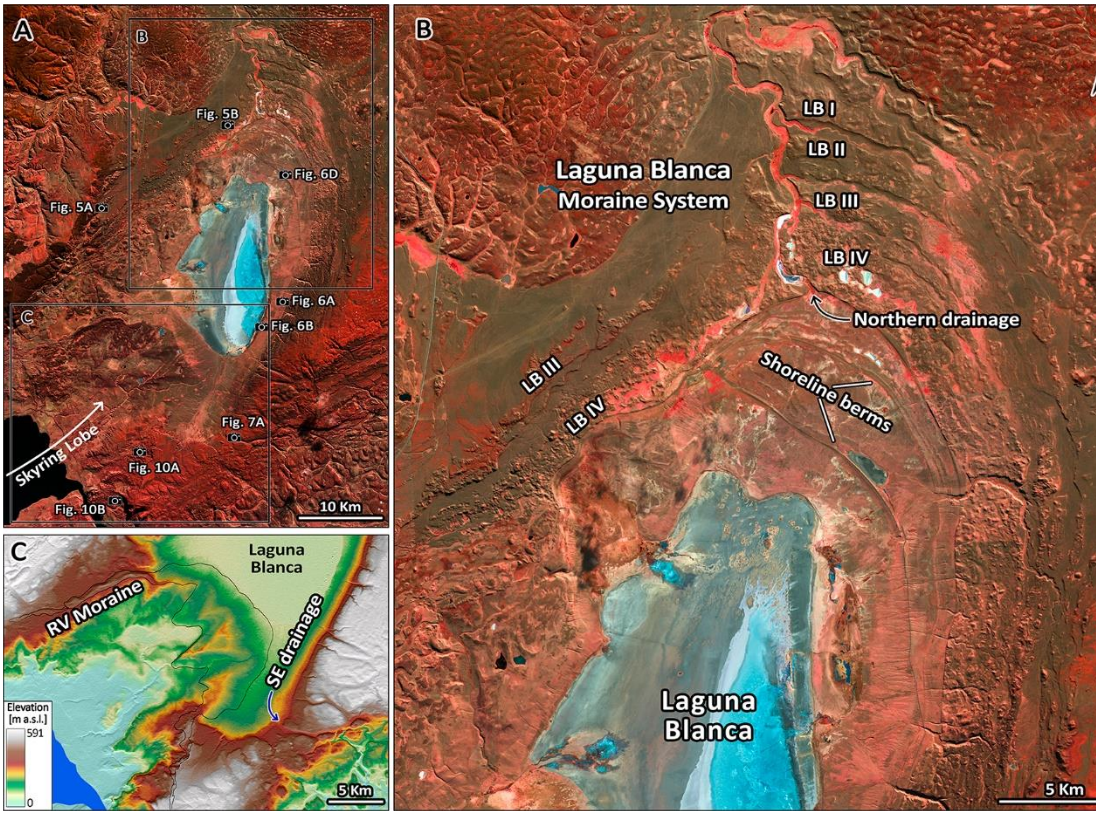

Figure 2.2. A) Sentinel 2 (band combination 843) image of the Seno Skyring ice lobe area. Former ice flow of the Skyring lobe was directed from Seno Skyring north-east to the Río Verde (RV) and Laguna Blanca (LB) moraine systems. B) Detailed image with focus on LB moraine system, showing its four different moraine belts, from older to younger LB **I**, LB **II**, LB **III** and LB IV respectively. Former shoreline berms and a northern drainage spillway of the palaeo Laguna Blanca are indicated. C) Hillshade and elevation colour ramp (SRTM) of the area around RV moraine system, black lines indicate the RV moraine extension. The south-eastern drainage spillway of the palaeo Laguna Blanca is marked. Note that the altitude of this drainage spillway is higher than the central (front) parts of the RV moraine, implying an ice dam must have been present.

Dating of organic material in fjord cores, suggest that towards the end of the last glaciation the Seno Skyring ice lobe had retreated back and was confined to the proximity of the Gran Campo Nevado ice cap by 13.9 ± 0.3 cal. BP (Kilian et al., 2007; 2013). Until the study we present here, no detailed mapping and chronological control existed for the Skyring lobe.

2.3. Methods

We undertook detailed geomorphological mapping and used the mapping to underpin the dating of key landforms to target glacial and deglacial events using cosmogenic ^{10}Be surface exposure dating, a ^{10}Be depth profile, optically stimulated luminescence (OSL) and radiocarbon dating methods. For ^{10}Be cosmogenic measurements, we took samples of boulders on moraines, cobbles on major outwash plains and palaeo-shoreline berms, and measured ^{10}Be concentrations to determine exposure histories. We also sampled one depth profile to determine the age of an outwash deposit using ^{10}Be. These approaches have been widely used in semi-arid regions of eastern Patagonia (e.g., Darvill et al., 2015; García et al., 2018; Hein et al., 2010; Kaplan et al., 2004; Mendelová et al., 2020). Furthermore, we collected lacustrine sediment and bog samples to date with OSL and radiocarbon, respectively.

2.3.1. Geomorphological Mapping

The glacial geomorphologic map was compiled from stereoscopic analysis of aerial photographs, satellite images, and digital elevation models (Table SC2.1; Supplementary Chapter 2). The geomorphological interpretations were fieldchecked over the course of several weeks of fieldwork campaigns in 2018 and 2019. Mapping of former shorelines was supported by hand-held GPS measurement transects up to 35 km along the different terrace levels. The map was prepared in ArcMap 10.7.1 (Figure 2.3).

2.3.2. ^{10}Be Dating

2.3.2.1. ^{10}Be Exposure Age Sampling

Moraines

Timing of former glacial margins were constrained through two different approaches. The first method was by the sampling of moraine boulders along the different ridges. At the Seno Skyring lobe, we sampled along LB and RV moraine systems (Figures 2.2, 2.3). For LB moraines, we collected samples from multiple crests located in LB moraine III and IV. For the RV Moraine, we collected samples at the outer crest of the southeast lateral moraine. The boulder and the sampling process followed the methods of Gosse and Phillips (2001). Sampled boulders were primarily granitoid (n = 17), with some quartzites (n = 4) and one quartz arenite, all embedded in stable positions on or near moraine crests. Heyman et al. (2016) suggested that taller boulders yield more consistent results, since their tops are less likely to have suffered exhumation. We sampled boulders that were >1 m high where possible (32%), but otherwise sampled smaller boulders with ranges of 60–99 cm (45%) and 45–59 cm (23%) high (Table 2.1). For the lower relief boulders, we were careful in avoiding boulders with signs of exhumation by a visual assessment of the moraine degradation. We sampled top surfaces using nail gun cartridges and/or a hammer and chisel, avoiding erosional signs such as fresh edges, spalling or fracturing. Boulder SSK1809, had prominent quartz veins, with mean relief of 20 mm above the rest of the rock surface. We took two different samples from this boulder: SSK1809a from the boulder matrix and SSK1809b from the quartz vein (Figures 2.4K-L). We interpret the ^{10}Be on moraine boulders as minimum ages for the moraine construction and associated glacial advance.

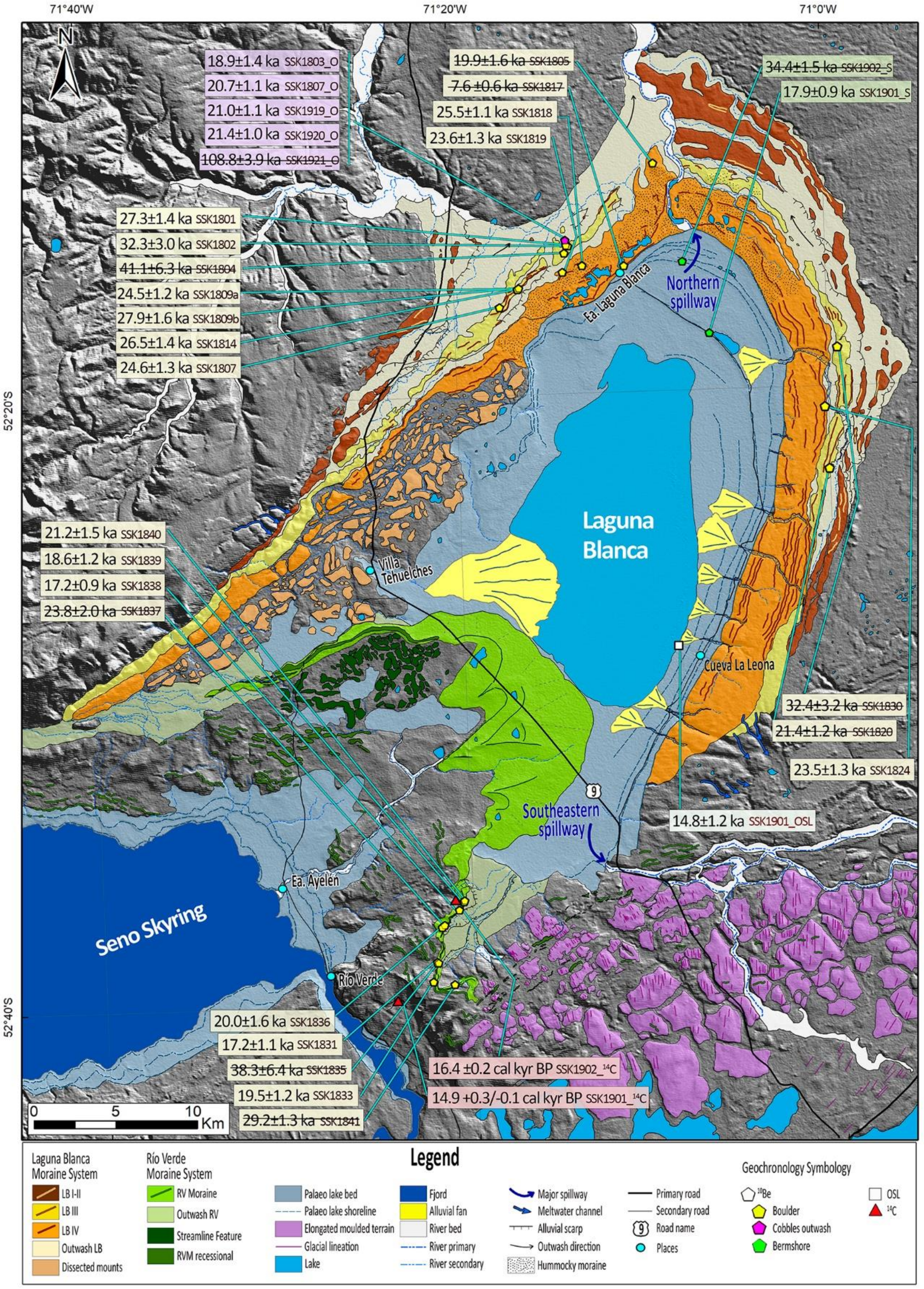

Figure 2.3. Geomorphological map of Skyring ice lobe area. Sample locations of the cosmogenic, OSL, and radiocarbon dates are indicated. Background is a hillshade from SRTM showing the topography. Dates treated as outliers are shown crossed-out, see text for discussion.

Table 2.1. Sample details and ^{10}Be concentrations from Skyring ice lobe and the outwash deposit located in Otway basin, associated with the southeastern Laguna Blanca spillway. The samples are grouped by landform.

Sample ID	Lat. (dd)	Lon. (dd)	Year collected	Alt. (m asl)	Thickness (cm)	Lithology	Boulder height (cm)	Shielding correction	Quartz dissolved (g)	10Be concentration (atoms/g)	±1σ (10Be) (atoms/g)
Seno Skyring ice lobe											
Laguna Blanca Moraine III											
SSK1801	-52.2558	-71.2333	2018/19	238	1.9	Quartzite	226	0.99996	23.16	147002	7644
SSK1802	-52.2529	-71.2313	2018	237	1.7	Granitoid	55	1.00000	21.77	174273	16260
SSK1804	-52.2571	-71.2333	2018/19	239	5.1	Granitoid	45	1.00000	7.00	216115	32612
SSK1807	-52.1496	-71.2304	2018	269	2.1	Granitoid	63	1.00000	20.72	136186	7150
SSK1809a	-52.2764	-71.2761	2018/19	251	1.4	Quartzite	63	1.00000	17.91	134406	6505
SSK1809b	-52.2764	-71.2761	2018	251	2.2	Quartz	63	1.00000	20.54	152020	8437
SSK1814	-52.2762	-71.2756	2018	247	1.5	Quartzite	45	1.00000	17.35	144463	7584
SSK1820	-52.3796	-71.0005	2018/19	289	3.1	Granitoid	80	1.00000	21.04	120066	6700
SSK1830	-52.3127	-70.9907	2018	270	2.7	Granitoid	129	0.99997	13.80	179303	17464
Laguna Blanca Moraine IV											
SSK1805	-52.2090	-71.1514	2018	209	1.3	Granitoid	70	0.99999	13.38	104498	8329
SSK1817	-52.2650	-71.1799	2018	201	1.7	Quartz arenite	84	1.00000	16.36	39226	3134
SSK1818	-52.2642	-71.2175	2018	209	1.6	Granitoid	127	1.00000	22.17	134047	5938
SSK1819	-52.2676	-71.2353	2018/19	217	2.1	Quartzite	100	1.00000	15.09	124716	6710
SSK1824	-52.3455	-71.0030	2018/19	246	1.9	Granitoid	104	1.00000	23.23	128084	7032
Río Verde Moraine											
SSK1831	-52.6455	-71.3671	2018/19	258	2.3	Granitoid	124	1.00000	17.02	94433	5921
SSK1833	-52.6561	-71.3713	2018	310	1.8	Granitoid	64	0.99996	16.86	113277	7114
SSK1835	-52.6459	-71.3670	2018	258	1.7	Granitoid	62	1.00000	11.49	212087	35016
SSK1836	-52.6262	-71.3618	2018	232	2.2	Granitoid	170	1.00000	17.91	107186	8553
SSK1837	-52.6250	-71.3596	2018	231	2.0	Granitoid	55	0.99997	20.91	128180	10908
SSK1838	-52.6170	-71.3459	2018	229	3.1	Granitoid	73	1.00000	21.65	91230	4780
SSK1839	-52.6127	-71.3413	2018/19	229	1.9	Granitoid	67	1.00000	18.47	99761	6594
SSK1840	-52.6123	-71.3415	2018	234	3.3	Granitoid	50	1.00000	21.40	113220	7869
SSK1841	-52.6580	-71.3519	2018	306	2.3	Granitoid	60	1.00000	21.70	168115	7616
Outwash Laguna Blanca Moraine III											
SSK1807_O	-52.2496	-71.2304	2018	230	3.8	Quartz	-	1.00000	22.13	109191	5525
SSK1803_O	-52.2495	-71.2296	2018	231	3.2	Quartzite	-	1.00000	13.44	99775	7114
SSK1919_O	-52.2520	-71.2337	2019	230	2.9	Quartz	-	1.00000	22.32	111624	5670
SSK1920_O	-52.2520	-71.2337	2019	230	3.1	Quartz	-	1.00000	23.49	113129	5408
SSK1921_O	-52.2520	-71.2337	2019	230	4.0	Quartz	-	1.00000	22.04	564700	19877

Table 2.1. (Continued) Sample details and ^{10}Be concentrations from Skyring ice lobe and the outwash deposit located in Otway basin, associated with the southeastern Laguna Blanca spillway. The samples are grouped by landform.

Sample ID	Lat. (dd)	Lon. (dd)	Year collected	Alt. (m asl)	Thickness (cm)	Lithology	Boulder height (cm)	Shielding correction	Quartz dissolved (g)	10Be concentration (atoms/g)	±1σ (10Be) (atoms/g)
Shorelines Berm											
SSK1901_S	-52.3047	-71.1030	2019	139	2.9	Quartz	-	1.00000	21.56	86798	4253
SSK1902_S	-52.2627	-71.1280	2019	163	3.1	Quartz	-	1.00000	21.95	170754	7633
<u>Outwash deposit in Otway lobe</u>											
Surface Samples											
SSKOH1911	-52.5996	-70.5482	2019	32	2.4	Quartz	-	0.999944	-	78400	3400
SSKOH1914	-52.5996	-70.5482	2019	32	2.5	Quartz	-	0.999944	-	52100	2200
SSKOH1915	-52.5996	-70.5482	2019	32	2.7	Quartz	-	0.999944	-	158700	5900
SSKOH1916	-52.5996	-70.5482	2019	32	2.4	Quartz	-	0.999944	-	88300	3200
CD12-OAZ-SS03	-52.5996	-70.5482	2012	32	6	Quartz	-	0.999944	-	73554	2072
CD12-OAZ-SS10	-52.5996	-70.5482	2012	32	6	Quartz	-	0.999944	-	120843	3153
CD12-OAZ-SS11	-52.5996	-70.5482	2012	32	6	Quartz	-	0.999944	-	70725	2242
Depth profile samples				**depth (cm)**							
SSKOH1901-P020	-52.5996	-70.5482	2019	-20	4	Quartz	-	0.999944	-	77100	2400
SSKOH1901-P040	-52.5996	-70.5482	2019	-40	4	Quartz	-	0.999944	-	66000	2400
CD12-OAZ-060	-52.5996	-70.5482	2012	-60	4	Quartz	-	0.999944	-	45811	4476
SSKOH1901-P075	-52.5996	-70.5482	2019	-75	4	Quartz	-	0.999944	-	48300	2300
CD12-OAZ-090	-52.5996	-70.5482	2012	-90	4	Quartz	-	0.999944	-	28932	3097
CD12-OAZ-120	-52.5996	-70.5482	2012	-120	4	Quartz	-	0.999944	-	35997	2763
SSKOH1901-P150	-52.5996	-70.5482	2019	-150	4	Quartz	-	0.999944	-	27100	1500
CD12-OAZ-190	-52.5996	-70.5482	2012	-190	4	Quartz	-	0.999944	-	18508	967

Sampled year 2018/19 is for boulders sampled in two consecutive years (2018 and 2019), this does not affect the age of the sample.

Density of 2.65 g/cm3 for all the surface samples.

Measurements of all the samples were normalized to NIST SRM4325 with nominal ^{10}Be/^{9}Be ratios of 2.79 10^{-11} and half-life of 1.36 Ma Nishiizumi et al., 2007).

For the Skyring ice lobe, the processed blank ratio was between 2.9 and 7.4% of the sample ^{10}Be/Be ratios. For the outwash deposit located in Otway basin the blank ratio was between 4 and 11%. The uncertainty of these corrections is included in the stated standard uncertainties.

Outwash Plains Associated to Moraine Margins

The second approach to dating glacial margins was to sample five quartz-rich cobbles embedded in the surface of an outwash plain grading from the LB Moraine III (Figures 2.4C–E). This follows the methodology of Hein et al. (2010; 2011), where outwash plain deposition is assumed to be broadly synchronous with associated moraine formation (Darvill et al., 2015; Mendelová et al., 2020). On imagery and in the field, the outwash plain was linked continuously to the external ridge of LB Moraine III, but the sample collection was located far enough (~100 m) from the moraine to avoid subsequent downslope deposition. The age of these cobbles provide the minimum age of the outwash deposition.

Palaeo Lake Levels

We sampled two distinctive former shorelines around Laguna Blanca for cosmogenic ^{10}Be exposure dating. These shorelines are located at the inner part of the frontal LB Moraine (Figures 2.2, 2.3) and we assume the source of material corresponds to till eroded by the lake. For each shoreline, we took one sample composed of an amalgamation of ~30 cobbles and large quartz pebbles (Mendelová et al., 2020). We collected the samples on flat top surfaces of wide beach ridges; these berm ridges are large-scale features and surrounded by relatively flat relief within a 2 km radius, so we are confident no material has been deposited on the surfaces since they were deposited. The age resulting from the amalgamated samples indicates a minimum age for the shoreline berm formation.

2.3.2.2. ^{10}Be Depth Profile from an Outwash located on the Seno Otway basin

Previous geomorphological mapping reconstructions (Darvill et al., 2014; Lovell et al., 2011), and our own work link an outwash terrace in the area formerly occupied by the Seno Otway lobe to a drainage event south-eastward from a palaeo Laguna Blanca proglacial lake associated with the Seno Skyring lobe. Dating this deposit should constrain the timing of lake drainage and provide limiting ages for glacier retreat. We adopted two approaches to dating methods on this deposit.

Firstly, we collected surface samples to obtain exposure ages. From the surface of the outwash terrace, we sampled seven monomineral quartz cobbles (Table 2.1).

Secondly, we samples a depth profile in the outwash and modelled nuclide concentrations using Monte Carlo simulations. This approach can be used to calculate the most likely age, erosion rate, and nuclide inheritance ranges of a deposit (Darvill et al., 2015; Hidy et al., 2010; Rodés et al., 2011). The outwash deposit is formed by unconsolidated material composed mainly of pebbles and coarse sand with matrix-supported, grading to different percentages along it. The sediments of the outwash terrace appear to have been deposited continuously, and the surface does not show clear evidence of post-depositional reworking, cryoturbation or bioturbation (e.g., surface meltwater channels are preserved), making it suitable for dating with this approach (Cogez et al., 2018; Darvill et al., 2015; García et al., 2021; Hein et al., 2009, 2011). We collected eight samples from this profile from 20 to 190 cm below soil depth through a section of a modern anthropogenic road-gravel quarry in the outwash at this location (Table 2.1). Depth profile samples were amalgams of quartz pebbles and sand from ~4 cm thick layers at each depth. Samples were collected in two stages from the same sequence, in 2012 and 2019, following the methodology of Darvill et al. (2015). Soil development on the outwash surface is poor, with an average thickness of ~15 cm. Because the stratigraphy is not homogeneous, we estimated the density for each stratigraphic layer and accounted for layer thickness. We estimated the percentage of clasts bigger than sand for each layer, to which we allocated a density of 2.7 g/cm^3. For the rest of the layer, the sand and porosity, we gave a density of 2.7 g/cm^3 and 0, respectively. The porosity values for sand and gravel were taken from the data for unconsolidated materials of Manger (1963), using the porosity range for each layer. We calculated the density proportional to the amount of each material (Hancock et al., 1999), yielding a density range of 2.1–2.3 g/cm^3.

2.3.2.3. ^{10}Be Laboratory Process

The boulders and surface cobble samples were prepared in a combination of the cosmogenic labs. The quartz isolation for moraine boulders and shorelines was performed at Universidad Católica in Santiago, Chile and Edinburgh University, United Kingdom. We obtained clean quartz using acid etching techniques following Hein et al. (2009) methods. The ^{10}Be/^{9}Be measurements were carried out at the Köln AMS, Germany (Dewald et al., 2013), normalized to the revised standard values reported by Nishiizumi et al. (2007). For methodological details refer to Supplementary Chapter 2 (SC2). Final ^{10}Be concentrations and uncertainties are reported in Table 2.1.

The samples from the outwash terrace located on the Otway lobe, were entirely prepared at Scottish Universities Environmental Research Centre as part of the United Kingdom NERC National Environmental Isotope Facility. The surface samples were treated individually, while the samples from the depth profile were treated as amalgams. For the details of the sampling process from quartz isolation and purification, BeO separation, and AMS analysis, see Supplementary Chapter 2 (SC2.1.2 Laboratory methods for ^{10}Be analysis). The ^{10}Be concentration, uncertainties, and sample details are given in Table 2.1.

2.3.2.4. ^{10}Be Exposure Age Calculation

The ages were determined with the online calculator, formerly known as the CRONUS-Earth online calculators, version 3 (Balco et al., 2008). We applied the Patagonian ^{10}Be production rate calculated from Lago Argentino (Kaplan et al., 2011). We use a general quartz density of 2.65 g/cm^3 for all the samples. The topographic shielding factor was negligible, with values between 0.999–1. We calculated the shielding by measuring the horizon geometry every 15° with a hand clinometer, then we converted these data to the shielding factors in the online calculator formerly known as CRONUSEarth (https://hess.ess.washington.edu). For calculation and discussion of results in context with the other results in the region, we follow previous workers in assuming zero erosion and no correction for vegetation or snow cover of the boulders. However, from sample SSK1809b, we can calculate an erosion rate and we briefly discuss its implications below. For the age calculations, we used the Lm scaling scheme (Lal, 1991; Stone, 2000). Selecting a different scaling scheme would not significantly affect our conclusions. The sample characteristics and ^{10}Be data are given in Table 2.1. For the moraine ages, we present the weighted mean of the boulders with one weighted standard deviation as uncertainty. To identify outliers in each moraine group of samples, we use chi-square ($\chi2$ R) statistics. This method rejects samples outside the 2σ envelope, considering the number of samples (Wendt & Carl, 1991). If $\chi2$ R < κ, the samples fall within the 2σ (Spencer et al., 2017). These calculations are made using the web calculator IceTea (Jones et al., 2019; http://ice-tea.org) when plotting a group of samples from a single moraine.

For the age comparisons with other ice lobes on the discussions, we recalculated previously published ages to Lm scaling scheme with the Patagonian production rate (Kaplan et al., 2011), with no correction for erosion, and no correction for snow or vegetation cover, to allow for direct comparisons between datasets.

2.3.2.5. ^{10}Be Depth Profile and Surface Ages from Outwash Deposit in the Seno Otway basin Calculation

For the depth profile and surface samples, we applied the ^{10}Be production rate from Kaplan et al. (2011), calculated in the online calculators formerly known as the CRONUS-Earth online calculators v.3 (Balco et al., 2008) using the Lm scaling scheme (Lal, 1991; Stone, 2000). Thus, we used production rates of 4.3644, 0.01803, 0.03818 atoms/g/year and attenuation lengths of 160, 5,850, 500 g/cm^2 for spallation and fast and negative muons, respectively. For surface samples, we assumed zero erosion and densities of 2.65 g/cm^3.

To model the depth profile age we use the approach from Rodés et al. (2011) and we fitted the depth profile model to our data using the same combine surface exposure-burial MATLAB scripts as described in Rodés et al. (2014). The model requires input ranges for the deposit's possible ranges of density, age, and erosion rate. We constrained the density according to our calculations, and we used a range between 2.1 and 2.3 g/cm^3. A sensitivity test with a broader density range of 1–3 g/cm^3, showed little effect on age, erosion rate and inheritance and so use of a smaller density range is justified. For the possible age range, we are confident based on chronology of other ice lobes (Darvill et al., 2015; García et al., 2018; Peltier et al., 2021), that in the region the ice filled the Otway basin during the last glacial cycle. Nevertheless, we are ultra-cautious and use an age range of 0–1.1 Ma, where the maximum age corresponds to the greatest Patagonian Glaciation (Meglioli, 1992; Singer et al., 2004). We did not constrain the erosion rate of the deposit since we did not have independent information to do so. For each sample depth, we applied a conservative ±2 cm measurement error, which corresponds to the 4 cm sampling strip.

The Monte Carlo method utilises different solutions that best fit the given variables, that include depth profile sample ^{10}Be concentrations, density, age-range, and erosion rate of the deposit. The modelling shows all the possibilities that adjust with the given variables within a one-sigma solution. We performed 50,000 models, and we obtained 3,771 possible results within one sigma of the data. Because this method is a probabilistic approach, it is possible to have different solutions that fit the given inputs. Thus, the model results are given in ranges, where different answers can be correct, especially if the input data are broad or unconstrained. Nevertheless, the model suggests the most likely data.

2.3.3. Optically Stimulated Luminescence

We used OSL dating to determine the age of raised lacustrine deposits around Laguna Blanca's margins. The OSL sample was taken from a 30 cm-thick sand layer, with medium sand grain size embedded within a lacustrine profile, located at the lowest palaeo lake terrace (T6). These sediments overlie glaciolacustrine sediments (with dropstones) but the context and sedimentology of the sampled layer corresponds to an alluvial fan deposit that is interfingered with lacustrine sediments and thus this age provide the timing of a higher lake levels previously to the erosion of level T6. Samples for luminescence dating were collected in opaque tubes hammered into the section and the ends sealed. These were prepared for analysis under subdued lighting conditions following the methodology of Smedley et al. (2016), explained in Supplementary Chapter 2 (SC2.1.3 Field and Laboratory methods for OSL analysis).

2.3.4. Radiocarbon

We use radiocarbon dating to constrain the peat initiation of two different sites located within and inboard of the innermost RV moraines, using a Wright Piston Corer. The samples were cleaned by wet sieving to remove any potential coal present. Cleaned samples were sent to the DirectAMS radiocarbon dating service for final preparation and measurement. We calibrated the ages to calendar years in CALIB 8.2 program (calib.org; Stuiver et al., 2021) using the SHcal20 curve (Hogg et al., 2020). We report the calibrated ages using the 2-sigma calibrated range.

2.4. Results

2.4.1. Geomorphology

The geomorphological relationships of the landscape observations are shown in the geomorphological map (Figure 2.3), and the criteria used to map them are explained in Table SC2.3 (Supplementary Chapter 2).

2.4.1.1. Laguna Blanca Moraine System

The Laguna Blanca moraine system comprises at least four distinctive moraine belts separated by clear outwash plains; they are LB I, LB II, LB III and LB IV from oldest to youngest (Figure 2.2B). They are located in an arcuate arrangement around Laguna Blanca. In the frontal section, 10 km separates LB I from LB IV. A major meltwater spillway of a palaeo Laguna Blanca that was bigger than the present, cuts through this moraine system from the northern point of the Laguna Blanca former basin. We use this outlet to divide the glacial margins into East and West. On the eastern side of the system, the moraines are confined to the high ground that separates the basins of the former Seno Skyring and Seno Otway glacier lobes. On the west, the moraines are more widely spaced than on the eastern side. The outwash plains are narrower at the lateral parts, and they widen—up to 2 km wide in some places—as they get closer to the front of the lobe. The landform preservation decreases towards the outer moraines due to subsequent meltwater erosion, partial, overriding of the older moraines by younger glacial advances and by moraine ridge degradation through time. The outer LB moraine (LB I and LB II) relief is restricted to discontinuous ridges that we link together as a margin due to continuity of associated outwash plains along an arcuate pattern. Nevertheless, these moraines have good local preservation in the northeast area of the ice lobe, with moraine belts ranging between 1 and 2 km wide. On the other hand, the two inner moraine belts (LB III and LB IV) are preserved almost continuously enclosing Laguna Blanca. Despite the relatively poor preservation of the outer belts, all four LB belts expose similar morphostratigraphic characteristics. They have relief in general between 10–15 m high, but in some places, they can be up to 20 m, and their distal slopes are about 7° and their proximal 9° (Figure 2.4A-G). To the east, the large dimension of the inner moraine belt (LB IV) stands out, where they are up to 4 km wide in some areas and have close to 40 km of continuous lateral extension. There, the LB IV has close to 10 parallel nested ridges. The morphology is very different from the central and western area where LB III and IV are formed by a group of hills or short ridges with little structure. Hummocky relief is common in the central area, with significant intermorainic depressions. The western area is pervasively affected by meltwater erosion. Several meltwater channels cut the moraines and the outwash plains with alignments subparallel to the moraine ridges. The meltwater channels can be traced upstream to the Seno Skyring ice lobe's southwest margin. Exposed sections along the moraine belts were scarce. Nevertheless, we identified two lacustrine sediment slabs within sections from LB I and LB IV (Figure 2.5). These slabs were located in near-horizontal positions with regard to the sediment's lamination. These sediments have pervasive climbing ripple cross-lamination structure and exhibit slight brittle deformation and are overlain by till.

2.4.1.2. Laguna Blanca Palaeo Lake

On the inboard margins of the LB moraines, we identified six distinctive raised shorelines corresponding to formerly higher levels of the palaeo Laguna Blanca (Figure 2.6). They are located on the western and eastern sides, named T1 to T6 from older (highest) to younger (lowest), respectively and the elevations of the terraces are illustrated in Figure 2.6E. T1 and T2, were only observed to the north, and they are just represented as terraces. T3 to T6 have a good lateral continuity to the south, their frontal part is in the forms of shoreline berms while the lateral parts are terraces, interpreted as cut-wave terraces, and they are better preserved on the east side (Figure 2.3). The different levels of the upper shorelines are separated by clear scarps, with the best example being the scarp between T3 and T4 with close to 10 m of relief. In the lower terraces, these scarps are less obvious, and we simply observe a change in the slope of the terraces. Furthermore, on the east side, several alluvial fans cover the terraces with material derived from erosion of LB moraines located upslope. Our GPS surveys show that the

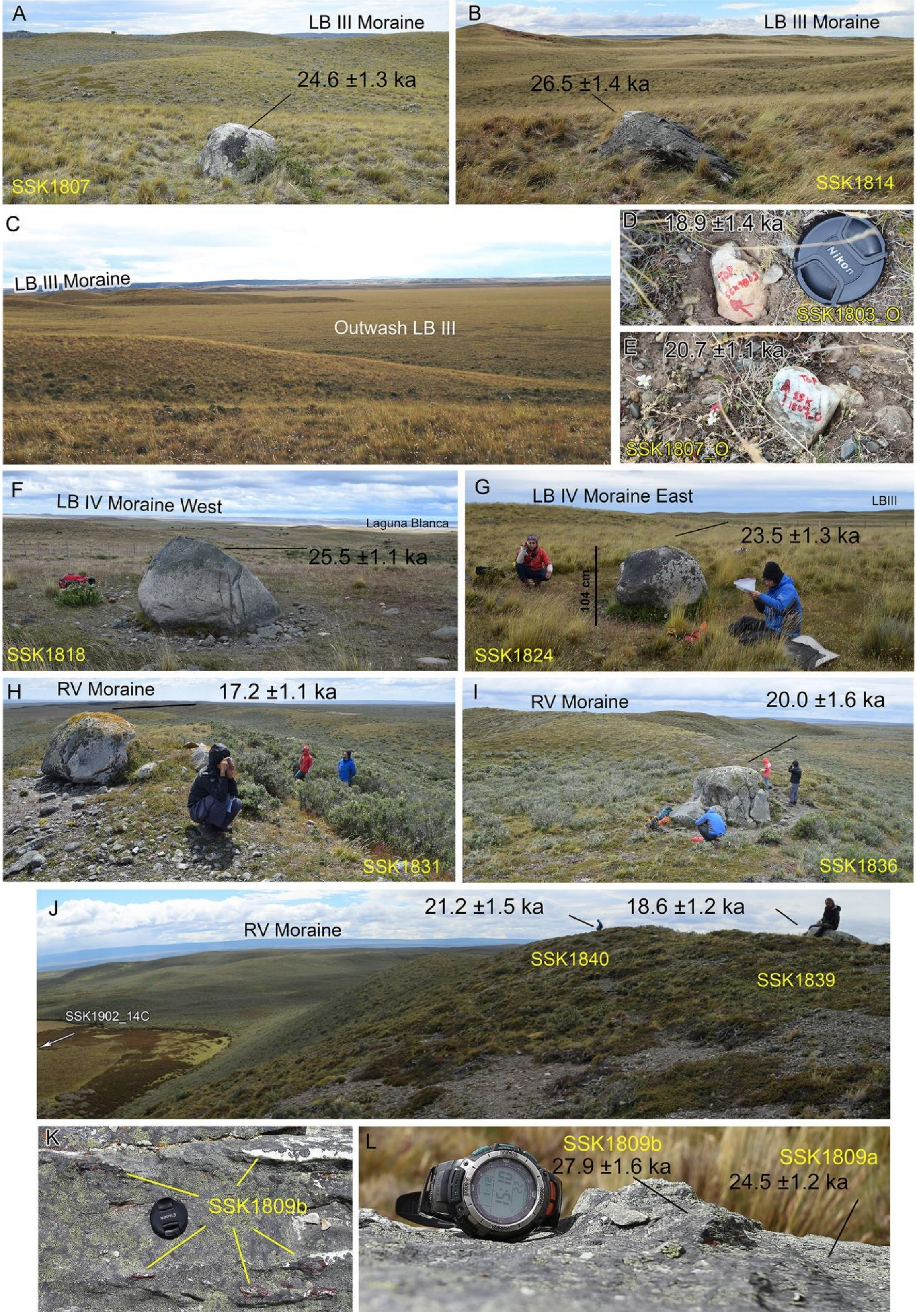

Figure 2.4. Examples of moraine boulder samples and outwash cobbles collected. A,B) Moraine boulders from LB III. C) LB III outwash. D,E) Cobbles collected from LB III outwash. F,G) Laguna Blanca IV. H–J) RV moraine. K,L) Sample SSK1809 showing the sampled quartz vein and sampled boulder surface.

terraces dip at low angles down towards the NNE (i.e., down-glacier direction). The greatest slopes are found on the highest shorelines, and they decrease to nearly horizontal angles towards the lowest (Figure 2.6E).

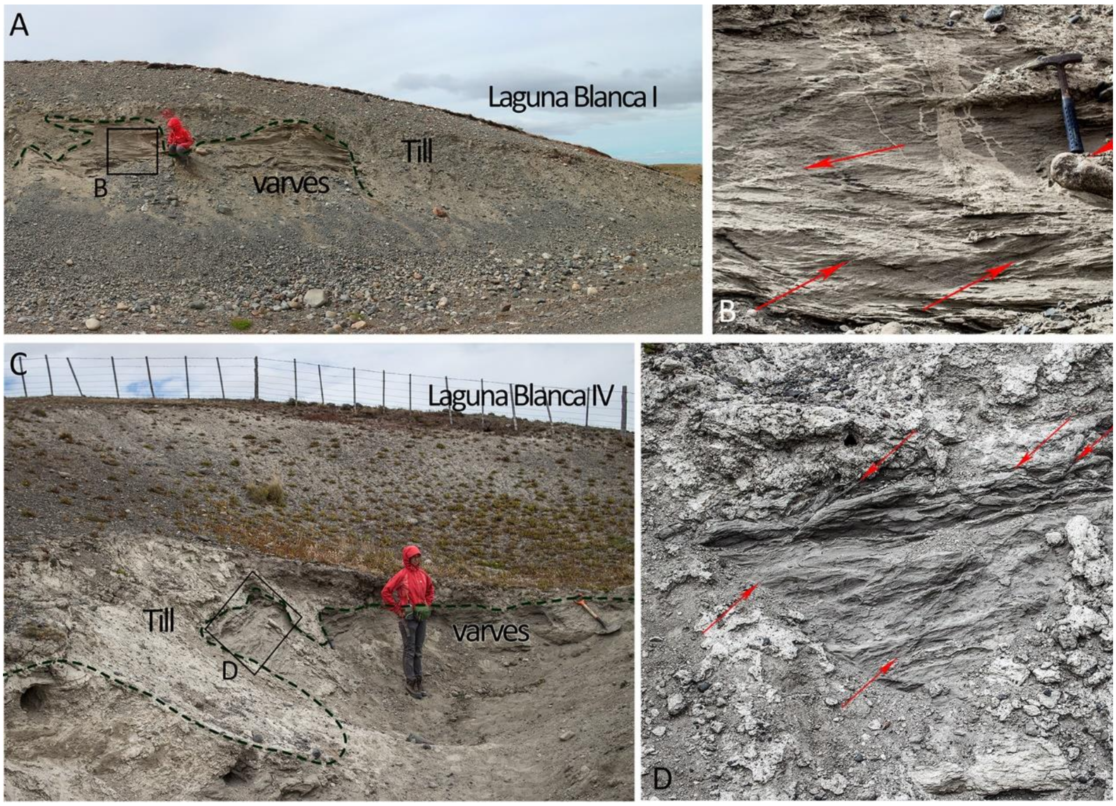

Figure 2.5. Cut profile from LB moraines, showing lacustrine sediments overlain by till. A,B). LB I. C,D). LB IV. The sediments have climbing ripple crosslamination structure. The sediments show evidence of brittle deformation indicated by red arrows.

We mapped two different former spillways for deglacial palaeolake Laguna Blanca. One, located in the north, cuts the frontal area of LB moraines, has an altitude ~185 m a.s.l, and is about 150 m wide. The northern spillway was active during the lake levels of T1 and T2 (Figure 2.6E). Once the lake level lowered from T2, this spillway was abandoned. The second spillway is located in the southeast of the Laguna Blanca basin and cuts through soft bedrock in a series of anastomosing channels towards the Otway ice lobe (Figure 2.3; Figure 2.7A). The southeastern spillway has an altitude ~183 m a.s.l, and is about 300 m wide. This spillway drains east, where it divides into several minor channels, braiding for about 30 km before reaching the Otway basin (Figure 2.7F). Downstream of the spillway there are broad outwash terraces aligned in a west-east direction and which wrap around discontinuous older moraine ridges in the Otway basin (Lovell et al., 2012; Darvill et al., 2014; Figure 2.7E-F). The morphostratigraphic relationship between the spillway and shorelines show that this spillway was active when the lake level was at T4.

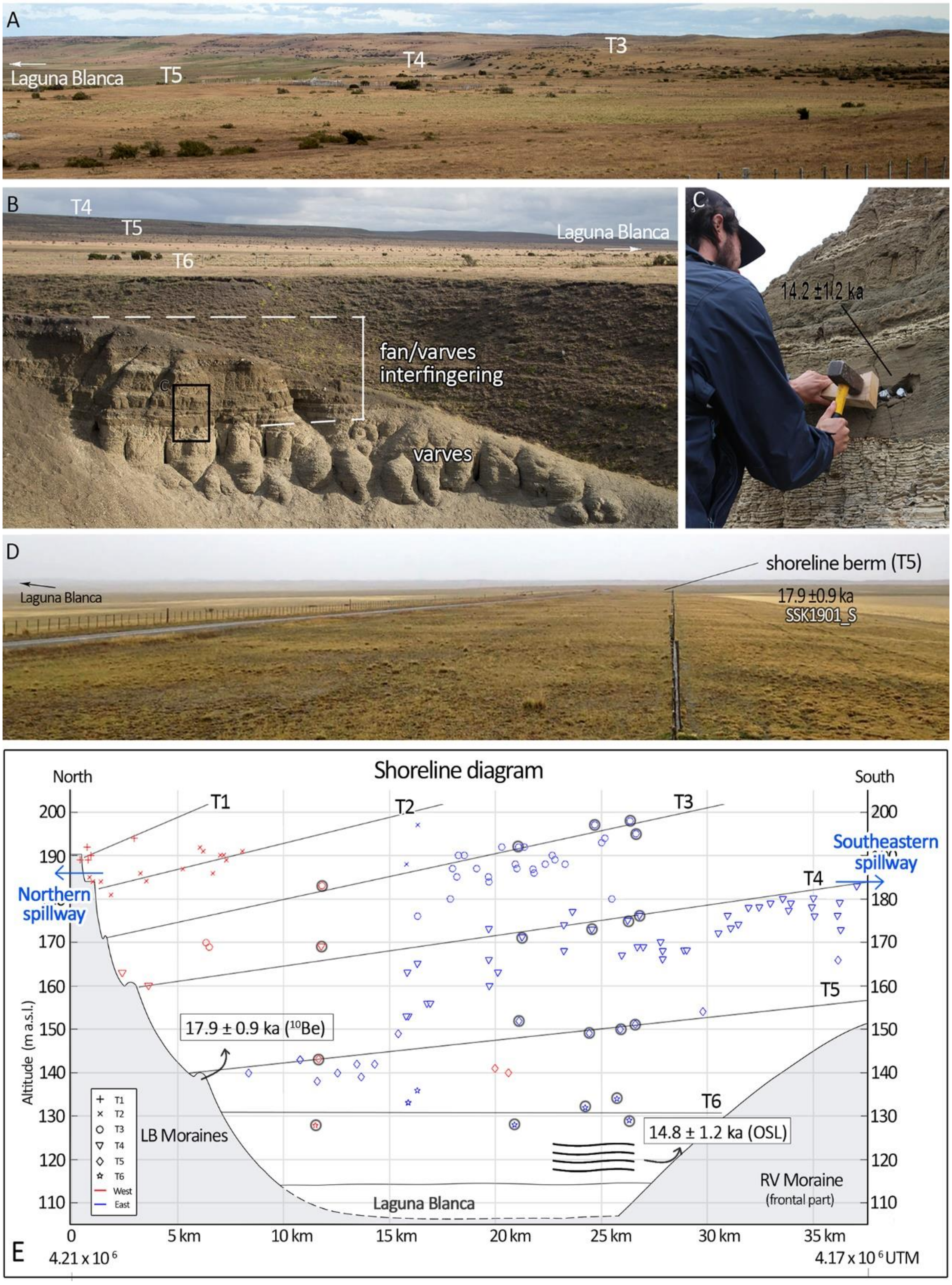

Figure 2.6. Palaeo shorelines of Laguna Blanca. A) Three terrace levels seen at the eastern side of Laguna Blanca. B) Incision of the lowest terrace, T6, exposes glaciolacustrine and alluvial fan sediments. C) OSL sample from a sand layer of the lacustrine profile (see panel b for location). D) Palaeo shoreline berm located at the north part of Laguna Blanca, this berm is related to T5. E) Shoreline Diagram of the former levels of Laguna Blanca. The symbols surrounded by a black circle correspond to the measurements done on the scarp base. The locations are marked of a ^{10}Be age of the shoreline berm on T5, and an OSL sample of a subaqueous alluvial fan taken from araised shoreline forming part of terrace T6. Data from west (red) and east (blue) are differentiated. The elevations and positions of the northern and southeastern drainage spillways are marked. See legend for shoreline/terrace numbering.

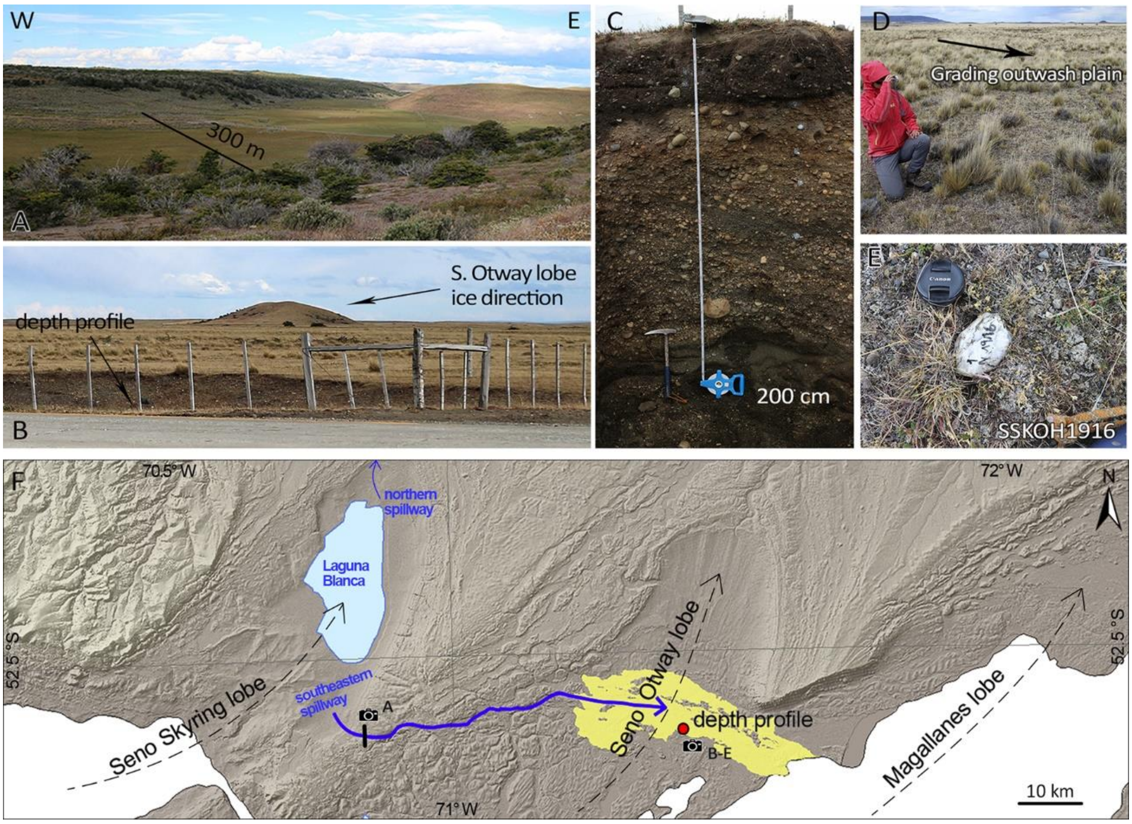

Figure 2.7. Geomorphological record of drainage of Laguna Blanca through the southeastern spillway. A) Southeastern drainage spillway viewed from the south. B) Moraines of the Otway lobe surrounded and partly-buried by a later outwash deposit on both distal and proximal sides. C) Depth profile of the outwash that buries the Otway moraines. D–E) Cobbles sampled for cosmogenic analysis on the surface of the outwash. F) Map showing the mapped drainage route from the southeastern spillway of the Seno Skyring basin towards the Otway lobe basin.

We speculate that the major size of the spillway may be due to it being the route for large volumes of water during a relatively rapid partial drainage of the lake as it lowered from T3 to T4 (Figure 2.6E). After the lake level decreased from T4, this second spillway also became abandoned. T5 and T6 formed subsequently when the lake did not have any apparent spillway.

In T6, several incisions cut the distal part of the terrace, exposing large sediment sections (52.4°S; 71.1°W), at the eastern part of the Laguna Blanca (Figure 2.6B). These sections show a consistent stratigraphy composed at the bottom by at least 6 m of varves composed of clay and silt intercalation, with mmscale horizontal lamination. Additionally, angular and rounded dropstones are embedded within the varves. On top of this unit, dropstone-free laminae are interfingered with sand and gravel with thicknesses ranging from 10 to 70 cm (Figure SC2.2; Supplementary Chapter 2). The sand and gravel layers have wedge-shaped beds becoming thinner towards Laguna Blanca and their base contact is always erosive, while in the varve layers the wedge shapes become thinner in the opposite direction. For OSL dating, we sampled a coarse sand layer located immediately on top of the 6 m of clay/silt unit (Figure 2.6C).

2 .4.1.3. Río Verde Moraine System

The younger moraine system RV is located about 30 km inboard of the LB moraine system. It consists of one prominent terminal moraine and numerous recessional smaller moraines. The morphology of the terminal moraine has a sharp change in morphology at an elevation of 160 m a.s.l. between the lateral and frontal parts. The higher parts of this moraine system, located between 160and 310 m a.s.l., are generally higher relief and sharper-crested than the LB moraines. In the higher, lateral sections, the relief of the ridges range from 30 to 35 m, and their distal and proximal slopes are close to 16° and 20°, respectively (Figures 2.4H–J). The frontal (central) section of this terminal moraine is at a lower elevation (between 120–160 m a.s.l.) with much broader, flat and rounded ridge crests. It is composed of four coalescent ridges in an arcuate shape (Figure 2.2C). This frontal feature can be mapped on imagery but is almost imperceptible in the field; its relief of about 20 m was unnoticeable on the ground due to its width of ~10 km.

Streamlined landforms are visible on the proximal part of the northwest RV moraine. They are low flat-topped hills with rounded limits, elongated concordant with the ice direction. We mapped discontinuous moraine patches about 8 km inboard from the outer RV belt. Further inboard of these recessional moraines are at least four distinctive shorelines terraces marked by the presence of sub-vertical scarps. These terraces step down in height from 60 m a.s.l. to the present shoreline of Seno Skyring to the west.

2.4.2. Geochronology

2.4.2.1. ^{10}Be Exposure Ages

Laguna Blanca Moraine System

The presence of boulders on the LB moraines is extremely scarce. Nevertheless, we processed thirteen boulders for ^{10}Be exposure cosmogenic dating from this moraine system. We present data from the moraine LB III and LB IV in this system (Table 2.2; Figure 2.4). Additionally, we processed four surface cobbles located in the outwash plain apparently grading from LB III (Figures 2.4C–E).

On LB III, we collected eight boulder samples, six from the western lateral part and two from the eastern part. Even though these moraines do not have continuous parallel ridges, the samples SSK1801, SSK1802 and SSK1820 were collected at the outer most part. SSK1807, SSK1809a and SSK1814 were at the intermediate position, SSK1804

Table 2.2. ^{10}Be ages for the study area, assuming 0 erosion rate.

Sample name	Lm			St			LSDn		
	Age ka	± Int ka	± Ext ka	Age ka	± Int ka	± Ext ka	Age ka	± Int ka	± Ext ka
Laguna Blanca Moraine III									
SSK1801	**27.3**	**1.4**	**2.7**	27.8	1.5	2.7	26.5	1.4	2.6
SSK1802	**32.3**	**3.0**	**4.0**	33.0	3.1	4.1	31.4	3.0	3.9
SSK1804 †	**41.1**	**6.3**	**7.1**	42.1	6.4	7.3	39.9	6.1	6.9
SSK1807	**24.6**	**1.3**	**2.4**	25.1	1.3	2.5	24.0	1.3	2.3
SSK1809a	**24.5**	**1.2**	**2.3**	25.0	1.2	2.4	23.9	1.2	2.3
SSK1809b*	**27.9**	**1.6**	**2.8**	28.5	1.6	2.8	27.2	1.5	2.7
SSK1814	**26.5**	**1.4**	**2.6**	27.0	1.4	2.6	25.8	1.4	2.5
SSK1820 †	**21.4**	**1.2**	**2.1**	21.8	1.2	2.2	20.9	1.2	2.1
SSK1830 †	**32.4**	**3.2**	**4.2**	33.1	3.3	4.3	31.5	3.1	4.0
Weighted mean (n=5): 26.3 ka; Wtd. 1SD: 2.3 ka; Wtd. 1SD + PR (3%): 2.4 ka									
Laguna Blanca Moraine IV									
SSK1805 †	**19.9**	**1.6**	**2.3**	20.2	1.6	2.3	19.4	1.6	2.2
SSK1817 †	**7.6**	**0.6**	**0.9**	7.6	0.6	0.9	7.5	0.6	0.9
SSK1818	**25.5**	**1.1**	**2.4**	26.0	1.2	2.4	24.8	1.1	2.3
SSK1819	**23.6**	**1.3**	**2.3**	24.1	1.3	2.4	23.1	1.2	2.3
SSK1824	**23.5**	**1.3**	**2.3**	24.0	1.3	2.4	23.0	1.3	2.3
Weighted mean (n=3): 24.3 ka; Wtd. 1SD: 0.9 ka; Wtd. 1SD + PR (3%): 1.2 ka									
Río Verde Moraine									
SSK1831	**17.2**	**1.1**	**1.8**	17.5	1.1	1.8	16.8	1.1	1.7
SSK1833	**19.5**	**1.2**	**2.0**	19.9	1.3	2.1	19.1	1.2	2.0
SSK1835 †	**38.3**	**6.4**	**7.1**	39.3	6.5	7.3	37.2	6.2	6.9
SSK1836	**20.0**	**1.6**	**2.3**	20.3	1.6	2.3	19.5	1.6	2.2
SSK1837 †	**23.8**	**2.0**	**2.8**	24.3	2.1	2.9	23.2	2.0	2.7
SSK1838	**17.2**	**0.9**	**1.7**	17.5	0.9	1.7	16.8	0.9	1.6
SSK1839	**18.6**	**1.2**	**2.0**	18.9	1.3	2.0	18.2	1.2	1.9
SSK1840	**21.2**	**1.5**	**2.3**	21.6	1.5	2.3	20.7	1.4	2.2
SSK1841 †	**29.2**	**1.3**	**2.8**	29.8	1.4	2.8	28.3	1.3	2.7
Weighted mean (n=3): 18.7 ka; Wtd. 1SD: 1.5 ka; Wtd. 1SD + PR (3%): 1.6 ka									
Outwash Laguna Blanca III									
SSK1807_O	**20.7**	**1.1**	**2.0**	21.1	1.1	2.0	20.3	1.0	2.0
SSK1803_O	**18.9**	**1.4**	**2.1**	19.2	1.4	2.1	18.5	1.3	2.0
SSK1919_O	**21.0**	**1.1**	**2.0**	21.4	1.1	2.1	20.6	1.1	2.0
SSK1920_O	**21.4**	**1.0**	**2.0**	21.7	1.0	2.1	20.9	1.0	2.0
SSK1921_O †	**108.8**	**3.9**	**10.0**	111.8	4.0	10.3	105.3	3.8	9.6
Weighted mean (n=3): 20.6 ka; Wtd. 1SD: 0.9 ka; Wtd. 1SD + PR (3%): 1.1 ka									
Shorelines Berm									
SSK1901_S	**17.9**	**0.9**	**1.7**	18.2	0.9	1.7	17.5	0.9	1.7
SSK1902_S †	**34.4**	**1.5**	**3.2**	35.1	1.6	3.3	33.4	1.5	3.1
Otway lobe Outwash terrace									
SSKOH1911	**17.8**	**0.8**	**1.7**	18.1	0.8	1.7	17.3	0.8	1.6
SSKOH1914	**11.9**	**0.5**	**1.1**	12.0	0.5	1.1	11.7	0.5	1.1
SSKOH1915	**36.1**	**1.4**	**3.3**	36.9	1.4	3.4	34.8	1.3	3.1
SSKOH1916	**20.1**	**0.7**	**1.8**	20.4	0.7	1.8	19.4	0.7	1.7
CD12-OAZ-SS03	**17.2**	**0.5**	**1.5**	17.5	0.5	1.5	16.7	0.5	1.4
CD12-OAZ-SS10	**28.2**	**0.7**	**2.4**	28.8	0.8	2.5	27.2	0.7	2.3
CD12-OAZ-SS11	**16.5**	**0.5**	**1.5**	16.8	0.5	1.5	16.1	0.5	1.4

SSK1809b* vein sample considered for calculating the erosion rate, but not included in the moraine age calculation. For the moraine age, we used the matrix boulder sample (SSK1809a).

† Outlier.

^{10}Be ages calculated in the online calculators formerly known as the CRONUS-Earth v.3 (Balco et al., 2008). We applied the Patagonian production rate of Kaplan et al. (2011), the calibration data set was obtained from calibration.ice-d.org. No shielding correction for snow cover or vegetation. Pressure flag: std. Summary statistics are calculated for each group of samples for a dated landform.

Ages are presented in three different scaling schemes. Lm is the time-dependant scaling scheme of Lal, 1991 and Stone, 2000, we use this for this study (highlighted in bold). St is the time independent scaling scheme of Lal (1991) and Stone (2000). LSDn is the time-dependent scaling scheme of Lifton et al. (2014). Ages are reported with 1 standard deviation internal (int) and external (ext),. Int include analytical uncertainty, and ext includes systematic uncertainties associated with scaling scheme and production rate. Ages are rounded using three significant figures. We report them with the weighted (wtd.) mean and wtd. 1 standard deviation (sd) and the wtd. sd + the production rate uncertainty PR (3%).

and SSK1830 were taken at the moraine's inner part. On LB III, three samples fall outside the 2σ envelope, therefore they would be considered outliers. Finally, for LB III, five boulders yielded ages ranging from 32.4 to 25.0 ka with a weighted mean of 26.3 ± 2.3 ka (Figure 2.8A).

On LB IV moraine, we sampled five boulders. Four of them (SSK1805, SSK1818, SKK1819, SSK1924) were located in the outer part of the moraine, and one (SSK1817) at the inner part. Two boulder ages were rejected as outliers, including the boulder located at the inner part of the moraine. The three samples yielded ages ranging from 25.5 to 23.5 ka, and a weighted mean of 24.3 ± 0.9 ka (Figure 2.8B).

We collected five cobbles from LB III outwash plain. One sample (SSK1921_O) was rejected as an outlier with an age of 108.8 ± 3.9 ka. The remaining four cobbles yielded ages ranging from 21.4 to 18.9 ka, with a weighted mean of 20.6 ± 0.9 ka (Figure 2.8D).

Río Verde Moraine System

In the RV moraine system, there were more abundant moraine boulders than in the LB moraines. We sampled nine boulders on the outer ridge of the eastern lateral section of the RV terminal moraine between 230–310 m a.s.l., above any potential palaoelake level (Figures 2.3, 2.4). Three samples (SSK1835, SSK1837, SSK1841) were rejected as outliers (Table 2.2). The remaining six (SSK1831, SSK1833, SSK1836, SSK1838, SSK1839, SSK1840) samples yielded ages ranging from 21.2 to 17.2 ka with a weighted mean of 18.7 ± 1.5 ka (Figure 2.8C).

Boulder Erosion Rate

We calculated the erosion rate for one boulder (SSK1809) in the Skyring area by sampling quartz veins standing out by approximately 20 mm from the upper rock surface (Figures 2.4K-L). The vein sample, SSK1809b, has an age of 27.9 ± 1.6 ka. Assuming the quartz veins have experienced zero erosion, we calculated a linear-erosion rate of 0.72 ± 0.04 mm/kyr for this quartzite lithology. We assumed a zero erosion rate for the boulders (Table 2.2) because the erosion rate calculated was just performed on one boulder, which may not represent all the other boulder positions or lithologies. Moreover, the use of zero erosion allows us to compare to other studies in southern Patagonia, which also widely assume zero erosion. Nevertheless, to illustrate the effects of potential erosion, we additionally provide the boulder ages for only quartzite lithology, calculated using a 0.72 mm/kyr erosion rate (Table SC2.4; Supplementary Chapter 2). The age difference is minimal when applying this erosion rate for boulders with quartzite lithology. Boulders dated to about 30 ka increase in ~600 years with the erosion rate correction, and boulders dated to about 20 ka increase by ~200 years, which is within the analytical uncertainty. Note that the vein age was utilised just for the erosion rate calculation, and for the LB III moraine age calculation we used the boulder matrix sample (SSK1809a).

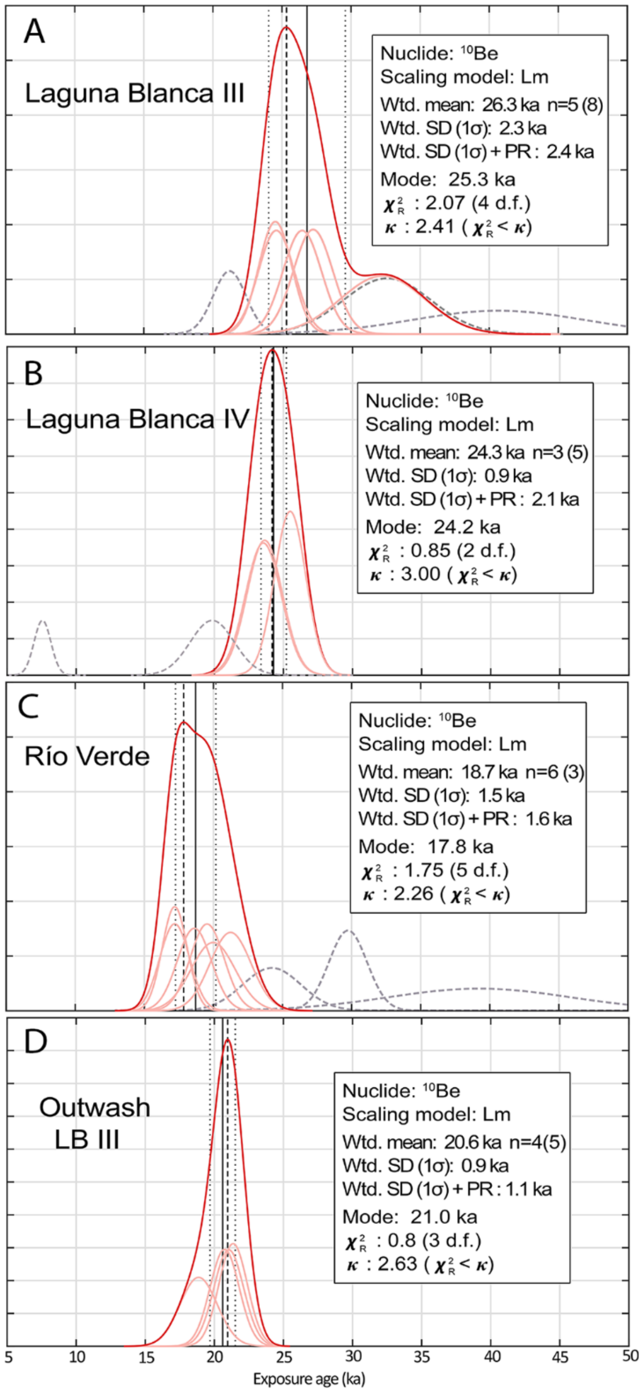

Figure 2.8. Probability density functions (“camel plots”) of the ages for moraines and outwash of the former Skyring ice lobe. All ages are calculated with the Patagonian production rate from Lago Argentino (Kaplan et al., 2011) and considering zero erosion. A) Laguna Blanca III. B) Laguna Blanca IV. C) Río Verde moraine. D) Outwash Laguna Blanca III. n corresponds to the number of samples used to calculate the weighted ages. Bracket numbers are all the samples processed, including outliers. The diagrams were plotted using IceTea (Jones et al., 2019), where the mode (black dashed line), weighted mean (solid black line) and weighted standard deviation (SD; black dotted lines) of the dataset are shown. The application also calculates the reduced chi-squared (χ2 R) and the associated criterion (κ). The outliers are shown as grey dashed lines; they were calculated following reduced chi-squared statistics.

Laguna Blanca Palaeo Lake

We ^{10}Be dated T4 and T5 palaeo-shoreline berms from palaeo Laguna Blanca. The sample SSK1902_S (T4) yielded exposure ages of 34.4 ± 1.6 and the sample SSK1901_S (T5), 17.9 ± 0.9 ka (Figure 2.3). We rejected the sample SSK1902_S since it is anomalously old compared to the LB moraines ages. The most likely explanation for the anomalously old age is that some cobbles sampled in T4 contained inherited ^{10}Be from previous exposure histories. Moreover, the age of a cobble (SSK1921_O) on the LB III outwash plain, ~88 kyr older than the rest of its group, supports the presence of material with inheritance in the area.

2.4.2.2 ^{10}Be From Outwash Deposit in Otway Lobe: Surface Samples and Depth Profile

The seven surface samples from the outwash deposit yielded apparent ^{10}Be exposure ages ranging between 11.9 and 36.1 ka (Table 2.2). Four of the seven samples range between 20.1 ± 0.7 and 16.5 ± 0.5 ka, with a weighted mean of 17.7 ± 1.3 ka. Due to the scattered age range, and potential for deflation or inflation of the sediment surface and possibility of inheritance (Hein et al., 2011), we treat these data as apparent ages (Figure 2.9G). The ^{10}Be concentration of the depth profile samples reduces with depth (Figure 2.9A), consistent with a post-depositional nuclide production in a stable deposit without mixing sediments (Hein et al., 2009). Two exceptions are the samples located at 60 and 90 cm depth that could have mixed sediments or material with more ^{10}Be inheritance concentration at the moment of deposition. It is also important to note that those two samples are the ones that have the largest uncertainty.

The ^{10}Be depth profile modelling results demonstrate a modelled age range between 18–1,101 ka (Figure 2.9B) but with a most likely age between 19 and 25 ka (99.3% of solutions lie in this range; Figure 2.9C). For simplicity, we report this here as 22 ± 3 ka, whilst noting that this does not imply a normal distribution of ages and that different ages in this range may be equally likely (Rodés et al., 2011). The model yields a median inheritance estimate of between 11,422 and 14,522 ^{10}Be atoms/g (Figure 2.9D). This indicates a minimum period of prior exposure longer than ~2 kyr, if all the clasts came from the surface of the eroded deposit. Nevertheless, we know that the cosmogenic radiation decays with depth, and it is very likely that not all the clasts along the profile were located previously on the surface. Therefore, this exposure time is considered a minimum period. Moreover, as we cannot rule out that the eroded channels were active in more than one drainage event, the outwash deposition could have included material that was previously exposed, even in older glaciations. The model does not seem to be sensitive to variations in the density (Figure 2.9E), and this is also supported by the sensitivity test performed with broader parameters. For the erosion rate we obtained a range of 0–39.7 mm/ka (Figure 2.9F). The possible age solutions (0.7% of model runs) older than 22 ± 3 ka (Figure 2.9H) can be ruled out as requiring an unrealistic amount of surface lowering (40–50 m). Such high erosion rates are not likely in arid eastern Patagonia and our geomorphology observations show the outwash surface is well

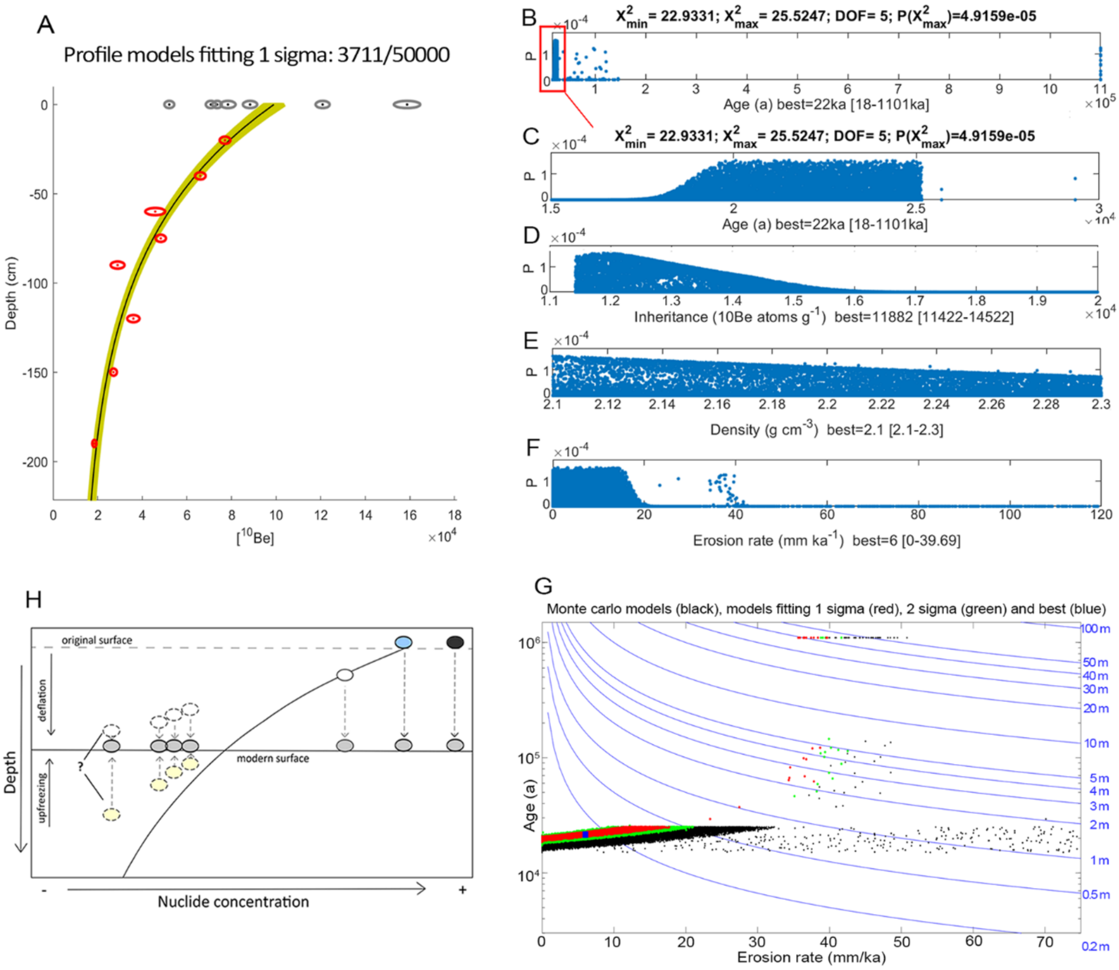

Figure 2.9. Depth profile model results from outwash deposit located in Otway ice lobe, associated with the southeastern Laguna Blanca spillway. A) Plot of ^{10}Be concentration of samples from the surface (grey circles) and depth profile (red circles), with their uncertainties as a function of depth. Green lines indicate the model results that fit within 1 sigma, the black line corresponds to the best fit model. B–F) Probability density distributions of the different outputs of the model: age, inheritance, density, and erosion rate. B) Shows the modelled ages plotted between 0–1,101 ka, whereas C) shows the ages plotted between 15–30 ka. G) Graphic showing relationship between age, erosion rate, and surface lowering. Red dots are model runs lying within 1-sigma of the data, green are those within 2-sigma, and black dots are other model runs. Model output shows 99.5% of data within 1-sigma lie within an age range of 18.6–25.1 ka, with a small component of well-fitting model runs that would require implausible (40–50 m) amounts of surface lowering. H) Schematic cartoon to explain scattered age of the surface samples and reasons for their difference in age from the depth profile modelling. The older samples could have been exposed to the cosmogenic radiation from the outwash terrace formation (blue sample). If the samples have a component of inheritance from earlier exposure, then the age will be older than the terrace (black sample). A deflation of the outwash will expose samples that were initially buried, resulting in younger than the outwash age (white). Younger samples could also be raised to the surface due to inflation processes, such as upfreezing (see Hein et al. (2009), and Darvill et al. (2015) for further discussion).

preserved with melt water channels with decimetre-scale scarps still visible on aerial photographs and imagery, and no signs of pervasive erosion.

We utilize the age modelled through the ^{10}Be depth profile approach (22 ± 3 ka), as the most reliable constraint for this outwash deposit formation and we regard the slightly younger date from surface cobbles as only an apparent age of the deposit.

2.4.2.3. Optically Stimulated Luminescence and Radiocarbon

The OSL sample SSK1901_OSL yielded a deposition age of 14.8 ± 1.2 ka. This sample was collected from a sand layer exposed along the T6 terrace (Figures 2.6B-C).

We constrained the deglaciation by ^{14}C dating of the glacial (inorganic) and peat sediment contact using two ^{14}C samples from two bog sites within and inboard of the RV moraines (Figure 2.10). One site is a peatbog occupying an intermorainic depression just inside RV terminal moraine. At this site, we cored through peat for 1,080 cm, until we reach lacustrine sediments. The sample SSK1902_14C consisted of amalgamated macro plant fossils collected right above the sharp contact between the peat and the lake sediments. The 2σ calibrated age range is 16,236–16,571 cal year BP, for convenience from here on we express the age as c.16.4 cal kyr BP (Table 2.3). Furthermore, the sample site of SSK1901_14C is a bog in an abandoned meltwater channel located inboard and at a lower elevation. There, we cored 575 cm of continuous peat until we reached coarse inorganic sand. The ^{14}C sample consisted of plant macrofossils obtained from just above the sharp contact between the inorganic sand and the overlying peat. The 2σ calibrated age range of the maximum probability is 14,781–15,143, from here on we express this age as c.14.9 cal kyr BP (Table 2.3). The cores from both sites showed sharp contact between inorganic sediments and the peat sedimentation. The type of sedimentology indicates a primary mire formation of peat initiation. This means that the peat originated on newly exposed waterlogged land (Quik et al., 2021; Ruppel et al., 2013). The abrupt nature of the contact suggests a deglaciation event (e.g., Hall et al., 2013; McCulloch et al., 2020).

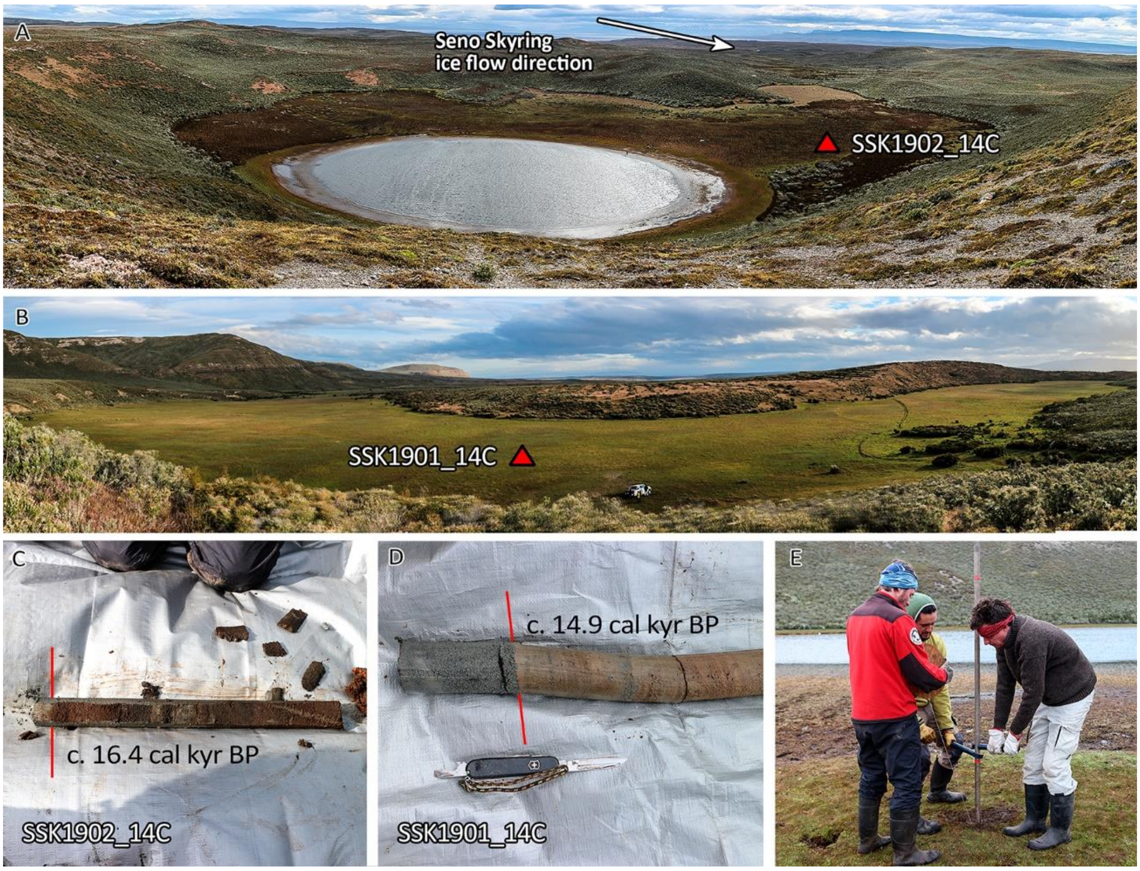

Figure 2.10. A–B) Sample location for radiocarbon dating in peat bogs (red triangles). In (A), the core was taken close to the margin of a lake sitting on the proximal side of the terminal RV moraine. In (B), the core was taken from an abandoned meltwater channel. C–D) Core samples from both sites, red lines indicate the contact between organic and inorganic materials, mud and sand sediment, respectively. E) Wright piston corer being used to sample SSK190214C.

Table 2.3. Radiocarbon sample details. The material from both samples is macro flora. SKK1902_C was collected in a peatbog next to intermorainic pond, and SKK1902_C from a bog in an abandoned melt water channel.

Sample ID	Location			Depth (cm)	Percent modern carbon ±1σ	^{14}C age ±1σ (yr BP)	2σ calibrated range (cal yr BP)	Date expressed in text (**cal kyr BP**)	Probability distribution (%)
	Lat.	Lon.	Altitude (m)						
SSK1902_14C	-52.61	-71.34	185	1080	18.359 ±0.095	13616 ±42	16236 - 16571	c. 16.4	100
SSK1901_14C	-52.67	-71.40	62	575	20.89 ±0.17	12579 ±65	14781 - 15143	c. 14.9	62.2

2.5. Discussions

2.5.1. Geomorphology and Sedimentology Interpretation

2.5.1.1. Laguna Blanca Moraines

We use our geomorphological mapping to compile a relative chronology of glacial advances and deglaciation, which we show in Figure 2.11, and for which we provide a geochronology in the following section.

During the LB moraine system formation, the glacier advanced several times, with at least four stable positions marked by LB I, LB II, LB III, and LB IV moraines (Figure 2.11A). From fine lacustrine sediments that we found in two places within the moraines LB I and LB IV, we suggest that the ice advanced over pre-existing glaciolacustrine deposits. In some places, the glacier detached and transported slabs of these basal sediments (Figure 2.5), emplacing them into the moraines by thrusting. Subsequently, these slabs of glaciolacustrine sediments were covered by till. Thus, the LB moraine system is at least partly glaciotectonic in origin (Benn & Clapperton, 2000a; 2000b; García et al., 2015; Glasser & Hambrey, 2002). Finally, we interpret an active retreat from LB IV (Bennett & Glasser, 1991; Sigfúsdóttir et al., 2018), with several stillstand positions indicated by the presence of more than ten parallel nested recessional moraines in the eastern part of the ice lobe (Figure 2.3).

2.5.1.2. Laguna Blanca Palaeo Lake

The glacier over deepening and the significant input of meltwater from the glacier front during the glacier retreat from LB positions allowed the formation of the Laguna Blanca proglacial lake. As the glacier retreated, this lake experienced different lake levels recorded by T1 to T6 palaeo shorelines. These shorelines dip slightly in a down-glacier direction (Figure 2.6E), which is expected as further upstream the ice thickness increases, producing a greater crustal loading, leading to larger postglacial isostatic uplift in the upstream parts of the former ice lobe (McCulloch et al., 2005a; Stern et al., 2011; Thorndycraft et al., 2019; Troch et al., 2022).

We mapped two different spillways for palaeo Laguna Blanca, located in the north and in the southeast, respectively (Figure 2.3). Today, they have similar altitudes. Nevertheless, we suggest the spillway located in the southeast, was considerably lower during its activity (~20 m), and as the terraces, it experienced isostatic uplift (Figure 2.6E). The lake initially drained to the north (Figure 2.11B). A subsequent decrease in the lake level, possibly accompanied by some isostatic rebound, abandoned the northern spillway. As the glacier retreated back from LB moraine positions, the southeastern

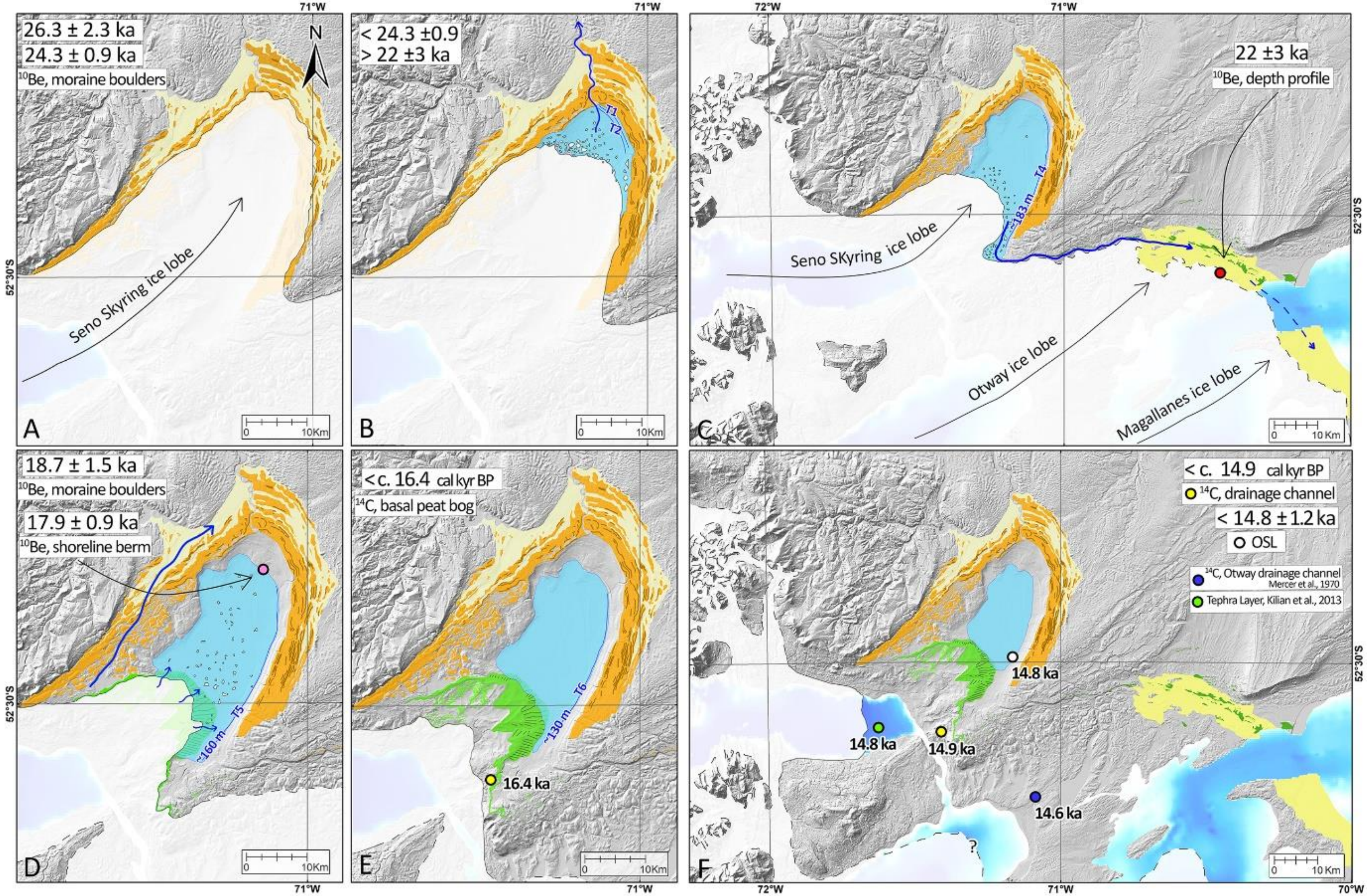
A
26.3 ± 2.3 ka
24.3 ± 0.9 ka
^{10}Be, moraine boulders
N
Seno Skyring ice lobe
0 10Km
B
< 24.3 ±0.9
> 22 ±3 ka
T1
T2
0 10Km
C
22 ±3 ka
^{10}Be, depth profile
T4
~183 m
Seno SKyring ice lobe
Otway ice lobe
Magallanes ice lobe
0 10 Km
D
18.7 ± 1.5 ka
^{10}Be, moraine boulders
17.9 ± 0.9 ka
^{10}Be, shoreline berm
~160 m
T5
0 10Km
E
< c. 16.4 cal kyr BP
^{14}C, basal peat bog
~130 m
T6
16.4 ka
0 10Km
F
< c. 14.9 cal kyr BP
^{14}C, drainage channel
< 14.8 ±1.2 ka
OSL
^{14}C, Otway drainage channel Mercer et al., 1970
Tephra Layer, Kilian et al., 2013
14.8 ka
14.8 ka
14.9 ka
14.6 ka
?
0 10 Km
71°W
72°W
70°W
52°30'S

Figure 2.11. Evolution of the former Seno Skyring ice lobe. A) Glacier position during the deposition of LB III and LB IV moraines. B) Formation of the Laguna Blanca proglacial lake with a northern spillway. During this period, the northern spillway served as drainage for T1 and T2 lake levels. C) Abrupt (partial) drainage of Laguna Blanca to the southeast reaching the Otway lobe region, lake level decreased rapidly from T3 to T4. D) Glacier position during the deposition of RV moraine; the frontal parts formed sub-aqueously under the lake level T5. During this glacial advance/stillstand, the outwash from LB moraines was reactivated at 20.6 ka. E) Minimum age of the glacier abandonment from RV moraine position. F) The Seno Skyring and Otway lobes retreated back to positions into the fjords, evidenced by land exposition and posterior deposition of organic material and tephra on top. At the same time, OSL dating of lacustrine sediments from the palaeo Laguna Blanca indicates a high stand of the lake level between T5 and T6. Note that the shoreline altitudes of the palaeo Laguna Blanca are from measurements taken at the southeastern area of the basin. Dashed lines around ice edges correspond to inferred limits.

spillway opened causing a lake drainage towards the southeast (Figure 2.11C), eroding and transporting a high volume of material that subsequently was deposited downstream as an outwash terrace in the Otway basin (cf. Darvill et al., 2014; Lovell et al., 2012). This event probably drained the lake level of T3 down to T4 where again it stabilised (Figure 2.6E). The interpretation of an abrupt drainage is based on the large size of the southeastern spillway, with a width of 300 m, double the size of the northern spillway, thus implying the loss of higher volumes of lake waters through this channel. Nevertheless, it is possible that these channels have been formed by more than one drainage event during multiple glacial-deglacial cycles. Furthermore, the scarp between T3 and T4 is a sharp prominent break (~10 m of relief) which may indicate a rapid drop in the lake level. The large outwash plains formed at the end of the channel conduits wrap around discontinuous moraine ridges. The similar altitudes between the distal and proximal part of those moraine ridges suggest a post-deposition outwash infill that partially buried pre-existing glacial landforms such as moraines. Following this stage, the lake level lowered further to stabilise at level T5, stopping the meltwater activity from Laguna Blanca to Otway Basin (Figure 2.11D).

From the stratigraphic section described in T6 from palaeo Laguna Blanca (Figure 2.6), we interpret two different depositional environments. At the base, we interpret the first 6 m as finely laminated varves composed of clay and silt intercalation including dropstones. The presence of varves and dropstones shows a direct glacier influence on sedimentation (Evans & Benn, 2021). Above this section, we interpret an interdigitation between subaqueous alluvial fan facies and varves. The clay and silt need a tranquil deposition environment, such as greater depths away from wind-related currents and from steep slopes (Zolitschka et al., 2015). We interpret that the different fan facies represent discrete pulses of tributary streams into the lake basin deposited under the lake level, deep enough and away from the direct influence of the slope to allow the subsequent deposition of varve layers. We interpret the source of the fans comes from the gullies directly east of Laguna Blanca.

2.5.1.3. Río Verde Moraine System

The RV moraine system marks a less extensive glaciation in Seno Skyring and has a different morphological character compared to LB with sharper slopes and higher relief. The dramatic change in morphology from the frontal part to the lateral part of RV outer moraines suggests deposition under different conditions. First, the very gentle slopes with low altitudes (120–160 m a.s.l) of the frontal portion of the RV moraine, with arcuate flat-top mounds and concave up glacier form is interpreted to be a group of subaqueous ice contact fans, where each fan was formed at the mouth of a subglacial conduit (Benn, 1996; Davies et al., 2018; García et al., 2015), discharging into the palaeo Laguna Blanca. In contrast, the lateral sections of RV have higher altitudes (from 160 to 230 m a.s.l.) and relief. They show sharp-crested moraine ridges, implying formation under subaerial conditions. The transition between these two morphologies occurs at 160 m a.s.l. and this is closely similar to the palaeo Laguna Blanca level during T5 (Figure 2.6E). We therefore interpret that this altitude marks the transition between subaerial and subaqueous environment and that the RV moraine was formed at the same time as T5 and that only the lower, central portion of the glacier forming RV was in direct contact with the lake (Figures 2.11D). Following the retreat from RV, the glacier retreated into Seno Skyring. The palaeo Laguna Blanca become detached from the damming ice. Any evolution of the proglacial paleolake formed afterwards was dammed by the RV landforms (Figures 2.11E-F).

2.5.2. Style of Glaciation at Skyring Ice Lobe

Previous studies in Southernmost Patagonia have proposed the existence of warm-based ice lobes with periods of polythermal conditions (Darvill et al., 2017; Glasser et al., 2008). These interpretations are mainly due to the presence of substantial glaciofluvial domains, large subglacial features such as drumlin fields, and brittle deformation observed within moraine sections (Benn & Clapperton, 2000a). Moreover, at Otway and Magallanes ice lobes, located immediately south of Seno Skyring lobe, a surging type of glacier activity has also been suggested (Lovell et al., 2012).

The landform assemblage of Skyring ice lobe indicates an active temperate glacial landsystem (Evans, 2003a). These environments are characterized by three main geomorphological domains, which indicate a wet-based glacier for at least part of the year. These landform associations are push moraines, subglacial deposits, glaciofluvial and glaciolacustrine domains (Chandler et al., 2020; Evans, 2003b; Evans & Twigg, 2002). In this study area, the LB glacial margin is at least partly composed of push moraines, which are best exposed at LB IV. There, the push moraine domain is represented by up to 10 consecutive nested ridges with lengths greater than 12 km, located at the east part of LB IV moraine. Furthermore, the glaciofluvial deposits are present in close association with the moraines throughout the study area including the extensive outwash terraces in the LB system and lateral parts of RV glacial margins. Glaciolacustrine environments were common during the retreat from LB moraine system and the formation of, and retreat from RV moraine system. Finally, we also noted the streamlined mounds moulded in the direction of ice flow and located in the proximal west slope of RV moraines, which are interpreted as forming via subglacial deformation.

Hummocky relief is not common in warm-based glaciers due to the scarce presence of supraglacial debris (Evans, 2003b; Evans & Twigg, 2002). However, hummocky terrain broadly occur in the frontal moraine area of the LB system (Figure 2.3). We attribute the source of supraglacial debris to englacial thrusting of the basal and subglacial sediments, forming a series of stacked moraines (Bennett et al., 1998; Hambrey et al., 1997; Johnson & Clayton, 2003). The glaciotectonic moraine thrusting is supported by the lacustrine sediment slabs found within moraine sections in LB moraines. In temperate environments, thrusting can occur due to ice flow compression in a reverse slope caused by a glacier over deepening (Glasser & Hambrey, 2002). Such a reverse slope is present inboard from LB moraines. On the other hand, the brittle deformation and the absence of ductile deformation in the lacustrine sediments from LB moraine sections (Figure 2.5) suggest that a rigid substrate facilitated thrusting as frozen sediments (Evans & England, 1991), likely to occur in permafrost environments or cold-based glaciers. Here, we hypothesized that the thrusting and stacking of sediment was facilitated by an ice lobe with polythermal conditions, as seasonal permafrost or coldbased margins (Glasser & Hambrey, 2003), as previously reported for the Magallanes ice lobe (Benn & Clapperton, 2000a). Therefore, the landform assemblage from Seno Skyring ice lobe suggests an active temperate glacial landsystem, with the ability to generate thrusting during the cold periods affecting a polythermal glacier.

2.5.3. Geochronology

Using the relative chronology derived from the geomorphological interpretations above we can place firm ages on several of the key events in the glacial history of the Seno Skyring lobe using our ^{10}Be, OSL and radiocarbon dating approach (Figure 2.11).

2.5.3.1. Boulder Erosion Rate

We calculated a linear erosion rate of 0.72 ± 0.04 mm/kyr for one boulder composed of quartzite lithology in LB moraines, assuming the erosion was constant since the boulder deposition. This value falls between previous calculations in Patagonia literature: Kaplan et al. (2005) estimated a maximum erosion rate of 1.4 mm/kyr in a boulder located at 46°S, while Douglass et al. (2007) constrained an erosion rate of 0.2 mm/kyr and, at 47–48°S, Mendelová et al. (2020) calculated an erosion rate of 0.035 mm/kyr from an outwash cobble.

2.5.3.2. Laguna Blanca Moraine System Ages

The surface exposure ages (^{10}Be) from the inner LB moraine system suggest that two Skyring ice lobe advances culminated by 26.3 ± 2.3 ka (n = 5) and 24.3 ± 0.9 ka (n = 3) when LBIII and LBIV were built, respectively (Figure 2.11A). The restricted access to LBI and LBII, the lack of preservation of these landforms on the east side and the absence of boulders mean that we are not yet able to date these outermost landforms. Our geomorphological interpretations suggest a relative contemporaneous formation of the whole LB moraine system, but we cannot yet rule out older ages for LBI and LBII. At the moment of the LB III and LB IV deposition, the glacier occupied almost the full extent of the basin, marking the near-maximum mapped ice extent. Therefore, we can establish that the Seno Skyring ice lobe reached full glacial conditions during the global Last Glacial Maximum (gLGM; MIS 2). Nevertheless, on a MIS 2 moraine, a boulder with an age of 41.1 ± 6.3 ka that we considered as an outlier is likely to contain inherited ^{10}Be from an unknown period of previous exposure. This could perhaps signify that the glacier was at or close to LB positions in an earlier advance, as expected based on neighbourhood chronologies recording middle MIS 3 (Darvill et al., 2015; García et al., 2018; Sagredo et al., 2011) or MIS 4 ice advances (Peltier et al., 2021).

The age of the outwash plain we mapped as linked to LB III yielded an age of 20.6 ± 0.9 ka. Taking the data at face value, this outwash age is 5.7 kyr younger than the LB III age (26.3 ± 2.3ka). From the assumption of an outwash formation during moraine deposition, we would expect that LB III and its associated outwash plain will have an age difference indistinguishable within uncertainties (Hein et al., 2009; Mendelová et al., 2020). The tight ages of the cobbles (Figure 2.8D) suggest this outwash plain was reactivated after the deposition of the older LB III moraine.

2.5.3.3. Palaeo Laguna Blanca Evolution: Partial Drainage Event and Palaeo Shorelines

The timing for a partial drainage event of the Laguna Blanca proglacial lake, when a retreating Seno Skyring ice lobe opened the southeastern spillway, and associated with the decrease of the lake level from T3 to T4, is constrained with an age of 22 ± 3 ka (Otway's outwash ^{10}Be depth profile). For the Otway lobe, this represents a minimum age for the glacial retreat from the "A" moraines (cf., Clapperton et al., 1995) that are partly buried by the outwash. Our date is consistent with recent dating of this ice margin between 23.9 ka (Peltier et al., 2021) which predates the outwash infill we have dated here at 22 ± 3 ka.

The paleolake abandoned the southeastern spillway by 17.9 ± 0.9 ka (SSK1901_S), the exposure age of the next lowest terrace, T5. The timing of RV moraine advance culmination (18.7 ± 1.5 ka) corresponds to the timing of the T5 shoreline berm within uncertainties. This agreement supports the geomorphological interpretations, where the frontal portions of RV moraine were deposited subaqueously under lake level T5 that covered the Laguna Blanca basin (Figures 2.11D). Our OSL age of subaqueous alluvial fan sands intercalated with fine lacustrine sediments suggest the palaeo lake Laguna Blanca persisted at the T6 level until at least 14.8 ± 1.2 ka.

2.5.3.4. Río Verde Moraine System Age and Deglaciation

The inboard RV moraines represent a glacial readvance, during a period between 21.2 and 17.2 ka, with a peak at 18.7 ± 1.5 ka (n = 6). The timing of RV moraine advance culmination also corresponds to the timing of the T5 shoreline berm within uncertainties (17.9 ± 0.9 ka). This agreement in ages supports the geomorphology interpretations, where the frontal portions of RV moraine were deposited subaqueously under lake level T5 (Figure 2.11D). During this glacial readvance we suggest there was a reactivation of the Laguna Blanca outwash noted above in point 5.3.2., and the meltwater from the SW side of the lobe was flowing downwards along the left LB III lateral moraine, depositing younger material over the outwash plain at 20.6 ± 0.9 ka.

Final deglaciation began after the glacier retreated from RV moraine positions. Two radiocarbons dates of peat initiation indicate minimum ages for abandonment of the RV moraines. For the outer part of RV moraines, we have a minimum deglaciation age of c.16.4 cal kyr BP (SSK1901_14C). Additionally, SSK1901_14C provides a minimum age of meltwater channel abandonment at c.14.9 cal kyr BP, and a total glacier retreat from the RV moraine system (Figures 2.11E-F).

2.5.4. Summary of Seno Skyring Ice Lobe Evolution

Our geomorphology and geochronology reconstruction from Seno Skyring ice lobe allows us to interpret the evolution of glacial advances and subsequent deglaciation. The moraine geochronology (^{10}Be) from the inner LB moraine system shows two glacial advances culminating at 26.3 ± 2.3 ka (n = 5) and 24.3 ± 0.9 ka (n = 3) for LBIII and LBIV, respectively (Figure 2.11A). After the ice retreated from LB moraines, a proglacial lake (palaeo Laguna Blanca) formed in front of the ice lobe that first drained to the Atlantic using the northern spillway through the LB moraines. This spillway served as a drainage for T1 and T2 lake levels (Figure 2.11B). Continued ice retreat expanded the lake south-westward and opened abruptly a new spillway to the southeast, which was active by 22 ± 3 ka (Figure 2.11C). We relate the formation of this new spillway to the lake level drop from T3 to T4. A final glacial advance deposited the RV moraine by 18.7 ± 1.5 ka (n = 6; Figure 2.11D). The geomorphology suggests the frontal portions of RV moraine were deposited subaqueously under the lake level T5 (17.9 ± 0.9 ka). After RV moraine system deposition, final deglaciation started in the area. The glacier abandoned the RV terminal moraine by at least c.16.4 cal ky BP and the whole RV system by c.14.9 cal ky BP (Figures 2.11E-F). Moreover, the absence of glacial influence on the sedimentology from the palaeo Laguna Blanca section could suggest the glacier did not further influence the area by 14.8 ± 1.2 ka (OSL). The final demise of the Seno Skyring glacier is recorded by marine core data in the fjord. The presence of a 14.8 ka airfall Reclus tephra in a marine core (Kilian et al., 2013; Stern et al., 2011) showed that the ice had retreated at least 30 km from the eastern shore by this time (Figure 2.11F), and Kilian et al. (2007) suggested that by 14 ka the ice was retreating into the upper parts of the mountains, thus becoming restricted to the Gran Campo Nevado icefield by then.

2.5.5. Glacial Advances in Southernmost Patagonia

From published geochronological records in southernmost Patagonia, we know there were multiple glacial advances during the last glacial cycle, including during the gLGM (26.6–19 ka; Clark et al., 2009). However, the morphostratigraphic pattern of ice advances, the timing of the local LGM (lLGM), and the extent of ice at the gLGM vary between different lobes draining the southernmost portion of the PIS. For example, during the gLGM there were extensive ice advances recorded in the Seno Skyring (52°S), Magallanes (52°- 53°S), Bahía Inútil-San Sebastián (53°S) and Torres del Paine lobes (51°S). But some lobes also showed prominent lLGM advances earlier in the glacial cycle: the Torres del Paine and Última Esperanza (51–52°S) ice lobes show culminations of glacial advances at 48.4 ± 1.7 ka and 48.6 ± 2.0, respectively (García et al., 2018). Similarly, in Bahía Inútil-San Sebastián lobe (53°S) in Tierra del Fuego, the ice maximum is inferred to have occurred at 45.6 ka (Darvill et al., 2015; Figure 2.12). These ice advances record the lLGM in the middle MIS 3, whereas a lLGM during MIS 4 has been recorded by the Magallanes Strait ice lobe (52°-53°S) at 67 ± 2.1 ka (Peltier et al., 2021). In contrast, our results at Seno Skyring ice lobe show full glacial conditions during gLGM at 26.3 ± 2.3 and 24.3 ± 0.9 ka during MIS 2, but no obvious indication of pre gLGM ice advances were dated, although we note that the outer LB I and II moraines remain undated. In any case, the morphostratigraphic position of the LB moraines differs from those in neighbour ice lobes exposing different ice extent through the last glacial cycle. It is notable that no single lobe in southern Patagonia appears to show all of the glacial advances recorded in the region, which in turn denote the need to for glacier records in different basins in order to obtain a complete picture of glacier/climate change during the last glacial period in Patagonia.

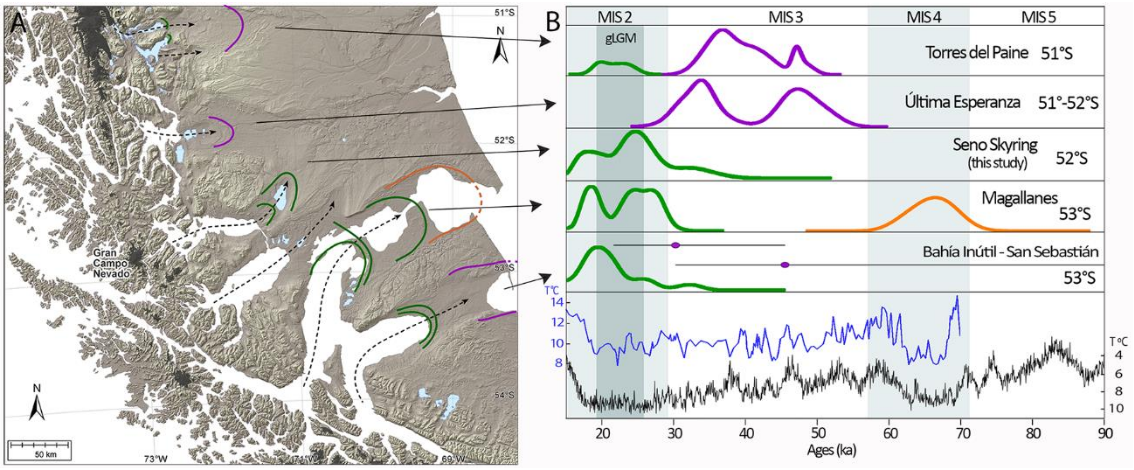

Figure 2.12. Southern Patagonia ice lobe extents and timing of occurrence of the moraine belts during the last glacial period from 15–90 ka. A) Map of major moraine belts which are coloured to match the geochronology in panel (B). Orange corresponds to MIS 4, purple to MIS 3 and green to MIS 2. B) Density functions (probability plots) of exposure ages of moraine boulders in Southern Patagonia moraine belts (this study; McCulloch et al., 2005b; Kaplan et al., 2008; Sagredo et al., 2011; García et al., 2018; Peltier et al., 2021). For the Bahía Inútil-San Sebastián ice lobe, the outer glacial margins were geochronological constrained through a cosmogenic nuclide depth profile approach performed on the outwash plain associated with their respective moraine (Darvill et al., 2015). These ages are indicated by a solid circle (purple) and their uncertainty by a horizontal line. The Sea Surface Temperature (SST) curve (blue) is from an off-shore core in northwestern Patagonia at 41°S (Kaiser et al., 2005) and the east Antarctic temperature record (black) from EPICA Dome C (Jouzel et al., 2007).

If we are to better understand the palaeoclimate of southernmost Patagonia two main questions need to be addressed: First, why do different lobes show different advance extension at similar times? Second, why does the timing of maximum extent differ between lobes?

There are a number of possible reasons for explaining the observed differences. First, there may be a sampling bias due to not all moraines being sampled. Second, there may be a preservation bias: particular moraine belts may have been eroded, overridden leading to an incomplete record of ice history. This is perhaps more likely to occur where there is a large MIS2 advance which may have eroded earlier landforms, which may be the case in Seno Skyring lobe. A third potential explanation is glaciological and topographic differences between ice lobes. For example, differences in basin geometry may control ice behaviour due to variations in the scale, shape and elevation distribution (hypsometry) of the ice drainage catchment (Anderson et al., 2012; Barr & Lovell, 2014; Furbish & Andrews, 1984; Kaplan et al., 2009), as may differences in substrate material (e.g., Benn & Clapperton, 2000b). A fourth set of explanations may lie in regional or local climatic differences. Understanding these influences could be best addressed through numerical modelling of the PIS. Nevertheless, here we provide some initial suggestions of potential explanations.

Patagonia is marked by strong W-E contrasts in precipitation (Garreaud, 2007). This contrast is caused by a rain shadow and continentality effects where the amount of precipitation falls rapidly as air masses rise over the Andes and move progressively east. The interplay of topography and precipitation may influence the geomorphic record of past glacial cycles. For example, those areas with higher elevation can grow more extensive glaciers because they have larger accumulation areas. This is the case for Torres del Paine, Última Esperanza, Magallanes and Bahía Inútil-San Sebastián lobes. These lobes also can start advancing earlier in a glacial cycle, having the potential to record older ice advances within the last glacial cycle. It is not the case where mountains are lower in their catchments, such as Seno Skyring and Seno Otway, since it will take more time for the area to be covered by ice and thus, spread away from the mountain zone (Sugden et al., 2002). Additionally, during the PIS build-up, higher areas will progressively develop an extensive ice sheet to the west (towards the precipitation source), producing the ice divide migration to the west, and provoking snow starvation effect to the east (Sugden et al., 2002). This can imply that during one glacial cycle, subsequent (younger) glacial advances reach more restricted positions, compared to previous advances (Mendelová et al., 2020). This will not be the case where altitudes of the mountains are lower, where the precipitation influence will affect the eastern area for a longer period, and younger glacial advances could have the potential to reach further positions beyond older advances. This could be one reason that in Seno Skyring, where the altitudes of the mountains are lower, the gLGM reaches close to maximum positions, and in the rest of Southern Patagonia, pre gLGM extents are significantly greater than gLGM limits. Moreover, the areas with lower mountains in their upper catchments may have a smaller orographic effect and so may experience greater precipitation over the glaciers.

2.5.6. Paleoclimate in Southernmost Patagonia

A cold temperature period prevailed during MIS 2 in Patagonia, according to Antarctic and Patagonian off-shore sea surface temperatures (SSTs) proxies (Blunier and Brook, 2001; Jouzel et al., 2007; Kaiser et al., 2005). The LB III and LB IV have ages of 26.3 ±

2.3 (n = 5) and 24.3 ± 0.9 ka (n = 3). LB III coincides with the onset of the gLGM and the coldest periods from East Antarctica. Moreover, the LB moraine ages are in agreement - within uncertainties -with the A limit moraine records from Magallanes ice lobe (Clapperton et al., 1995), dating to 25.7 ± 0.8 and 23.9 ± 0.8 (Peltier et al., 2021) and the C limit in Bahía InútilSan Sebastián dating 23.2 ± 1.3 ka (McCulloch et al., 2005b; Figure 2.12). Humidity records in Patagonia during this period (e.g., Heusser et al., 1996; Moreno et al., 2015) suggest wetter conditions for the northern part of Patagonia, and drier for the south, implying a northern migration of the SWWs (Hulton et al., 2002; Moreno et al., 1999; Rojas et al., 2009). The wetter and colder conditions for north-central Patagonia are supported by the ice maxima in central-eastern Patagonia during the gLGM (Douglass et al., 2006; Hein et al., 2010; Kaplan et al., 2004; Leger et al., 2021). Despite the apparent reduction in the precipitation in southern Patagonia for the MIS 2 period, the PIS outlets advanced between about 100–250 km from present-day ice. Therefore, the precipitation in the area should have been sufficient alongside the sharp decrease in temperatures to develop full glacial conditions in the area. Peltier et al. (2021) suggest a mean annual temperature reduction in 4.5°C temperature, when a decrease in 25% of precipitation occurred for southernmost Patagonia during MIS 2.

By the end of the LGM and shortly before the onset of the last glacial termination, a less extensive glacial readvance, inboard from the LGM positions, and culminated at 18.7 ± 1.5 ka, represented in Seno Skyring by the RV moraine system. This broad pattern occurs for several other glacier outlets: in the Magallanes lobe, there are two short periods of glacial readvance/stillstand at 18.1 ± 0.8 and 19.1 ± 0.6 ka (Peltier et al., 2021) and a similar age for the “D limit” in Bahía Inútil-San Sebastián lobe with ages 19.7 ± 2.0 ka (Kaplan et al., 2008; McCulloch et al., 2005b). At Torres del Paine the TDP I moraine dates to 21.7 ± 2.0 ka (García et al., 2018). Considering the timings of these moraines within their uncertainties, there appears to be a close concordance in the timing of a readvance or stillstand at the end of the gLGM, showing a clear regional pattern.

After the RV moraine formation in Seno Skyring lobe, our geochronology shows that by c.16.4 cal kyr BP deglaciation was underway and by 14.8 ka, the glacier was already in the fjord area (Kilian et al., 2013). A synchronous retreat is observed in the Otway ice lobe, where Mercer (1970) reports a minimum deglaciation age of 14.6 cal kyr BP, for the ice abandonment close to the eastern shore of the Otway fjord (Figure 2.11F). Similarly, in the Magallanes and Bahía Inútil-San Sebastián lobes, deglaciation records suggest the glacier retreated to the northern part of Isla Dawson before c. 16.6 cal kr BP (McCulloch et al., 2005b; Mcculloch & Bentley, 1998). Other studies suggest that the glacier was already in the Darwin Cordillera by 16.8 ka, which corresponds to the accumulation area from Magallanes and Bahía Inútil-San Sebastián lobes (e.g., Hall et al., 2019; 2017; 2013). These deglaciation events follow a sharp climatic amelioration that occurred after ~18 ka (Caniupán et al., 2011; Jouzel et al., 2007; Kaiser et al., 2005), which marks the onset of the last glacial termination in Patagonia also (Denton et al., 2010; Moreno et al., 2015). After the increase in temperature, at 18.1 ka the PIS experienced a rapid ice thinning (Boex et al., 2013) and an extraordinarily fast recession (Darvill et al., 2017; Davies et al., 2020; Moreno, 2020). By 14 ka the Seno Skyring ice lobe had retreated to the inner fjords close to Gran Campo Nevado, losing more than 80% of its length compared to its maximum of the last glacial cycle (Kilian et al., 2007).

2.6. Conclusions

Our geomorphology and geochronology reconstructions demonstrate that the Seno Skyring ice lobe reached full glacial conditions during the gLGM, marked by the LB III and IV advances by 26.3 ± 2.3 (n = 5) ka and 24.3 ± 0.9 ka (n = 3). During the ice retreat from the LB moraine system, a proglacial lake developed, which initially drained to the north. As the ice retreated, a new spillway opened towards the southeast by 22 ± 3 ka. A glacier readvance deposited the inboard RV moraines by 18.7 ± 1.5 ka (n = 6), before the onset of the deglaciation. By at least c.16.4 cal ky BP and from the whole RV system by c.14.9 cal ky BP.

We compare our new glacier record from Seno Skyring to published records from other lobes in southernmost Patagonia. There are differences in the morphostratigraphic pattern and timing of advances between lobes, with no single lobe recording all the advances seen regionally. We speculate that some of the differences in the ice extent throughout the last glacial period may be related to the snow starvation effect in response to a northward migration of the westerlies and/or a westward migration of the ice divide during the PIS build-up throughout the last glacial period. Nevertheless, right after the gLGM and before the Termination, broadly synchronic glacial advances with relatively reduced extents are recorded along southern Patagonia.

Chapter 3. Exploring Palaeo Climate along Patagonia during the last glacial cycle using Ice Sheet Modelling Part I: Modelling set-up and climate parameter sensitivity


Aysén fjord, central Patagonia

3.1. Introduction

Terrestrial geochronology constraints in Patagonia show that the ice maxima of different outlets from the ice sheet occurred at different times during the last glacial cycle (e.g., Darvill et al., 2015; García et al., 2018; Figure 3.1). Overall, there is a regional tendency for northern and southern Patagonia to have maximum ice extents earlier, during MIS 3 (Darvill et al., 2015; Denton et al., 1999; García et al., 2018; 2021) and MIS 4 (Peltier et al., 2021). On the other hand, Central Patagonia shows mostly ice maxima during MIS 2 (Douglass et al., 2006; Hein et al., 2010; Kaplan et al., 2004; Leger et al., 2021). There are still many uncertainties about the drivers that controlled this asynchrony, however, the literature suggests this may be most likely due to changes in the climatic conditions along the last glacial cycle (Darvill et al., 2015; García et al., 2018; Kaiser et al., 2005;). One approach to tackling this uncertainty is to test the response of the Patagonian Ice Sheet to different climatic forcing scenarios through numerical modelling tied to geochronological constraints. Ice sheet models for Patagonia with a focus on the Last Glacial Maximum are scarce (Hubbard et al., 2005; Hulton et al., 1994; 2002; Yan et al., 2022; Wolff et al., 2023), and they have not tackled the asynchrony problem. However, more recently there is more data availability, such as the increase in the geochronological constraint for the ice extent and better quality of bed elevation, which includes the fjord bathymetries and ice-free topography for Patagonia, all of which can be combined to improve model outcomes. Moreover, the advances in ice sheet modelling allow better consideration of the glaciological and physical parameters (e.g., flow across ice-ocean boundaries, isostatic adjustments, among others). In this work, we use the Parallel Ice Sheet Model (PISM; Bueler & Brown, 2009; Winkelmann et al., 2011) to test the response of the Patagonian Ice Sheet to a range of possible palaeoclimate scenarios (Chapters 3 and 4). In this chapter, the model set-up, including the input data required for the Patagonia region, is described. Thereafter, the glaciological and physical parameter selection, as chosen according to the literature or via sensitivity tests are determined. With the model set-up, we test the ice sheet response to steady-state climate scenarios for the LGM by decreasing the temperatures and modifying the precipitation by different magnitudes. The outcome of Chapter 3 is therefore an understanding of the parameter and model configuration required to produce an LGM ice sheet similar to that known from geological evidence. This is then used as the basis for time-dependent modelling of the PIS under a range of climate scenarios in Chapter 4.

3.1.1. Previous numerical modelling in Patagonia

Previous reconstructions of the former Patagonian Ice Sheet (PIS) during the Last Glacial Maximum (LGM) through numerical modelling are scarce, but initial work was done nearly 30 years ago, and most numerical studies explore the climatic influence on reconstructing glaciation. The first modelling reconstruction of the PIS was done by Hulton et al. (1994) using a shallow ice approximation model which does not enable physically-based streaming flow. They modified the Equilibrium-line Altitudes (ELAs) along Patagonia to account for changes in temperature and precipitation. Through mass

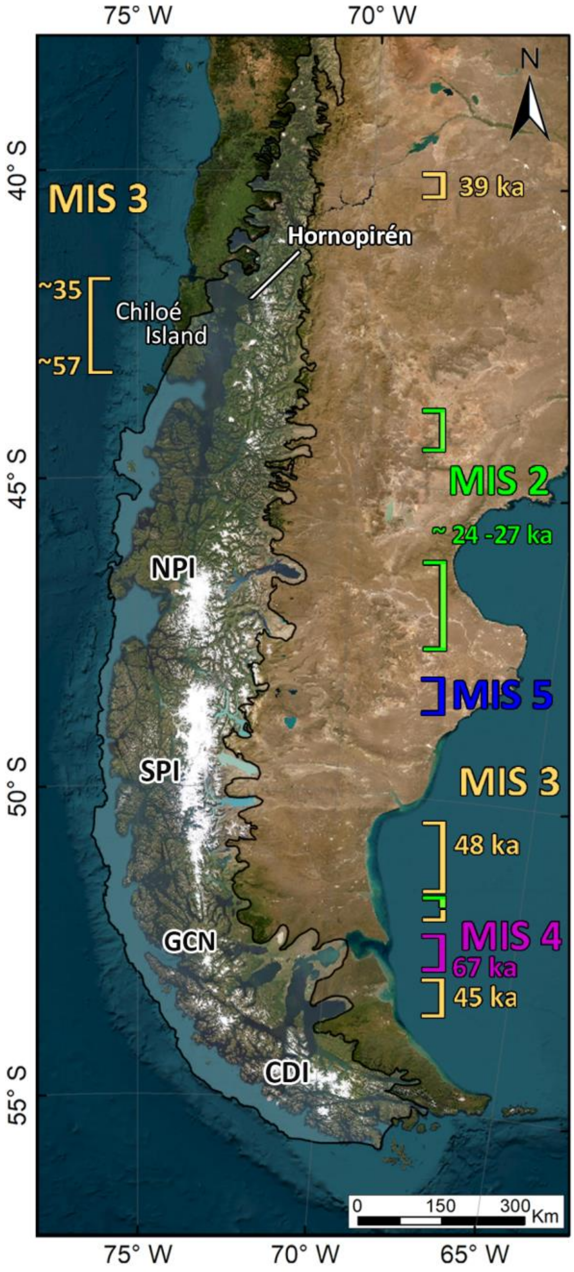

Figure 3.1. Timings for the ice maxima of the former Patagonian Ice Sheet during the last glacial period. The black line corresponds to the Patagonian Ice Sheet extent at the global Last Glacial Maximum (c. 24 ka; Davies et al., 2020). The brackets show the latitudinal extent of the ice maxima for a certain period. The brackets are opened towards the dated ice lobes, either on the western or eastern side of the Andes. A regional tendency can be appreciated, where Northern and Southern Patagonia reached their maximum extensions between 30-50 ka during MIS 3, except for an earlier occurrence at MIS 4 in Southernmost Patagonia. On the other hand, in Central Patagonia, the ice maxima occur in a close agreement between 27 – 24 ka (MIS 2), relatively contemporaneous to the global Last Glacial Maximum. NPI: Northern Patagonian Icefield, SPI: Southern Patagonian Icefield, GCN: Gran Campo Nevado Ice Cap, CDI: Cordillera de Darwin Icefield.

balance sensitivity tests, they concluded that to reach the LGM ice extent, they needed to decrease air temperatures by about 3°C along the full latitudinal range of Patagonia, together with an increase in precipitation by 0.7 m/yr in northern Patagonia (around 42°S) and a decrease of 0.7 m/yr in the south (around 50°S), was also necessary. However, this ELA-focussed approach does not distinguish the role of the individual climatic factors (such as temperature, precipitation and wind). Therefore, the climatic interpretation contained some uncertainty (Hulton et al., 2002). Later, Hulton et al. (2002) reconstructed the LGM extent and subsequent deglaciation. For the LGM reconstruction, they applied a uniform decrease in temperature of 6°C. The precipitation in the model was forced by the windspeed from the Pacific Ocean to the west blowing moisture onto the PIS such that they applied uniform wind speed gradients for the whole of Patagonia during the LGM which imposed a lower wind speed in the south and an increase in the centre, to try and simulate expected conditions following the hypothesised movement of the SWWs. However, this approach produced an overgrown ice sheet in the centre of Patagonia and underestimated the northern and southern extent. The modelled ice sheet had an ice volume of 500,000 km^3 which was a global sea level equivalent of a 1.2 m drop at the LGM. For the deglaciation pattern, they sharply increased the temperature by 7°C and observed a rapid melt-driven collapse within centuries for the ice sheet in northern Patagonia and a slower response for central and southern parts (43-53°S) of the ice sheet. Importantly, when those model reconstructions were performed, the geochronological constraints and contrasts between outlets were less well understood than now, but the modelling simulations agreed on the necessity to modify the precipitation distribution along the PIS in order to correctly simulate the ice extent for the LGM.

Hubbard et al. (2005) performed a time-dependant reconstruction of the PIS between 45 and 48°S, by using an ELA modification approach within a shallow-shelf model. Better geochronological constraints on the ice extent to the east had been developed (Kaplan et al., 2004). Hubbard et al, (2005) concluded that the western part of Patagonia was more sensitive to ELA changes than the eastern side, and it needed only 400 m of ELA lowering to achieve an extensive advance to the continental shelf. However, in the eastern PIS, the ELA modification needed to be up to 900 m lower to achieve the LGM extent of, for example, the Buenos Aires ice lobe (46°S). For the deglaciation, they observed a slow wane of the ice sheet until the Antarctic Cold Reversal (cf. 14,500 years). This was followed by a subsequent rapid collapse to quite similar extents to today’s position of the Northern Patagonian Ice Field.

More recently, and almost twenty years after the previous modelling, Yan et al. (2022) used the PISM to conduct steady-state tests using a range of different palaeoclimate model outputs from the PMIP project for the LGM to reconstruct the whole LGM PIS. They forced a degree day model using these climate inputs, enabling PISM to grow ice for the LGM and then compared the ice extent with the geochronology records compiled in PATICE (Davies et al., 2020). However, they had significant difficulties in meeting the ice extent along the whole of Patagonia. Reconstructions with a good fit in the south underestimated the ice extent in northern Patagonia. The contrary occurs when trying to meet the ice extent of northern Patagonia: an overgrown ice sheet results in the south. They attributed these difficulties to the uncertainties in the positive degree-day factor for ice and in the temperature changes during an annual cycle, which the climate model outputs used to force the ice model do not incorporate.

Most recently, the ice thickness of the LGM extent was reconstructed using an inverse modelling approach, by assuming a perfectly plastic (isotropic) ice rheology (Wolff et al., 2023). This used the trim-line altitude and the lateral extent for the LGM located in the Pueyrredón ice lobe (47°S) to define the upper and marginal extent of the ice because these have been well-dated by Boex et al. (2013) and Hein et al. (2010), respectively. They calculated the ice thickness from that outlet and extrapolated it to the rest of Patagonia. They obtained an ice volume for the whole PIS at 24 ka of 554,067 km^3 and a sea-level contribution of 1.38 m to the global sea level, surprisingly similar to the original Hulton et al. (2002) modelling.

Past reconstructions for specific regions have also been developed, with a focus on understanding the climatic conditions of the LGM, late glacial and deglaciation periods. For instance, Peltier et al. (2021) through a shallow ice approximation model, suggest that to meet the ice extent recorded by the geochronology in the Magallanes ice lobe (53°S) for the LGM (on the lee side of the Andes), cooler (4.5 - 5.5°C colder) and drier (25% less precipitations) conditions than today are needed. For the late glacial, Leger et al. (2021) employ a 2D model reconstruction of an ice lobe , also on the lee side of the Andes at 43°S, and suggest that at 18 ka the climate in that area should have been cooler (between 1.9 – 2.8°C colder) and wetter (between 50 – 380% more) than present-day conditions. Moreover, Muir et al. (2023) performed a temperature reconstruction between 44-47°S for the late glacial, with a positive degree day mass balance model constrained by moraine chronologies. The result is a drop in paleo temperatures of ~3°C with no precipitation change from the present for the Antarctic Cold Reversal (cf. 14.7-13.0 ka; Pedro et al., 2016). And a subsequent increase of the temperatures in 0.6°C or a reduction of 20-25% in precipitation during the Younger Dryas (cf. 12.9-11.7 ka; Blunier and Brook, 2001). For a more restricted area at San Lorenzo Ice Cap (47°S), Martin et al. (2022) through an ice cap reconstruction, find that to fit the geochronology extent at 12.1 ka, colder and wetter conditions are needed, specifically a reduction of the temperatures of 2°C and increase in the precipitation of 150% from present conditions. In summary the regional modelling efforts yield a complex set of potential inferences on past climate with most agreeing with the whole-PIS efforts that colder, wetter conditions were present during past glaciation.

3.2. Methods. Modelling set up

We use the open-source PISM (Bueler and Brown, 2009; Winkelmann et al., 2011) to test the response of the whole Patagonian Ice Sheet to different palaeoclimate configurations in order to determine which scenario(s) produce(s) the best fit to the reconstructions of the former Patagonian Ice Sheet, recently synthesised in the PATICE project (Davies et al., 2020). PISM is widely adopted in palaeo simulations of Greenland and Antarctica (e.g., Golledge et al., 2012a; Solgaard et al., 2011), but also on alpine glaciers, ice fields and palaeo ice sheets around the globe, such as New Zealand (Golledge et al., 2012b), the European Alps (Becker et al., 2016; Seguinot et al., 2018) and the Himalaya (Yan et al., 2020).

This work focuses on understanding the past climate conditions that governed Patagonia during the last glacial cycle. Therefore, the approach is to first set the physics and glaciological parameters for the model to a fixed suite of values based on previous work and on a set of sensitivity tests. Then using that as a basis, test the effects of climate resolution and air-temperature standard deviation options on the surface melting. Finally, in Chapter 4, having the model set up with an appropriate set of parameters from this chapter, we will test different scenarios for the forcing climate in transient simulations such that the influence of changing the climatic patterns between modern and a range of SWW scenarios are explored independently.

3.2.1. Stress Balance

Simulations of the stress balance within a flowing ice mass can be best reproduced by a Full Stokes model, which considers all the driving stress against the ice flow. The problem with such model is that it has very high computational demand. Therefore, it is not possible to use it for long-term simulations. As a solution for this, some simplified models for stress balance exist. The most common is the shallow approximations, which PISM provides (Bueler & Brown, 2009). This method simplifies the mathematical equations by simplifying the ice geometry by assuming shallow ice sheets with small depth-to-width ratios. This allows simulations of larger areas at a much lower computational cost to run (Winkelman et al., 2011).

The shallow approximation models include shallow ice approximation (SIA) and shallow shelf approximation (SSA). In PISM, these options can be used separately on their own or combined into the hybrid model (SIA+SSA), depending on the context of the modelling area. The SIA is by definition, the non-sliding model. In SIA, the basal shear stress is so high that the vertical shear stress dominates over other stress components (Winkelmann et al., 2011). Therefore, the variation of their horizontal velocities is much smaller than in the vertical (Bueler, 2021). It applies well to the grounded ice, especially close to the ice divides where there is no sliding. On the other hand, in the SSA the basal shear stress is zero or very small, so the velocity and the deformation are uniform through the vertical layers. This law applies well on ice shelves or ice streams, where the topography is gentle, with no or little basal resistance to flow (Bueler & Brown, 2009). The hybrid option SIA+SSA superposes the velocities computed by SIA and SSA, allowing a smooth transition between ice frozen to the bedrock and fast-flowing ice, such as in the interior of the ice sheets to warm-based outlets glaciers or ice shelves (Bueler & Brown, 2009; Martin et al., 2011; Winkelmann et al., 2011). This allows corridors of fast flowing ice to be appropriately represented in ice sheet simulations. For Patagonia, where there are transitions from mountain glaciers to outlet glaciers and floating ice in the fjord and offshore areas, we consider that the hybrid model works well for transiting from one context to another.

3.2.2. Input Data

The modelling domain includes the past extent of the Patagonian Ice Sheet, which expands south from ~ 37.8°S to the end of the American continent (Davies et al., 2020). This extent consists of a region of 2160 km in length and 960 km wide (Figure 3.2 A). The model simulations are run with an equally-spaced horizontal grids of 4 km resolution and simulating a vertical domain of up to 5000 m in the ice and 2000 m in the thermal bedrock layer. The model requires a series of boundary conditions for the study area: bed elevation, sea level changes, climate input and geothermal heat flux. The input files for these boundary conditions are built from their original resolution and bilinearly interpolated to 1 km. PISM then uses these inputs and down samples them to lower resolution as required for particular simulations. The description below describes the physical and glaciological parameters we have constrained and the reason for our selection. For detailed information on our choices for key variables in PISM, see Table 3.1. All other variables were set to default values, as described in the online manual (www.pism.io/docs/; PISM 2.0.6 documentation, 2023).

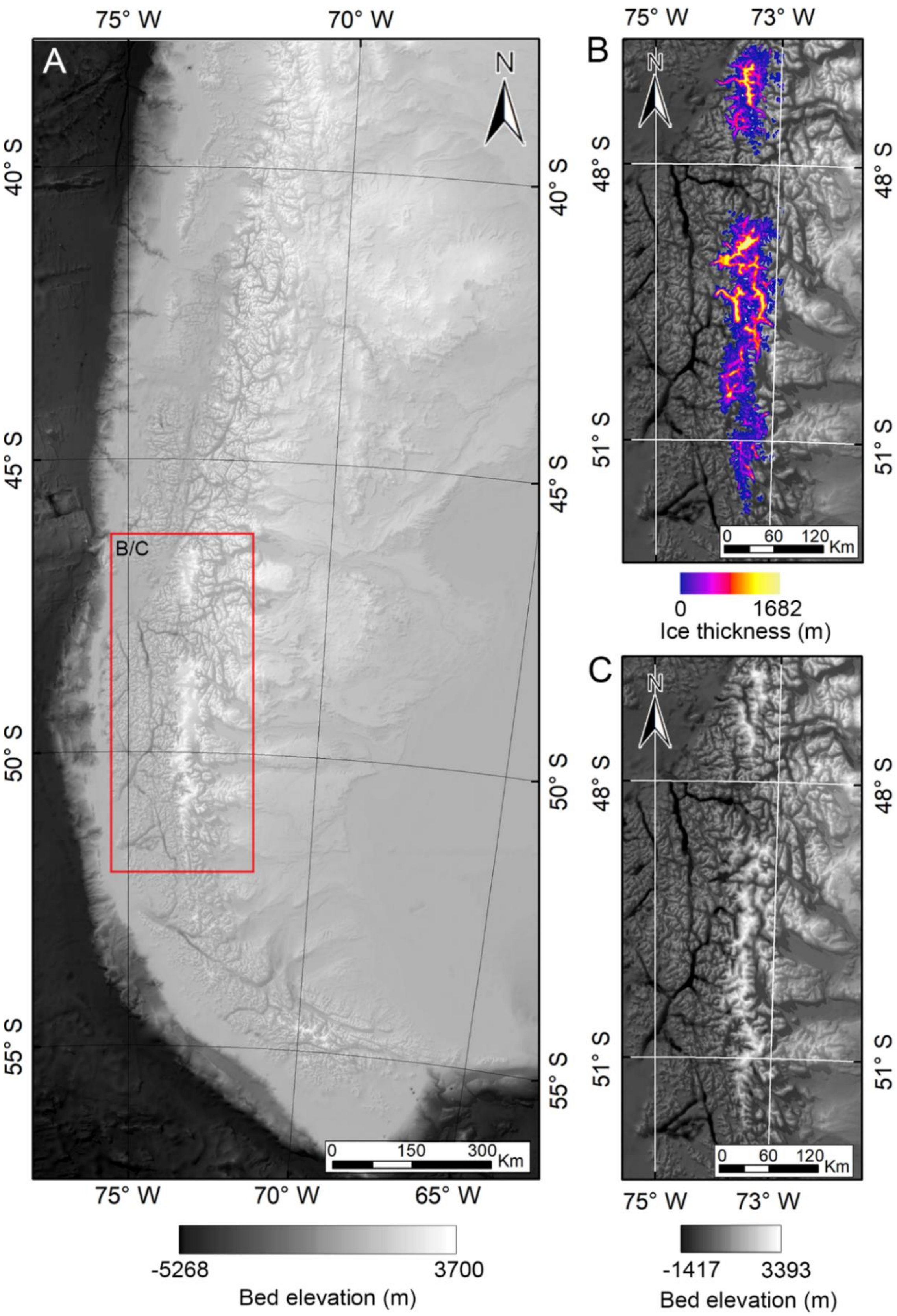

Figure 3.2. Basal boundary conditions for the modelling. Bed topography input model. A) Topography and bathymetry from GEBCO. B) Ice thickness of the Northern and Southern Patagonian Ice Fields (Millan et al., 2019). C) Bed elevation with the ice thickness subtracted (compare the topography with A).

Table 3.1. Physical and glaciological variables that we modify on the model according to parameters that best adjust to Patagonia.

Bed deformation		Value	Reference
Mantle viscosity		1×10^{20} Pa s	Mark et al., 2022
Mantle density		3300 kg m^{-1}	Lingle and Clark (1985)
Lithosphere flexural rigidity		5×10^{24} N m	Lingle and Clark (1985)
Mass balance			
Temperature of rain precipitation		275.15 °K	Model default
Temperature of snow precipitation		273.15 °K	Model default
Snow melt factor		3.5 mm $°C^{-1}$ day^{-1}	Möller et al., 2007; Schneider et al., 2007
Ice melt factor		7.0 mm $°C^{-1}$ day^{-1}	Möller et al., 2007; Schneider et al., 2007
Air temperature lapse-rate		-6.5 °C m^{-1}	Bravo et al., 2019
Refreezing fraction		0.6	Model default
Ocean heat flux		0.005 m s^{-1}	Martin et al., 2011
Ice flow enhancements			
sia_e	enhancement factor for SIA	2	Cuffey and Paterson, 2010
ssa_e	enhancement factor for SSA	1	Cuffey and Paterson, 2010
Basal sliding			
q	pseudo-plastic sliding exponent	0.25	Aschwanden et al., 2013
Φ_0	minimum till friction angle	20°	-
Φ_1	maximum till friction angle	40°	-
b_0	altitude of min. till friction angle	0 m a.s.l	-
b_1	altitude of max. till friction angle	400 m a.s.l	-

3.2.2.1. Bed topography

For the bed topography, we use the data available in the General Bathymetric Chart of the Oceans (GEBCO) year 2020, as it includes the topography and bathymetry from the fjords and offshore area, with a resolution of 15 arc seconds (equivalent to ~500m; Figure 3.2. A). We do not account for the bathymetry of the large lakes, mostly located in the eastern part of Patagonia because of a lack of publicly available lake bathymetry data. This partly arises because several of the lakes are politically sensitive because they straddle the border between Chile and Argentina. In these areas, the modelled ice flows over a flat base at the elevation of the lake surface: we discuss some of the impacts of this omission in the discussion.

Patagonia today hosts three main ice fields: the Northern Patagonian Icefield (NPI), Southern Patagonian Icefield (SPI), and Cordillera Darwin Icefield (CDI). The Northern and Southern Patagonian Ice fields are substantially larger than the CDI (Glasser et al., 2008). Millan et al. (2019) provide a compilation of the thickness of these ice fields by combining airborne gravity and radar data. The ice thickness reaches up to 1.6 km, and data are provided at a horizontal resolution of 500 m. GEBCO data considers the ice field masses as surface topography; therefore, in order to determine the true bedrock surface, we subtract the Millan et al. (2019) ice thickness from GEBCO in order to determine the bed under ice-free conditions (Figure 3.2. B-C). We ignore the glaciofluvial post-sedimentary infill on the piedmont areas of the outlet glaciers, as we do not have parameters to quantify the thickness of the infill. Additionally, the bed elevation is modified during our simulations to account for sea level change, where we apply a changing curve for the last glacial cycle (Yokoyama et al., 2018; Figure 3.3), reaching its minimum of -134 m at the global LGM (Lambeck et al., 2014).

The isostatic adjustment of the bed in response to the ice load is corrected by the application of the Lingle-Clark earth model incorporated in PISM (Bueler et al., 2007; Lingle & Clark, 1985). This model considers an elastic lithosphere lying over a viscous homogeneous upper mantle. We use the average global values (Table 3.1) for the lithosphere flexural rigidity and mantle density (Lingle & Clark, 1985), as Patagonia has no measured constraints. For the mantle viscosity, we chose a representative number from the complex tectonic context of Patagonia, 1 x 10^{20} Pascal second (Mark et al., 2022; Figure 3.4 B).

3.2.2.2. Basal Heat Flux

The geothermal heat flux corresponds to the heat emerging from the crust, and its interactions in the boundary between ice and ground play a significant role in the distribution of ice temperature. Higher geothermal heat flux produces larger areas with temperate basal ice, generating larger ice velocities at higher elevations (Pittard et al., 2016) and potentially generating basal melting if high enough and/or combined with thicker/faster ice. For the basal heat flux, we use a global model of Goutorbe et al. (2011; Figure 3.4 A), which is based on heat flow measurements, and an integration of the known Earth's structure, such as lithospheric thickness and geotectonic contexts from the different areas.

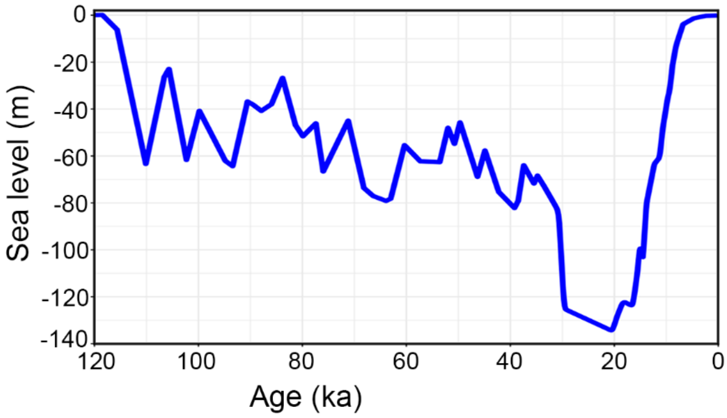

Figure 3.3. Key boundary conditions for the modelling. Sea level changes during the last glacial cycle, from 120 ka to the present (Yokoyama et al., 2018).

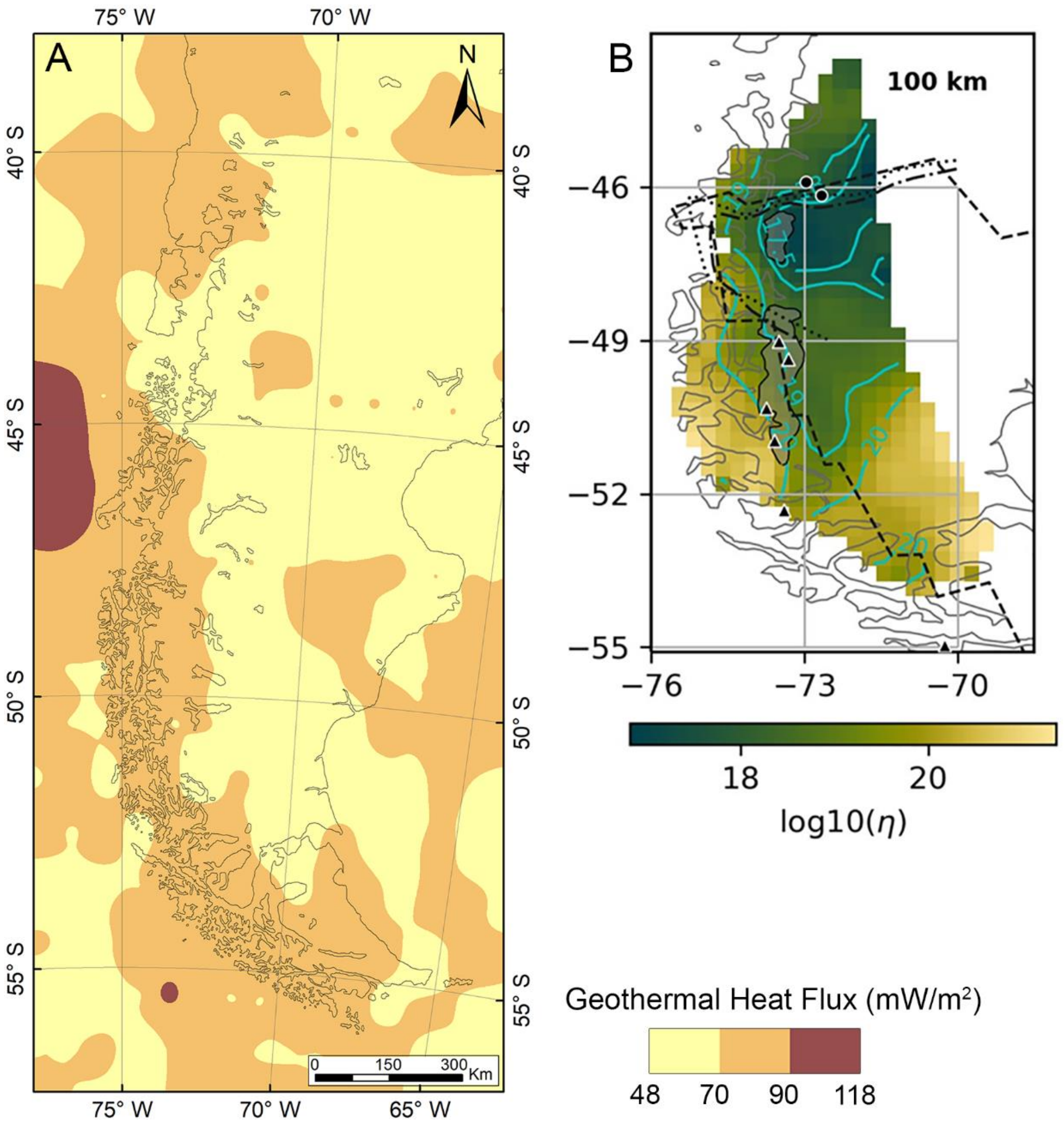

Figure 3.4. Key boundary conditions for the modelling. A) Geothermal heat flux (Goutorbe et al., 2011). B) Mantle viscosity of southwest Patagonia at 100 km depth, units are Pa s (Mark et al., 2022).

3.2.2.3 Modern Climate Input

For climatic input, we use modern mean monthly temperature and precipitation of 30 arc sec resolution (~1km), obtained from Worldclim 2 (Figure 3.5; Fick & Hijmans, 2017). These data are produced using climate models to interpolate between measurements from meteorological stations around the world. When comparing these interpolated data products with the raw climate data from Chilean and Argentinian stations, we see a close agreement in the temperature values, with no more than one degree of difference between them. However, for the precipitation although we find a close agreement on the precipitation in northern Patagonia, where there is a reasonable density of meteorological stations, we see larger differences between the Worldclim2 vs. known

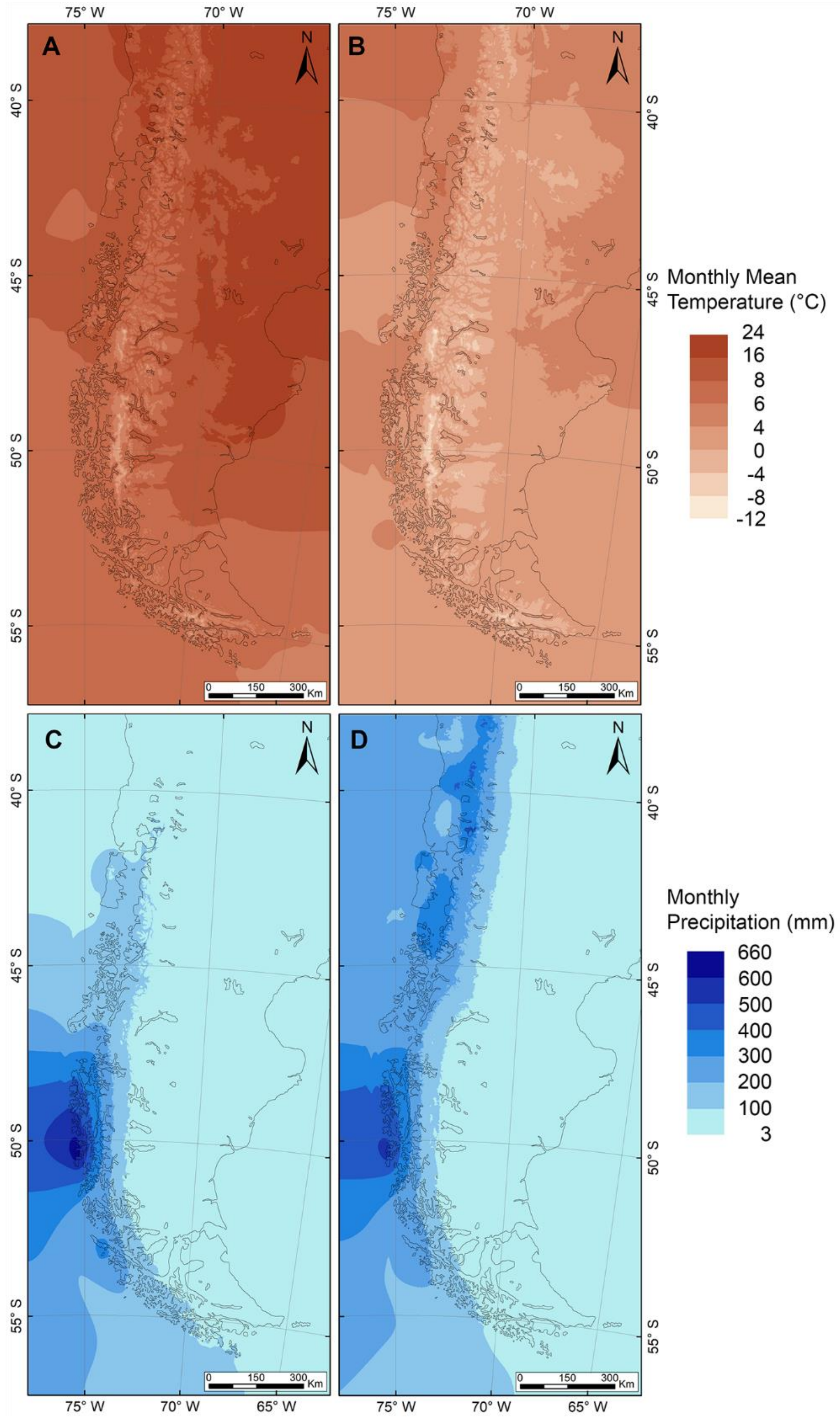

Figure 3.5. Monthly mean climatic inputs. Only January and July are plotted. Top, January (A) and July (B) mean temperature. Bottom, January (C) and July (D) Precipitations. Data obtained from WorldClimate2 (Fick and Hijmans, 2017), the offshore area is interpolated from the data on the continent.

precipitation values in the western part of the central-south region of Patagonia. For instance, at the Hornopirén station (41.9°S,72.4°W; Dirección General de Aguas, Chile), the observed precipitation data are ~1500 mm per year higher than the Worldclim2 data. In the same way, in the Gran Campo Nevado Ice Cap (52.8°S,73°W; Weidemann et al., 2018), the Worldclim2 model underestimates precipitation by an even larger amount: ~4000 mm per year. The problem faced by this study is that the differences are not systematic in a way that we could apply a uniform adjustment, and other climatic models also underestimate the precipitation in the western part of Patagonia. The cause may be linked to complex topography not resolved by the climate models but we do not consider it further here. Despite these differences, we chose the Worldclim2 model for our simulations due to its higher resolution, and we later consider this underestimation bias directly when reconstructing the palaeo climate scenarios.

Worldclim2 has data only on the terrestrial regions, so for the offshore area, we extrapolated the precipitation and temperature values from the continent such that the values at the coast are kept constant as you move offshore. Due to the lack of geological constraint on the ice extent in Patagonia's offshore areas, especially in the west (Davies et al., 2020) we consider the extrapolated offshore climate data does not introduce significant errors in our analysis, nor does it affect our conclusions.

3.2.3. Physical and glaciological parameter choices

3.2.3.1. Ice Flow enhancement

Enhancement factors are applied as an adjustment to the general ice flow laws, which account for the anisotropy of the ice due to differences in grain size, fabric and/or impurities (Albrecht et al., 2020). In PISM, the SIA and SSA enhancements (SIA_e and SSA_e, respectively) are present in the parametrisation of the viscosity of the glaciers (Aschwanden et al., 2013), and an increase of the enhancement makes the ice softer and prompt to flow more easily. A value of 1.0 means no enhancement hence harder/stiffer ice. To produce the enhancement on PISM, SIA uses enhancement values larger than 1.0 and SSA lower than 1.0 (Albrecht et al., 2020). The enhancement factors are normally used as tuning parameters for the ice dynamics (Aschwanden et al., 2013). As we aim to use fixed glaciological parameters to explore climate forcing, we use values of SIA_e of 2 and SSA_e of 1 (Table 3.1), which have been shown to be plausible for temperate glaciers and ice shelves, respectively (Cuffey & Paterson, 2010, p. 76). To explore the effects of our use of fixed enhancement factors (model 1; Table 3.2) we performed some tests with different values (Table 3.2) to see the effect on the ice volume. The increase of SIA_e to 8 (model 2) produces less volume for the grounded and floating ice (Figure 3.6 A), but the effect on the floating ice is minor (Figure 3.6 B). On the other hand, the increase of SSA_e to 0.6 (model 3) produces slightly higher volume along the whole area when compared to the fixed parameters, but this impact is more significant on the grounded ice (Figure 3.6 A), influencing the ice stream in general (Albrecht et al., 2020). Moreover, Figure 3.7 shows that an increase in the SIA_e to 8, produces slower basal ice velocity at the centre of the ice sheet. While the increase of SSA_e to 0.6 does not produce visible changes in the ice velocities. Neither sensitivity test generates changes on the outlet glaciers located at the east of the ice sheet.

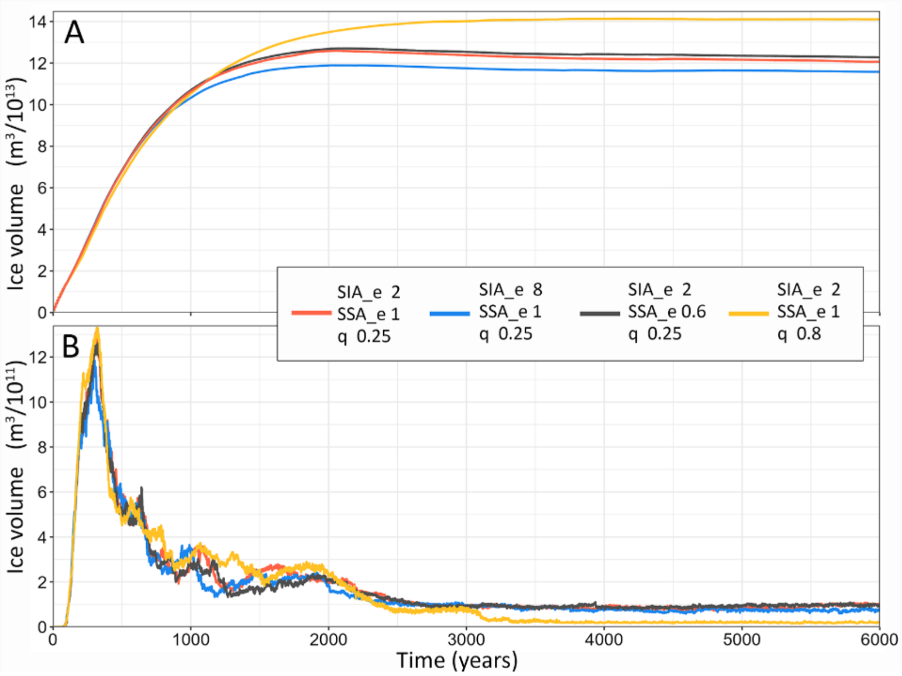

Figure 3.6. Ice volume sensitivity tests to evaluate the influence of the SIA/SSA enhancement factors and the plasticity component (q). All these simulations are run until equilibrium, with decrease in air temperature to -6°, with modern precipitation configuration and a gradual decrease of the sea level to -134 m. A) Corresponds to the ice volume for grounded ice. B) Corresponds to the ice volume for the floating ice. The red curve shows the results from the parameters used in this work, which are elected according to the literature that best fits the Patagonian glacial environment.

3.2.3.2 Basal sliding

In PISM, the basal sliding for SSA assumes that the glaciers slide over a layer of till, and it is based on the resistance that the bed opposed against the ice. This depends on two physical components: the plasticity and the yield stress of the till.

The plasticity of the till corresponds to the till deformation, and in PISM is controlled by the value of *q* ($0 \leq q \leq 1$), which is the sliding exponent. When q = 0, the till has no deformation and the basal sliding is purely plastic along the ice-till interface (Albrecht et al., 2020). Values of q greater than 0, generate a pseudo-plastic sliding, which considers a till deformation. As the q value increases towards 1, the underlying sediment becomes

Table 3.2. Sensitivity tests performed in this work in order to test the response of Patagonia to different glaciological parameters and climatic factors that affect the surface melt and different climatic scenarios.

ID	Ice flow		Basal Sliding	Mass Balance					Palaeo Climate Forcing	
				Climate Resolution		air-temp standard deviation				
	sia_e	ssa_e	q	yearly	monthly	fixed	linear	spatial/seasonal	temp.	precip.
Glaciological Parameters										
1	2	1	0.25		x			x	-6	1.0
2	8	1	0.25		x			x	-6	1.0
3	2	0.6	0.25		x			x	-6	1.0
4	2	1	0.8		x			x	-6	1.0
Surface Melt Parameters										
5	2	1	0.25	x		x			-6	1.0
6	2	1	0.25	x			x		-6	1.0
7	2	1	0.25		x	x			-6	1.0
8	2	1	0.25		x		x		-6	1.0
9	2	1	0.25		x			x	-6	1.0
Steady State Climate Sensitivity Tests										
10	2	1	0.25		x			x	-6	1.0
11	2	1	0.25		x			x	-6	1.2
12	2	1	0.25		x			x	-6	1.5
13	2	1	0.25		x			x	-7	1.0
14	2	1	0.25		x			x	-7	1.2
15	2	1	0.25		x			x	-7	1.5
16	2	1	0.25		x			x	-8	1.0
17	2	1	0.25		x			x	-8	1.2
18	2	1	0.25		x			x	-8	1.5

For all the models we apply a calving thickness threshold of 20 m for the fjords and 600m for the offshore area (Figure 3.4 B). For the basal sliding constraint, we apply a Φ=20° for bed elevations below modern sea levels (0 m) and Φ=40° for locations higher than 400 m a.s.l, the values change linearly in between.

softer, and the basal resistance increases. Lower q values favour higher ice basal velocities, while higher q values yield lower velocities due to the increase of the till deformation. We use a value of q=0.25 for our simulations (model 1; Table 3.2), which is an appropriate value for glacial states (Albrecht et al., 2020; Aschwanden et al., 2013). Nevertheless, we perform a sensitivity test with q=0.8 (model 4; Table 3.2), to see the effects on the simulations. They show that with an increase in the till deformation (> q), the ice volume of the grounded ice increases (Figure 3.6 A) whilst the ice volume of the floating ice decreases (Figure 3.6 A). Moreover, the basal ice velocity increases at the centre of the ice sheet, but it decreases on the rest of the ice sheet, such as ice shelves and outlet glaciers (Figure 3.7).

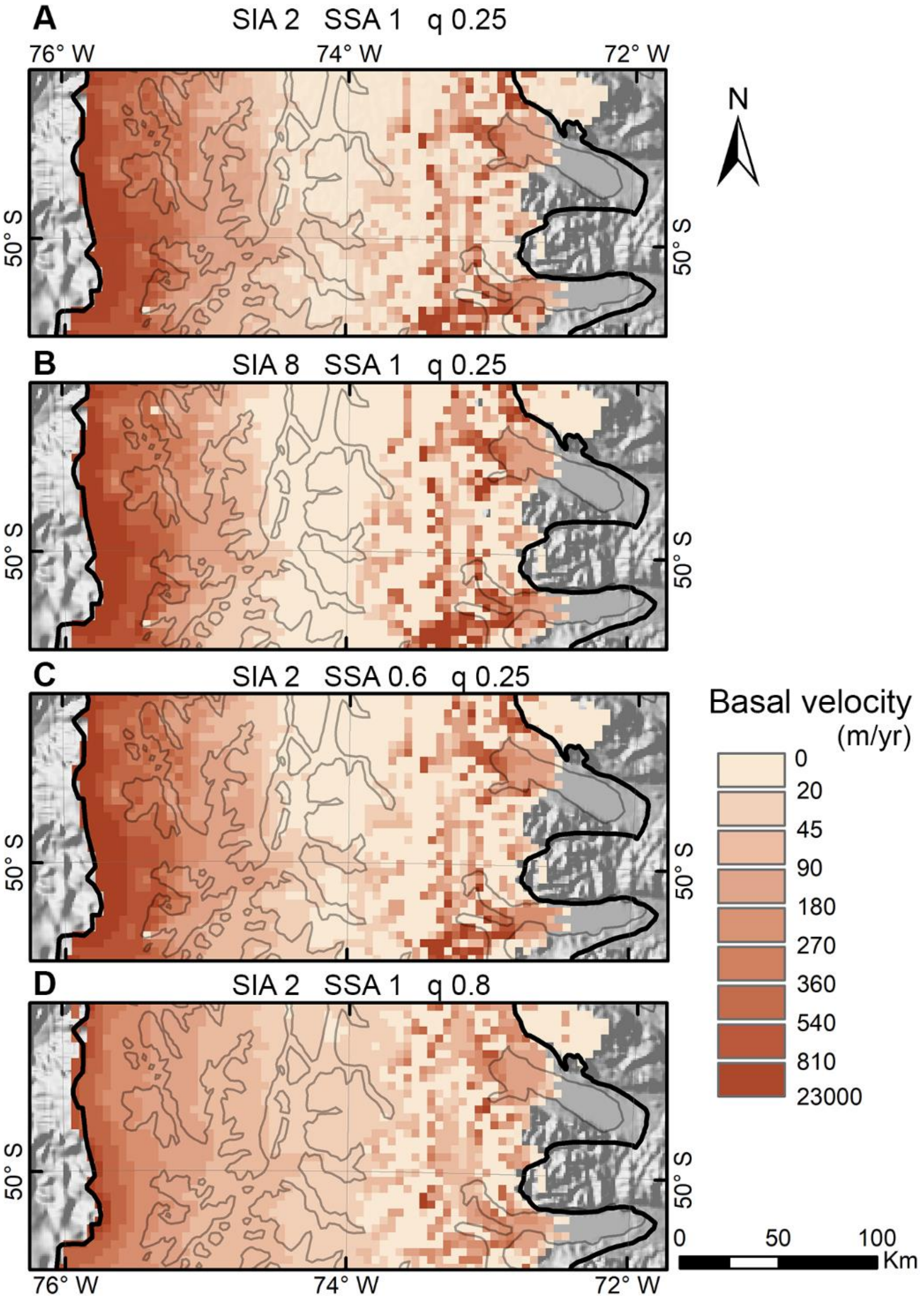

Figure 3.7. Basal sliding sensitivity tests to evaluate the influence of the SIA/SSA enhancement factors and the plasticity component (q). A) Corresponds to model #1. B) Corresponds to model #2. C) Corresponds to model #3. D) Corresponds to model #4. All these simulations are run until equilibrium, with decrease in air-temperature to -6°, with modern precipitation configuration and a gradual decrease of the sea level to -134 m. The black line corresponds to the ice extent during the LGM (Davies et al., 2020).

The yield stress corresponds to the maximum stress that the till can resist before it starts to deform, following the Mohr-Coulomb criteria (Cuffey & Paterson, 2010, p. 266). In PISM the yield stress of the till depends on the friction angle (Φ) and the effective stress.

The friction angle uses lower values for weaker basal material, such as till associated with marine sediments, and higher values for more resistant materials, such as intercalation between high friction till and direct bedrock (Martin et al., 2011). We therefore use a Φ=20° for bed elevations below modern sea levels (0 m) and Φ=40° for locations higher than 400 m a.s.l, and Φ changes linearly in between those elevations. A similar approach has been used in other places, which have coastal components (Aschwanden et al., 2013; Seguinot et al., 2016). Moreover, most of the outlet glaciers in the eastern part of Patagonia have elevations between 150 – 250 m a.s.l., and according to our formula, their basal friction values are close to Φ=30°, which is the typical value for till friction angle (Cuffey & Paterson, 2010, p. 268).

3.2.3.3. Calving Flux

The main ice mass loss factors in the PISM modelling are the surface mass balance and the calving of the frontal flux on any floating ice. The mass loss of the basal ice, such as sub-shelf and sub-sheet, melting and refreezing, is negligible in the model (Martin et al., 2011). Therefore, for these last variables, we use the model default parameters of 60% for refreezing and 0.005 ms^{-1} for the ocean heat flux (Table 3.1).

To choose a calving method in PISM we tried various approaches but these caused the model to crash (see below). Instead, the calving method used in these simulations considers a combination of the water depth with the total thickness of the floating ice, since the calving rate increases with water depth (Benn et al., 2007). Although, this method is a simplistic way to approach the calving, we note that there are almost no constraints on past calving at the margins of the PIS. In the model, all the floating ice under a certain thickness threshold of the ice column is calved off (Figure 3.8 B). Two water depth categories were considered for the modern ocean (fjord and offshore areas) only, as the bathymetry of the large palaeo and modern proglacial lakes is not included here (Bed elevation section 3.2.1.1).

Initially, the PISM configurations we tested create floating ice with zero basal resistance, which results in high-velocity gradients as ice transitions from steep mountain terrain directly into fast-flowing marine-terminating areas, making the model crash consistently. To avoid this velocity gradient problem, we remove the model boundary condition that applies frontal resistance to the floating ice. The consequence of this is that the ice shelf grows to unrealistically large extents, several hundreds of kilometres beyond the continental shelf (e.g., Figure 3.8 A). To eliminate the large ice shelves, we therefore calve all floating ice below 600 m thickness in offshore areas and below 20 m thick in fjord areas (Figure 3.8 B), allowing the ice to develop in the fjords but also to prevent it growing too far beyond the continental shelf edge. We apply a mask of 600 m in the offshore area, even though in these simulations, most of the ice grounds to the edge of the continental shelf (Figure 3.8 A). The value of 600 m is an average number between thin (< 200 m) and thick ice shelves (~1000 m) calculated for modern conditions in Antarctica (Griggs & Bamber, 2011). This value avoids the generation of any thin floating ice beyond the continental shelf, which would be unsustainable for very deep areas. However, this does not affect the model interpretations since the offshore area has few constraints on the ice sheet extent, and previous ice sheet reconstructions assume the ice did not extend farther than the continental shelf edge (Davies et al., 2020). On the other hand, the fjord area is important, especially for the fjords with an easterly direction where there is a geochronological constraint and during the colder periods of the last glacial cycle, the easterly fjords were proglacial lakes. A calving threshold of 50 m has been documented for tidewater outlets (Van der Veen, 2002; 1996), but we use 20 m because proglacial lakes don't have a tidal influence and consequently there is less flotation effect expected (Benn et al., 2007).

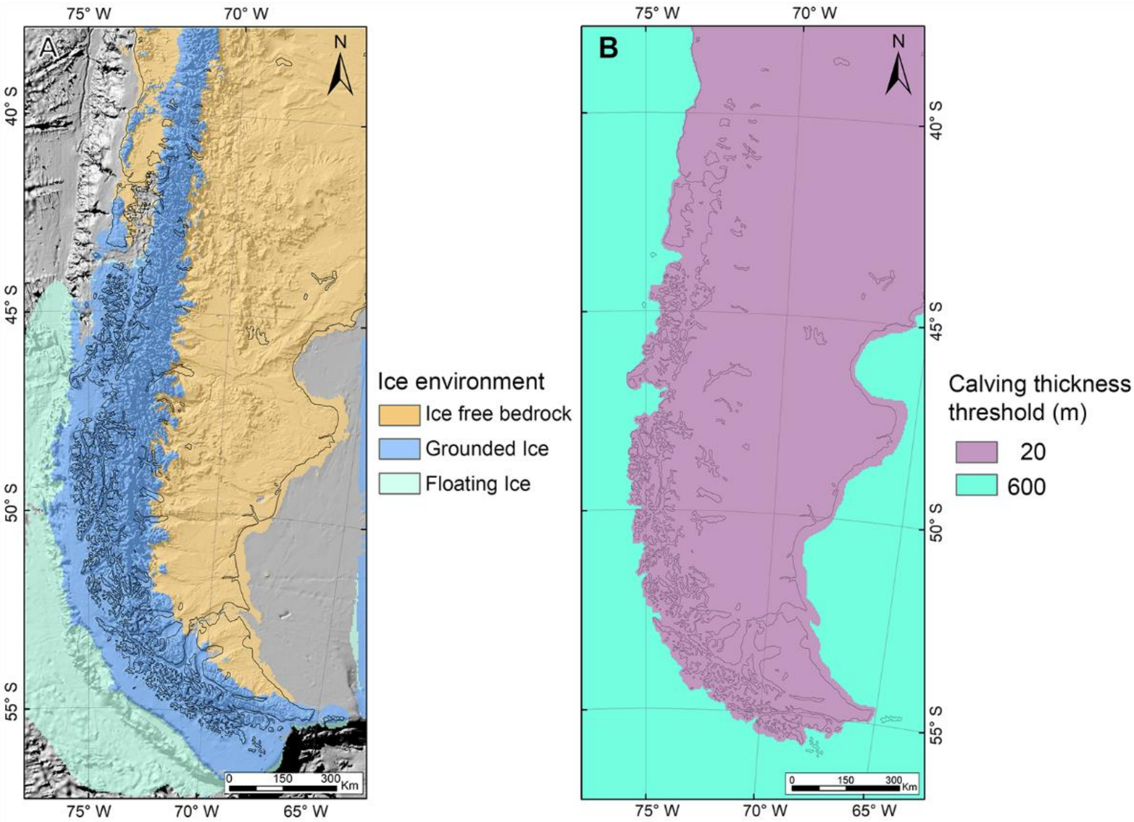

Figure 3.8. A) Ice environment of the Patagonia simulation without frontal stress on the floating ice. An extensive ice shelf (floating ice) develops towards the west with hundreds of km beyond the continental shelf. On the hillshade underneath, the continental shelf can be appreciated. Note the periodicity of the model, it allows the ice to run in a circular environment and it appears on the east side of the modelling domain. B) Calving thickness threshold we set to avoid the development of very large ice shelves. Any floating ice below the thickness threshold will be calved off.

3.2.4. Surface Mass Balance

Having set up the physical and glaciological parameters for the model, we explore the influence of the climate resolution and different options for the air-temperature standard deviation, in the way it affects the surface melting.

With PISM, the simulations can be driven by a range of surface mass balance approaches, but here we apply a Positive Degree Day (PDD) model which means for every degree above 0°C, a certain thickness of snow and ice is melted per day. The accumulation and ablation are calculated using a temperature threshold, where all the precipitation occurring at temperatures below 0°C is converted to snow and all above 2°C as rain, respectively. The temperature thresholds are provided by the mean air temperature from the climatic forcing inputs. In order to simulate daily variabilities in the temperature, PISM assumes a normal temperature distribution with the mean temperature and with a given air temperature standard deviation value and chooses the temperature within this range by a stochastic method based on Calov & Greve (2005).

Here we assume that the amount of melt that occurs on the ice and snow per PDD in the past was similar to today's standards. Therefore, for the simulations, we use modern values calculated on an easterly outlet of the Gran Campo Nevado Ice Cap (52°S), Patagonia. These melt factors are 3.5 mm°C^{-1}day^{-1} for snow and 7.0 mm°C^{-1}day^{-1} for ice (Möller et al., 2007; Schneider et al., 2007). These values sit within modern melt factor values from different regions of the world, ranging between 2.5 – 11.6 mm°C^{-1}day^{-1} for snow and between 5.4 – 20 mm°C^{-1}day^{-1} for ice (Hock, 2003). The mass balance computations for the simulations in this thesis are performed on a weekly basis.

3.2.4.1. Influence of the climate input resolution and air-temperature standard deviation

Palaeo ice sheet simulations often use yearly mean climate inputs due to the scarce availability of data, especially in remote areas. However, by doing this, seasonal variabilities could be underestimated with low temporal climate resolutions (Seguinot, 2013). For instance, reaching the freezing point could occur less frequently than is the case in reality or, on the contrary, extremely high temperatures during the melt season may not be correctly simulated. Furthermore, the standard deviation (SD) of the daily temperature that is applied to control the daily variabilities is known to differ seasonally and spatially, especially in larger regions. Consequently, the final mass balance calculation is influenced by the selection of parameters that control the deviation of climate away from the mean (Fausto et al., 2011; Rogozhina & Rau, 2014; Seguinot, 2013).

Having defined the physics and glaciological parameters of the model set-up, we perform sensitivity tests that apply either yearly or monthly climatic data and explore the use of different methods for controlling the air temperature SD. We do this to understand the importance of the temporal resolution of the mean climate and the variation of the air-temperature SD on a seasonal basis and in a large area such as the whole of Patagonia. PISM allows three options to set the air temperature SD. The first option is to use a constant value of temperature SD for the whole area (Ritz, 1997). Second, a linear method where the temperature SD depends on terrain or ice surface altitude (Fausto et al., 2011) or the air temperature (Seguinot & Rogozhina, 2014). The third option is a spatial and seasonal variation of the temperature SD (Seguinot, 2013). To explore which option to use in our simulations, we tested each of these choices.

Constant air-temperature standard deviation

We first performed a test with yearly and monthly climatic data and a constant value for the air-temperature SD (models 5 and 7; Table 3.2). We chose a value of 3, which is a representative value for a fixed SD for the whole Patagonia according to global climatic data (e.g., ERA-Interim; Seguinot, 2013). The climatic data provide a global spatial distribution of the air-temperature SD through the different months of the year.

Linear air-temperature standard deviation method in relation to the surface temperature

To explore the second option, we followed a methodology similar to Seguinot & Rogozhina (2014), which uses the observation that the temperature SD over a glacierised area is largely related to the variations in the surface temperature (Seguinot & Rogozhina, 2014). From this assumption, we calculate a linear relationship between temperature and temperature SD for the Northern and Southern Patagonian Ice fields area (Figure 3.9. A), following the methodology of Seguinot & Rogozhina (2014), who performed this calculation over the glacierised part of Greenland. From ERA-40 reanalysis data (Uppala et al., 2005), we collected 44 years of historical data for the long-term monthly mean temperature (Tm) and the long-term monthly SD (SDm). With these data, we determine the linear relationship that best fits the data (Figure 3.9 B) through a least-square regression. The linear relationship is expressed in the following equation $SDm = -0.07xTm + 2.23$, which indicates that at lower surface temperature, the larger the temperature standard deviation. This temperature dependant relationship can also be correlated seasonally, where summer has lower values of air-temperature SD and winter has higher values (Figure 3.9 B). This method is meant to be applied only to glacierised areas. If this linear temperature SD is extended outside this area, they should be compared to local weather stations (Seguinot & Rogozhina, 2014). However, due to the scarcity of weather stations along Patagonia and the availability of high temporal resolution data, we are not able to compare them with local weather stations. Nevertheless, we test this approach and apply it to the yearly and monthly climatic input data (model 6 and 8; Table 3.2).

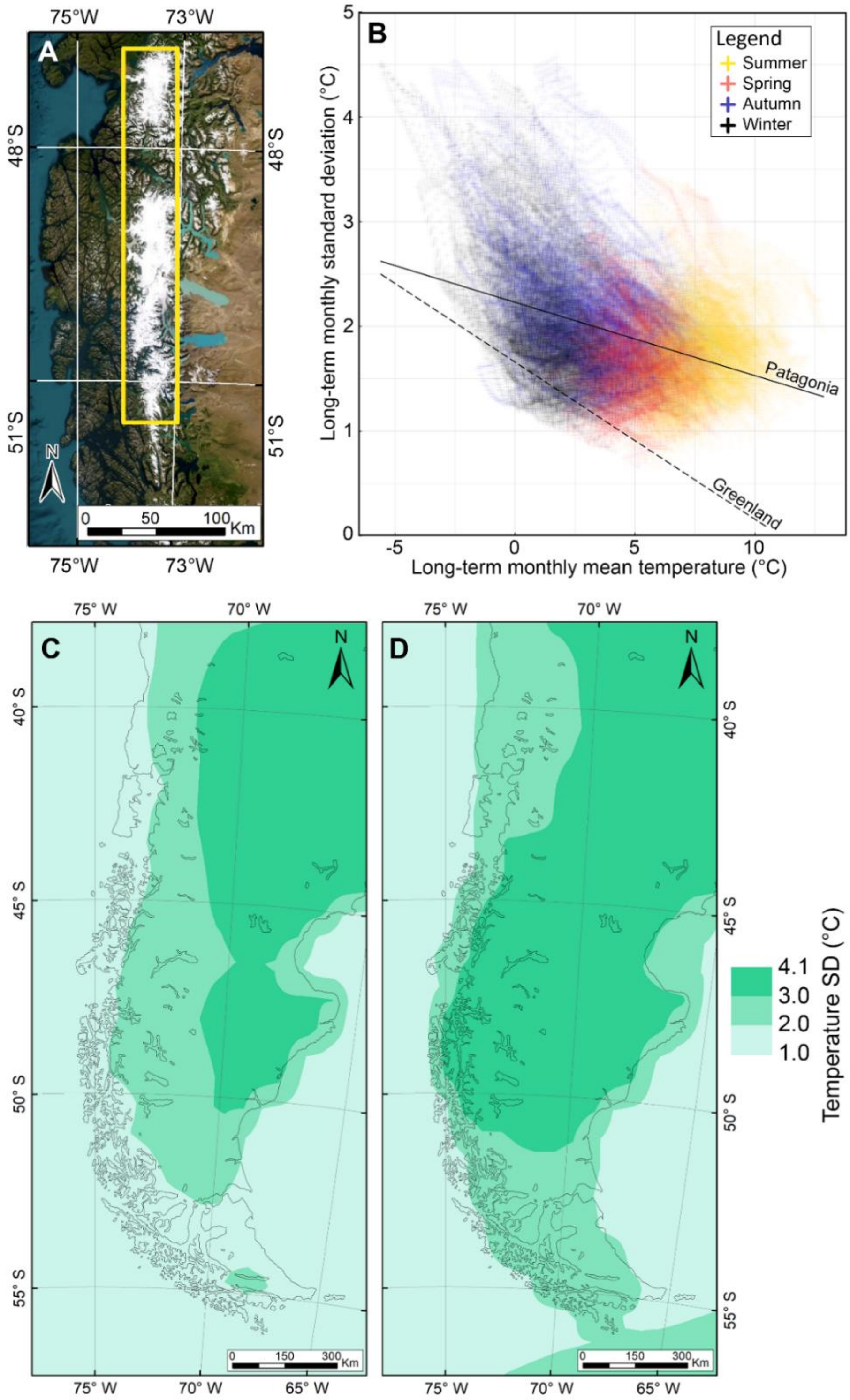

Figure 3.9. Air-temperature standard deviation (SD) methods to simulate diurnal air temperature variabilities. In the top panels a linear temperature SD approach in relation to the surface air temperature is illustrated. A) Long-term monthly mean temperature vs long-term monthly SD data has been obtained from the yellow polygon (ERA-40 reanalysis data) to calculate a linear relationship for the air temperature SD. B) Plot of the data collected from the area of polygon in A, which shows the long-term monthly mean air temperature vs long-term monthly SD data, sorted seasonally. The continuous black line corresponds to the slope that best fits the relationship between the air temperature SD and the air temperature in Patagonia. This linear relationship indicates that the higher the temperature, the smaller the air temperature SD, and vice versa, and this is directly related to the seasons of the year. The dashed line corresponds to the slope that best fits the data in Greenland (Seguinot & Rogozhina, 2014). The bottom panels show the spatial and seasonal air temperature SD approach, which uses a spatial variation for each month. C) January (C) and (D) July temperature SD obtained from Seguinot (2013).

Seasonal and Spatial temperature standard deviation method

The third option is for air temperature SD to vary through the year and within regions, in order to account for the known tendency for higher values to occur during winter months and in continental regions. These changes can be highly significant when modelling large ice bodies such as we are in modelling the whole of Patagonia. We use monthly and spatial variations of the air-temperature SD (model 9; Table 3.2) from Seguinot (2013). They provide global outputs of long-term monthly mean air temperature SD, calculated from daily mean surface air temperature four times during the day, using the ERA-Interim reanalysis (Dee et al., 2011). As the temperature SD varies monthly, we use this approach only with the models that have monthly climatic input.

3.2.4.2. Analysis of the climatic input resolution and temperature standard deviation method

To explore the effect of the climate resolution and the type of air-temperature SD option on the surface melting, the response of Patagonia to those different parameters is tested. The tests are performed with yearly climatic data using two temperature SDs; a constant SD of 3 (Figure 3.10 A), and the linear SD method calculated for Patagonia (Figure 3.10 B). Moreover, we run tests with monthly climatic data, using the previous temperature SD methods (Figure 3.10 C-D) plus the seasonal and spatial SD (Figure 3.10 E). In these sensitivity tests, we only modify the air temperatures by decreasing them by a constant value of -6°C, and we keep the precipitation constant and in its modern configuration.

The analysis of the simulations between yearly and monthly climatic input shows a big difference in the ice extent, independent of the SD method used (Figure 3.10). The yearly climatic input simulations have larger extensions for the ice sheet than the monthly data, expanding more than 100 km to the east in the southern part of Patagonia. To simulate the same effect using temperature alone, with monthly data, would imply more than 1 -degree decrease in temperature for the larger extent simulation. This situation might indicate an underestimation of the higher temperatures during the melt season in the annual climate simulation, letting the model have larger areas with positive mass balance. This assumption is based on the consideration that the more detailed resolution of the monthly data should represent a scenario closer to the observed data (Seguinot, 2013). On the other hand the different methods used for the air temperature SD produce a similar ice extent, as all the methods have little variation in the air temperature SD, between 1 to 4 degrees.

Additionally, we verify that the linear method calculated for the Patagonian Ice Fields can be extended to the rest of Patagonia, even though there are not enough meteorological

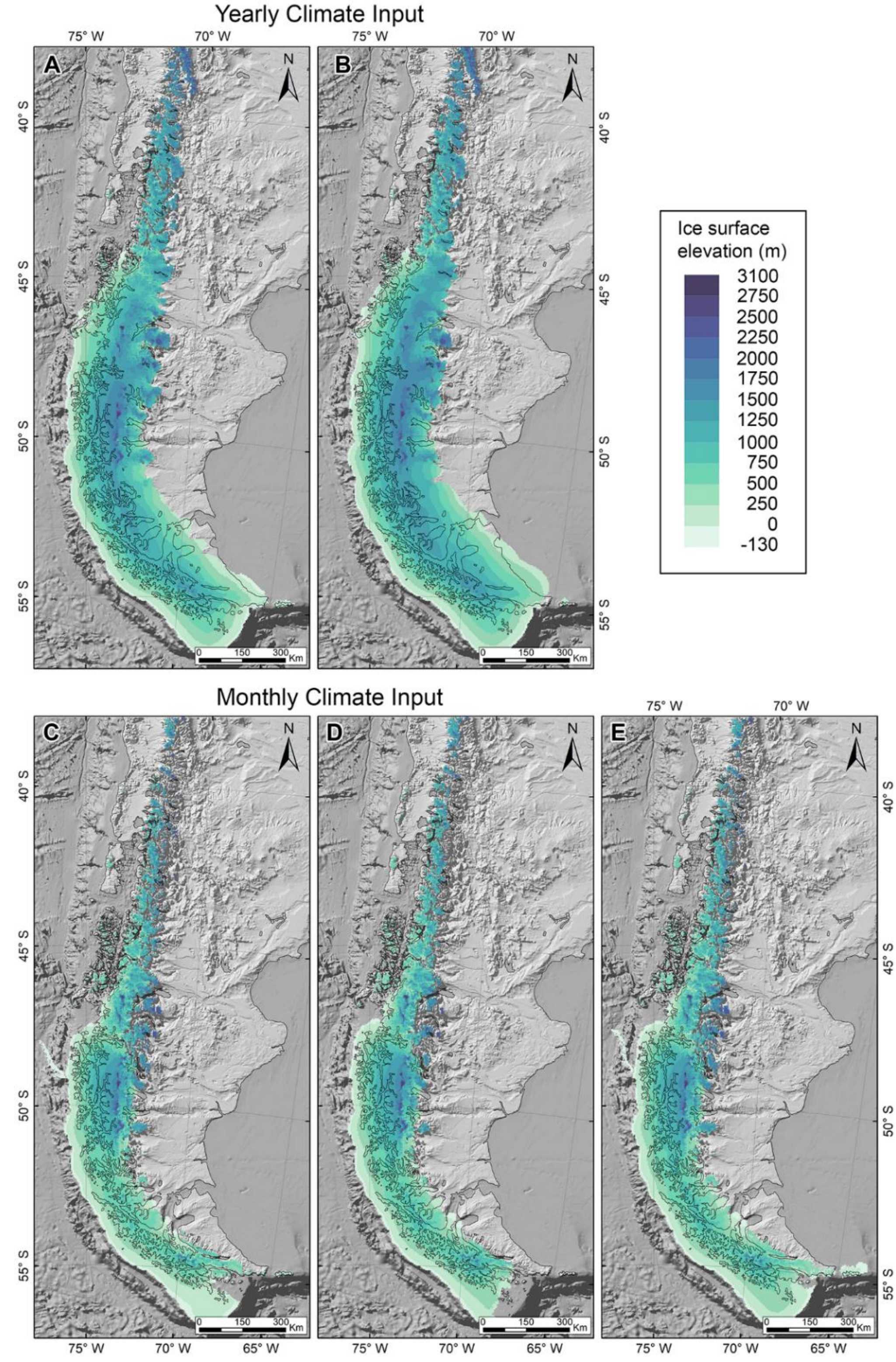

Figure 3.10. Sensitivity tests to evaluate the temporal resolution of the climatic input, yearly (top) vs monthly (bottom), and different methods of temperature standard deviation (SD). All these simulations are run until equilibrium, with the decrease in temperature to -6°, with the modern precipitation configuration and a gradual decrease of the sea level to -134 m. Top, simulations use yearly-mean climatic inputs. A) the temperature SD has a constant value of 3. B) uses the linear temperature SD method. Bottom, monthly-mean climatic input. C) constant temperature SD of 3. D) linear temperature SD method. E) Seasonal and spatial variation of the temperature SD. This figure demonstrates how the selection of the different climatic approaches affects the extent of the resulting ice sheet. For instance, using monthly climate forcings (bottom) gives more restricted ice extent than using yearly (top). The different methods to simulate the air temperature SD yield similar ice extent for the region of Patagonia (compare C-E).

stations to compare this data, as it builds a very close ice sheet configuration to the simulation using the seasonal and spatial temperature SD.

To summarise, we decide to use the higher temporal resolution (monthly) for the climatic data and to use the temporal and spatial variation option for the temperature SD for the remaining simulations in this work because this approach shows a closer agreement with the real climate data (Seguinot, 2013).

3.3. Steady State Sensitivity Tests

With the model set-up as described above, we performed a suite of steady-state simulations of Patagonia at the LGM (~24 ka) and observe the simulations sensitivity to changes in temperature and precipitation. We completed an ensemble of 9 different options, conducting simulations for combinations that apply a uniform decrease in air temperature of 6°, 7°, or 8°C at the same time as scaling modern precipitation pattern by factors of 1.0, 1.2 or 1.5 to keep or increase the precipitation at the LGM (Table 3.2).

We further analyse some of the better model runs from the ensemble to see the sensitivity of Patagonia to the temperature and precipitation and to examine how well the resulting ice sheet fits with the geomorphologically constrained LGM extent. To evaluate the ice extent of the model's results with the geochronological reconstructed margins, we assign four categories to the quality of the fit, as follows:

- Poor: Most lobes have ice extents that are >100 km short of the reconstructed margin.
- Fair: Most lobes have ice extents that are between 50 and 100 km short of the reconstructed margin.
- Good: Most lobes have ice extents that are within ~50 km of the reconstructed margin (either too extensive or too restricted).
- Excess: Most lobes have ice extents that exceed of the reconstructed margin >50 km.

We find that Patagonia's response to glaciation is different along the regions. For instance, in the north, we observe that a reduction in air temperature of 6°C, with constant modern precipitation (model 10), develops only isolated patches of ice. However, the response in the rest of Patagonia is different because under the same conditions a continuous ice sheet develops from central Patagonia (~45°S) to the south, reaching the continental shelf border to the west at 48°S all the way to the south. To the east, the glaciers are mostly still confined to the mountain valleys in central Patagonia, while in the south, some outlet glaciers are starting to form (Figure 3.11 A). This climate forcing generates ice extent with a poor fit to known LGM extent in the north and in central Patagonia. Southern Patagonia has a good fit, although even in this area, the ice extent is still tens of km short of meeting the known ice extent from the geomorphology.

When increasing the precipitation by a factor of 1.5 and keeping the temperature constant by 6°C (model 12; Figure 3.11B), northern Patagonia develops considerably more ice for previous runs. The fit with the geomorphology of this model in the north is poor, but better than previously, but the glaciers still need some tens of kilometres of expansion before they would reach the LGM extent, especially in the area of Chiloé Island in northwestern Patagonia (~42°S), where the modelled ice margin lies about 100 km inland from the known maximum extent. Nevertheless, in the central south the ice extent of this model has a good fit with the geomorphology in most of the outlets, and where it does not, only a little expansion (tens of km) would be needed to match the known extent. Likewise, the ice extent results of this model are very similar to decreasing the temperature to -7°C and increasing the precipitation to a factor of 1.2 (model 13, Figure 3.12 A).

When decreasing the temperature to -8°C and keeping the precipitation constant by a factor of 1.0 (model 16), a continuous ice sheet develops along the whole of Patagonia, filling most of the mountain valleys with ice, and with ice reaching the continental shelf to the north, at ~42°S. In the northern sector, the ice extent has a fair fit, especially to the East, but to the West some outlets and piedmonts lobe recorded by the geomorphology are ice-free, for instance inwards of Chiloé Island in northwestern Patagonia (~42°S). Central Patagonia shows a good fit compared to the geomorphology. In the South, the situation is different, as the ice sheet extends significantly to the east, exceeding the known extent by tens of kilometres (Figure 3.11 C).

Finally, when decreasing the temperature by 8°C, but increasing the precipitation by a factor of 1.5 (model 18), an overgrown ice sheet develops along the whole Patagonia, with coalescent piedmont outlets developing in the terrestrial regions such that it is hard to distinguish between individual ice lobes (Figure 3.11 D). This climate forcing generates an ice sheet, where it fits, exceeds the geomorphologically mapped extent along the whole of Patagonia, especially in the southeastern region.

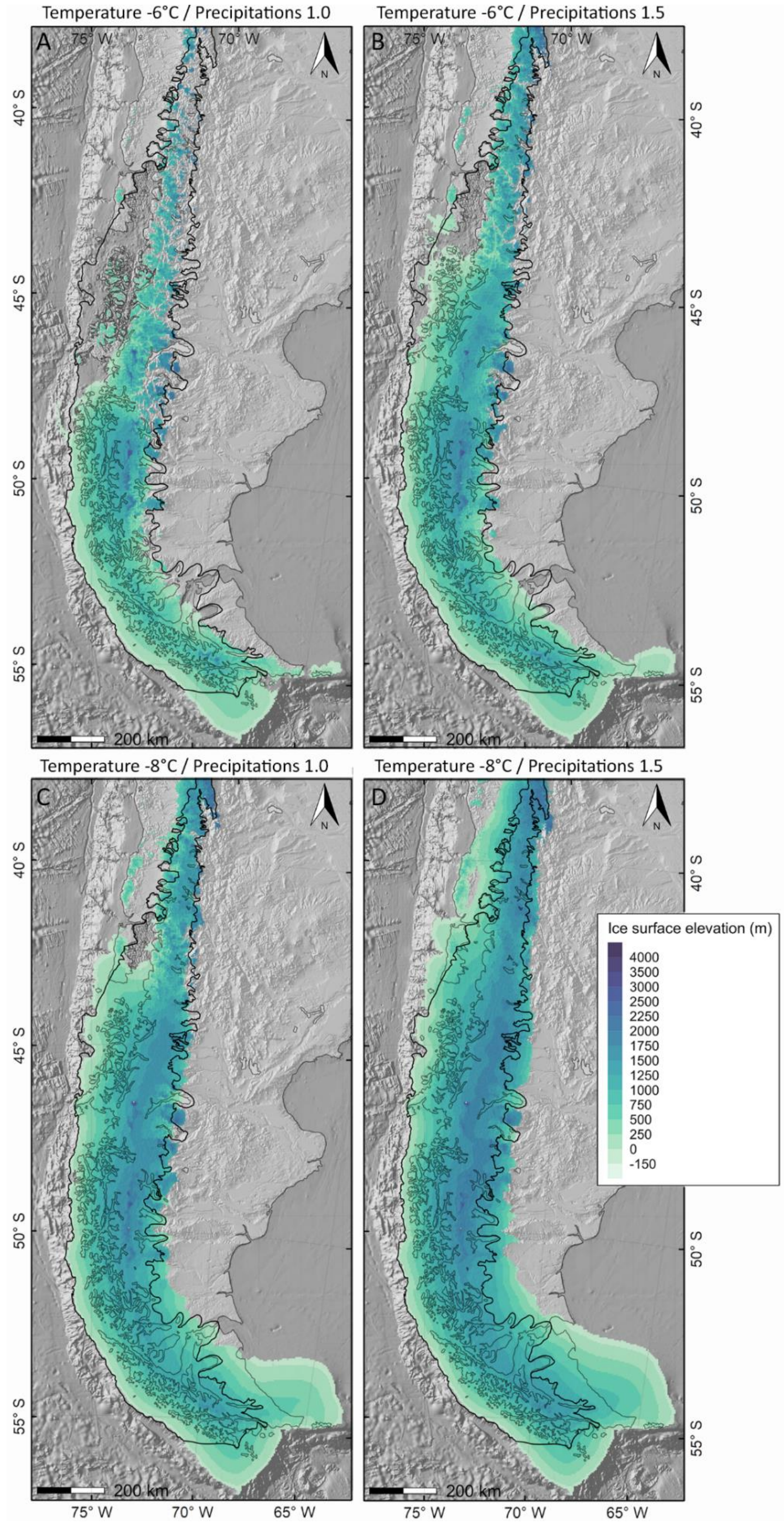

Figure 3.11. Ice extent in Patagonia from different climatic forcing to test their sensitivity to glaciation while applying changes in the temperature and precipitation. The modern temperature and precipitation configuration has been scaled by different factors and they are indicated on top of each panel. Moreover, the glaciological and climatic parameters for each model are indicated in Table 3.2, and the results correspond to A) Model #10, B) Model #12, C) Model #16, D) Model #18. This figure shows an overall bracket of the past climatic conditions necessary to simulate the ice extent during the LGM. It suggests that the temperatures were between 6 to 8° cooler than today and that forcing the climate with the modern configuration of the precipitations does not produce results that fit with the LGM extent along the whole of Patagonia. The coarse black line corresponds to the ice extent during the LGM (Davies et al., 2020).

3.4. Discussion

This chapter explores different parameters in order to create a baseline set-up of the ice sheet model for Patagonia. We explain the reasons for the chosen physical parameter values and for the mass balance computation. Following that, our tests of the glaciation response of Patagonia to a perturbed steady-state modern climate configuration showed that the scale of ice masses that would develop under those degrees of cooling and precipitation enhancement can vary very significantly over space. Nevertheless, these model experiments give us insight into the likely climate required to develop the PIS around the LGM, providing a framework for further experiments in Chapter 4.

3.4.1. Model Physical Parameters

The tests on the ice flow and basal sliding parameters show us that they have a varied impact on the ice thickness and velocities, but the ice extent remains relatively unaffected. Interestingly, altering either of the ice flow enhancement values shows minimal impact on the ice thickness and velocities of the PIS. However, an increase of the till deformation parameter (q=0.8), produces larger ice volume changes and a significant decrease in the ice velocities on the outlet glaciers and ice shelves.

The limited variation in ice volume and velocities may partly be a function of the coarse model resolution. In higher-resolution simulations, the bed elevation is better represented and this allows the model to better solve the ice flux of the topographycally-controlled outlet glaciers, and it is crucial for resolving ice streams, because with finer resolution, the ice sliding velocity can locally increase (Albrecht et al., 2020; Martin et al., 2011). The piedmont and outlet glaciers in northwestern and eastern Patagonia are between 20-40 km wide, which in the model corresponds to only 5 to 10 pixels. This could be a reason why for this work the model did not simulate significant differences in basal sliding velocity or pattern despite the modification of the basal sliding and ice enhancement parameters.

The coarse model resolution could also be the cause of the incapability of the simulations to isolate the outlet glaciers from the inter-lobe areas, as the geomorphology shows outlets with well-developed lateral moraines especially in eastern Patagonia (e.g., Darvill et al., 2014; Glasser et al., 2008). In the more mountainous alpine areas, each pixel of ice exceeds the mountain valley constrain, overestimating the possible glaciated area. This is especially the case in the higher terrain of the inter-lobe areas where the coarse resolution of the modelled inter-lobe ice seems to merge with (i.e. it is not distinct from) outlet glaciers, giving the idea that adjacent lobes coalesced. However, the geomorphology shows a clearer distinction between ice lobe and inter-lobe ice extent and character, with marked lateral moraines along the outlet and piedmont glaciers

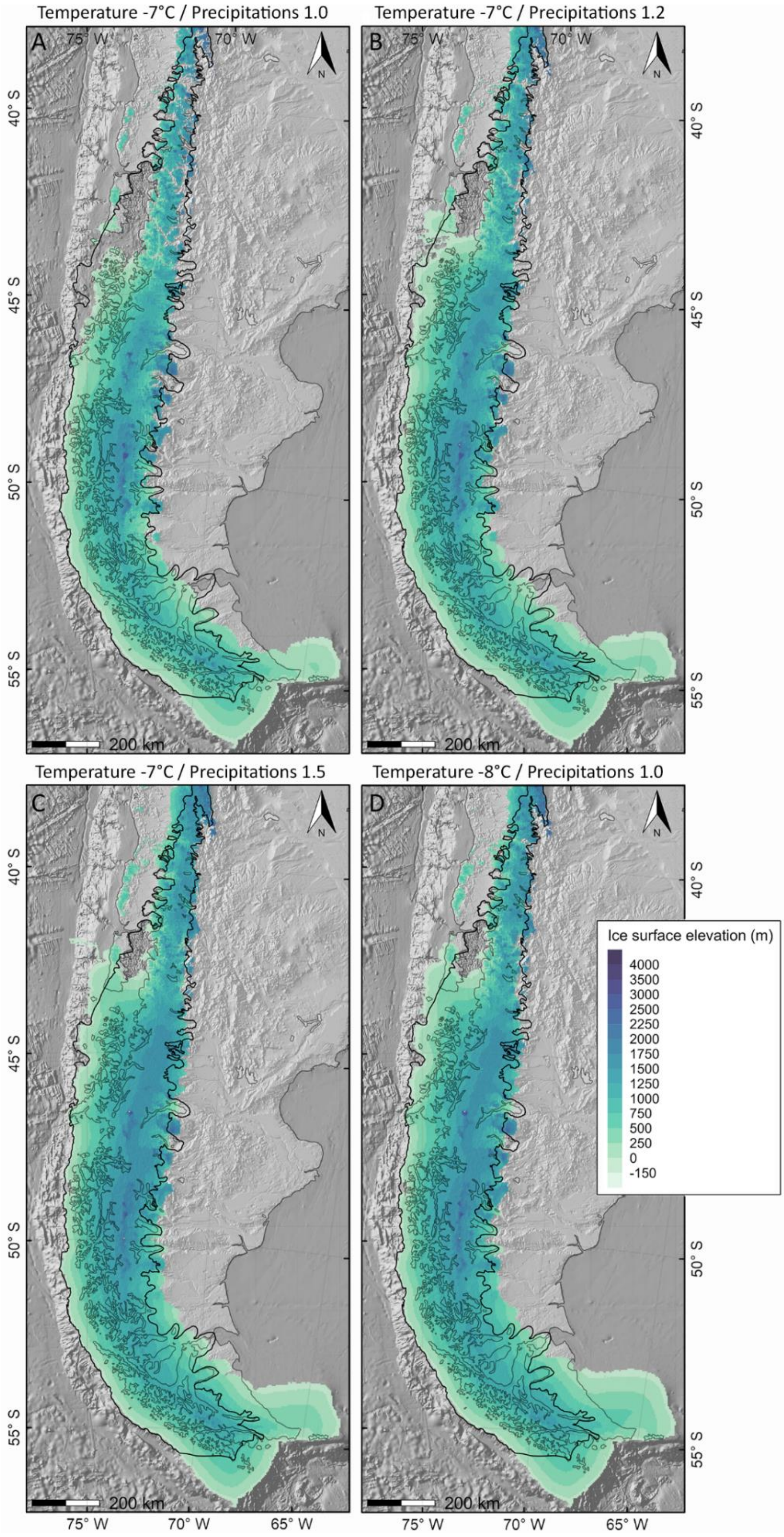

Temperature -7°C / Precipitations 1.0

Temperature -7°C / Precipitations 1.2

Temperature -7°C / Precipitations 1.5

Temperature -8°C / Precipitations 1.0

Figure 3.12. Models from the climatic forcing sensitivity test that their ice extent fit the best to the geochronology extent for the LGM. The modern temperature and precipitation configuration has been scaled by different factors and they are indicated on top of each panel. A-B) Better fit for the central south of Patagonia. C-D) Better fit for northern Patagonia. The glaciological and climatic parameters for each model are indicated in Table 3.2, and the results correspond to A) Model #13, B) Model #14, C) Model #15, D) Model #16. The coarse black line corresponds to the ice extent during the LGM (Davies et al., 2020).

(Davies et al., 2020; Glasser et al., 2008). This may also be linked to our topographic boundary conditions: the lack of lake bathymetry in the GEBCO data set (see section 3.2.1.1 Bed topography) means that for several of the simulated outlets they are advancing across a flat surface that is at a higher elevation than the true lake bed. This means they will be composed of thinner, and thus slower moving ice, and this may lead to an under-prediction of ice extent in the lobate areas with lakes.

Given the modelled ice margin cannot be easily modified by altering parameter choices in our model framework, and given that the ice lobes are reasonably well represented, we therefore have confidence that our model setup is appropriate for capturing the key outlet features of the PIS. However, in interpreting any model (e.g. in Chapter 4), we will account for the limited ability to capture inter-lobate ice configurations.

3.4.2. Climate input

The temporal resolution of the temperature input has a high effect on the mass balance results. For Patagonia, using yearly data generates ice with larger extents than using the monthly data (Figure 3.10). Assuming that the detailed input would more closely simulate reality (Seguinot, 2013), we suggest the mean annual temperature might be biased towards lower temperatures, underestimating the higher extreme temperatures during the melt season and therefore in the yearly approach becomes inappropriate.

The air temperature SD is an important factor to consider in the mass balance, as it simulates the changes in the temperatures possible during a given day. However, in Patagonia the choice of SD method has little effect on the mass balance computation, as the seasonal and spatial variations are small, between 1 to 4°C. This might be a special case for Patagonia, as the continentality is small compared with northern Hemisphere scenarios, and the marine influence greatly buffers the extreme temperatures (Kang et al., 2015).

3.4.3. What do the experiments tell us about the likely climate at the LGM?

The simple steady-state climatic sensitivity tests done for Patagonia show that the responses of the ice sheet to climatic perturbations are different between regions, especially between the North and South. Overall, northern Patagonia needs to experience more extreme conditions in order to be glaciated than is the case in the central south. For steady-state simulations, the model suggests that northern Patagonia can reach close to known LGM extents (Davies et al., 2020) by applying a decrease of 7°C in air temperature and by increasing the precipitation by a factor of 1.5 (model 15; Figure 3.12 C) or by applying a decrease of 8°C in air temperature alongside a precipitation factor of 1.0 (model 16; Figure 3.12 D). For the central south, the conditions needed are different, requiring a decrease in air temperature of 7°C with precipitation factors of between 1.0 to 1.2 (models 13 and 14; Figure 3.12 A and B, respectively). The northern part of Patagonia could be more sensitive to precipitation than to air temperature because the former PIS was confined to the high mountain areas with an alpine glaciation style (Glasser et al., 2008; García, 2012), therefore the high altitudes would mean that it was already cold enough to generate ice. In central southern Patagonia, however, the outlet glaciers of the PIS extended largely over low elevation relief (Benn & Clapperton, 2000a; Bentley et al., 2005; Darvill et al., 2014).

None of our sensitivity experiments produced a model with consistently good fits along the whole of the PIS. To meet the ice extent constrained by the geomorphology, it therefore appears necessary to perform a change in the precipitation pattern so that it deviates spatially from the modern one. This is because when the fit in the north is poor the fit in the south is good and vice-versa, when obtaining good fit in the north, an overgrown ice sheet with an excess fit results in the south. Therefore, to obtain a better fit for the whole Patagonia, we suggest wetter conditions must prevail in the north during the LGM period. This agrees with previous PIS reconstruction focused on climatic approaches (Hulton et al., 1994; 2002) and will be tested in Chapter 4.

These steady-state simulations therefore provide the foundations for a further set of experiments which aim to apply time-evolving patterns of temperature change alongside precipitation changes that evolve away from the modern distribution. This is consistent with previous work which proposes that the Westerlies either shift or expand, bringing with them changes in precipitation distribution. Such simulations will be therefore described and applied in Chapter 4 in order to test hypotheses of past westerly wind evolution and their impact upon the growth, extent and retreat of the PIS.

3.5. Conclusions

In this chapter, the set-up for a PISM model for the PIS is developed. We find that:

- By analysing and testing a range of physical and glaciological parameters, we are able to simulate an ice sheet along Patagonia according to the topographic and glacial environment conditions of the region (e.g., basal sliding transition from hard to soft sediment, or simulation of warm based glaciers). Nevertheless, there are limitations in the representation of the PIS, for instance overestimation of ice extent in the inter-lobe area or poor representation of the basal sliding conditions, which are likely related to the coarse model resolution. The key parameters are outlined in Table 3.1.

- By conducting tests of the mass balance computation in relation to the temperature standard deviations we determine how this might impact PIS extent. We find that using a monthly mean temperature resolution, with a standard deviation that varies spatially and seasonally, should represent better the real conditions that occurred in Patagonia because they have better detail in time and space.

- The variations to the modern climatic conditions along Patagonia have developed an ice sheet in the area, which is an expected response that agrees with the area's geomorphology on a large scale. As a consequence, we are confident that the model set-up is suitable for using as a basis for further testing of the impact of different climatic conditions over the last glacial cycle on the PIS.

- By conducting climatic sensitivity tests we observed that northern Patagonia is particularly sensitive to precipitation changes, while the central south is sensitive to both precipitation and air temperature evolution. The importance of this is that it demonstrates that different parts of the PIS react more, or less strongly to different components of the climate.

In summary, the key finding of this chapter, therefore, is that in order to perform a full reconstruction of the PIS ice extent that fits well with the known geomorphologically mapped LGM extent along the whole Patagonia it is necessary to apply a climate pattern that is not only differentially colder depending on location, but also one that applies precipitation in significantly different patterns from the modern. In particular, we demonstrate that is it necessary to increase the precipitation in northern Patagonia in order to develop an LGM ice extent that fits with the mapped evidence.

Chapter 4 Palaeoclimate along Patagonia during the last glacial cycle through Ice Sheet Modelling. Part II: transient simulations

Huishue lake, northwestern Patagonia

4.1. Introduction

The geochronology records in Patagonia show an asynchrony between different outlets for the maximum ice extents through the last glacial cycle. In general terms, the ice maxima in northern and southern Patagonia occurred during MIS 3 (Darvill et al., 2015; Denton et al., 1999; García et al., 2018; 2021; Zech et al., 2011) and MIS 4 (Peltier et al., 2021). However, central Patagonia shows a different scenario, where most of the geochronology indicates ice maxima later in time, during MIS 2, contemporaneous with the global Last Glacial Maximum (LGM; Douglass et al., 2006; Hein et al., 2010; Kaplan et al., 2004; Leger et al., 2021; Figure 4.1). Moreover, in this area there is one ice lobe with ice maxima at the end of MIS 5 (Mendelová et al., 2020). Reasons for this asynchrony are unclear, but it has been suggested this could be most likely related to changes in climatic factors, such as the shifting of oceanic and atmospheric systems in response to the Antarctic sea-ice expansion (Darvill et al., 2016). The Southern Westerly Winds (SWWs) are directly linked to the precipitation in the area, in that their position controls the configuration and amount of precipitation in Western Patagonia (Garreaud, 2009). There is a strong agreement that the SWWs have a northward displacement during cold periods and move southwards during warm periods (e.g., Bertrand et al., 2014; Kaiser et al., 2005; Lamy et al., 2004; 2010). Moreover, suggest that the northward shift of the SWWs represents a glacial-mode climate, and the more southerly position an interglacial-mode for the Southern Hemisphere. Nevertheless, the pattern of the movement is not clearly known, as some refer to a migration of the SWWs core (Hulton et al., 2002) - implying a northern translation of the existing distribution of the highest precipitations - while others believe that the core expands northwards, with a northward movement and spreading-out of the distribution of precipitation from its previous position. An expansion scenarios therefore leads to less intense precipitation, similar to the contemporary winter pattern of the precipitation (Kaiser et al., 2005). Moreover, the northern extent of any core displacement is also unknown. A better understanding of the past climatic conditions would provide insights regarding Patagonian Ice Sheet (PIS) behaviour in terms of the pattern and timing of ice sheet growth and decay and the ice dynamic processes associated with this. Therefore, this chapter explores past ice sheet response to climate using a numerical ice model forced by a range of plausible SWW changes. To do this we apply a modern precipitation configuration for precipitation plus we create four alternate palaeoclimatic scenarios for the precipitation following the different SWW migration patterns proposed in the literature. We use the Parallel Ice Sheet model (PISM), as previously setup in Chapter 3, to model the ice sheet response to these different scenarios for the last glacial cycle (last 120 ka), and explore what climatic conditions are needed to simulate the ice extent at 45, 35, 25 and 15 ka, according to recent syntheses of the geochronology records (Davies et al., 2020). In addition, we analyse regionally the ice dynamics for the different climatic scenarios and discuss implications for understanding past ice behaviour.

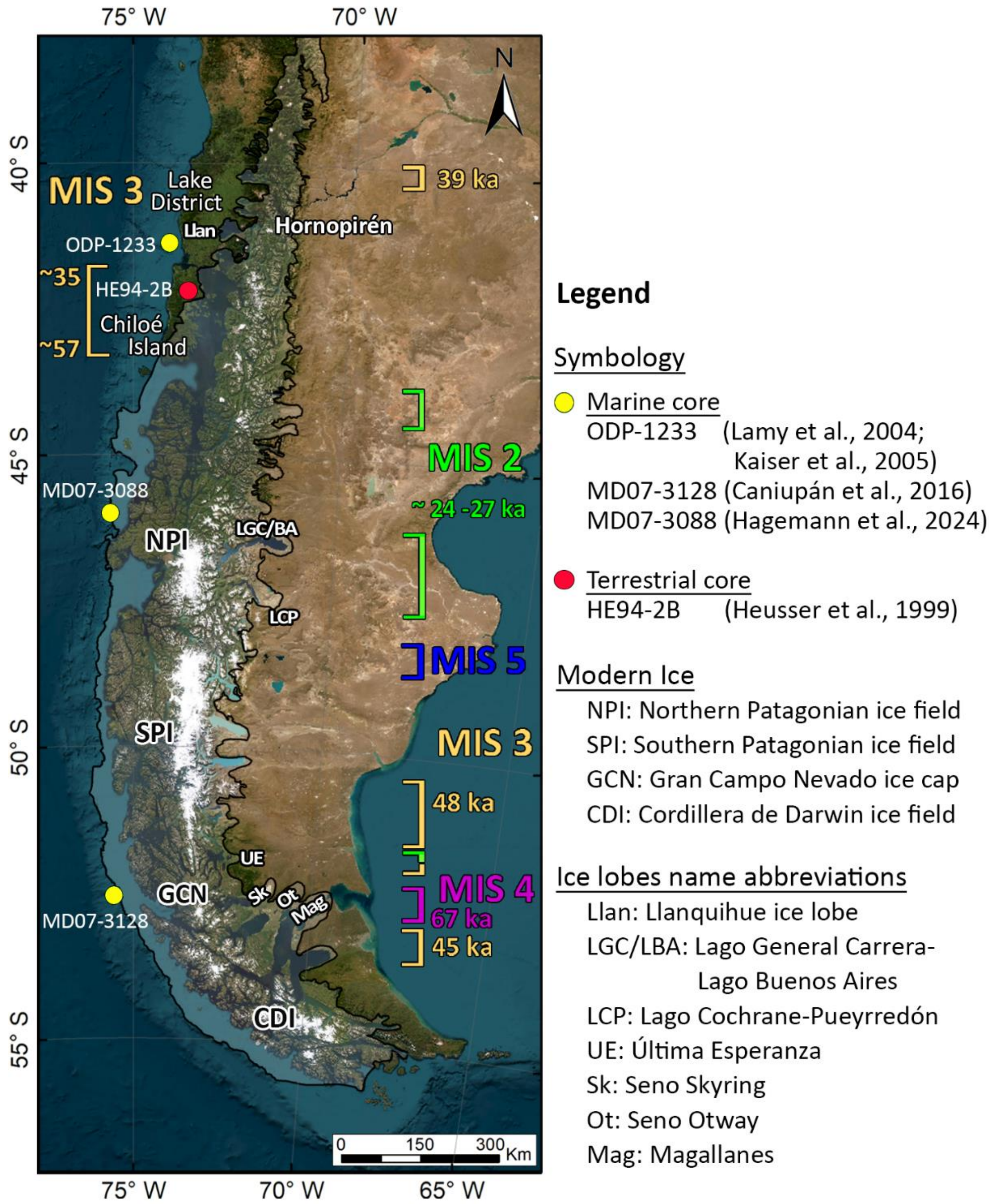

Figure 4.1. Timings for the ice maxima of the former Patagonian Ice Sheet during the last glacial period. The black line corresponds to the Patagonian Ice Sheet extent at the global Last Glacial Maximum (cf. 24 ka; Davies et al., 2020). The brackets show the latitudinal extent of the ice maxima for a certain period. The brackets are opened towards the dated ice lobes, either on the western or eastern side of the Andes. A regional tendency can be appreciated, where Northern and Southern Patagonia reached their maximum extensions between 30-50 ka during MIS 3, except for one earlier outlet maximum at MIS 4 in Southernmost Patagonia. On the other hand, in Central Patagonia, the ice maxima occur in a close agreement between 27 – 24 ka (MIS 2), relatively contemporaneous to the global Last Glacial Maximum, with one outlet maximum in MIS 5a.

4.1.1. Palaeoclimate during the last glacial period, including the LGM

Palaeoclimate records in Patagonia are concentrated along the western margin, and they do not extend through the whole glacial cycle. Continuous palaeoclimate proxies in Patagonia earlier than the LGM are mostly restricted to the marine records obtained from cores drilled on the continental shelf of western South America (Lamy et al., 2004; 2010; Kaiser et al., 2015; Caniupán et al., 2016) and one terrestrial core in a mire located in the north of Chiloé Island (Heusser et al., 1999; Figure 4.1). In these cores, there is a close agreement between the variation of the sea surface temperature (SST) in Patagonia and in the temperature records from Antarctica (Lamy et al., 2004; 2010; Kaiser et al., 2015; Caniupán et al., 2016). In contrast, the records of Patagonia temperatures from palynological and marine proxies show many differences with temperature records from Greenland's ice cores (Heusser et al., 1999). As well as the correspondence to Antarctic temperature changes, the marine records show a high rate of sedimentation during the coldest intervals of the last glacial period (e.g., MIS 4 and MIS 2), implying more runoff in Northwest Patagonia and an overall wetter climate (Lamy et al., 2004; 2010; Kaiser et al., 2015). This is supported by palynological records from northwest Patagonia which indicate that the area was between ~1500 – 2000 mm/yr wetter than today during the LGM (Heusser et al., 2006; Villagran, 1990), and the temperatures were about 6 – 8°C lower than the present (Denton et al., 1999; Heusser et al., 2000; 2006; Villagran, 1990). On the other hand, on the lee side of the Andes, in northern Patagonia, palynological records showing only open vegetation in the area, suggest drier and colder conditions than today (Bianchi & Ariztegui, 2012).

Even though the few palaeo proxy records give an idea about the climate of the past, it is still difficult to construct accurate palaeoclimate scenarios. For instance, the climate simulations completed for the Paleoclimate Modelling Intercomparison Project Phase III (PMIP3; Braconnot et al., 2012; Taylor et al., 2012) underestimated the proxy data of the precipitation by about ~70-80% in Northwestern Patagonia (Berman et al., 2016). This underestimation in precipitation is also evidenced in an ice sheet model reconstruction where, using PMIP3 model output to simulate the PIS, it was not possible to achieve the ice extent specified by the geochronology (Yan et al., 2022). This may partly be due to the way the PMIP3 experiments compute climate, with feedbacks between ice surface elevation and climate not being calculated dynamically over time.

Here we take a different approach to developing paleoclimatic forcing for transient simulations using the ice sheet model developed in Chapter 3. Due to the lack of continuous records of the temperature and an incomplete understanding of the precipitation configuration for the last glacial cycle, we instead perform sensitivity tests with different temperature and precipitation scenarios to explore the climate, and thus the SWW evolution, that best reproduces the ice extent registered by the geochronology constraints.

4.2. Methodology: palaeoclimate forcing.

4.2.1. Palaeotemperature Forcing

Due to the close agreement between the variation in SST from Western Patagonia and variation in Antarctic temperatures, we use EPICA's records from East Antarctica Dome C (Jouzel et al., 2007, Figure 4.2) to force the climate: this record is widely used and has the clear advantage of extending the full length of the last glacial cycle.

We ran the simulations from 120 ka, when the air temperature was assumed to be similar to today. From there, we apply a scalar offset in the temperature following the scaled EPICA curve (Jouzel et al., 2007). This scaling is explained in section 4.2.3. Additionally, we apply an environmental lapse-rate, which adjusts the surface temperature with the changes in the surface elevation produced by ice build-up and decline, or sea level change. Observed temperature lapse-rates in Patagonia are -5.5°C/km for the West and -7.2 °C/km for the East part of the Southern Patagonian Ice Field (Bravo et al., 2019). PISM only allows a single value, so in these simulations, we apply a value of -6.5 °C/km, which is the average value in the troposphere (Barry & Chorley, 2009) and lies between the values for east and west Patagonia. In PISM, the temperature varies according to the reference topography that the climate input has (Worldclim2) using the lapse-rate. For instance, the climatic input provides the temperature above the modern Northern and Southern Ice Fields. However, when subtracting the ice thickness to the initial bed elevation, the temperature in that area increases following the lapse-rate value.

4.2.2. Palaeoprecipitation forcing

Palaeoprecipitation proxies from northwestern Patagonia indicate, in general, higher runoff for colder periods, and more specifically for the LGM suggest conditions between 1500-2000 mm wetter than today. Moreover, our steady state sensitivity tests with modern precipitation configuration (Chapter 3), show that a climate forcing with not only colder temperatures but also wetter conditions than today are needed for northern Patagonia, to grow an ice sheet with the LGM extent along the whole of Patagonia. For the South, there is no climatic constraint, however it is likely that it was slightly drier because the SWWs had moved north and colder conditions reduce environmental humidity. As manifested in the modelling set-up, our precipitation inputs underestimate the precipitation in western Patagonia, especially in the southwest, where the climate model has precipitation about 60% lower than today's measurements (Gran Campo Nevado station, 3.2.1.3. Climate Input section). Therefore, it is necessary to consider

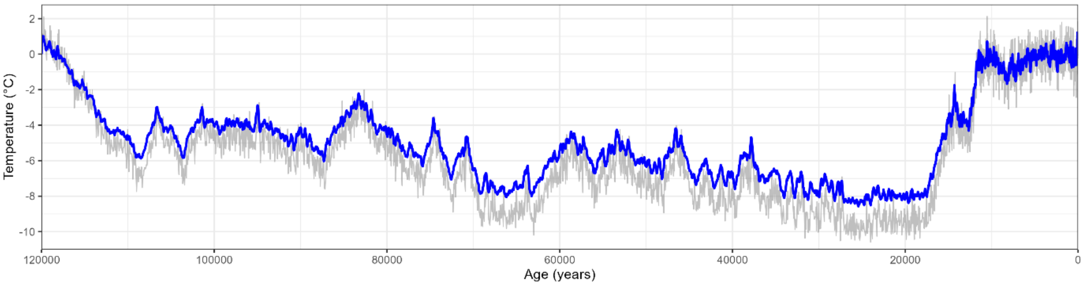

Figure 4.2. Paleo temperature records used to force the temperature changes of the model for the last 120 thousand years. The temperatures are obtained from East Antarctica Dome C (EPICA; Jouzel et al., 2007). Grey lines correspond to the original temperatures. Blue lines are the temperatures smoothed by a 5-point running mean and scaled by a factor of 0.85 (See text for discussion).

that while we make the overall precipitation wetter, the values from the southwestern area, are still relatively lower than today's data.

To force the palaeoprecipitation, we use five different scenarios. One is the 'Modern precipitation' configuration (Figure 4.3 A). We then create four scenarios supported by the literature that represent different interpretations of the configuration of the precipitation during the cold periods of the last glacial cycle. They are 'Central migration', 'Central expansion', 'Northern migration' and 'Northern expansion'. To build these palaeo scenarios, we assume that the current position of the SWWs corresponds to a 'warm' pattern, which has a core of precipitation concentrated between 50-51°S. From there, we create a displacement of the SWWs to more equatorial positions by translating the isohyet pattern northwards. To ensure east-west precipitation gradients are correctly located when creating the precipitation scenarios, we considered the orographic effects of the topographic barriers of the Andes Cordillera. To do this, we ensured that the highest west-east values were located at the western foot of the mountains, as they are today.

In the first palaeo scenario, we perform a 'Central migration' of the modern SWWs core, transporting the core from ~50°S to ~47°S (Figure 4.3 B), creating a wetter Central Patagonia, and a drier Southern Patagonia. Secondly, we perform a 'Central expansion' of the SWWs (Figure 4.3 C), where we expand the SWWs core to central Patagonia, but the intensity of the core weakens. The amount of precipitation in the South is kept similar to today. As an alternative and because the northern extent of the SWWs core is not clearly understood, we perform a similar displacement of the SWWs core, but this time to northern Patagonia. In this third scenario of 'Northern migration', we transport the core to northern Patagonia at ~42°S (Figure 4.3 D), creating a wetter northern Patagonia, and

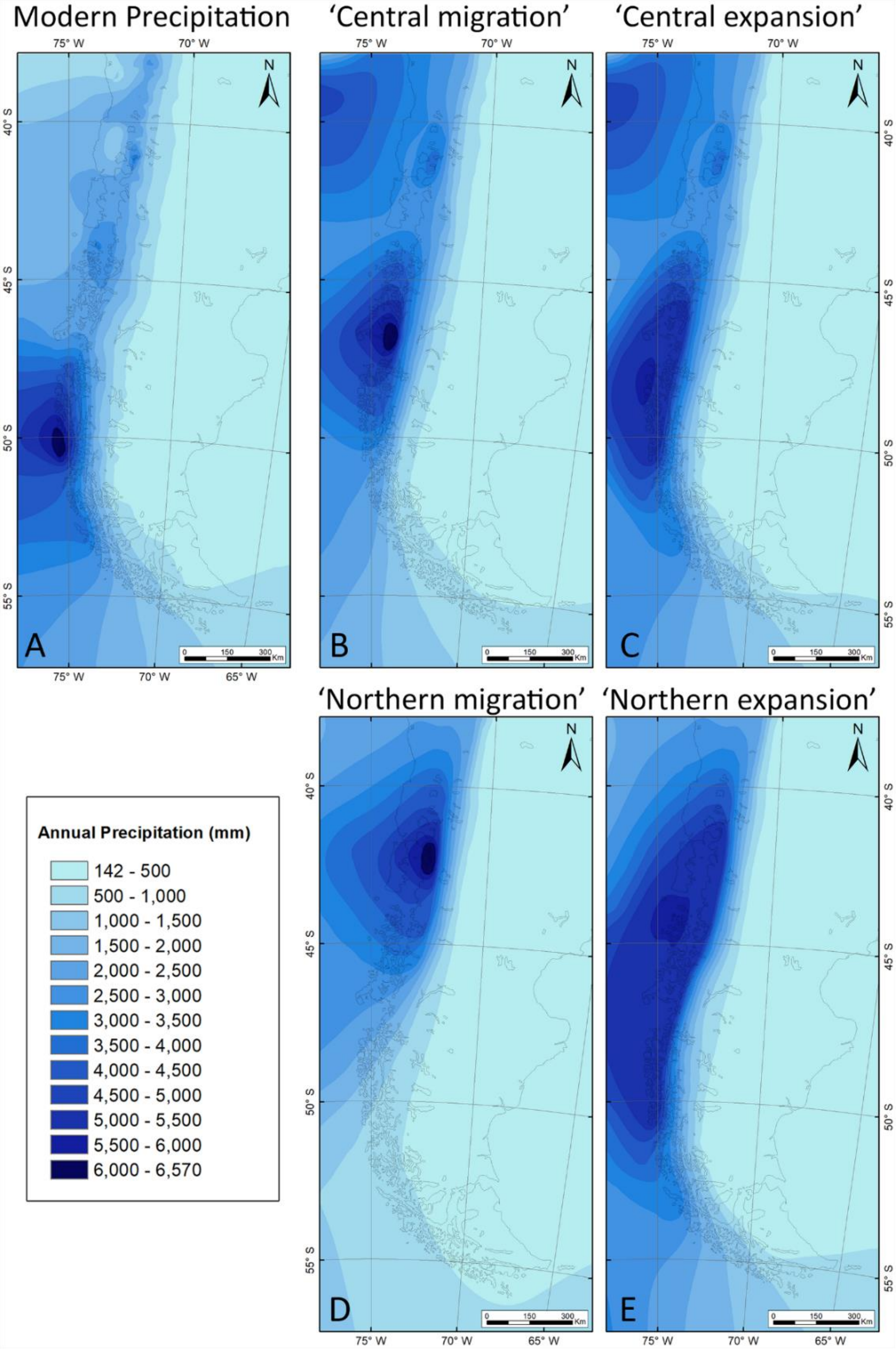

Figure 4.3. Precipitation scenarios used to force the different models. A) Modern precipitation scenario, corresponds to the present day precipitation distribution, where the precipitation is concentrated in a core between 50-51°S. B) 'Central migration' scenario, we transport the core to central Patagonia at ~47°S, creating a wetter Central Patagonia and a drier Southern Patagonia. C) 'Central expansion' scenario, we expand the SWWs core to central Patagonia, but the intensity of the core weakens. The amount of precipitation in the South slightly less than today. D) 'Northern migration' scenario, we transport the core to northern Patagonia at ~42°S, creating a wetter Northern Patagonia, and a drier Southern Patagonia. E) 'Northern expansion' scenario, we expand the SWWs core to northern Patagonia, but the intensity of the core weakens. This scenario keeps slightly less precipitation in Southern Patagonia than today.

a drier Southern Patagonia. Finally, we create a fourth scenario of ‘Northern expansion’, where we expand the SWWs core to northern Patagonia (Figure 4.3 E), but the intensity of the core weakens. This scenario keeps the same amount of precipitation in Southern Patagonia as today. In all four situations, eastern Patagonia becomes drier by ~50%.

4.2.3 Set-up of time-varying forcing

The climatic proxy records in Patagonia for the last glacial cycle, indicate that the temperature was between 6°- 8°C colder than today (Denton et al., 1999; Villagrán, 1990; Heusser et al., 2000; 2006). The temperature records from EPICA show up to a 10°C cooling relative to the present (Fig. 4.2) (when smoothed using a 5-point running mean). The EPICA record is recording temperature change at high elevation on the Antarctic Ice Sheet and therefore is a larger cooling than would have been experienced in Patagonia, but the temporal pattern of temperature change is likely to have been similar between Antarctica and Patagonia. Therefore, to match the Patagonian proxy data, we run experiments where we scale the EPICA temperature by a factor of 0.85, 0.75 and 0.65, resulting in a maximum decrease in temperatures of -8.5°, -7.5° and -6.5°C respectively, all of which maxima occur at ~24 ka. Thus the timing of warming and cooling is paced by EPICA but the magnitude of warming and cooling is less extreme than occurred on the Antarctic plateau, and are more consistent with the Patagonian proxy data.

For precipitation, our palaeo scenarios already show wetter conditions for central and northwestern Patagonia. Nevertheless, we broaden these settings to allow for changes in total precipitation, scaling the precipitation by factors of 0.8 and 1.2: resulting in three precipitation amounts for each precipitation scenario, 0.8, 1.0 and 1.2. We combine each of the three temperature and three precipitation scaling factors, and this results in 9 climatic variations for each of the five spatial precipitation scenarios (Table 4.1), giving a total of 45 models. We run all the models from 120 ka to present, with the glaciological and positive-degree day model set-up parameters described in Chapter 3.

4.3. Results: Palaeoclimate model and fit to ice sheet history

4.3.1. Influence of the precipitation scenario on the ice extent

To assess the glaciation response of Patagonia to the different precipitation scenarios, we assess every one of the 45 model runs against dated geomorphological constraints from the PATICE project (Davies et al., 2020). To outline this process of evaluation we begin here by showing the analysis of the model’s results from the five precipitation scenarios described in section 4.2.2., and forced by the same scaling factors: temperature scaled by a factor of 0.85 and the precipitation by 1.0. Thus, in these runs

Table 4.1. Ensemble of the model's climate forcing. The EPICA temperatures for the last glacial cycle are combined with the five precipitation scenarios. The temperatures are scaled by factors of 0.85, 0.75 and 0.65, while the precipitation is scaled by factors of 0.8, 1.0 and 1.2, yielding a total of 45 climatic scenarios. Id refers to the scenario number, which we use subsequently to identify the results of individual simulations. T=temperature, Pp=precipitation.

		Precipitation scenarios											
		Id	**Modern Pp**	Id	**Northern migration**	Id	**Northern expansion**	Id	**Central migration**	Id	**Central expansion**		
Temperature scaling factors	T 0.85	**1**	T0.85/Pp0.8	**10**	T0.85/Pp0.8	**19**	T0.85/Pp0.8	**28**	T0.85/Pp0.8	**37**	T0.85/Pp0.8	Pp 0.8	**Precipitation scaling factors**
		2	T0.85/Pp1.0	**11**	T0.85/Pp1.0	**20**	T0.85/Pp1.0	**29**	T0.85/Pp1.0	**38**	T0.85/Pp1.0	Pp 1.0	
		3	T0.85/Pp1.2	**12**	T0.85/Pp1.2	**21**	T0.85/Pp1.2	**30**	T0.85/Pp1.2	**39**	T0.85/Pp1.2	Pp 1.2	
	T 0.75	**4**	T0.75/Pp0.8	**13**	T0.75/Pp0.8	**22**	T0.75/Pp0.8	**31**	T0.75/Pp0.8	**40**	T0.75/Pp0.8	Pp 0.8	
		5	T0.75/Pp1.0	**14**	T0.75/Pp1.0	**23**	T0.75/Pp1.0	**32**	T0.75/Pp1.0	**41**	T0.75/Pp1.0	Pp 1.0	
		6	T0.75/Pp1.2	**15**	T0.75/Pp1.2	**24**	T0.75/Pp1.2	**33**	T0.75/Pp1.2	**42**	T0.75/Pp1.2	Pp 1.2	
	T 0.65	**7**	T0.65/Pp0.8	**16**	T0.65/Pp0.8	**25**	T0.65/Pp0.8	**34**	T0.65/Pp0.8	**43**	T0.65/Pp0.8	Pp 0.8	
		8	T0.65/Pp1.0	**17**	T0.65/Pp1.0	**26**	T0.65/Pp1.0	**35**	T0.65/Pp1.0	**44**	T0.65/Pp1.0	Pp 1.0	
		9	T0.65/Pp1.2	**18**	T0.65/Pp1.2	**27**	T0.65/Pp1.2	**36**	T0.65/Pp1.2	**45**	T0.65/Pp1.2	Pp 1.2	

only the precipitation location differs (i.e. model ids #2, #11, #20, #29, #38). For this example of the analysis, we compare the ice sheet extent at the 35 ka timeslice for all the climate forcings (Table 4.1), and we assess their fit against PATICE extent at this time (Davies et al., 2020).

Forcing the model with the 'Modern precipitation' scenario (#2) produces a good reconstruction in central and southern Patagonia; however, to the north, there is insufficient ice growth, producing a poor fit (Fig 4.4 A). This climate forcing creates a continuous ice sheet from 44°S to the southern end of the continental shelf. Between 46-56°S, the ice extent has a good fit with the geochronology at 35 ka, especially on the western margin where the ice reaches the edge of the continental shelf. To the east, the model reconstructs well the ice extent on the inter lobe area, however it is some tens of kilometres too restricted to meet the ice extent for some of the larger eastern outlet glaciers. In the centre-north, the ice sheet narrows to a region centred on the cordillera, reducing its extent on the continental shelf. In northern Patagonia, the glaciers are restricted to the high mountain areas. There the glaciers range in size, forming ice fields and ice caps. In northern Patagonia, this model produces a poor reconstruction of the ice sheet at 35 ka, as the ice extent is >100 km short of the extent recorded by the geomorphology, especially in the Chiloé area of western Patagonia (Figure 4.4 A).

The 'Northern migration' scenario (#11) generates an ice sheet along the north and centre of Patagonia and two minor ice sheets in the south (Figure 4.4B). This reconstruction produces a good fit with the geomorphology in northern Patagonia, especially in the northern region. However, at the Chiloé Island latitude, the ice extent is some tens of kilometres too small to meet the geomorphological evidence. The ice development in central and southern Patagonia is not enough to reconstruct the ice sheet according to the geomorphology records, resulting in a poor fit. In the central south, the ice sheet extends only to the mountain region with higher altitudes, leaving the fjords and continental shelf ice-free. In southern Patagonia, the ice sheet extends beyond the western fjords and covers most of the continental shelf. Nevertheless, most parts of the easterly fjords are free of ice and fall >100 km short of reconstructed margins at 35 ka (Figure 4.4 B).

The ‘Northern expansion’ scenario (#20) produces a continuous ice sheet that develops from 39°S all the way to the south end of Patagonia (Figure 4.4C). In the north, most of the mountain valleys are covered by ice. From the 43°S the ice sheet reaches the edge of the continental shelf and from there, it extends all the way to the southern end of the continental platform with a constant lateral width. To the east, in central Patagonia, incipient outlet glaciers form and extend beyond the Cordillera, while in the south the outlet glaciers extend farther to the east, covering almost all the easterly fjords. The ice extent of this reconstruction has a fair fit in northern and central Patagonia while a good fit in the centre, when comparing with the geomorphology records at 35 ka (Figure 4.4 C).

Forcing the model with a ’Central migration’ scenario (#29) generates, in the north, ice in the form of ice fields and ice caps, and they are confined to the mountainous area (Fig 4.4D). From 43°S to the south, it forms a continuous ice sheet that reaches the edge of the continental shelf all the way to the southernmost area. Nevertheless, central Patagonia has a wider ice extent than southern Patagonia. To the east, central Patagonia has outlet glaciers that extend beyond the cordillera domain, while to the south, there are outlet glaciers, but they are constrained by the fjords, and most of the easterly fjords are not completely covered by ice. The ice extent of this model has a fair fit with the geomorphology records constrained at 35 ka in central Patagonia. However, this is not the case for northern and southern Patagonia, where this climate forcing produces a poor fit, with ice extent ~100 km inboard of the geomorphology records (Figure 4.4 D).

The ’Central expansion’ scenario (#38) produces ice fields and isolated glaciers restricted to the mountain areas in the north (Fig. 4.4E). This scenario creates a continuous ice sheet from the 43°S to the south. To the west, it occupies the continental shelf at 44°S; from there, the ice sheet has a continuous lateral extent between 250 to 300 km all the way to 57°S. To the east, in central and southern Patagonia, the outlet

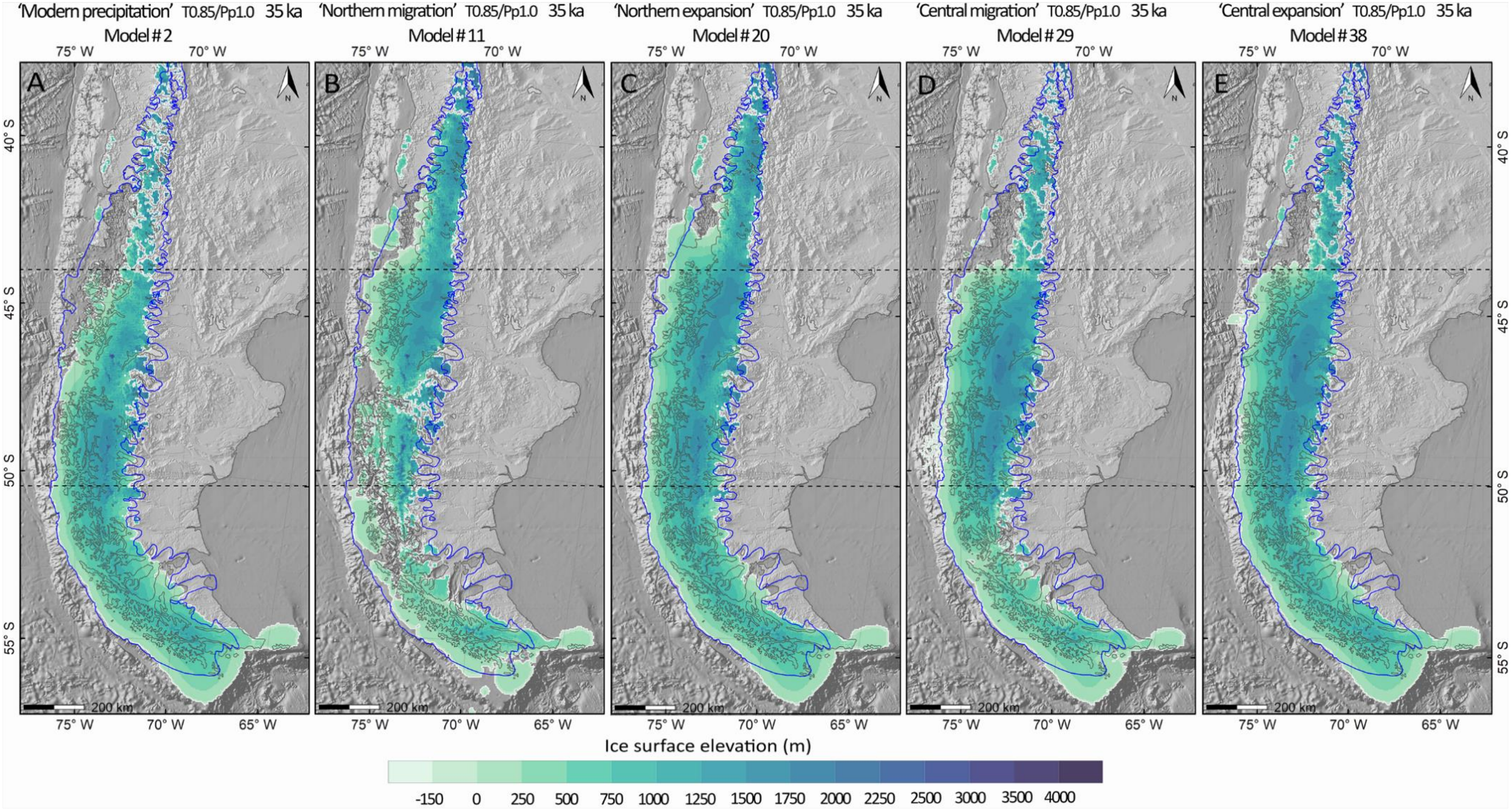

Figure 4.4. Ice surface elevation at 35 ka, resulting from models forced by the five different precipitation scenarios proposed in this work and the temperatures forced by the EPICA curve. In all of them, the precipitation is scaled by a factor of 1.0 and the temperatures by a factor of 0.85. A) Modern precipitation scenario. B) Northern migration scenario. C) Northern expansion scenario. D) Central migration scenario. E) Central expansion scenario. The blue line corresponds to the ice extent constrained at the 35 ka timeslice (Davies et al., 2020).

glaciers extend beyond the mountainous domain; in the south, most of the easterly fjords are completely covered by ice. This climate forcing makes an ice sheet with good fit for the reconstruction at 35 ka in central and southern Patagonia, however, in the north, the ice extent is restricted to the mountainous areas, leaving ice-free outlets, valleys and piedmonts that, according to the geochronology, constraint should be glaciated at this time (Figure 4.4 E).

Based on the 35 ka timeslice and temperature scaling of 1.0 and precipitation of 0.85 the 'Northern Expansion' precipitation scenario seems to produce the best fit to the geological record. This provides helpful context as we now move to look at effects of varying temperature and precipitation scaling, and the quality of fit to the geomorphological record throughout the glacial cycle.

4.3.2. Quality of fit

To evaluate the quality of fit of our models, we do snapshots - similar to the data-model comparison described above for #2, #11, #20, #29, #38 - for all of the forty-five models and for each of 45, 35, 25 and 15 ka timeslices (All the figures are in the Supplementary Chapter 4; SC4). To make this evaluation manageable we show the quality of fit assessment of these different models to northern, central and southern Patagonia, and this is visually, summarised in Figure 4.5. The PATICE project (Davies et al., 2020) has performed reconstruction of the ice extent every five thousand years starting at 35 ka to 0.2 ka. Nevertheless, we also include a snapshot at 45 ka, because there are at least three ice lobes in Southern Patagonia that record ice maxima around that period (Darvill et al., 2015; García et al., 2018). We do not consider older snapshots, as there is either no geochronological constraint or, if any, it is restricted to only one ice lobe. This is the case for the Magallanes and Belgrano ice lobes, in MIS 4 (Peltier et al., 2021) and MIS 5a (Mendelová et al., 2020), respectively. Additionally, we do not consider ages younger than 15 ka because the rapid ice retreat confines the glaciers to the narrow valleys, close to the source area, and the coarse resolution of the model (4 km), comparable in magnitude to many valley widths, does not allow us to draw conclusions on detailed patterns of deglaciation.

For the model fit evaluation, we use the categories described in Chapter 3 (section 3.3 *Steady State Sensitivity Tests*). They are: Poor, Fair, Good and Excess. These evaluations are restricted to the ice extent, as the only significant ice thickness constraints we have are from modelling methods (Wolff et al., 2023), but we explore thickness variations further in the discussion. For every snapshot, we assess the ice extent against the geochronology reconstruction in northern, central and southern

Patagonia (Figure 4.5). One exception is the snapshot at 45 ka, where we only assess the fit for southern Patagonia. As follows:

Our analysis reveals a number of key observations of the relative success of the model ensemble. Models with temperatures scaled by a factor of 0.65 (Figure 4.5 bottom row), generally have poor fit of ice extent with the geological record. Some exceptions of this poor match occurred at 25 ka, where fair and good fit is observed, especially where precipitation is scaled by a factor of 1.2 (e.g., models #36 and #45).

When increasing the forcing temperatures to a factor of 0.75 (Figure 4.5 centre row), the model results adjust better to the ice extent records, especially in central Patagonia (e.g., models #33 and #42), and in the south when the precipitation is higher and concentrated in that area (models #6, #24, #42). Nevertheless, poor fit can be found in north and southern Patagonia, especially with modern precipitation and migration scenarios, respectively (e.g., models #5, #14 and #32).

Forcing the runs with temperatures scaled at a factor of 0.85 (Figure 4.5 top row) results in better fit than warmer temperatures. In other words, the greater the cooling the better the fit. However, no model reconstructs the ice extent in southern Patagonia well for 45 ka. The models forced with *modern precipitation* scenarios, have difficulties reproducing the ice extent from the geochronology in northern Patagonia, in most of the snapshots but the 25 ka (models #1-#3). Nevertheless, the fit increases for the central-south part of Patagonia. The models forced with the *northern migration* scenario, show an ice sheet that responds better in both northern and central Patagonia, with fair to good extent in those areas (models #10-12). At 25 ka, the fit exceeds the extent of the geological constraints in northern and central Patagonia. The general ice extent in southern Patagonia is poor, only producing a fair fit at 25 ka. When forcing the glaciations with the *northern expansion* scenario, there is a good fit along the whole ice sheet, at 35 ka, when scaling the precipitation with a factor of 1.2 (model #21). But, for the 25 ka, the model generates an overgrown ice sheet with respect to the geochronology records. The *central migration* precipitation forcing produces, in general, an ice sheet with a larger extent in central Patagonia, but poor for the northern and central parts (models #28 and #29). Lastly, forcing the model with the *Central migration* scenario produces fair to good fit along the whole of Patagonia, especially at 25 ka with a precipitation factor of 0.8 and 1.0 (model #37 and #38 respectively). None of the models produce a good fit with the geomorphology constraint at 15 ka along the whole of Patagonia. However, there is a good fit either in the north, with the *northern migration* scenario or in the south when forcing the climate with the scenarios with *modern precipitation* (model #1) or the

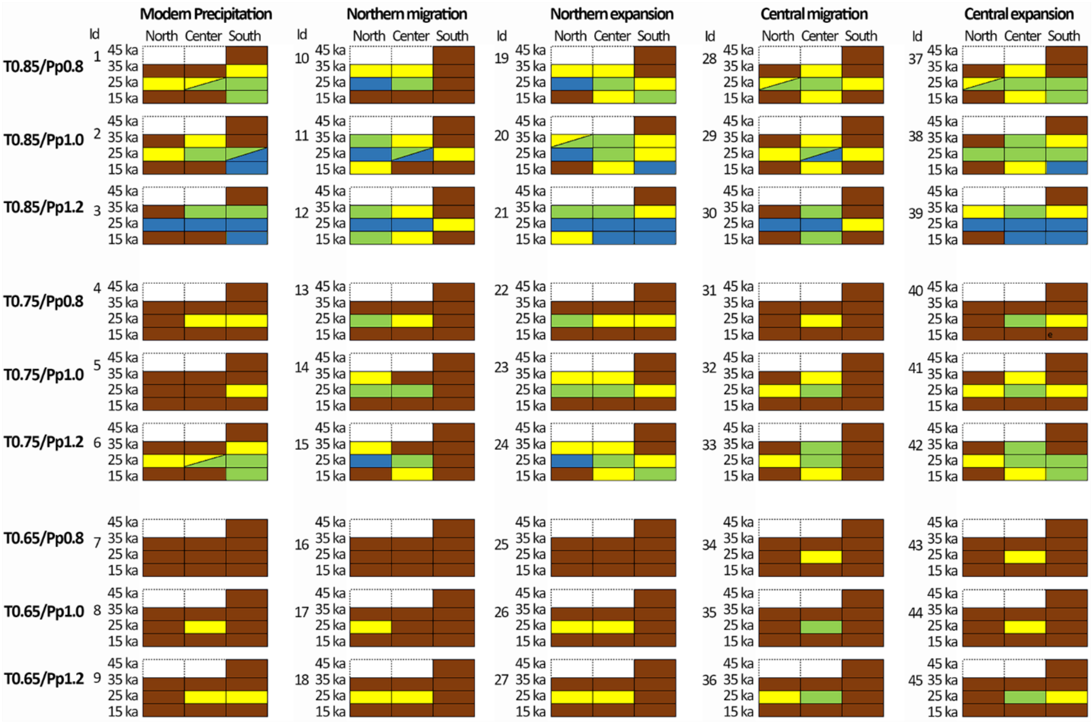

Figure 4.5. Assessment of fit of the 45 models with the geomorphology records constraint by the geochronology, at 45 ka, 35 ka, 25 ka and 15 ka. Each column corresponds to a precipitation scenario, and the rows represent the scaling factor for the temperatures and precipitation. Colour categories: brown: poor; yellow: fair; green: good; and blue: excess. See text for definitions of quality of fit. This figure shows that better fits occur with colder temperatures (e.g. when scaling the temperature by a factor of 0.85). Moreover, the better fit along northern, central, and southern Patagonia at a specific time is reproduced better with expansion precipitation scenarios (northern and central), than the other scenarios.

northern and central expansion scenarios (models #19, #37), which keep the precipitation similar to today in the south.

From the analysis of the fit of the ice extent for the forty-five models with the geomorphology constraint records, we observe that it is very hard to simultaneously fit well to the ice extent in northern, central and southern Patagonia with the same climate forcing. Alternatively, when a model shows good fit with the geochronology along the whole of Patagonia, it does not match for all of the age snapshots. Figure 4.5 shows that no model reproduces the ice extent at 45 ka, this might be related to the climate forcing selection (e.g. EPICA records for the temperature), this is further discussed in section *4.4.1.2. Modelling misfit and possible causes*. Nevertheless, forcing the climate with a *northern expansion* scenario and with a temperature and precipitation scaled by factors of 0.85 and 1.2, respectively, produces a good fit for the snapshot at 35 ka (model #21; Figure 4.6). Even though, the fit is only fair in the south at 35 ka, this climate forcing is the one that produces a better match with the geomorphology records. Moreover, forcing the climate with a *central expansion* scenario with a scaling in the temperatures and

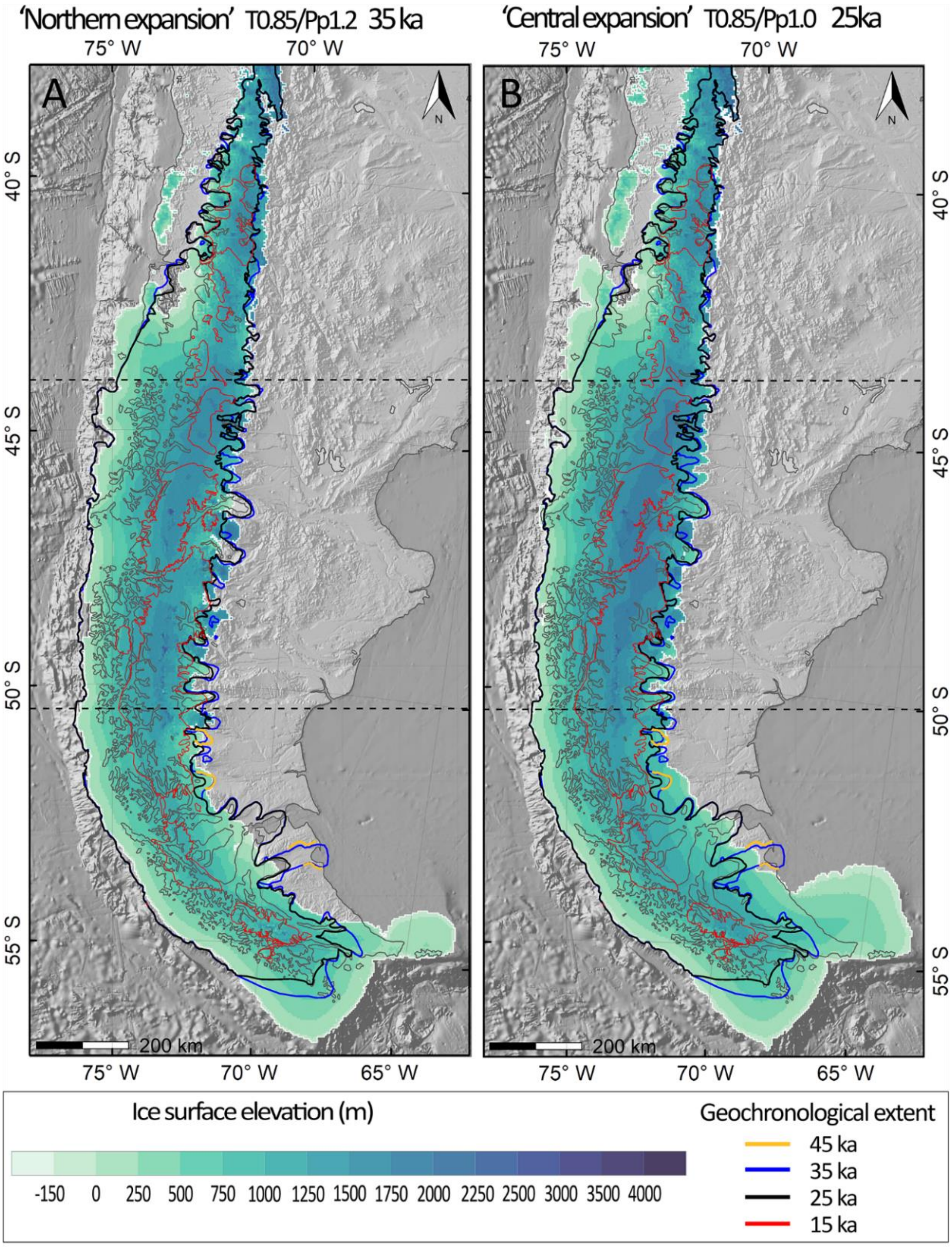

Figure 4.6. Models that have the best fitting ice extent at 35 and 25 ka; the model domain is divided in northern, central and southern Patagonia (boundaries shown by dashed lines). A) Model #21, which is forced with a *Northern expansion* precipitation with temperature and precipitation scaled by 0.85 and 1.2, respectively. B) Model #38, which is forced with a *Central expansion* scenario with temperature and precipitation scaled by 0.85 and 1.0, respectively. The Geochronology extent at 35 and 15 ka is from the PATICE project (Davies et al., 2020), and at 25 ka is modified from PATICE by including Seno Skyring (Lira et al., 2022) and Magallanes ice lobes (Peltier et al., 2021). The ice extent at 45 ka is from Darvill et al. (2015) and García et al. (2018).

precipitation by 0.85 and 1.0, respectively, generates a good fit for the snapshot at 25 ka along the whole of Patagonia (model #38; Figure 4.6). For 15 ka there is no clear candidate for best fit with models #12, 19, 37, 42 all showing similarly good fit, but these include 3 of the 5 scenarios (namely northern migration, northern expansion and central expansion).

From now on, the description of the model results will be only for the models whose ice extent best fits with the geomorphology records constrained by the geochronology. In this case, model #21 reproduces the best the ice extent at 35 ka, while model #38 does so for 25 ka. Due to the equivocal results for 15 ka we do not analyse any model for this timeslice.

The complete animation of both models (#21 and #38), with snapshots every 100 years from 120 ka to the present, can be found in the Durham University library repository under the following link https://collections.durham.ac.uk/files/r21r66j1202

4.3.3. Ice Sheet dimensions

To obtain the ice sheet's dimensions, we chose the largest ice extent and volume around the snapshot at 35 and 25 ka. Thus, for the model that best simulated the ice extent at 35 ka, we extract the ice dimensions at 34 ka, and for the 25 ka, we use the data at 24.7 ka.

The dimensions of the Patagonian Ice Sheet at 34 ka (model #21) correspond to an area of 594,000 km^2 and a total ice volume of 437,400 km^3. The dimensions during the gLGM, at 24.7 ka (model #38), had an area of 629,232 km^2 and a total ice volume of 442,230 km^3.

The sea-level equivalent corresponds to the sea-level changes that would occur if all the grounded ice above flotation (not displacing sea water) from the model melts, and this is distributed uniformly over the global ocean. PISM considers a constant global ocean with an area of 362.5x10^6 km^2 (Cogley et al., 2010). The sea-level equivalent variations for all the models through the last glacial cycle are plotted in Figure 4.7. However, we highlight model #21 (turquoise) for 34 ka and model #38 (red) for 24.7 ka. Model #21 produces an ice sheet with a sea-level equivalent of 0.99 m at 34 ka. Model #38 produces a sea-level equivalent of 1.04 m at 24.7 ka (Figure 4.7).

4.3.4. Deglacial history

It is important to point out that the presence of reverse slope topography on water-terminating glaciers is an important factor in the deglaciation. As the grounding line retreats into deeper water, this promotes greater ice flux at the grounding line, allowing thicker ice to float and thus accelerating ice retreat (Schoof, 2007). This is particularly

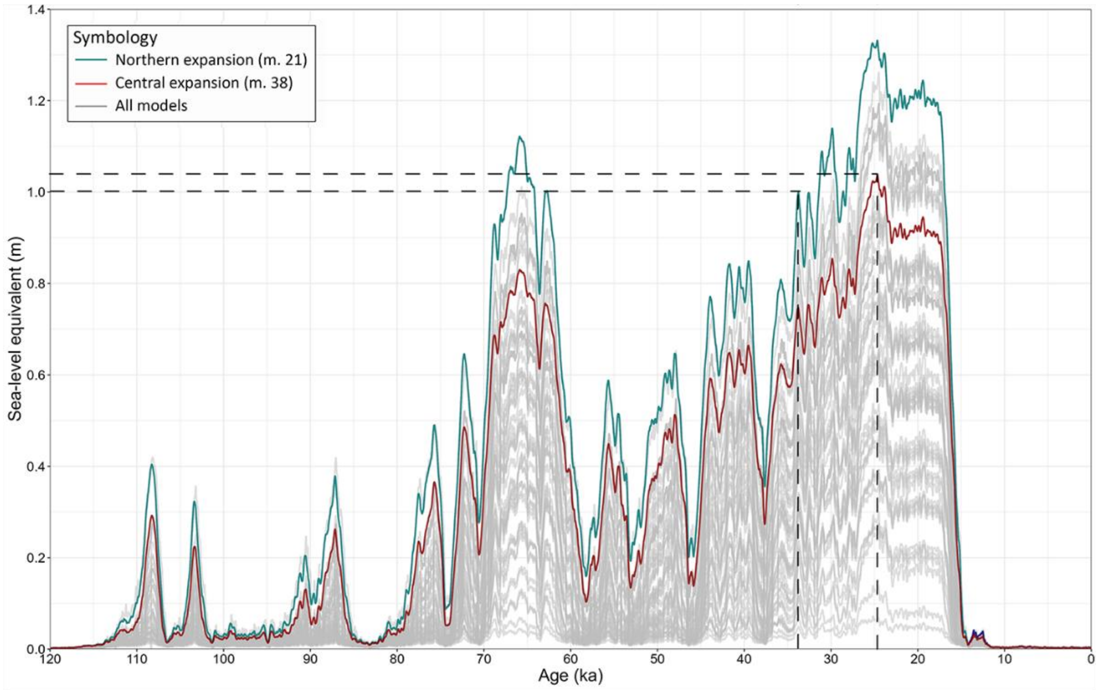

Figure 4.7. Sea-level equivalent of the modelled PIS in the forty-five simulations produced in this work (grey) through the last glacial cycle. The two models that fit the best at 34 ka (model #21) and 24.7 ka (model #38) are highlighted in green and red, respectively. Dash lines guide the x and y axis intersection.

the case on the western (marine) and southeastern (lakes) sides of the ice sheet, where the glaciers advanced into water distal to the Andes. A full analysis of the effects of this factor in deglaciation would require further analysis of the grounding line dynamics, requiring an adaptation of the 3D PISM to a 2D marine ice sheet model (e.g., MISMIP; Pattyn et al., 2012).

For the late glacial and deglaciation pattern, we analyse the ice sheet reduction from its peak that occurred during the global LGM (~24 ka), assessed using the model simulation at 24.7 ka. To do this, we describe only the model that fits best the ice extent at 25 ka, which is the one forced with a *central expansion* precipitation scenario and climate scaled by T0.85/Pp1.0 (model #38). Therefore, for the deglacial history, we only consider the increase in the temperature, and not the changes in the precipitation configuration due to displacements of the SWWs.

After the peak of the modelled ice extent (24.7 ka), the temperature forcing decreases gradually until ~18 ka. Although the change from 24 to 18 ka is <1°C, the PIS reacts significantly in some areas. Northern Patagonia starts losing ice mass immediately and by 18 ka, the ice extent area has shrunk to ~82% of the maximum ice extent at 25 ka, and its volume has reduced by ~53% (Figure 4.8). The rest of Patagonia has a very different response. Central Patagonia has a very stable reaction to the onset of warming with only minor reduction in area and volume. The ice extent in this region decreases

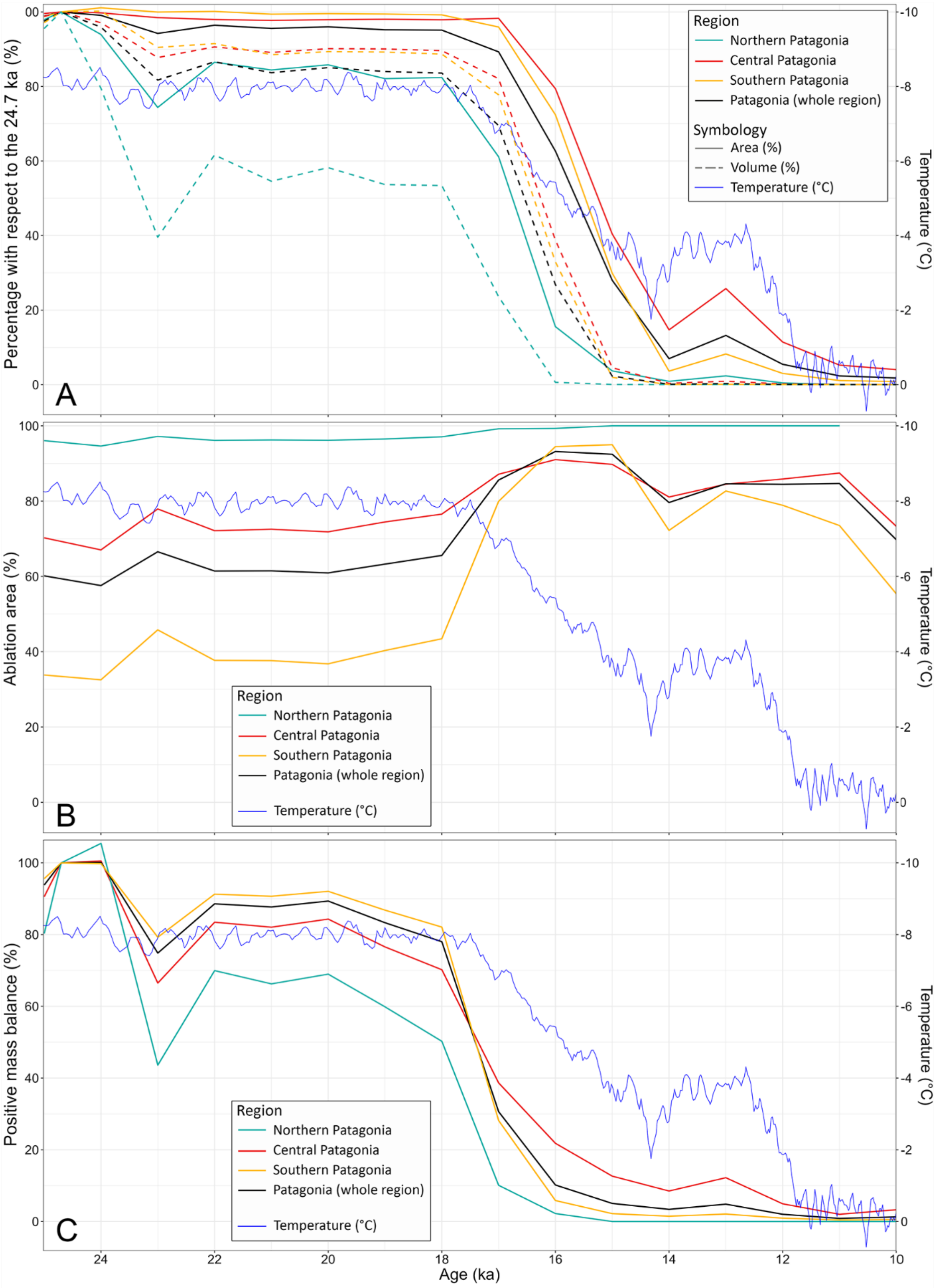

Figure 4.8. Ice sheet deglaciation pattern from 25 to 10 ka. A) Percentage of the ice extent and ice volume, with respect to the maximum ice extent and volume at 24.7 ka (100%). B) Percentage of the ablation area, marked by the area with negative mass balance at each time in percentage. C) Positive mass balance reduction in percentage, from the peak of the glaciation at 24.7 ka. Data are from model #38, which is the simulation that best reproduces the ice extent at 25 ka. The graphs show data for individual regions (northern, central and southern Patagonia) and for the whole of Patagonia. The temperature data (blue line) is obtained from EPICA, and is the record used to force these models. Note that the temperature scale is reversed (coldest at top).

only by 3% at 18 ka, and the volume reduces to ~89% of the maximum volume at the LGM (Figure 4.8). The response of Southern Patagonia is similar to Central Patagonia: from 25 to 18 ka, the ice extent stays relatively constant, decreasing by only 1% at 18 ka, while the ice sheet thins, losing ~11% of volume by 18 ka (Figure 4.8). At 18 ka, the ice sheet border lies slightly inside the geological extent at 25 ka. This is mostly perceptible inland of Chiloé Island, in Northern Patagonia where the ice extent at 18 ka is underestimated by ~10km (Figure 4.9 A).

The causes of ice volume changes can also be understood by looking at the area of negative mass balance (area below ELA) across the PIS which rises markedly in all regions during the onset of deglaciation and particularly sharply in southern Patagonia. (Figure 4.8B). The ability of the areas of positive mass balance (Figure 4.8C) to maintain the ice sheet becomes increasingly limited during the deglaciation, and by 16 ka, only 10% of the residual ice sheet has positive mass balance, helping to drive the very rapid deglaciation at this time. By 12-10 ka in this model a near-modern configuration has been established (Figures 4.8, 4.10). These are explained in detail on the surface mass balance section (Section 4.3.5.2).

Between 18 and 14.3 ka, the temperature rises by ~6°C; this sharp change in temperature produces a large reduction in the ice mass and drastic changes in the configuration of the PIS. In Northern Patagonia, only 3% of the ice area is left by 15 ka and ~1% by 14 ka, while the ice volume is less than 1% of its peak by 15 ka. Central and Southern Patagonia also show a sharp reduction in the ice extent, but Southern Patagonia loses proportionally more ice mass than Central Patagonia. Maps of model output show that by 16 ka, the northern region of the PIS detaches from the rest, and it is confined to isolated glaciers in the high mountain area (Figure 4.9). Central and Southern Patagonia show a reduction in ice extent, especially on the outlet glaciers (Figure 4.9 B). By 15 ka, the PIS extends from 45°S to the end of the continent, and its lateral extent has retreated from the outlet glaciers on the east and from the edge of the continental shelf, but it still occupies the fjords on the west. By 14.9 ka the central and southern parts of the PIS are divided at approximately 48°S, north of the Seno Skyring ice lobe Figure (4.9 C). At 14.8 ka, the southern part divides in two (Figure 4.10 A). Subsequently, at 14.7 ka, the central region of the former PIS is divided in two, resulting in four separate ice fields along the centre and south of Patagonia, located between 45°S-48°S, 48°S-52°S, 52°S-53°S and at 54°S (Figure 4.10 B). By 14 ka, Central Patagonia had lost 86% of the ice area achieved during the LGM, while Southern Patagonia had lost 97%. For both regions, the ice volume is close to zero at this time.

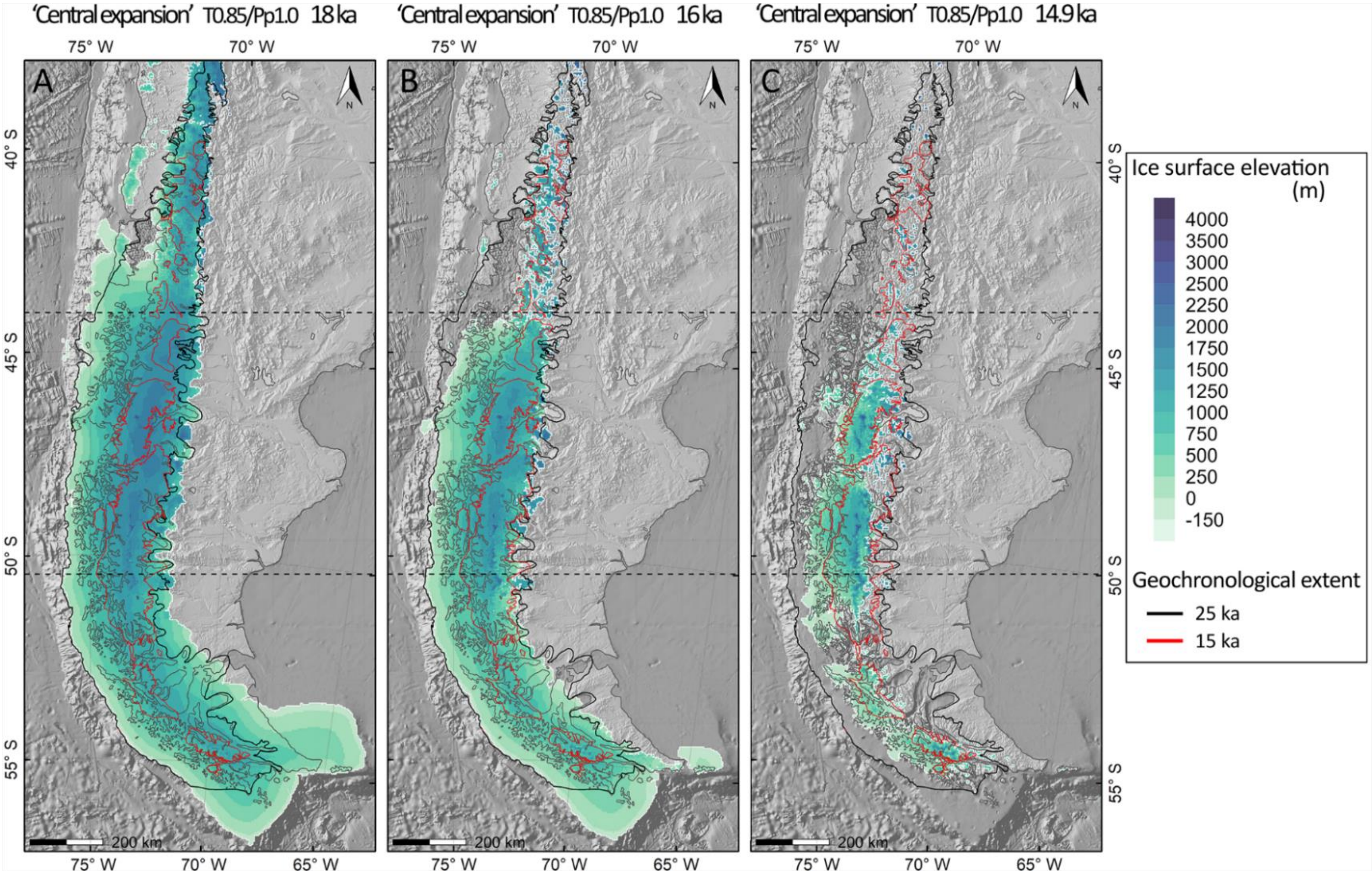

Figure 4.9. Ice extent of the model #38 during the late glacial and deglaciation. Model #38 is forced with Central expansion precipitation scenario and it is the model that best fits the geochronology at 25 ka. Snapshots of the model are taken at 18 ka (A), 16 ka (B) and 14.9 ka (C.) The Geochronology extent at 15 ka is from the PATICE project (Davies et al., 2020), and at 25 ka is modified from PATICE by including Seno Skyring (Lira et al., 2022) and Magallanes ice lobes (Peltier et al., 2021). This figure shows that after the 18 ka the deglaciation is more rapid in northern Patagonia than the rest, and the model does not fit the 15 ka PATICE margin in this area.

Between ~14 and 12 ka, there is a climate cooling during the Antarctic Cold Reversal (cf. 14.6-12.8 ka; Lemieux-Dudon *et al.*, 2010) this produces a slight increase of the ice thickness along the whole region, but has little effect on overall ice volume (Fig 4.8A), and the coarse resolution or the broad time step of the model (every 100 years) appears to prevent a clear change in ice extent. From 12 ka onwards, the temperature increases gradually to 10 ka, from ~-2.5°C cooling to temperatures close to present. In Northern Patagonia, the ice masses disappear almost completely at this time. In Central and Southern Patagonia, the little mass gain that occurred during the climate reversal wanes to values that correspond to 3 to 1% of the maximum ice extent in Central and Southern Patagonia, respectively. By 11 ka, the configuration of the remnants of the PIS is similar to today's ice extent, marked by the Northern, Central, Cordillera de Darwin and the Gran Campo Nevado Ice Fields, plus minor ice caps along central and southern Patagonia, such as Santa Inés Ice cap (Figure 4.10 C).

4.3.5. Ice dynamics

4.3.5.1. Ice velocity and basal sliding

In addition to using the model to explore PIS behaviour through time in terms of extent and volume, it is useful to analyse the changes in glaciological parameters such as ice velocity and basal sliding. The basal and surface ice velocities, have similar 'trends' in terms of how they react regionally and through time. Throughout the whole glaciation, the highest velocities are found in two distinct domains, one is at the edge of the ice shelves along the western (oceanic) margin, and the other is where the slopes are steeper and closer to the edges of the ice sheet. This latter is the case for almost the whole western margin of Patagonia where gradients are very steep with outlets sometimes descending from high elevation to sea level in a matter of a few 10s of km. In central and southern Patagonia we observe this pattern when the area starts to glaciate (e.g. 45 ka), so the steep slopes coincide with the edges of the ice sheet. Nevertheless, as the ice sheet grows, those steep valleys get localised at a more inner position on the ice sheet, and due to colder conditions, the ice velocities decrease. The lowest velocities prevail mainly in the central part of the ice sheet, where the altitudes are higher and close to the ice divide. Additionally, lower velocities are also found at the edges of the outlet glaciers, especially those ones located in eastern Patagonia. Moreover, we observe that as the climate cools, the ice velocities decrease.

At the peak of the ice sheet extent, in northern Patagonia, valley glaciers show very high velocities, reaching up to > 800m/yr. In this area, the slope gradient to the west is particularly steep, where glacier heads are located ~ > 800 m a.s.l. and the altitude decreases close to the sea level in only tens of km of lateral extent. In the central part of

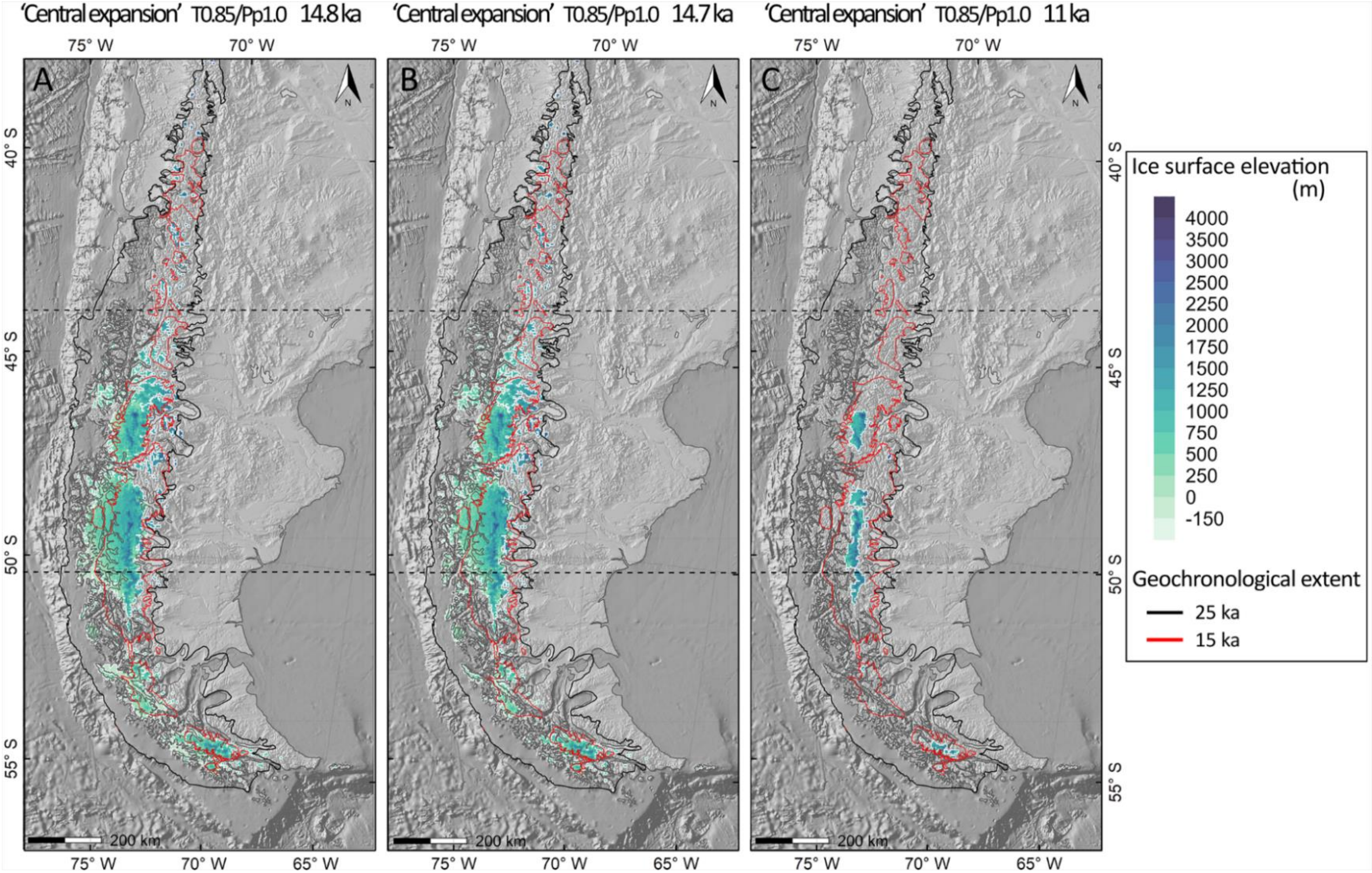

Figure 4.10. Ice extent of the model #38 during the late glacial and deglaciation. Model #38 is forced with Central expansion precipitation scenario and it is the model that best fits the geochronology at 25 ka. Snapshots of the model are taken at 14.8 ka (A), 14.7 ka (B) and 11 ka (C.) The Geochronology extent at 15 ka is from the PATICE project (Davies et al., 2020), and at 25 ka is modified from PATICE by including Seno Skyring (Lira et al., 2022) and Magallanes ice lobes (Peltier et al., 2021). This figure shows that central Patagonia is less sensitive to deglacial conditions than the northern and southern regions.

the ice sheet, the basal ice velocities decrease considerably to less than 20 m/yr (Figure 4.11 A-B).

In central Patagonia, the highest velocities are located on the edges of the ice shelves in the west. In the central area of the ice sheet, the glaciers almost have no movement, with low surface velocities (0-20 m/yr) close to the ice divides and low basal velocities, between 0 to 20 m/yr. Meanwhile, to the east the basal and surface velocities increase along the outlet glaciers, especially on the more external areas of the outlets and where there are distinct troughs; there the basal velocities are higher and surface ice velocities can reach up to ~300 m/yr, which is the case of Buenos Aires and Pueyrredon ice lobes. Between the glacier outlet margins the edge of the ice sheet flows very slowly (Figure 4.11 C-D).

In the south, the ice velocities behave similarly to Central Patagonia, highest velocities are located at the edge of the ice shelves, and around the period of 35 ka some high velocities spots appear around Cordillera de Darwin. The lowest velocities are found close to the centre of the ice sheet and on the basin divides between outlets. Outlet glaciers facing east show sliding, at ~35 ka, and basal velocities go up to ~180 m/yr, while at ~ 25ka, the basal velocities decrease to ~90 m/yr, as conditions get colder (Figure 4.11 A).

4.3.5.2. Surface Mass Balance

We do not analyse the mass balance at 45 ka, as none of the models have reproduced the ice extent recorded by the geomorphology constraints in Southern Patagonia. For the 35 ka timeslice (Figure 4.12), we use the *northern migration* scenario *(scaled by T0.85/Pp1.2;* model #21) and for the 25 ka (Figure 4.13), we use the central expansion scenario (scaled by T0.85/Pp1.0), (model #38) as those climate forcing reproduce in a better manner the ice sheet extent at those respective times. For the late glacial and deglaciation period, we analyse the same model as for the deglaciation (section 4.3.4.), which is the one that best adjusts to the ice extent at 25 ka (model #38). With this, we explore the response in the mass balance to the changes in temperature. Additionally, the coarse resolution of the model does not allow for detailed analysis, preventing us from determining a precise altitude range of the Equilibrium-Line Altitude (ELA) at a local scale. However, we are able to map the ELA of the ice sheet at a regional scale. For instance, we can determine whether the ELA is located in the high mountains or lowland areas. Moreover, from the model it is possible to calculate the total accumulation and ablation area (4.8 B) and, with this, explore the variations in the mass balance (Figure 4.8.C).

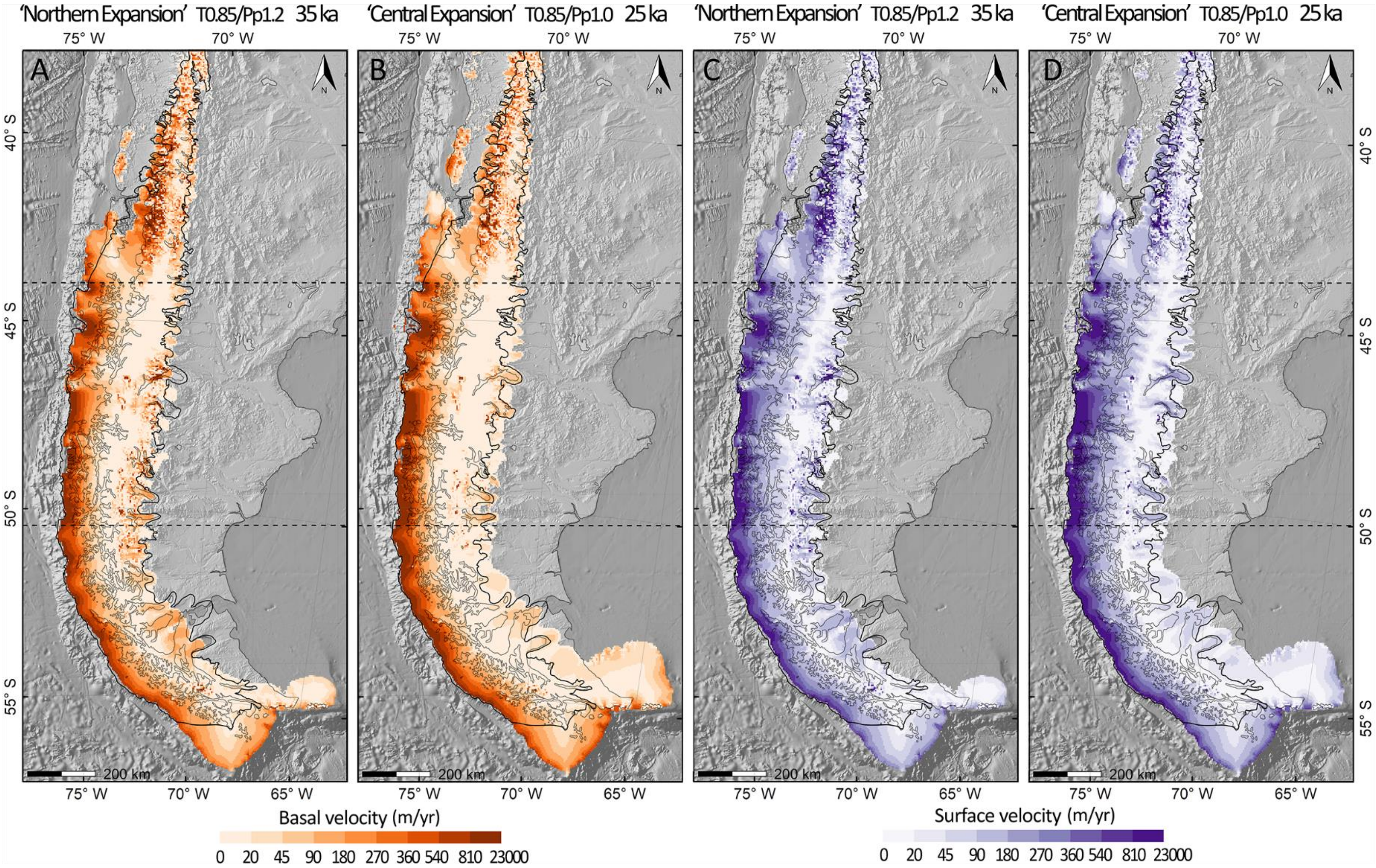

Figure 4.11. Ice velocities of the Patagonian Ice Sheet for the model that best fits the ice extent according to the geochronology records. A) Basal ice velocity of model #21 at 35 ka. B) Basal ice velocity of model #38 at 25 ka. C) Surface ice velocity of model #21 at 35 ka. D) Surface ice velocity of model #38 at 25 ka. The black line corresponds to the geochronology constraint at 25 ka (Davies et al., 2020). Dashed lines divide the model domain in northern, central and south.

From the mass balance analysis, we observe that northern, central and southern Patagonia react very differently to the changes in the accumulation and surface melt at the peak of the ice sheet extent (~35, 25 ka). Northern Patagonia has a similar mass balance tendency at 35 and 25 ka, but the mass balance trends within central and southern Patagonia vary through time.

Mass balance during peak of the ice sheet extent

Northern Patagonia is the region with most mass loss per unit area, where most of the ice sheet area has a negative mass balance, ~99% at 35 ka and ~95% at 25 ka, while only 1 to 5% of the area gains mass, respectively (Fig 4.8B). The mass balance in this region has a strong dependency on the altitude. There is little surface melt in the high mountain area (up to 2000 kg/m^{2}yr at 35 ka; 1000 kg/m^{2}yr at 25 ka), this increases slightly on the valley glaciers (9000 kg/m^{2}yr at 35 ka; ~6000 kg/m^{2}yr at 25 ka) and it has higher values when the glaciers flow away from the mountains, for instance on the piedmont lobes in the Lakes District and Chiloé area in western Patagonia (12000 kg/m^{2}yr at 35 ka; ~8000-9000 kg/m^{2}yr at 25 ka). On the other hand, the highest values of surface accumulation concentrate in the high mountain areas with values up to ~6500 kg/m^{2}yr at 35 ka, and ~3500 kg/m^{2}yr at 25 ka, whereas in the lowland areas, the accumulation reduces drastically to less than ~2000 kg/m^{2}yr at 35 ka and 1500 kg/m^{2}yr at 25 ka (Figure 4.12-4.13).

In central Patagonia, the mass balance is also dependent on the altitude, similar to northern Patagonia, but in central Patagonia the area with overall mass loss is smaller. From the total area, ~88% has a negative mass balance at 35 ka and ~70% at 25 ka, whereas the area with positive mass balance is 12% and 30% (Fig 4.8B). Most of the melt occurs in the lowland areas, especially on the glacier outlets that flow east (e.g., Lago General Carrera/Buenos Aires and Pueyrredón ice lobes), there melting reaches values up to 8000 kg/m^{2}yr at 35 ka and 25 ka. The majority of mass gain occurs on the high plateaus where today are located the northern and southern Patagonian Ice Fields (Figure 4.1). The precipitation distribution drives the accumulation pattern, it has the highest amount on the windward side of the mountains (up to 6500 kg/m^{2}yr at 35 ka; 4000 kg/m^{2}yr at 25 ka) and decreases drastically to the east (up to 1000 kg/m^{2}yr at 35 ka and 25 ka; Figure 4.12-4.13).

Southern Patagonia is the region with the lowest area of negative mass balance, and this varies considerably with the changes in temperatures through time. The net mass loss occurs over ~82% of the ice sheet at 35 ka, but only 30% at 25 ka, while areas experiencing overall mass gain cover a total of ~18% at 35 ka and 70% at 25 ka. In this region, the mass balance is related to the altitude (Figure 4.12A) and also to the amount

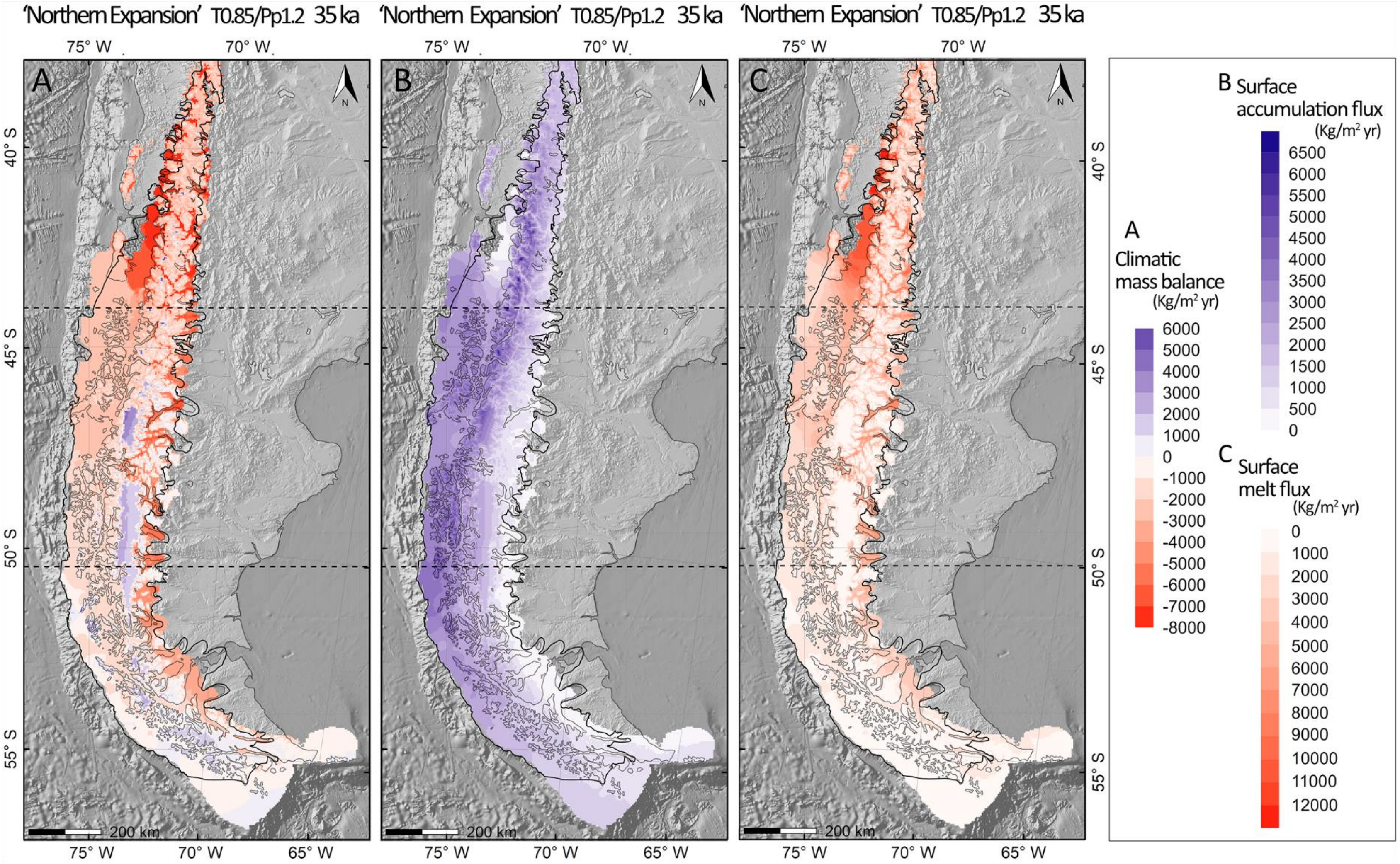

Figure 4.12. Maps of mass balance at 35 ka, produced by model #21. A) Overall mass balance. B) Surface accumulation flux. C) Surface melt flux. Black line corresponds to the geochronology constraint at 25 ka (Davies et al., 2020). Dashed lines divide the model domain in northern, central and south.

and distribution of the precipitation (Figure 4.13A), as the overall temperatures are lower than in the rest of Patagonia. In the times of peak ice sheet extent (e.g., 35 - 25 ka), the melt is very low; most of the area has a surface melt of less than 2000 kg/m^{2}yr. The amount of melt increases slightly on the easterly outlet glaciers, where it reaches up to 4000 kg/m^{2}yr at 35 and 3000 kg/m^{2}yr at 25 ka. The surface accumulation is driven by the precipitation configuration, similar to central Patagonia. Therefore, the highest amount of accumulation occurs on the western margin of the ice sheet, where it reaches up to ~3000 kg/m^{2}yr at 35 ka and 25 ka, and it decreases rapidly on the lee side of the Andes to less than 500 kg/m^{2}yr.

Mass balance during late glacial and deglaciation

The slight warming of 1°C, between the 24 ka to the 18 ka, produces an almost immediate effect in the reduction of positive mass balance along Patagonia (Figure 4.8C). This reduction impacts the amount of melting differently through the regions. Northern Patagonia is the most affected region, and by 18 ka the accumulation area has reduced by ~50%. With the abrupt warming between 18 – 14 ka, the proportion of the area with a positive mass balance sharply declines, reaching close to zero values by 15 ka, this tendency continues almost constant to the rest of the deglaciation. By 17 ka, the whole glaciated area is located in the ablation zone, and by 11 ka, there is no glacier preserved in the area (Figure 4.8B).

Central and southern Patagonia show similar tendencies in the mass balance adjustments, but the changes in the centre are more subtle. In this area, the reduction in the positive mass balance by 18 ka is only 30% and 18% from the peak, for central and southern Patagonia, respectively (Figure 4.8C). The warming between 18 and 14 ka produces an immediate fall in the positive mass balance area, but now southern Patagonia leads the major reduction, with a remaining positive mass balance of ~5% by 16 ka, while central Patagonia has ~20%. During the Antarctic Cold Reversal, there is a slight increase in the area with positive mass balance, especially in central Patagonia. In terms of the ablation area, after the peak in the last glaciation (~25 ka), the area of negative mass balance increases slightly by 7% and 10% for the centre and south, respectively, by 18 ka. The sharp increase in the temperature between 18 - ~14 ka produces a sharp increase in the area of negative mass balance, but this stabilizes for ~1kyr (between 16-15 ka), and it decreases until the 14 ka, despite temperatures increasing through this period. There is not a strong response to the climate reversal 14-12 ka and indeed the area with negative mass balance rises slightly through the latter part of this period and from 11 to 10 ka, it decreases again (Figure 4.8B). In Central and

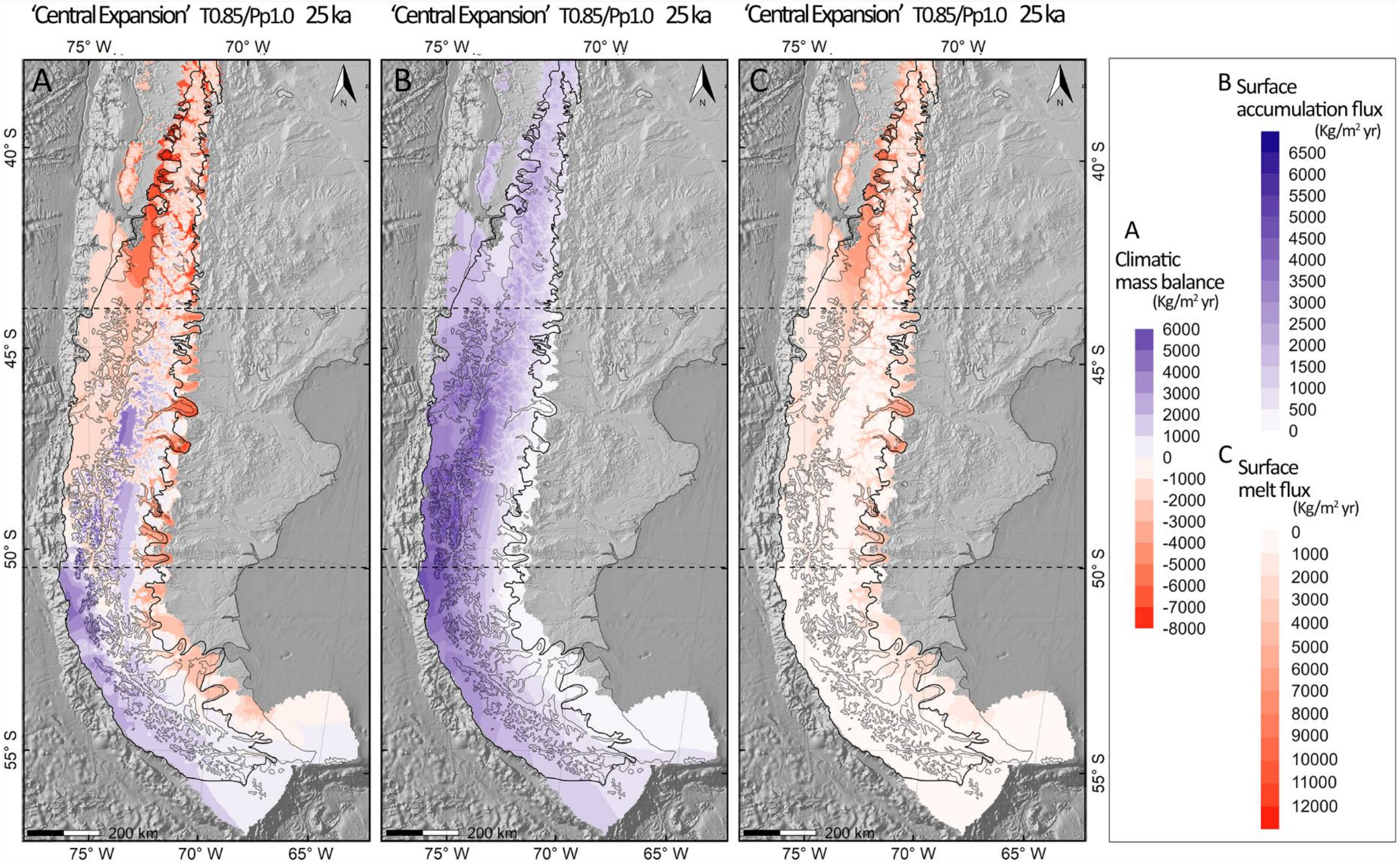

Figure 4.13. Maps of mass balance at 25 ka, produced by model #38. A) Overall mass balance. B) Surface accumulation flux. C) Surface melt flux. Black line corresponds to the geochronology constraint at 25 ka (Davies et al., 2020). Dashed lines divide the model domain in northern, central and south.

Southern Patagonia, the area experiencing negative mass balance increases radically in the lowland areas; this first occurs in the east, where the low levels of surface accumulation are insignificant compared to the increase of surface melt. This response is delayed in the lowland area of the western part of the PIS, where to reach a negative mass balance, it is necessary to reduce the surface accumulation, after which the surface melt becomes dominant in the area. Despite the large amount of mass loss in the lower areas, the overall mass loss of the high mountain areas occurs slowly, especially on the plateaux that today host the northern and southern Patagonian ice fields in Central Patagonia, and Cordillera de Darwin Ice Field in the south, where the mass balance stays positive until deglaciation.

4.4. Discussion

4.4.1. Analysis of the simulations with the different palaeoclimate scenarios

Forcing the models with the palaeoclimate scenarios proposed to explore the past climatic conditions in Patagonia for the last glacial cycle can overall simulate the main features of the PIS reasonably well and with realistic defensible climates. For instance, we successfully reproduce the narrow extent of the PIS in the north, where the ice sheet is mostly constrained by the topography (Glasser et al., 2008; García, 2012), and flow to lowland areas in the forms of piedmont lobes in northwestern Patagonia. To the south, the ice sheet widens to the west, as we reproduced well the decrease of sea-level according to the proxy data, the ice sheet develops successfully through the ‘modern fjords valley’, and to the western end of the continental shelf (DaSilva et al., 1997; Glasser & Ghiglione, 2009), producing tide water glacier termini. To the east, the ice sheet develops outlet glaciers that extend beyond the mountain constraint, flowing eastwards for several tens of km (Bentley et al., 2005; Clapperton et al., 1995; Darvill et al., 2014). However, forcing the model with the different palaeoclimatic scenarios proposed in this work, shows very clearly that the location of the SWWs is absolutely critical to growing an ice sheet that agrees with the geomorphology constraints, and the SWWs configuration (precipitation scenario) did change through the last glacial cycle. Moreover, despite the overall good fit of some of our simulations to the geological constraint, there are some misfits that could be related to the palaeoclimate construction, glaciological uncertainties, and lack of geochronological constraints at some periods.

4.4.1.1. Modelled palaeoclimatic conditions along the last glacial cycle

There is a relative agreement that the SWWs move northwards during cold periods (e.g., Bertrand et al., 2014; Kaiser et al., 2005; Lamy et al., 2004; 2010), for instance during the last glacial cycle. However, the pattern of SWWs movement is not yet clearly understood, and some literature refers to a migration of the SWWs' core (Hulton et al., 2002), and others as an expansion, similar to the winter configuration (Kaiser et al., 2005). In this work, we observe that forcing a glaciation with the different proposed palaeoclimate scenarios gives a strong insight about how the position of the SWWs may have been located during the last glacial cycle in order to meet the dated geomorphology constraints. A first-order conclusion is that the simulations performed with the modern precipitation configuration (Chapter 3; 4) do not create an ice sheet in Patagonia that fits well against the geochronological constraints. Instead, the simulations confirm that it is necessary to have wetter conditions than today in northern Patagonia. By applying wetter conditions in the north, either through migration or expansion of the SWWs' core, with the right scaling of the temperature and precipitation, successfully creates an ice sheet in the north. However, to reproduce the correct ice sheet extent along the whole of Patagonia, it is also necessary to keep similar amounts of precipitation than today in southern Patagonia, something that the migration scenarios fail to reproduce. As a consequence, the simulations presented here show that to meet the ice extent recorded by the Patagonian-wide geomorphology constraints through the last glacial cycle, it is necessary to expand the core of the SWWs to northern latitudes rather than produce only a migration of the core. In more detail, the simulations show that the climate which best reproduces the ice sheet constrained at 35 ka corresponds to a 'northern expansion' (T0.85/Pp1.2), while at 25 ka, it corresponds to a 'central expansion' (T0.85/Pp1.0). We also note that within our simple scenario-testing framework we experienced difficulties achieving appropriate ice extents at 45 and 15 ka. These difficulties could be due to a number of reasons, and these are explored in the next section of this thesis.

Therefore, from the modelling, we suggest that a '*northern expansion'* scenario would favour ice maxima conditions in northern and southern Patagonia during late MIS 3 (e.g., 35 ka), and a '*central expansion'* scenario would favour ice maxima in central Patagonia during early MIS 2 (LGM). This latter palaeoclimatic scenario can also produce ice maxima in southern Patagonia. However, we explain later that the asynchrony in the ice maxima is at least partly related to how the climate and ice interacts with local controls and is not purely a consequence of climatic conditions. These two palaeoprecipitation scenarios suggest that northern and central Patagonia were wetter than present during MIS 2 and 3. To quantify the changes from the modern pattern, Figure 4.14 shows the differences in the yearly precipitation amounts that are produced in the model climate which is itself shown in Figure 4.3a. The '*northern expansion'* scenario implies that the west of northern and central Patagonia have an increase to a maximum of 3000 mm. While in southwestern Patagonia, where the core of the SWWs is located today, the palaeoprecipitations were slightly drier than today (between -500 to -1000 mm), as the core expands to the north. The '*central expansion*' scenario suggests that central western Patagonia has an increase in the precipitations, leading to a maximum of 3000 mm and northwestern of 1500 mm. The conditions in southwestern Patagonia are similar to the northern expansion scenario, with palaeoprecipitations drier than today in about -500 to -1000 mm. For both scenarios, eastern Patagonia experienced slightly drier conditions.

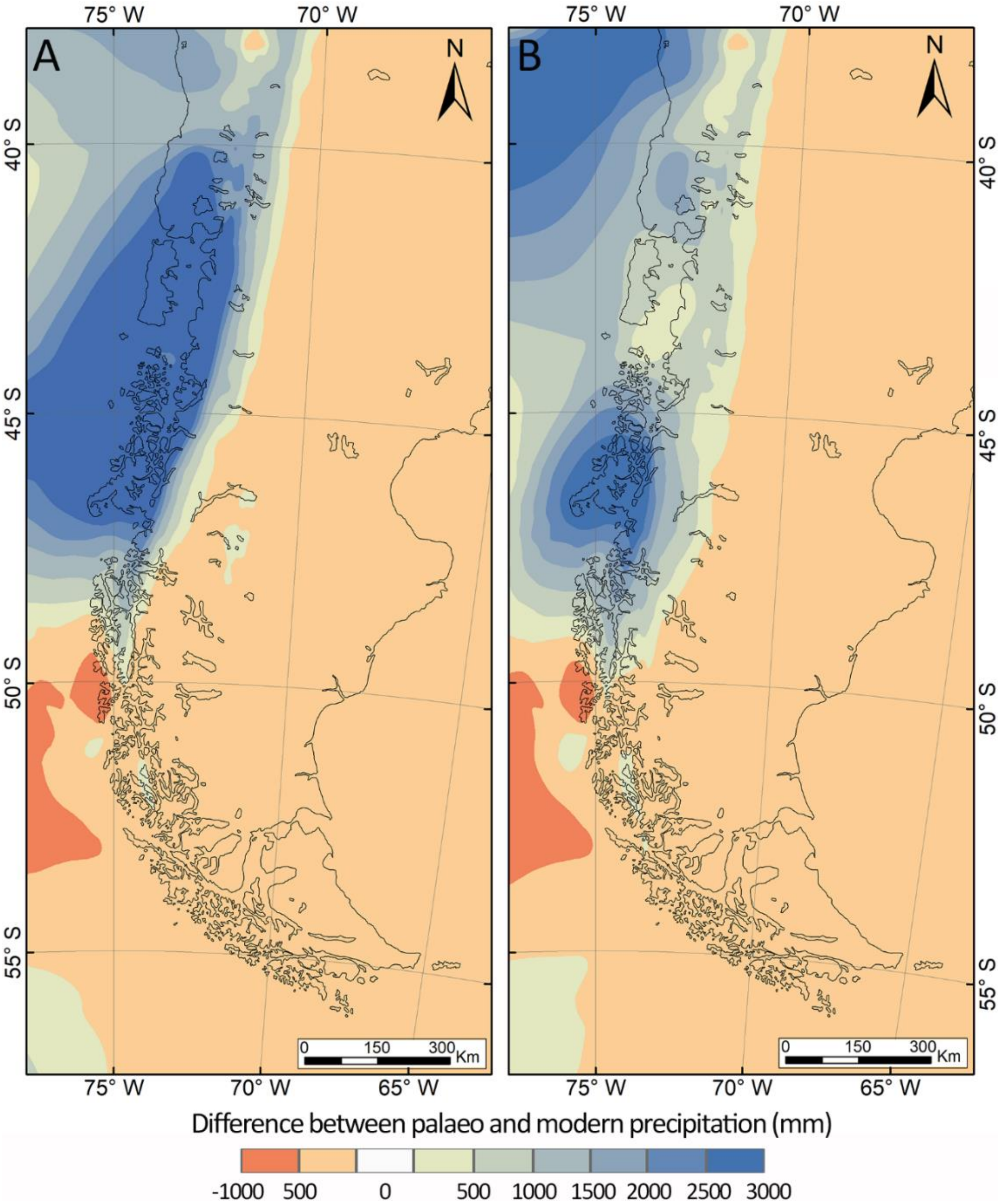

Figure 4.14. Precipitation differences (mm) between palaeo precipitations scenarios with modern annual precipitation. A) Northern expansion scenario. B) Central expansion scenario.

4.4.1.2. Modelling misfit and possible causes

Despite reasonably good simulations of the PIS on a broad scale at different moments of the last glacial cycle, there are some misfits with the PATICE extent, where ice deficiency occurs in some areas and excess in others. Some of the causes could be related to palaeoclimate selection, model limitations, and/or a few geological or glaciological constraints.

The poor fit of the ice extent from the model simulations with the geochronology, at 45 and 15 ka snapshots could be for a number of reasons. One of them could be due to the palaeoclimate selection; in this work, we force the temperatures only with records from East Antarctica (EPICA dome C; Jouzel et al., 2007). Even though East Antarctic records show a good agreement with the SSTs in Western Patagonia (Lamy et al., 1999; 2004; Kaiser et al., 2005; Caniupán et al., 2016), we cannot rule out impact from other parts of the globe. For instance, the temperature records from West Antarctica could potentially be more appropriate as their proximity to Patagonia. However, they are scattered and do not extend through the entire last glacial cycle. Nevertheless, they indeed show some differences with East Antarctica records; for instance, in the range 48-44 ka, EPICA records have warming temperatures, while West Antarctica shows lower temperature records between Antarctic warm events (Blunier and Brook, 2001; Buizert et al., 2015). This could be a reason that our models show little agreement with the geochronology at 45 ka. Moreover, so far, there are only three outlets that date back to early MIS 3 (Darvill et al., 2015; García et al., 2018) and so we lack a full range of spatial constraints. Another climatic influence that cannot be ignored is the northern hemisphere signal, the influence of which has long been debated for Patagonia (e.g., Darvill et al., 2016; Sugden et al., 2005), especially for the northern-central regions (Glasser et al., 2012; Hajdas et al., 2003; Moreno et al., 2001). Additionally, it is necessary to acknowledge the little or non-existent geochronology constraints at some periods in Patagonia, which is expressed in the confidence level in the PATICE limits. For instance, at 15 ka, PATICE limits are marked with low confidence along most of Patagonia (Davies et al., 2020).

The ice extent simulated for the LGM (25 ka), has also some differences from the PATICE limit. In these simulations, the modelled ice sheet extends all the way to the southern edge of the continental shelf (-56.9°S) in the South. However, the LGM limit from PATICE extends with low confidence only to the Southernmost archipelago in South America, which includes Cape Horn. A recently-published stratigraphic study in one of those islands provides information that this area was glaciated during the LGM (Hodgson et al., 2023), which would elevate the confidence to PATICE extent, and there is no reason to discard that the simulations could be correct. Likewise, the ice sheet reconstruction produced by Hulton et al. (2002) achieved a similar ice extent to this work.

Moreover, the palaeoclimatic scenarios created, here specifically the precipitation were built with the aim of having a broad idea about the past climate conditions along the last glacial cycle, but without much climatological detail as they are built from translating an extending modern patterns rather than built from first climatological principles. Therefore, as noted previously, in some areas the precipitation may be under- or overestimated. This might particularly be the case in southeastern Patagonia, where the ice sheet extends about 200 km beyond the modern coastal margin in Tierra del Fuego, coalescing with the Ice Fields formed in Isla de los Estados, which, according to the literature, were not connected during the LGM (Möller et al., 2010). This appears to be a consistent feature in our models and may suggest we have overestimated precipitation in all models in this part of the domain.

An outstanding misfit within these simulations and PATICE extent is the incapability of the simulations to resolve clearly between the outlet glaciers and the inter-lobe areas. The geomorphology, especially in eastern Patagonia, shows clear lobate geomorphological features such as the moraines in the various outlet valleys, and these are separated by more restricted inter-lobate areas of former ice (e.g., see maps in Davies et al., 2020; Glasser et al., 2008; Lira et al., 2022). In comparison, the model tends to show straighter margins and less ‘lobate’ features, and thus seems to overestimate ice extent in the inter-lobate areas. In Chapter 3, we attribute this problem to the model's coarse resolution (4 km/pixel). Another challenge we face has been to reproduce local basal sliding conditions of these glaciers, for which there are some constraints from the geomorphology evidence (Glasser and Jansson, 2005). This might be due to the challenge of parameterising basal sliding which is unconstrained in the model, or to the quality of the input topography. The Ice sheet models generally use a simplified basal motion, where changes are accomplished by modifying the subglacial sediment plasticity. However, the reality is more complex, and various processes are involved, such as infiltration of surface meltwater, changes in the subglacial sediment cover over time, among others (Gowan et al., 2023). On the other hand, the model's coarse resolution reduces the details of the topography. Additionally, the topography does not include any bathymetry for the lakes, and this may influence the terminal sections of the outlets, where the simulated glaciers slide over a flat and higher-elevation surface, meaning that these thinner simulated glaciers would advance with lower velocities than may have been the case in reality.

Finally, during ice retreat, this version of PISM does not produce proglacial lakes in the overdeepening cavities above sea level, which we know did happen in the case of some palaeolake topographies (e.g. Laguna Blanca in the Seno Skyring ice lobe). The absence of proglacial lakes would likely have consequences for the retreat velocity patterns, not least because a calving process would have been in operation in reality but is not simulated here unless the glaciers specifically terminate in a fjord.

4.4.2. Patagonian Ice Sheet dimensions and behaviour

4.4.2.1. Ice Sheet dimensions

Given that our models of the PIS produce some good fits against the PATICE data, we make a preliminary comparison of our modelled ice sheet for the LGM with the previous model simulations.

The ice sheet dimension of this model during the LGM at 24.7 ka had a total ice volume of 442,230 km^3 and a sea-level equivalent of 1.04 m. These values fall in between those from previous simulations. Yan et al. (2022) obtained a sea-level equivalent of 0.477 m for the LGM, but they pointed out that their reconstruction underestimates the value obtained by spatial reconstructions like PATICE (Davies et al., 2020), and they struggle to reproduce the northern portion of the PIS with the geochronology records. On the other hand, the values from this work, are slightly lower than other ice sheet modelling work. Hulton et al. (2002), through a climatic approach and using a 10 km modelling resolution, obtained an ice volume of 500,000 km^3 and with a global sea level equivalent of a 1.2 m drop at the LGM. With a much finer model resolution (100 m), Wolff et al. (2023) produced a PIS reconstruction with a volume of 554,067 km^3 and a sea-level contribution of 1.38 m for the LGM. Wolff's reconstruction should be the closest to the real dimensions so far, as it is performed through an inverse modelling approach from the constrained ice extent of a major part of the PIS and using thickness constraints from one outlet. Despite this, the ice sheet extent from this work still has over and under estimations, and the ice volume is affected by model resolution (Albrecht et al., 2020), but the ice sheet dimensions are similar to previous models. However, we emphasise that our volume and extent data should be treated carefully, as this was not the aim of the modelling.

4.4.2.2. Ice velocities

The glacier basal sliding marked by the basal velocities (Figure 4.11), agrees with the warm-based temperate glacial environments described for Patagonia from geomorphological and sedimentological evidence (e.g., Benn and Clapperton, 2000a; Glasser et al., 2008; Lovell et al., 2012). We also show some agreement with the polythermal conditions inferred from geomorphology along the glacier margins (Glasser et al., 2008; Darvill et al., 2017), shown in the model by the decrease to almost zero of the ice sliding on the edges of the grounded outlet glaciers. The simulations show higher ice velocities for the 35 ka timeslice than for the 25 ka, which could have been influenced by higher atmospheric temperatures during the late MIS 3 than during the LGM (EPICA; Figure 4.2). The larger basal sliding could be a driver of enhance the greater ice extent during MIS 3.

4.4.2.3. Topographic controls on PIS

The topographic differences (namely, differences in the distribution of area with altitude or in the slope gradient) and the variations in the ELA position along Patagonia led to a very different modelled distribution and style of the ice sheet along Patagonia. Northern Patagonia is characterised by the high position of the ELA, even during the peak of the glaciations (Figure 4.12-4.13). This region of Patagonia might sustain a larger proportion of ice sheet below the accumulation area (>95%; Figure 4.8B) for two reasons: one is the high snowfall that the area receives and the other is the large ablation (Figure 4.13). This could increase the basal sliding velocities, which, in combination with the steep slopes, enhance sliding in the valley glaciers. The enhanced sliding could allow the glaciers to flow down to lower altitudes, which is likely to be the case especially in northwestern Patagonia where the presence of piedmont lobes is characteristic. However, the loss of ice sheet area sharply reduces the accumulation input, the glaciers vanish almost instantly, and by 17 ka, the glaciers were restricted only to the high mountain area (Figure 4.15A).

In Southern Patagonia, during ice maxima, the ice sheet extended through low gradient terrain adjacent to the downstream glacier positions for tens of kilometres (Figure 4.15C). The low gradient ice surface makes the area highly susceptible to warming temperatures, where small changes in the ELA, produces big changes in the accumulation/ablation areas (De Angelis, 2014; Mcgrath et al., 2017; Nesje, 1992). According to the mass balance maps, the eastern outlet glaciers had significant portions of their area located in the ablation zone, and the dominance of fluvioglacial landforms and numerous meltwater channels as marginal landforms supports the idea of significant active melting along their length (e.g., Darvill et al., 2017). Additionally, the sharp increase in the temperatures during deglaciation, causes large ice masses to melt. The fact that the ice volume from central and southern Patagonia reach close to zero values within a further 1 kyr earlier (17 ka) than minimum values of the ice extent (16 ka), could indicate there was a stagnation of ice during the retreat (Figure 4.8A), where proglacial lakes were absent. Overall, during the ice retreat, the model agrees with the geochronology, whereby ~15 ka, the ice retreated to the fjords and by 14 ka, the ice was restricted to the upper parts of the mountains (Kilian et al., 2007).

The PIS in central Patagonia has similarities with northern and southern Patagonia. During the LGM, the ice sheet covered the high mountain areas as in the North, but it extended several km beyond the mountains through outlet glaciers, like in the South. However, in central Patagonia, the ice with low gradient surface was less extensive (Figure 4.15B). Therefore, this area was less susceptible to the changing temperatures than in the South. Additionally, the Andes broaden in this region, resulting in larger areas of the ice sheet being situated over steep topography, which makes this area less sensitive to the increase of the ELA than the South. Moreover, central Patagonia is characterised by having the highest average altitudes along the Patagonian Andes, thus allowing larger accumulation areas. This topography makes this region more resilient to further deglaciation once the glaciers are confined in the mountain area. Bendle et al. (2017) mention that the deglaciation in central Patagonia was modest until the 17 ka timeslice, when a major outlet glacier was located at the eastern end of Lago Buenos Aires, which is similar to the modelling extent (Figure 4.15B). Nevertheless, the model shows an earlier retreat during the advanced deglaciation. For instance, the separation of the central part of the PIS into northern and central Patagonia occurs at ~14.7 in the simulations, while from geomorphological reconstructions this occurs later in time, marked by a western drainage of a lake dammed by the ice, with data suggesting that the lake drainage occurred after 12.8 ka (Turner et al., 2005) and before 8.5 ka (Glasser et al., 2016). The difference between the model and the geochronology could be explained in a number of different ways. For instance, the palaeoclimate reconstruction could be successful in representing the ice extent on a broad scale, but when zooming in to small details, it can be under or overestimated, especially considering that the model and climate were run to a 4 km spatial resolution. Another possibility could be related to the coarse resolution of the simulated ice, which can face some problems when representing narrow features, such as the glaciers in the fjords, providing an apparent earlier ice retreat.

4.4.2.4. Deglaciation pattern

The PIS retreat in this simulation (model #38) is driven by the increase of the ice mass loss in response to the rising temperatures. The area with net negative mass balance is related to the glacier hypsometry, where glaciers with flat surface areas are more susceptible to ELA variations as there is more area involved per unit change in the altitude; on the contrary, steep glacier surfaces make glaciers less susceptible to the ELA variations (De Angelis, 2014; McGrath et al., 2017; Nesje, 1992). The hypsometry patterns vary along Patagonia and therefore, the ice sheet retreat pattern is very different between the regions and through time, as the ice sheet surface evolves through the last glacial cycle. Moreover, there is a latitudinal factor playing an important role in the glacier

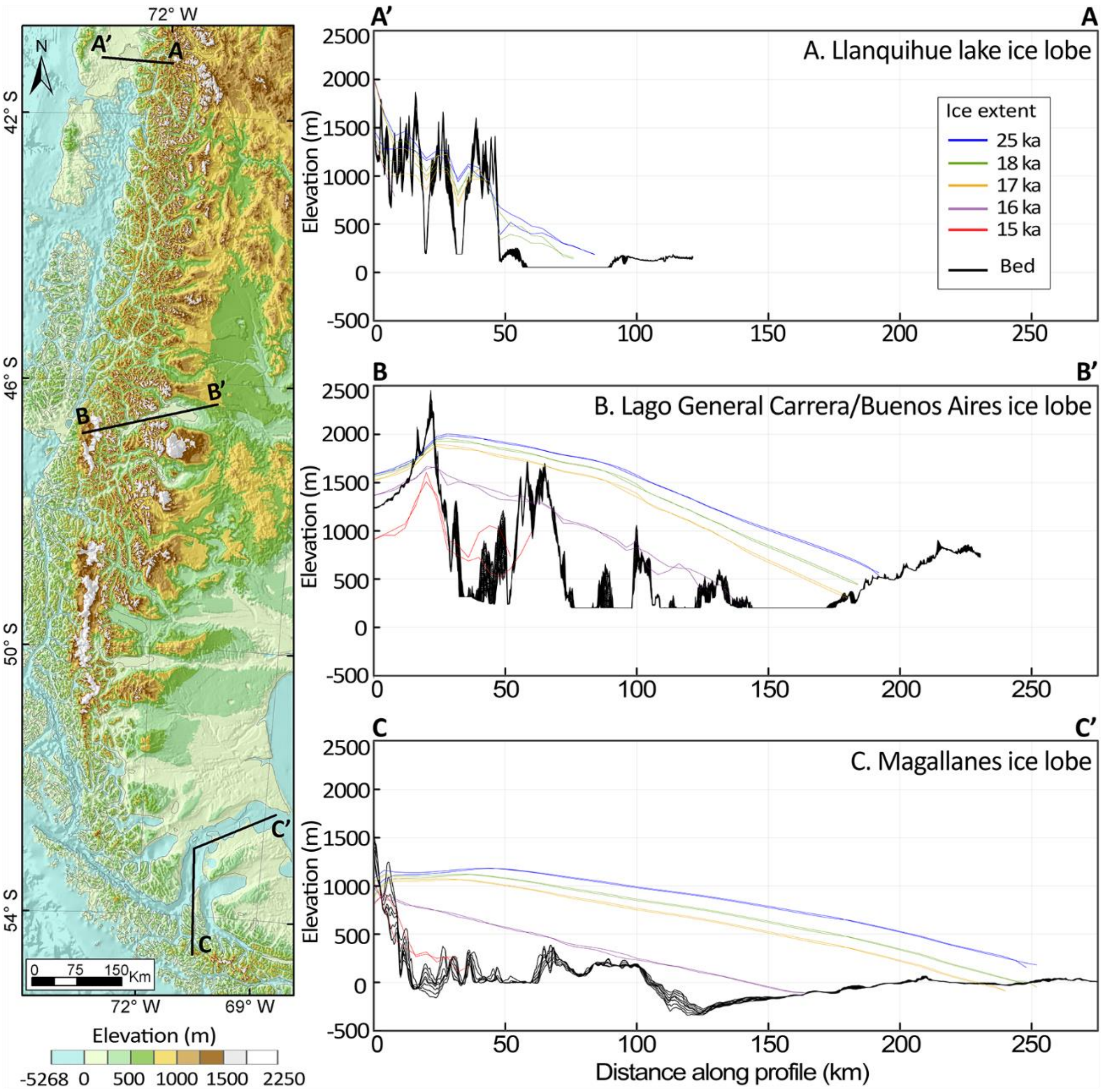

Figure 4.15. Ice lobes' long profile from different regions in Patagonia, showing the characteristic topography of each region, and the ice extent at different time intervals from the LGM to deglaciation. Left, shows the elevation changes along Patagonia and the location of the profiles. Right, shows the A) Llanquihue ice lobe located in northern Patagonia. B) Lago General Carrera/Buenos Aires ice lobe, located in central Patagonia. C) Magallanes ice lobe, located in southern Patagonia. The swath width is 2 km for the topography of all the profiles and 4 km for the ice surface. The topography for A and B is from SRTM (30m resolution); note that in the Llanquihue and General Carrera/Buenos Aires lakes, the bathymetry is absent. For C the bed topography is from GEBCO (450 m resolution), as it considers the bathymetry of the fjords. The ice profiles are obtained from model #38 (Central expansion T0.85/Pp1.0; 4 km resolution).

mass loss, where, naturally, northern Patagonia is warmer than the south, and this marks the baseline of a higher ELA position, when considering only the temperature. However, it is important to treat these deglaciation patterns carefully, because in the model modifications in the temperature are considered with a fixed precipitation configuration (Central expansion T0.85/Pp1.0). This is especially important because it has been proposed that there was a fast southward movement of the SWWs after 18 ka (Moreno et al., 2001), with positions in similar configurations to today by ~14 ka (McCulloch et al., 2000).

Northern Patagonia is characterised by a high ablation setting, even during the peak of the glaciation. This is due to a higher ELA position; over 95% of the ice sheet is located in the ablation area (Figure 4.8B). The slight warming from 24 ka to 18 ka of 1°C has an immediate effect in a decrease in the accumulation area by 50% by 18 ka (Figure 4.8C), and this is reflected in an almost instant response to the deglaciation, decreasing its area to ~80% and volume to ~60% by 18 ka (Figure 4.8A). Subsequently, the sharp decrease in the accumulation area from 18 to 14 ka, produces an immediate ice retreat in northern Patagonia. Even though the rate at which the proportion of glacier area with a positive mass balance decreases after 17 ka in the north, the ice area and volume reduction are almost linear until 16 ka. This change might indicate a change to a steeper topography at the ELA height, as the temperature keeps rising constantly. After a slight readvance during the Antarctic Cold Reversal, the glaciers in northern Patagonia disappeared. The large amount of ablation and the decrease in the accumulation area, due to the SWWs contraction at the start of deglaciation (Moreno et al., 2015), contributes to the fast disappearance of this portion of the ice sheet.

In Southern Patagonia during the peak of the glaciation, only 33% of the ice sheet was in the ablation area (Figure 4.8B); these areas mostly correspond to the easterly outlet glaciers (Figure 4.13A), which flow with a very low gradient for hundreds of km away from the mountains. A small increase in temperatures in this area, such as 1°C between 25 -18 ka, produces a decrease of ~20% in the accumulation area (Figure 4.8C), this seems to have little effect on the ice volume and it is almost insignificant to the ice extent, this is probably due to a large feeding area, which continues feeding the glaciers downstream. After 18 ka, the sharper increase in the temperatures produces an immediate reaction in the positive mass balance reduction by 17 ka. However, this change leads to the retreat in central and southern Patagonia by ~1 kyr (Figure 4.8). Southern Patagonia is the most affected area in this period, as when the ELA rises in low-gradient terrains, it produces larger areas under the ablation zone than in steeper landscapes (Davies et al., 2022; De Angelis 2014; McGrath et al., 2017), such as the case of the rest of Patagonia or when the ice sheet is confined to the mountain regions later in time. As the deglaciation continues, the ice volume and area decrease linearly. However, the volume approaches zero by 15 ka, with the ice area reaching zero by 14 ka.

The ice sheet behaviour in Central Patagonia is similar to southern Patagonia in the pattern of deglaciation, such as the lags between mass balance changes and deglaciation, but the response in Central Patagonia is less extreme. This is because, the topography of central Patagonia resembles the southern region to only a certain extent. For instance, a smaller portion of the outlet glaciers extend towards low-gradient terrains, making this region less sensitive to temperature changes (or the ELA changes). However, as the overall extent of the ice sheet in central Patagonia is lower than in the South, the mass balance response to temperature changes is faster. At the peak of the glaciation, 70% of the ice sheet's area was in the ablation zone, which is more than double the case in southern Patagonia proportionally (Figure 4.8B). For the period 25-18 ka, central Patagonia shows a slightly larger decrease in the ice's area than the South (Figure 4.8A). This could be due to the larger area experiencing ablation, and the lack of overdeepening in the topography in the modern lakes located in central-eastern Patagonia could show an apparent earlier retreat. However, during the sharp increase in temperature after 18 ka, southern Patagonia shows proportionally the least decrease in the accumulation area along Patagonia. This might be due to the position of the ELA, confined to steeper areas than in the South, making central Patagonia less sensitive to the temperature. During the Antarctic Cold Reversal, central Patagonia experienced the largest increase in the glacial extent of Patagonia. However, after this temperature reversal period, the ice retreat continued, and central Patagonia continues to show the lowest retreat rate with respect to the other regions. Today, this area hosts the two largest remnants of the former PIS: the Northern and Southern Patagonian Icefields (Davies et al., 2020).

4.4.3. How does the model fit with the geomorphology and geochronology recorded for the Seno Skyring ice lobe and its surroundings?

The Seno Skyring ice lobe experienced full glacial conditions during the global LGM, with its near-maximum ice extent limits at 26 and 24 ka (Chapter 2; Lira et al., 2022). During this period, the model reaches close to the geochronological extent, within 10-15 km, at Seno Skyring, Seno Otway and at the Magallanes ice lobe (Figure 4.16 A). However, for Última Esperanza and Bahía Inútil-San Sebastián lobes, the modelled ice sheet overestimates the geochronological extent by more than 30 km.

At 18 ka, the modelled ice sheet has a larger extent than during the LGM, but the ice is thinner (Figure 4.16B). These larger extents disagree with the geomorphology, where glacial readvances younger than the LGM are recorded at inner positions in all of the outlets but not at Seno Otway, which lacks geochronology at this time. The literature shows the presence of proglacial lakes developed during post-LGM retreat, situated within LGM moraines for Última Esperanza, Seno Skyring and Magallanes lobes (Bentley et al., 2005; Çiner et al., 2022; García et al., 2018; Lira et al., 2022). However, the model does not consider the formation of lakes in over-deepening areas in the continent above sea level. Therefore, an accelerated ice retreat due to calving is not considered in the model, and this could be a reason for the degree of mismatch at this

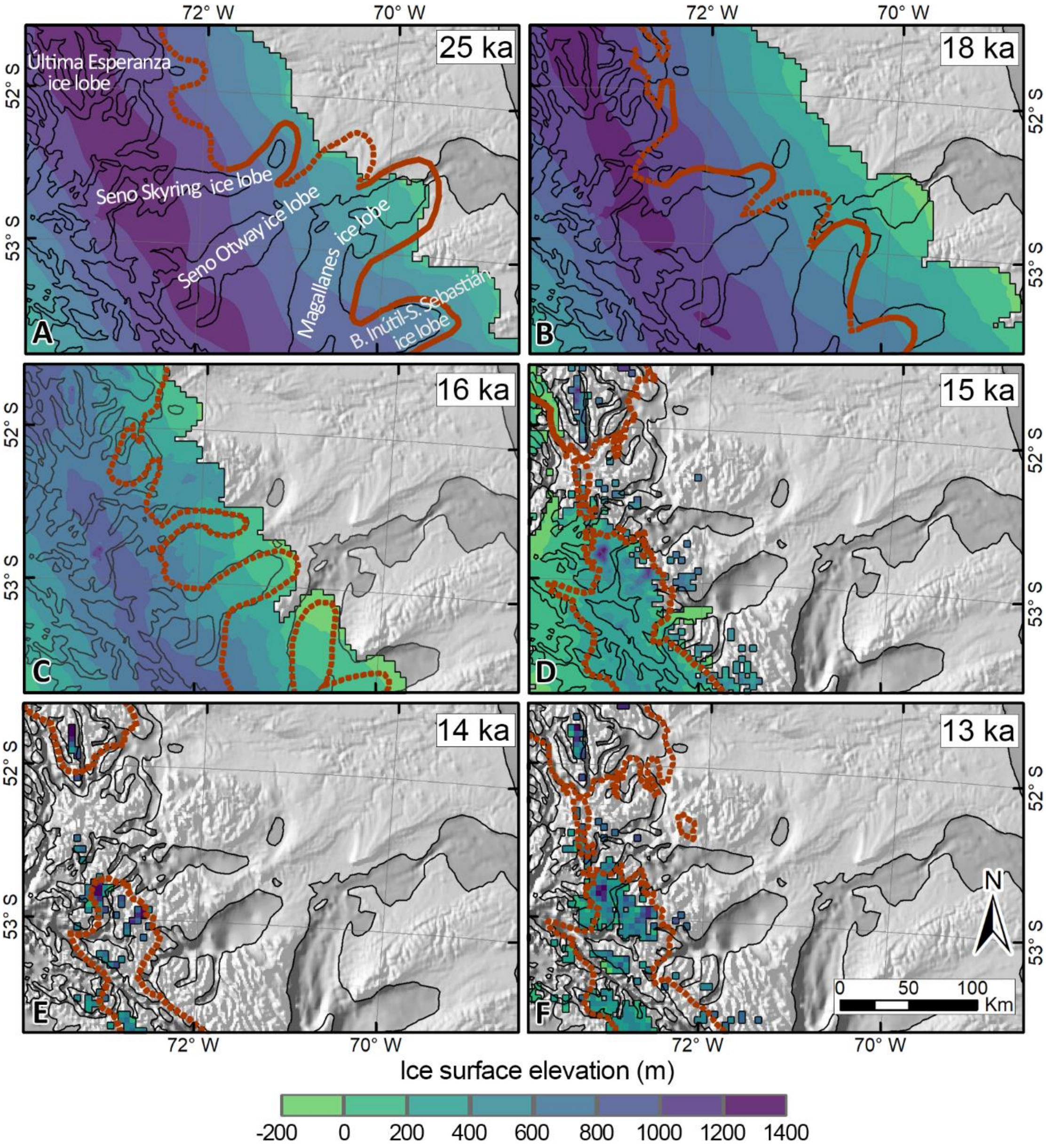

Figure 4.16. Comparison between the modelled ice extent and the geomorphology constrained by the geochronology of southeastern Patagonia, during the LGM and deglaciation. Model #38 is forced with 'central expansion' precipitation scenario and it is the model that best fits the geochronology at 25 ka. Continuous brown lines correspond to a direct geochronological constraint of glacial positions. Dashed lines correspond to inferred glacial position from minimum ages for glacial abandonment. A) 25 ka, B) 18 ka, C) 16 ka, D) 15 ka, E) 14 ka and F) 13 ka.

time. Alternatively, or in conjunction, it is possible that some movement of the SWWs occurred in reality which we do not test for in the model in a dynamic manner.

At 16 ka, we infer the ice position based on maximum deglaciation ages from peat bogs and marine cores (Kilian et al., 2007;2013; Lira et al., 2022; McCulloch et al., 2005; Mercer, 1970). The fit of the modelling extent at this time is close to the ice position inferred from the geochronology (Figure 4.16C). At 15 ka, the ice margins of the geochronological records are scarce, and even PATICE traces the ice margin with low confidence during this period (Davies et al., 2020). The modelled results show a difference in behaviour between outlets. For example, in the Última Esperanza ice lobe, the glaciers' extent is highly reduced at this time, and their positions are restricted to the high altitudes of the feeding catchment. In contrast, in the Seno Skyring and Otway lobes, the ice retreats, but the glaciers still reached low elevation areas; for instance, their margins are confined to the inner fjords of the outlets (Figure 4.16D). This difference in retreat behaviour between the ice lobes could be related to topographic contrasts, where Seno Skyring and Otway lobes have feeding areas located at higher altitudes and thus larger accumulation zones than the Última Esperanza ice lobe. As a consequence of this hypsometric variation, the height-mass balance feedbacks of each lobe is likely to differ. This difference shows an example of outlets with a more advantageous position (Seno Skyring and Otway) compared to the other (Última Esperanza) during a hypothetical readvance. In terms of LGM extent, this could also be a process which enables the later near-maxima ice conditions of the Seno Skyring lobe during early MIS 2, while the Última Esperanza ice lobe reached its ice maxima earlier during MIS 3 (García et al., 2018), and the MIS 2 advances reached more inner positions (Çiner et al., 2022). By 14 ka, the modelled glaciers along the whole PIS retreat back to positions similar to today's margins (Figure 4.16E). After this time, at 13 ka, the model produces a glacier readvance, with a larger extent than at 14 ka, in response to the ACR event (Figure 4.16F). At this period, there is almost no geochronological constraint, and the modelled glacier margins are smaller than the ice extent inferred by PATICE.

4.4.4. Palaeoclimate in Patagonia during the last glacial cycle

The model simulations suggest that to match the ice extent derived from the geomorphological evidence, the SWWs must have an expanded position to northern latitudes, creating wetter conditions for the North, but keeping similar conditions in the South. Based on best-fitting model runs, the northern extent of this 'expanded' core varied through the last glacial cycle; the simulations suggest that during late MIS 3 (~35 ka) the SWWs most likely had an expanded position to northern Patagonia. Subsequently, during the LGM (~25 ka) the SWWs still had an expanded position but this had likely slightly contracted to central Patagonia. Proxy data indicate that after 18 ka, the northern positions of the SWWs started a fast contraction south, and by ~14 ka, the SWWs had a location similar to today (McCulloch et al., 2000).

Whilst we constructed our basic precipitation scenarios with the limited proxy evidence in mind, it is worth returning to these proxies here and assessing whether our modelling results are in agreement with the proxy data. The terrestrial and marine proxies in

Patagonia show that during cold periods, northwestern Patagonia became wetter. In this case, the most logical thing would be to think that during the coldest time of the last glacial cycle, the SWWs might have been in their most northerne positions, such as during the LGM (~25 ka). However, our model simulations show a different pattern, where at 35 ka, the SWWs are in more northern positions than at 25 ka (LGM).

The SWWs' position is governed by the Sub-Tropical Front in the North and the Sub-Antarctic Front in the South (Hobbs et al., 1998). The Antarctic sea-ice expansion produces the northwards shifting of the Sub-Antarctic Front, producing colder temperatures on the coast of Patagonia (Lamy et al., 2004). SSTs in northern Patagonia (site 1233; Lamy et al., 2004; Kaiser et al., 2005) record warmer temperatures at 35 ka than 25 ka. This infers that the Sub-Antarctic Front was in more southern latitudes at 35 ka, therefore a more southern SWWs position. On the other hand, a marine core from central Patagonia has a phase with terrigenous input during late MIS 3, suggesting a more northern positions of the SWWs (Hagemann et al., 2024). It has been proposed that the forcing mechanism that drives these changes in the Southern Ocean is the Antarctic sea-ice movements (Darvill et al., 2016). Along the last glacial cycle, most of the area around Antarctica had high sea ice during MIS 4 and MIS 2 and a reduction during MIS 3. Nevertheless, the Scotia region, located in southern Patagonia, seems less sensitive to climate changes and shows high sea ice during the whole glacial period (Chadwick et al., 2022). Moreover, once the Southern Ocean had been stratified, it might have been hard to break down those conditions (Denton et al., 2021), keeping the SWWs in lower latitudes between MIS 4 and MIS 2. On the other hand, the northern extents of the SWWs could be controlled by tropical influences, allowing a more expanded position during MIS 3. The linkages between northern controls and the position of the SWWs is not yet well understood (Lamy et al., 2007). Moreover, it is wort noting that there are orbital factors that generate optimum conditions for glaciation at 35 ka, such as longer winter duration and lower summer insolation than during the gLGM for the Southern Hemisphere. These orbital factors could have played an important role in enhancing the glaciation during this period, however it has been proposed that this should be accompanied by climatic feedback (Darvill et al., 2016). In conclusion the proxy data show some disagreement and remain potentially consistent with the modelled maximum northward position of the SWWs at 35 ka.

4.4.5. Asynchrony of the LGM

Geomorphological and sedimentological records suggest that Patagonia reached full glacial conditions several times during the last glacial cycle (Denton et al., 1999; Moreno et al., 2015; Smedley et al., 2016;). However, the maximum ice extent differs between regions. In general terms, the PIS had ice maxima during early MIS 3 in northern (Denton et al., 1999; García et al., 2021; Zech et al., 2011) and southern Patagonia (Darvill et al., 2015; García et al., 2018) but a later maximum in central Patagonia, during MIS 2 contemporaneous to the global LGM (Kaplan et al., 2004; Douglass et al., 2006; Hein et al., 2010; Leger et al., 2021). From the modelling simulations, this asynchrony can be explained through climatic changes along the last glacial cycle, differences in the topography between the northern, centre and southern Patagonia and variations in the glaciological parameters and physical processes of the PIS along the different periods.

The transient model simulations through the last glacial cycle, show numerous glaciations during the colder periods. However, full glacial conditions along the whole Patagonia are only possible with an expanded configuration of the SWWs to northern domains. The first full-glacial advance in the last glacial cycle should have occurred during MIS 4, where prolonged cold conditions on the SST and Antarctic temperature proxies are shown. However, the records show that only one outlet located in southernmost Patagonia recorded ice maxima during this time (Peltier et al., 2021). We infer that limited glacier development occurred before this period, as the planet was starting to cool down after the last interglacial. This minor development of the PIS is supported by evidence of MIS 5a glacial advance in an isolated ice cap, located at the eastern part of the Andean axis. Mendelová et al. (2020) propose that the formation of that ice cap was facilitated as the main ice sheet located along the Andes (western from this ice cap) was still building up, this would allow the precipitation to reach eastern locations and thus this ice cap. Later, during late MIS 3, with a ‘northern expansion’ position of the SWWs’ core, the PIS extended to full glacial conditions again, but this time reaching farther positions, overriding most of the MIS 4 records. Ice maxima during this period are recorded in some outlet glacier imprints, in northern (Denton et al., 1999; García et al., 2021; Zech et al., 2011) and southeastern Patagonia (Darvill et al., 2015; García et al., 2018). The wetter conditions in northern Patagonia suggested by the modelling simulations, could have contributed to the larger ice extents in this area. Moreover, warmer temperatures during MIS 3 than MIS 2, could have influenced the surface and basal velocities, generating higher basal sliding and with this allowing the glacier outlets to reach farther ice extents during MIS 3. During the warmer periods of the glacial cycle (e.g., the limit between MIS 3 and MIS 2), the ice sheet retreated from full-glacial conditions to the mountain regions, and this likely followed similar patterns to the last deglaciation we have modelled, with dominant topographic controls. The deglaciation pattern shows that the ice sheet in central Patagonia had retreated less than the rest of Patagonia for mainly two reasons: the overall higher altitudes in the region allow larger accumulation areas, and the mainly steep topography makes this area less sensitive to the increase of the ELA than southern Patagonia. The last glacial advance to full-glacial conditions occurred during the LGM, facilitated by a shift to an expanded core of the SWWs to a ‘central expansion’ position. In central Patagonia, the glaciers were likely to have a more advantageous position after the penultimate deglaciation, which contributed to reaching farther extents, overriding the MIS 3 moraines, resulting in an ice maximum contemporaneous to the LGM (Kaplan et al., 2004; Douglass et al., 2006; Hein et al., 2010; Leger et al., 2021). On the other hand, the MIS 2 margin in northern and southern Patagonia formed terminal moraines tens to a few kilometres inside MIS 3 moraines. The more restricted extent of this glacial advance, could be related to the more retreated positions that the glaciers reached during the warming period after the MIS 3 advance, taking more time to cover the area to full glacial conditions than central Patagonia. Moreover, the colder conditions during MIS 2 than MIS 3 could have facilitated more accumulation but less ice sliding, producing thicker ice but with less extension. Nevertheless, we do not discard other parameters that could have affected the asynchrony but are not included in the modelling. For instance, PISM produces a western migration of ice divides, but the static precipitations do not allow to simulate the snow starvation to the East, which could also play an important role, and this has been proposed as a reason for the MIS 3 maxima in Southern Patagonia (García et al., 2018) with the exception of the Seno Skyring ice lobe (Lira et al., 2022). Moreover, we do not discard other factors that can control the asynchrony such as orbital parameters and differences in the isostasy accommodation.

4.5. Conclusions

In this chapter, through ice sheet modelling, the pattern of the PIS's growth and retreat for the last glacial cycle has been investigated. The key findings are:

- In testing the glaciation response of Patagonia to different palaeoclimatic scenarios, the simulations show that to obtain full glacial conditions along the whole of the PIS it is necessary to have wetter than modern conditions in northwestern Patagonia, but to keep similar to modern precipitation conditions in the South. These conditions are achieved with an expanded core of the SWWs to northern latitudes rather than producing a migration of the core to the North, the latter of which would lead to conditions in the South being too dry.

- By comparing the ice extent of the different simulations to the geomorphology constrained by the geochronology, it can be suggested that the SWWs’ configuration (precipitation scenario) changed through the last glacial cycle. For the early MIS 3, the best fit of the modelled ice sheet is achieved by forcing the palaeoclimate with a '*northern expansion'* precipitation scenario with a scaling factor of T0.85/Pp1.2, and for the early MIS 2 (LGM) follow a '*central expansion'* precipitation pattern with a scaling factor of T0.85/Pp1.0. This means that during MIS 3 and MIS 2, the overall temperature along Patagonia ranged between 8 to 6 degrees colder than today and that north and central western Patagonia experienced wetter conditions than today.

- The model that best fits the LGM extent (climate forced by '*central expansion'* T0.85/Pp1.0) yields a sea-level contribution of 1.04 m. This value is slightly lower than previous reconstructions performed for the PIS (Hulton et al., 2002; Wolff et al., 2023), and we attribute this difference to the coarse horizontal resolution.

- The comparison between the position of the outlets constrained by the geochronology with the modelled ice extent for southeastern Patagonia, shows a relatively good agreement during the LGM (25 ka). However, during the late glacial between 25 and 18 ka, the model does not aacount for the creation of the proglacial lakes described in the literature, overestimating the ice extent compared to the geomorphology records, as the calving effect is not considered. For the rest of the deglaciation, the geochronology is not well constrained, making it difficult to assess the model's behaviour.

- There is a latitudinal factor that naturally results in a gradient of the ELA along the PIS. During the peaks of the glaciations (e.g., LGM) Northern Patagonia has a higher ELA, confined to the high mountain area. Whereas to the south (central and southern Patagonia), the ELA decreases gradually in altitude. This contributes to the differences in the ice sheet distribution and style of glaciation along Patagonia, for instance, from the alpine glaciation style in the north to the larger ice sheet extent in the lowland areas in central and southern Patagonia.

- The topographic differences between central and southern Patagonia, produce different mass balance responses of the ice sheet as the temperature evolves through time. In the South, the low gradient of the outlet glaciers' ice surface topography makes the area more susceptible to temperature changes, for instance, a small increase in the ELA altitude produces a large decrease in the accumulation area and a large increase in the ablation area. However, the outlet glaciers of Central Patagonia have steeper slopes which makes the area more resilient to changes in the ELA elevation because small changes in ELA only result in small changes to accumulation or ablation area. Finally, central Patagonia has the highest elevations on average of the whole of Patagonia, and therefore accommodates larger accumulation areas than the rest of the PIS, which may be a contributing reason why the PIS in this area is more resistant to deglaciation and has different timings for maximum ice extent in comparison to the north and south.

- The major implication, therefore, of the model simulations performed in this work is to suggest that the asynchrony in timings of the ice maxima in Patagonia is likely related to the interaction of different controls. Here this work shows that climatic and topographic controls likely acted together to produce the asynchrony. To reach full glacial conditions along the whole of Patagonia is only possible with an expanded configuration of the SWWs to northern latitudes. This is achieved during late MIS 3 (northern expansion) and early MIS 2 (central expansion), according to the geochronology constraints. Between these two stages, a deglaciation phase occurs, and this impacts central Patagonia to a lesser degree, because it is more resilient to temperature changes (section above) than the other regions of the PIS, thus, producing less ice retreat proportionally than the North and South. Subsequently, during the glacial readvance during MIS 2, the ice sheet in central Patagonia has a more advantageous position because of its topographic situation and this enables the ice sheet to reach a greater extent in a shorter time, likely obliterating any MIS 3 records. On the contrary, the glacial readvances in northern and southern Patagonia need more time to reach full glacial conditions, reaching a smaller ice extent than during MIS 3, therefore in this area, moraine records from MIS 3 and MIS 2 are preserved. This hypothesis could be tested in the future using an ice sheet model forced by a more dynamically evolving SWW configuration as opposed to static scenario testing.

Chapter 5. Discussion

Diego de Almagro island, southwestern Patagonian fjords

5.1. Summary

The aim of this thesis is to understand what factors are involved in the asynchrony of the local Last Glacial Maximum (LGM) glacier extents along Patagonia by exploring the controls of the ice growth and retreat of the Patagonian Ice Sheet (PIS). To meet this aim, this thesis has applied a range of different approaches: combining an assessment of geomorphology and geochronology for one previously under-studied outlet, and then conducting ice sheet modelling of the whole of the former PIS. Specifically, chapter 2 has produced a new glacial geomorphological map accompanied by novel geochronology of key events of glacial advance and retreat in the Seno Skyring ice lobe, located in southeastern Patagonia. Chapter 3 explores the physical and climatic parameters needed to grow an LGM ice sheet along Patagonia by steady-state ice sheet modelling. Chapter 4 runs a series of transient ice sheet modelling experiments and then brings together all the elements of the work conducted within this project and therefore in this latter role it brings together the overarching discussion chapter for this work. More specifically, Chapter 4 investigates the climatic conditions needed to simulate PIS growth and decay such that it matches with geomorphological and chronological constraints (both published and the new constraints from Chapters 2 and 3), by testing different paleoclimatic scenarios with transient ice sheet modelling simulations throughout the last glacial cycle. In doing this, the latter chapter also addresses the controls on the spatial asynchrony in the timing of the maximum ice extent in Patagonia.

This chapter returns to the original research questions and summarises the key findings for each of these. It also provides an account of some of the recommended future work that emerges from this thesis.

5.2. Main Discussions

This work combines geomorphology, geochronology, and ice sheet modelling to simulate past glacial conditions during the last glacial cycle along Patagonia. Using these different approaches, we aim to understand the past climatic conditions and the drivers that led to the growth and retreat of the PIS during the last glacial cycle and what controlled the different timings of the ice maxima in the different regions.

Importance of linking together the geomorphology, geochronology and modelling.

Geomorphology and geochronology together provide our most robust constraints for past glaciation in the area and they are crucial to constraining the ice sheet model for many reasons. First, they allow us to initiate the model, as the model parameter choice is based partly on evidence of past glacial history; for instance, a general consideration is whether the past ice sheet was characterised primarly by cold or warm base glaciers (Cuffey & Peterson, 2010). Moreover, a good way to test the modelled ice sheet is through a comparison of the ice behaviour, such as basal sliding and ice velocities, against the geomorphological imprints. For instance, in Patagonia, the presence of drumlins or thrusting moraines provide evidence for fast-flowing glaciers in some outlets (Benn and Clapperton 2000b; Glasser and Jansson, 2005; Lovell et al. 2012).

Once a reliable model has been set up, climatic simulations based on palaeoclimatic proxies can be performed in order to understand past climatic conditions. The extent of the resulting ice sheet is compared to the geochronologically constrained geomorphology, allowing us to evaluate whether the proposed climate is appropriate or not, and if it produces an excess, lack, or a good ice extent. Ultimately this approach should provide a range of possible climatic conditions and a most likely ice sheet configuration for Patagonia. This indicates that good ice sheet modelling relies on good constraints of glacial geomorphology and geochronology on one hand and accurate palaeoclimatic proxies on the other.

In addressing the research aim, a series of research questions were addressed, and the findings relating to these are summarised and discussed below.

5.2.1. Geomorphology and Geochronology of the Seno Skyring ice lobe

What were the glacial extent and retreat pattern of the Seno Skyring glacier: a key ice lobe that lacks geochronological constraints during the last glacial period? Is this pattern comparable to its neighbouring ice lobes?

Through a detailed mapping of the glacial geomorphology of the Seno Skyring ice lobe, SE Patagonia, along with new geochronological constraints of key events during the last glacial cycle, in Chapter 2 we demonstrated the presence of two moraine systems that correspond to the last glacial cycle. The outer and older moraine system is named Laguna Blanca (LB) and was built subaerially. The inner and younger system is named Río Verde (RV), and the frontal part was built subaqueously under the palaeo-Laguna Blanca lake, which developed during deglaciation. Surface exposure ^{10}Be dating methods were applied to boulder samples collected from both glacial margins. LB moraines reached close to ice maxima at 26.3 ±2.3 and 24.3 ±0.9 ka, contemporaneous with the gLGM, while in RV moraines an age of 18.7 ±1.5 ka was obtained. Radiocarbon dating from the base of peat bogs inside these moraines suggests an ice retreat from the RV position by at least c. 16.4 cal kyr BP. This geochronological pattern shows similarities and differences to other lobes in southern Patagonia. The outer moraines differ in the timing of the ice maxima from the rest of Southern Patagonia, where dated ice lobes have an ice maxima occurrence during MIS 3 and MIS 4. However, a glacial readvance in Seno Skyring at ~18 ka is found to be present in all of the dated ice lobes of the region.

5.2.2. Steady-state Ice Sheet Modelling along Patagonia

How sensitive is the LGM ice sheet to non-climatic controls (e.g. changes in glaciology, subglacial conditions, topography)?

Sensitivity tests with different ranges of physical parameters related to the ice flow and basal sliding, impact the ice thickness and velocities of the PIS outlets. However, our tests showed that the PIS ice extent was relatively insensitive to these parameters, and we therefore used previously published work to further guide us on parameter choice. This gives us confidence that the PIS extent can be successfully simulated through ice sheet modelling to test different climatic scenarios.

Can we successfully simulate the LGM ice sheet extent along Patagonia? What climate conditions are needed to grow an LGM ice sheet for Patagonia?

Through steady-state ice sheet modelling using the Parallel Ice Sheet Model (PISM), we have been able to simulate the growth of a 'maximum' ice sheet along Patagonia by scaling the modern climatic conditions (temperature and precipitation) by different factors (Chapter 3). Following the set of sensitivity tests which explored the required glacial parameters (such as basal friction, positive degree day factors etc.), the climatic adjustments were then applied. In northern Patagonia, the LGM extent recorded by the geomorphology is achieved by either a decrease of 7°C in temperature along with an increase in precipitation by a factor of 1.5, or a decrease of 8°C in temperature and retaining a modern precipitation pattern (scaling factor of 1.0). However, in central-south Patagonia the conditions are different. To grow the ice sheet to the LGM extent, it is necessary to decrease the temperatures by 7°C and scale the modern precipitation by a factor of 1.0-1.2. None of the climatic sensitivity tests produced a simulated ice sheet with a good fit along the whole of the PIS. This suggests that to meet the LGM ice extent constrained by geomorphology, it is necessary to modify the spatial distribution of the modern precipitation pattern to produce wetter (and thus larger ice) conditions in northern Patagonia.

5.2.3. Transient Modelling Simulations of the Patagonian Ice Sheet

Can we simulate the PIS through the last glacial cycle?

This thesis presents the first transient simulations of the dynamic evolution of the PIS (Chapter 4). A range of precipitation scenarios based on the palaeoclimatic proxies in the area were developed to address the previously identified issue of the need to have a wetter climate in the north in order to simulate enough ice at the LGM. These scenarios, which variously included expansion and migration of core westerly-driven precipitation, are also used to test the manner in which the SWWs (Southern Westerly Winds) evolved over the last glacial cycle. These climates were used with the ice sheet model (PISM) in a transient mode, and were used to force the model over the full glacial cycle (120 ka - today) using a scaled temperature curve from the EPICA ice core in East Antarctica. The simulations successfully enable the ice sheet to expand from a no-ice scenario, dynamically reaching maximum ice extents (at a range of times) and to dynamically retreat to the present-day extent. By testing the palaeoclimatic scenarios against the geomorphological extent constrained by existing (PATICE) and new (Chapter 2) geomorphology and geochronology, we found that the best simulations are achieved by a climate that represents an expansion of the SWWs' core to either northern or central Patagonia, where the northern extent of the core varies through time. This suggests that the palaeoclimate of northern and central western Patagonia had wetter conditions than today, while southern Patagonia had precipitation conditions similar to modern. The modelled PIS, during the global LGM extent, yields a sea-level contribution of 1.04 m and extends continuously from 38°S to the end of the continental shelf in the South (56.9°S). In northern Patagonia, the ice sheet has a narrow pattern constrained to the mountainous area, with piedmont lobes that flow to the lowland areas. In central and southern Patagonia, the ice sheet widens to the west, covering the continental shelf, and to the east, it develops outlet glaciers extending beyond the mountain constraint for several tens of km.

What controls the retreat pattern of the Patagonian Ice Sheet?

The pattern of the ice sheet retreat varies between regions, and the work completed here demonstrates that this is likely due to latitudinal and topographic differences. With respect to the latitudinal factor, northern Patagonia is more affected by changes to temperature due to its higher ELA position, even during the glaciation. The increase in temperature during the onset of the deglaciation and the high ablation setting produces an immediate response in decreasing the accumulation area in the northern PIS, thus causing a faster ice retreat than is seen in other parts of the PIS. Regarding the topography differences, Central Patagonia has, on average, the highest elevations and steepest slopes, while the outlet glaciers in Southern Patagonia flow over a particularly low-gradient topography to the east. As a consequence, during deglaciation, the rising of the ELA in response to the warming climate has a more significant impact in southern Patagonia due to the low gradient of the ice surface topography, causing a significant decrease in the proportion of the glacier area, which experience less accumulation. Central Patagonia, however, is more resilient to deglaciation because the steeper ice surface slopes and the higher overall elevations mean that the change in scale of either the accumulation or ablation areas are relatively smaller. Therefore, as a consequence of interactions between the ice surface and the climate in areas of high/steep elevation vs. lower/flatter elevation, during deglaciation, Central Patagonia has a slower retreat rate, initially losing less ice area and volume than northern and southern Patagonia.

Can we understand what controls the asynchrony in the timings of the maximum ice extent in Patagonia?

The modelling conducted here suggests that the asynchrony in the timings of the ice maxima along Patagonia is likely related to the interaction of climatic and topographic controls. On the one hand, an expansion of the SWWs' core to northern latitudes is needed to reach full glacial conditions along the whole of Patagonia. On the other hand, the topographic differences along the PIS lead to a more resilient Central Patagonia to deglaciation changes than for the other areas. As a result, this area has a lower ice retreat rate, thus, producing a more advantageous position for a subsequent glacial advance, needing to cover less distance to reach full glacial conditions than northern and southern Patagonia. A good example of the implications of this topographic difference is that the largest remaining ice fields in Patagonia (northern and Southern Patagonian ice fields) are located in Central Patagonia. Nevertheless, we do not discount the presence of other factors producing an effect on the asynchrony, that this ice sheet modelling does not consider. Since we apply constant precipitation scenarios through the glacial cycle we cannot rule out the effect of changes to the precipitation scenarios within the glacial cycle (e.g. expansion changing to migration and so on).

5.3. Further Work

The discussions from this work lead to several future research ideas to better constrain the past glacial and climatic conditions along Patagonia. This will contribute to a better understanding of the reasons for the asynchrony dilemma in Patagonia.

Improve the glacial geological constraints of the PIS

Many outlets still lack geochronological constraints. The work we present here (Chapter 2) fills an important gap in the Seno Skyring area of Southern Patagonia. The large improvement in recent years has shown that despite the existence of a regional pattern to the timings on the ice maxima, there are also local asynchronies within regions, such as in the case of the Seno Skyring ice lobe.

Moreover, the western margin of the PIS is largely unconstrained south of Chiloé Island, as most of the studies have focused on the terrestrial records. For instance, our simulations let the ice grow until the edge of the continental shelf at the western margin of the PIS, which is an inferred boundary by PATICE (Davies et al., 2020). Constraining the geological history of this margin, would be useful to better understand the climate of western Patagonia, as this area is directly exposed to the SWWs' influence. This would, however, require marine geological investigations in areas notoriously difficult to work in because of weather and relatively infrequent passage of suitable research vessels.

Projects like PATICE have been useful in inferring the whole margin of the PIS from key constraint regions at different time slices from 35 ka to the present. Nevertheless, nowadays there is potential to expand these time slices to earlier reconstructions (pre-35 ka; e.g., Darvill et al., 2015; Denton et al., 1999; García et al, 2018; 2021; Zechs et al, 2011), which would be very helpful to test some of the earlier advances and their synchrony postulated by others (e.g., Darvill et al., 2015; García et al, 2018).

Additionally, the details of the deglaciation pattern and chronology are poorly known. Now that ice sheet models are capable of dynamically simulating evolving PIS behaviour, more constraints are needed to understand whether the simulations are responding correctly, and for the correct reasons, during deglaciation. The understanding of the factors that drove these asynchronies may benefit from an expansion in the knowledge of the timings of the PIS fluctuations. A similar approach has been undertaken during the BRITICE-CHRONO project dating the maximum extent and retreat of the last British-Irish Ice Sheet (Clark et al., 2022).

Improve the palaeoclimatic proxies.

Continuous palaeoclimatic records that extend beyond the LGM are scarce and mostly confined to marine cores located in the Pacific sector of western Patagonia. This situation produces large uncertainty in the palaeoclimatic conditions for the whole region. To better reproduce the palaeoclimate along Patagonia, it is necessary to increase the coverage of climatic proxies. For instance, targeting peat bogs and other records which can be used to reconstruct palaeo-precipitation in northern Patagonia would be useful, and this could help to assess the northern extent of the SWWs during the last glacial cycle. The palaeoclimatic conditions of eastern Patagonia are still largely unknown, and peat records do not exist in the semi-arid environment of eastern Patagonia. However, the expansion of the sedimentological, geochemical and palynological records on lakes such as Lago Cardiel (48.9°S; e.g., Quade & Kaplan, 2017) and Laguna Potrok Aike (51.9°S; e.g., Schäbitz et al., 2013; Zolitschka et al., 2013) could broaden the understanding of the palaeoclimate. Potential under-studied areas to explore could be the lakes Musters and Colhué Huapi, located in central eastern Patagonia (45.5°S), outside the glaciation cover and with significant size to assume that it was not dried during the last glacial cycle.

Produce more sophisticated palaeoclimate models.

The palaeoprecipitation scenarios reconstructed in Chapter 4 are based on a few climatic proxies and were constructed to test previously defined hypotheses about the evolution of the palaeoprecipitation patterns along Patagonia during the last glacial cycle. Nevertheless, to quantify and better understand past climatic conditions, these scenarios should be built with deeper climatological knowledge, accompanied by denser climatic proxy data, as mentioned above. In particular, the transient simulations performed in this work use a time-dependent temperature, whereas the precipitation scenarios are fixed and do not vary over time. Chapter 4 gives insights into the changes in the precipitation configuration for the last glacial cycle at different moments (e.g., late MIS3 and early MIS2). However, the simulations did not evolve the spatial pattern of precipitation scenario from one SWWs' configuration to another. Doing so may help in understanding when and how the SWWs evolved as well as aiding understanding of how the PIS responded to the SWWs' evolution. This likely requires closer integration with an improvement of palaeoclimate models of southernmost South America.

Better ice sheet model resolution and boundary conditions.

In Chapter 3, the limitations of the coarse-resolution ice sheet model are outlined. Simulations with a finer resolution (e.g. smaller than 4 km/pixel) would enable a better approach to simulating and understanding bedrock-ice sheet interaction, thus providing more clues about the non-climatic controls that might affect the PIS fluctuations. In tandem with this, constraints on the bathymetry of the modern lakes in eastern Patagonia would help produce a better bed topography for use in simulations. This is particularly crucial given the importance of the ice surface hypsometry and its interaction with climate (mass balance) for driving the timing and pattern of PIS maxima and retreat patterns.

Chapter 6. Conclusions

Cerro Castillo and Tamango Lake, Central Patagonia

6.1. Main Conclusions

This thesis presents new understandings of the past glacial conditions along Patagonia through the last glacial cycle. In particular, it addresses a long-debated topic about the past configuration of the SWWs, which is directly related to the precipitation in the area. Moreover, the analysis of the entire PIS behaviour allows comparison within and between different regions, suggesting different responses to the evolving climate. In addition, reasons for the asynchrony in the timings of the maximum ice extent along Patagonia, are explained through the combination of analysis of climatic factors and topographic controls.

The key conclusions are the following:

- The geochronological constraints from the ice margins of the Seno Skyring ice lobe indicate that the outlet reached near maxima ice conditions during early MIS 2, contemporaneous to the global LGM, which is a different tendency from its neighbour lobe, where ice maxima have been dated to have occurred earlier during MIS 3 and MIS 4.
  Additionally, these time differences reveal that the asynchrony of the ice maxima is not only regional (such as differences between northern, central and southern Patagonia) but also happens locally, affecting individual ice lobes within a region. This implies that even closely adjacent lobes, with likely similar climates, can have different responses and that therefore, non-climatic influences may play a role in this asynchrony.

- The ice sheet modelling forced with different climatic scenarios performed in this work shows that the SWWs' position fluctuated during the last glacial cycle along Patagonia. This fluctuation was driven by an *expansion* of the SWWs' core to northern latitudes rather than just a migration of the modern core, and the northern extent of the SWWs’ varied through the last glacial cycle. The model results show that an expanded configuration of the SWWs’ core to northern Patagonia was the most favourable scenario for MIS 3, while a more contracted position with the SWWs’ core expanded only to central Patagonia was optimal for early MIS 2. This expansion to the northern latitudes is an important factor in enabling optimal conditions for glaciation in this region. These results address a long-debated topic that central and northwestern Patagonia had wetter conditions in the past than today, while in southern Patagonia precipitation was similar to today.

- The mass balance analysis during the deglaciation along the PIS suggests that northern, central, and southern Patagonia had very diverse responses to the climatic changes throughout along the last glacial cycle. These differences are, on one hand, because of a latitudinal effect, as the PIS extended for about 1800 km in a north-south direction. This makes northern Patagonia considerably warmer than the other areas, thus resulting in a higher ELA position confined to the high mountains, even during the peak of the glaciation. On the other hand, the ice surface topography plays a key role in differentiating central and southern Patagonia. In the South, the eastern outlets are characterised by low-gradient ice surface topography; this makes this area more susceptible to temperature changes, as a minor increase in the ELA produces a large increase in the ablation area. On the contrary, the ice surface topography in central Patagonia has steeper gradients, making this area more resilient to changes in the ELA, as a minor increase in the ELA produces only a small increase in the ablation area. Additionally, central Patagonia has the highest elevations on average compared to the other regions, supporting the presence of larger accumulation areas. This might contribute to the region being less sensitive to deglacial conditions relative to the rest of Patagonia.

- The transient ice sheet modelling simulations for the PIS demonstrate that full glacial conditions were reached for the whole of Patagonia, and to extents that approached the PIS maxima, several times before the LGM throughout the last glacial cycle. This acts as a reminder that ice volume in Patagonia was significant and sustained for a significant part of the last glacial cycle.

- From the modelling simulations, the asynchrony of the timing and extent of the ice maxima can be explained through climatic changes throughout the last glacial cycle and the differences in the topography between northern, central and southern Patagonia. The past position of the SWWs was crucial in causing the temporal asynchrony of the maximum ice extent, particularly as this produced wetter conditions in northern Patagonia, which enabled the development of full glacial conditions along the whole of Patagonia (e.g., during MIS 4 or MIS 3). During the warmer phases of the glacial period, the pattern of the ice retreat likely followed a similar pattern to the deglaciation, and shows that central Patagonia may have been more resilient to deglaciation than northern and southern Patagonia. This is because central Patagonia has the highest elevations on average, allowing larger accumulation areas, while the steeper ice surface topography means this area is less likely to have been affected by the rising temperatures and variations of the ELA than southern Patagonia. Consequently, during a new glacial advance (e.g., global LGM during MIS 2), central Patagonia would have a more advantageous position that influenced the reach of farther positions of the ice, surpassing previous ice margins, resulting in an ice maximum later than the rest of Patagonia. In the same period the glaciers in northern and southern Patagonia were in a more retreated position during the glacial re-advance, producing less extended glaciers than the previous glacial advances, resulting in ice maxima earlier than in central Patagonia. Moreover, these topographic differences also apply to adjacent lobes and may explain some of the local asynchrony we see, such as in the Seno Skyring ice lobe of southern Patagonia.

Supplementary Material

SC2. Supplementary Material Chapter 2 (SC2)

SC2.1. Extended Methods

SC2.1.1. Geomorphological mapping imagery

Table SC2.1. Imagery information details

Imagery source	Type	Resolution	Band combination	Source
Aerial Photographs	Photograph	1:70,000	-	*Servicio Aéreo Fotogramétrico*, Chile. www.saf.cl
Sentinel 2	Satellite Image	10 m	8 4 3	European Space Agency https://scihub.copernicus.eu/dhus/#/home
Google Earth	Satellite Image	-	-	https://earth.google.com/
Shuttle Radar Topography Mission	DEM	30 m	-	USGS EROS Center https://opentopography.org/

SC2.1.2. Laboratory methods for ^{10}Be analysis

SC2.1.2.1. ^{10}Be Laboratory process

The boulders and surface cobbles samples were prepared in a combination of the cosmogenic labs from Pontificia Universidad Católica in Santiago, Chile, and Edinburgh University, UK. AMS measurements were done at Köln University, Germany. Whereas the samples from the outwash terrace located on the Otway lobe, were prepared entirely at Scottish Universities Environmental Research Centre (SUERC) as part of the UK NERC Cosmogenic Isotope Analysis Facility (CIAF).

SC2.1.2.2. Moraine boulders and cobbles from outwash moraine and shoreline berms

The quartz separation was done at Universidad Católica (UC) in Santiago, Chile and Edinburgh University, UK (EU). At UC, the samples were crushed and sieved to yield the 750-125 µm size fraction. Then, the samples were treated with aqua regia (HNO_3:HCl=3:1) in order to eliminate any organic material and carbonates. The next step was a flotation process, where the samples were treated with 0.4%HF, and then some drops of eucalyptus oil were added, along with a mix of water and dodecylamine with CO_2 gas. This allowed the feldspar and micas to acquire hydrophobic characteristics and thus float and be removed. Following this, the ferromagnesian minerals were separated from the rest of the sample by density separation with heavy liquid. Finally, the samples were leached in acid solutions of 1% HF and 0.8% HNO_3, in an ultrasound bath for three days.

Samples prepared at the University of Edinburgh's Cosmogenic Nuclide Laboratory were crushed and sieved to isolate the 250-710 μm grain fractions, which were etched in an HCl and H_2SiF_6 solution on a shaker table for at least two days to remove/weaken non-quartz minerals. The samples were then etched a minimum of three times (24 h each) in a dilute HF and HNO_3 solution in a heated ultrasonic bath to purify remaining quartz grains and remove meteoric ^{10}Be (Hein, 2009). ^{10}Be was selectively extracted from 7-23 g (average 19 g) of the pure quartz following standard methods from Hein et al. (2009). The samples and process blanks (n =4) were spiked with 0.25 mg of ^{9}Be carrier (Scharlau Be carrier, 1000 mg/l, density 1.02 g/ml).

All ^{10}Be concentrations are based on 2.79 x 10^{-11} nominal ^{10}Be/^{9}Be ratio (Nishiizumi *et al*., 2007) for NIST SRM4325 standard and a ^{10}Be half-life of 1.36 Ma. The ^{10}Be/^{9}Be measurements were carried out at Cologne AMS (Dewald et al., 2013), normalized to the revised standard values reported by Nishiizumi et al. (2007). The ^{10}Be concentration is reported after substraction of the ^{10}Be atoms from the respective blanks. Process blank corrections ranged between 2.9% and 7.4%.

SC2.1.2.3. Depth profiles

For the depth profile samples all physical and chemical preparation and ^{10}Be/^{9}Be AMS measurements were carried out at the Scottish Universities Environmental Research Centre (SUERC) as part of the NERC Cosmogenic Isotope Analysis Facility (CIAF). Surface cobbles were treated individually, whereas depth samples were treated as amalgams. All samples were crushed whole, milled and sieved, and the >250 μm to <500 μm fraction was then passed through a roll magnetic separator to separate the non-magnetic minerals prior to chemical analysis. Feldspars were separated by froth flotation. The quartz was then isolated and purified by repeat etching in 2% HF and 2% HNO_3 in high-energy ultrasonic tanks to dissolve non quartz minerals and remove >30% of the starting mass to avoid contamination by meteoric ^{10}Be. Quartz purity was assayed by ICP-OES. All samples were dissolved in 40% HF dry-downs on a hotplate. Dried samples were converted to chloride form and 0.2 mg of ^{9}Be carrier was added to each sample. The solutions were passed through anion exchange columns to remove Fe and other contaminants, and then through cation exchange columns to separate Ti, Be and Al. The separate Be fractions were precipitated as $Be(OH)_2$ and converted to BeO at 900°C. BeO was mixed with Nb powder (1:6) and pressed into Cu cathodes for AMS analysis.

^{10}Be/^{9}Be ratios were measured on a 5MV tandem accelerator together with quality control standards. Measured nuclide ratios were normalised to NIST-SRM4325, with nominal ^{10}Be/^{9}Be ratio of 2.79 × 10^{-11}. The reported uncertainties of the nuclide concentrations include 2.5% for the AMS and chemical preparation. Blank corrections ranged between 4 and 11% of the sample $^{10}Be/^{9}Be$ ratios. The uncertainty of the blank measurements is included in the stated uncertainties. All nuclide concentration data are given in Table 2.1 (Main text).

SC2.1.3. Field and Laboratory methods for OSL analysis

Samples for luminescence dating were collected in opaque tubes and prepared for analysis under subdued lighting conditions. To calculate the environmental dose-rate throughout burialfor each sample, U, Th and K concentrations were measured for ca. 80 g of the bulk sedimentsample using high-resolution gamma spectrometry. Water contents of 5 ± 2 % were estimatedconsidering the field and saturated water contents, and the environmental history for each sample. Cosmic dose-rates were calculated after (Prescott & Hutton, 1994). Environmentaldose-rates determined for all samples are shown in Table SC2.2. Grains of K-feldspar were used to determine equivalent doses (D_e). Samples were first treated with a 10 % v/v dilution of 37% HCl and with 20 % v/v of H_2O_2 to remove carbonates and organics, respectively. Dry sievingthen isolated the grainsize used for analysis, which was then subject to density separation using sodium polytungstate (<2.58 g cm^{-3} K-feldspar dominated) and not etched using hydrofluoric acid. Finally, grains of K-feldspar were mounted on a 9.8 mm diameter aluminiumsingle-grain disc for analysis, which contained a 10 by 10 grid of 300 µm (212 – 250 µm grainsize) diameter holes to ensure each hole contained only one grain.

All luminescence measurements were performed using a Risø TL/OSL DA-15 automated single-grain system equipped with a $^{90}Sr/^{90}Y$ beta source (Bøtter-Jensen et al., 2003) fitted witha blue filter pack (BG39, Coring 7-59) in front of the photomultiplier tube. Single aliquot regenerative dose (SAR) protocols (Murray & Wintle, 2000) were used for the post-IR IRSLanalyses performed at 225 °C (Thomsen et al., 2008), termed the $pIRIR_{225}$ signal. A preheat temperature of 250 °C for 60 s was used prior to stimulations of 2 s using the infra-red laser at 225 °C. The IRSL signal measured performed at 50 °C prior to the $pIRIR_{225}$ measurement and the elevated temperature bleach of 330 °C for 200 s at the end of each L_x/T_x cycle were performed using the IR LEDs. The location of the single-grain discs was performed at room temperature, rather than elevated temperatures to prevent thermal annealing of the IRSL signal (after Smedley & Duller, 2013). The first 0.3 s and final 0.6 s of stimulation were summed to calculate the initial and background IRSL signals, respectively. The grains were accepted after applying the following screening criteria and accounting for the associated uncertainties: (1) whether the test dose response was greater than three sigma above the background, (2) whether the test dose uncertainty was less than 10 %, (3) whether the recycling and OSL-IR depletion ratios were within the range of ratios 0.9 to 1.1, and (4) whether recuperation was less than 5 % of the response from the largest regenerative dose.

Grains from sample SSK1901_OSL were used for dose-recovery experiments and successfully recovered a given dose within 10 % using the $pIRIR_{225}$ signal. Fading rates (*g*-values, Aitken 1985) were determined for three aliquots of each sample and normalised to a t_c of two days (Huntley & Lamothe, 2001; Fig. 6). The large uncertainties on the individual *g*-values measured were derived from the uncertainty in the fit of the data, which is typical of fading measurements for the pIRIR signal (e.g., Smedley et al. 2016). To derive a more reliable estimate of the fading rate, the weighted mean and standard error for all the samples was calculated for $pIRIR_{225}$ signals (0.4 ± 2.0 %/decade). Given that the $pIRIR_{225}$ fading rate is lowwith large uncertainties for each sample (Table SC2.2) and in line with previous $pIRIR_{225}$ studies (e.g.,Kolb & Fuchs, 2018; Roberts, 2012; Trauerstein et al., 2014), we did not correct the $pIRIR_{225}$ ages for fading.

D_e values were calculated from all grains passing all the screening criteria. The minimum age model (MAM; Galbraith & Laslett, 1993; Galbraith et al., 1999) was applied to determine anage for the samples as the asymmetrical D_e distributions suggested the samples were partiallybleached prior to burial (Fig. 1). The scatter in the D_e distribution arising from intrinsic and extrinsic sources were combined in quadrature to determine σ_b for the MAM (Smedley et al., 2019). The overdispersion values arising from intrinsic sources for sample SSK1901_OSL (32 ± 1%) were derived from the dose-recovery experiments, while the over-dispersion arising from variability in the internal dose-rates of K-feldspar grains for both samples was assumed to be10 % (after Smedley & Pearce, 2016). Additional over-dispersion (20 %) was incorporated to account for the variability in single-grain D_e distributions caused by external microdosimetry (after Smedley et al., 2017). The D_e values were then divided by the environmental dose-ratesto determine an age for each sample (Table SC2.2).

Table SC2.2. Luminescence dating results for sample SSK1901_OSL (212-250 µm) from the Skyring lobe. Environmental dose-rates were determined using high-resolution gamma spectrometry. The dose-rates were calculated using the conversion factors of Guérin et al. (2011) and alpha (Bell, 1980) and beta (Guérin et al., 2012) dose-rate attenuation factors. Water contents (5 ± 2 %) were estimated considering the field water contents, and the environmental history for eachsample; these values are expressed as a percentage of the mass of dry sediment. An internal K-content of 10 ± 2 % (Smedley et al., 2012) were used to determine the internal dose-rates. An a-value of 0.10 ± 0.02 (Balescu & Lamothe, 1993) was used to calculate the alpha dose-rates. Cosmic dose-rates weredetermined after Prescott and Hutton (1994). Dose-rates were calculated using the Dose Rate and Age Calculator (DRAC; Durcan et al., 2015). The *g*-values (%/decade) were measured using the pIRIR225 signal for three aliquots of K-feldspar for each sample, normalised to 2 days and are presented as weighted means and standard errors. The number of grains that were used to determine a D_e value (n) are shown as a proportion of the total grains measured (N). The MAM was used to determine the D_e for age calculations, applying a σ_b value of 0.4.

Sample	U (ppm)	Th (ppm)	K (%)	Internal dose-rate (Gy/ka)	External alpha dose-rate (Gy/ka)	External beta dose-rate (Gy/ka)	External gamma dose-rate (Gy/ka)	Cosmic dose-rate(Gy/ka)	Total dose-rate(Gy/ka)	*g*-value (%/dec.)	n/N	OD(%)	D_e (Gy)	Age (ka)
SSK1901_OSL	1.70±0.19	7.46±0.19	1.02±0.19	0.77±0.15	0.10±0.02	1.06±0.14	0.76±0.05	0.24±0.02	2.92±0.21	0.4±2.0	183/4600	62±1	43.2±1.8	14.8±1.2

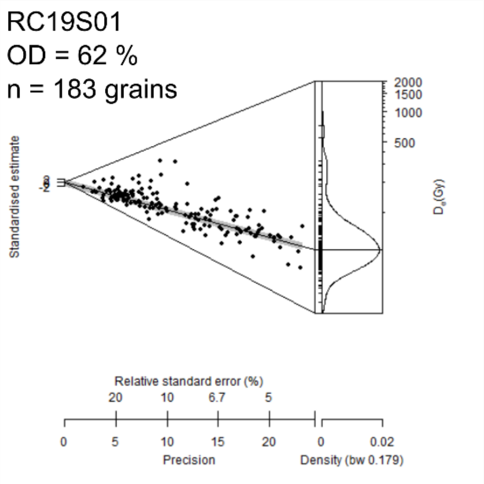

Figure SC2.1. Abanico plots of the D_e values determined for OSL dating, where the grey shading shows the MAM D_e for each distribution.

SC2.2. Extended Results

SC2.2.1. Geomorphological mapping criteria

Table SC2.3. Geomorphological mapping identification criteria.

Landform		**Criteria**
Moraine belts	:	Continuous group of rounded hills that have lateral continuity and overall arcuate plan form, consistent with a former glacial margin at a particular time.
Moraine systems	:	Group of moraine belts linked together by broad association in space and by similar morphology. Interpreted as being deposited during semi contemporaneous origin, due to similarities in shape, grade of erosion and spaced close to each other
Ridges/crests	:	Group of hills that have curvilinear continuity, generally located within the moraine belts.
Outwash plain	:	Low relief and low angle surface formed by glaciofluvial sediments in the distal part of the moraine margin.
Dissected mounts	:	Rounded mounds with high amplitude crests that are cut by water channels.
Streamline mounts	:	Low relief mounds with rounded borders or limits, their shape is elongated in a direction of former ice flow.
Alluvial deltas	:	Deltas formed at the mouth of a river by the downhill accumulation of material transported by river channels.
Paleo shorelines	:	Former shorelines indicating previous lake levels. At the Skyring lobe, these can either be in the form of broad, rounded shoreline berms, usually located at the front part of the lobe, or as low angle planar shoreline terraces, located at the lateral margins of the lake.
Paleo lakes	:	Former lakes or former lake extensions, identified by the presence of former shorelines or flattish relief surrounding current lakes.
Major meltwater spillway	:	Major erosional channel cut into rock or sediment, produced by former paleo lake drainage.
Meltwater channels	:	Elongate erosional features cut into rock or sediment, which can flow away from moraines or sub-parallel to them where they can mark a former ice margin position.
Scarps	:	Small cliffs cut in sediments or rock, usually by (glacio) fluvial erosion in the study area.
Lakes	:	Isolated water bodies.
Fjords	:	Glacial valleys flooded by marine water.
Elongated bedrock	:	Bedrock eroded such that outcrops are elongated shapes in a former ice direction. Likely formed under subglacial conditions. At the Skyring area this bedrock is mostly relatively soft rock (sandstone).
Glacial lineation	:	Long, narrow elongated features shaped in the direction of former ice flow. With length to width ratios approx. 20:1.

SC2.2.2. Stratigraphic log from Terrace 6 section

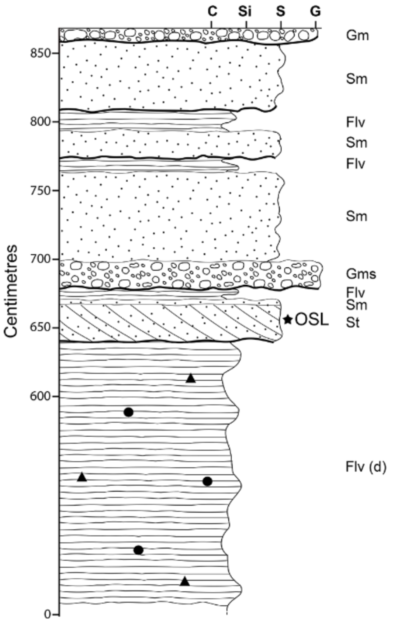

Figure SC2.2. Stratigraphic log from an exposure into T6. Codes for horizontal scale are C, Si, S and G for clay, silt, sand and gravel respectively. Lithofacies codes, Gm (clast-supported gravel), Sm (massive sand), Flv (fine lamination with varves), Gms (matrix-supported gravel), St (medium to very coarse sand with trough cross-bedding), d (dropstones), thicker contact is erosive, from Evans and Benn (2021). Star indicates the location of the OSL sample shown in Figs 6 and 7 (main text).

SC2.2.3. Erosion rate applied to quartzite lithology boulders.

Table SC2.4. ^{10}Be ages for boulders with quartzite lithology from Skyring ice lobe, an erosion rate of 0.7mm/kyr is applied.

Sample name	Lm			St			LSDn		
	Age ka	± Int ka	± Ext ka	Age ka	± Int ka	± Ext ka	Age ka	± Int ka	± Ext ka
Laguna Blanca Moraine III									
SSK1801	**27.69**	**1.47**	**2.75**	28.28	1.51	2.81	26.94	1.43	2.66
SSK1809a	**24.87**	**1.23**	**2.42**	25.37	1.25	2.47	24.24	1.20	2.34
SSK1814	**26.87**	**1.44**	**2.67**	27.44	1.47	2.73	26.16	1.40	2.59
Laguna Blanca Moraine IV									
SSK1819	**23.97**	**1.32**	**2.40**	24.44	1.342	2.445	23.36	1.28	2.324

^{10}Be ages calculated in the online calculators formerly known as the CRONUS-Earth v.3 (Balco et al., 2008). We applied the Patagonian production rate of Kaplan et al. (2011), the calibration data set was obtained from calibration.ice-d.org. No shielding correction for snow cover or vegetation. Pressure flag: std. Summary statistics are calculated for each group of samples for a dated landform.

Ages are presented in three different scaling schemes. Lm is the time-dependant scaling scheme of Lal, 1991 and Stone, 2000, we use this for this study (highlighted in bold). St is the time independent scaling scheme of Lal (1991) and Stone (2000). LSDn is the time-dependent scaling scheme of Lifton et al. (2014). Ages are reported with 1 standard deviation internal (int) and external (ext). Int include analytical uncertainty, and ext includes systematic uncertainties associated with scaling scheme and production rate. Ages are rounded using three significant figures.

SC4. Supplementary Material Chapter 4 (SC4)

Transient simulations: Timeslices for 45ka, 35 ka, 25 ka and 15 ka.

Model # 1: 'Modern precipitation' T0.85/Pp0.8

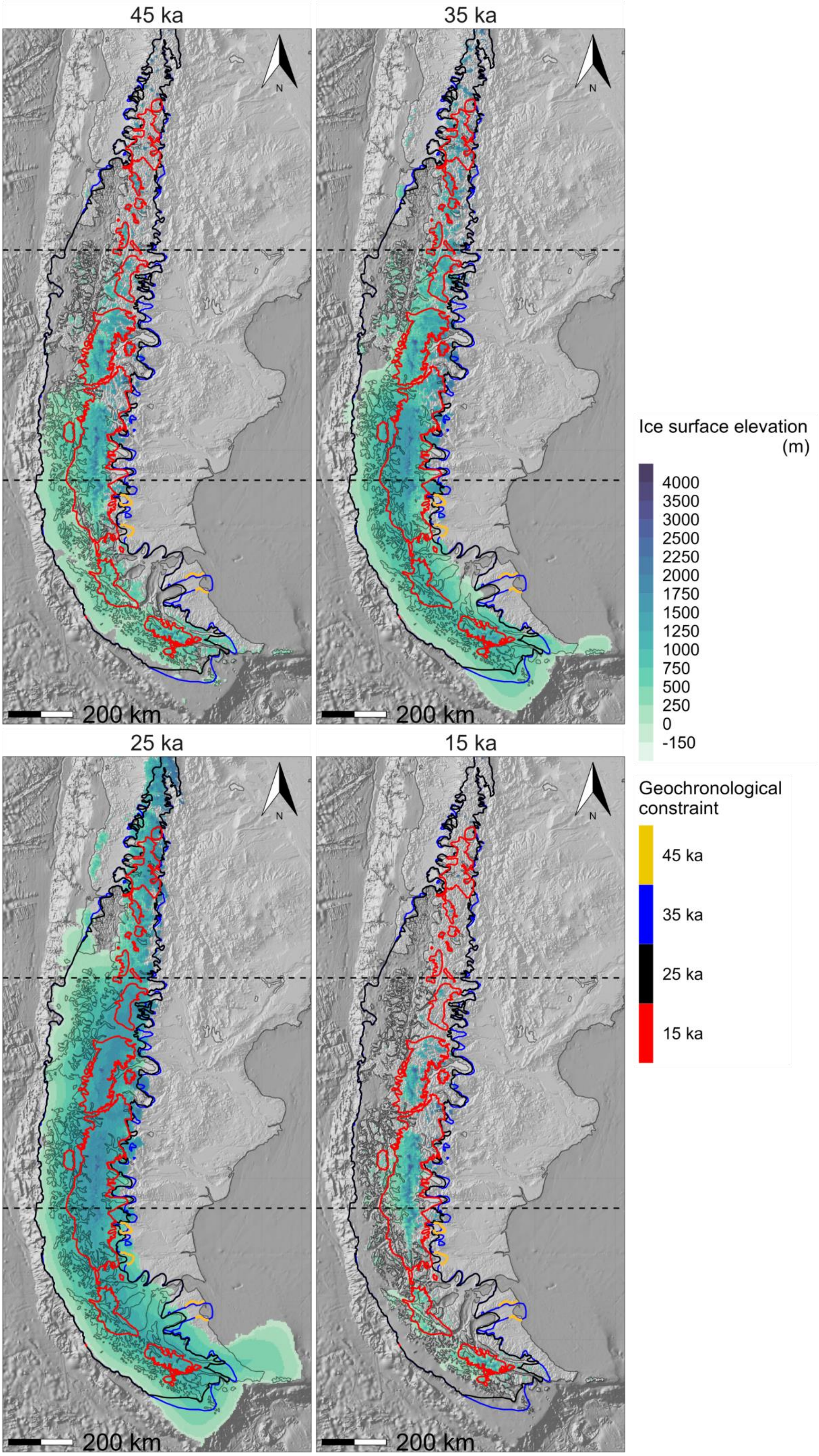

Model # 2: 'Modern precipitation' T0.85/Pp1.0

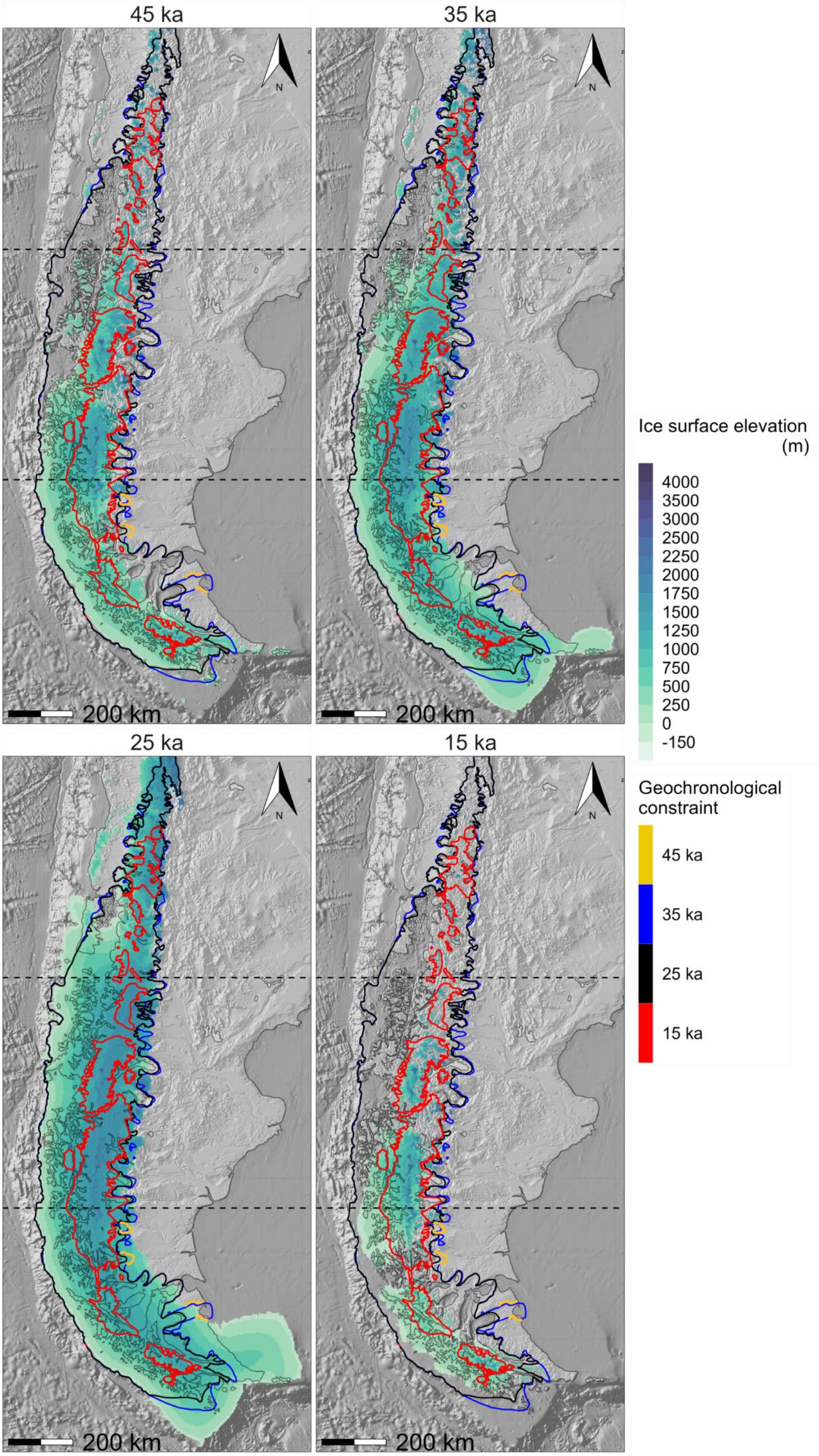

Model # 3: 'Modern precipitation' T0.85/Pp1.2

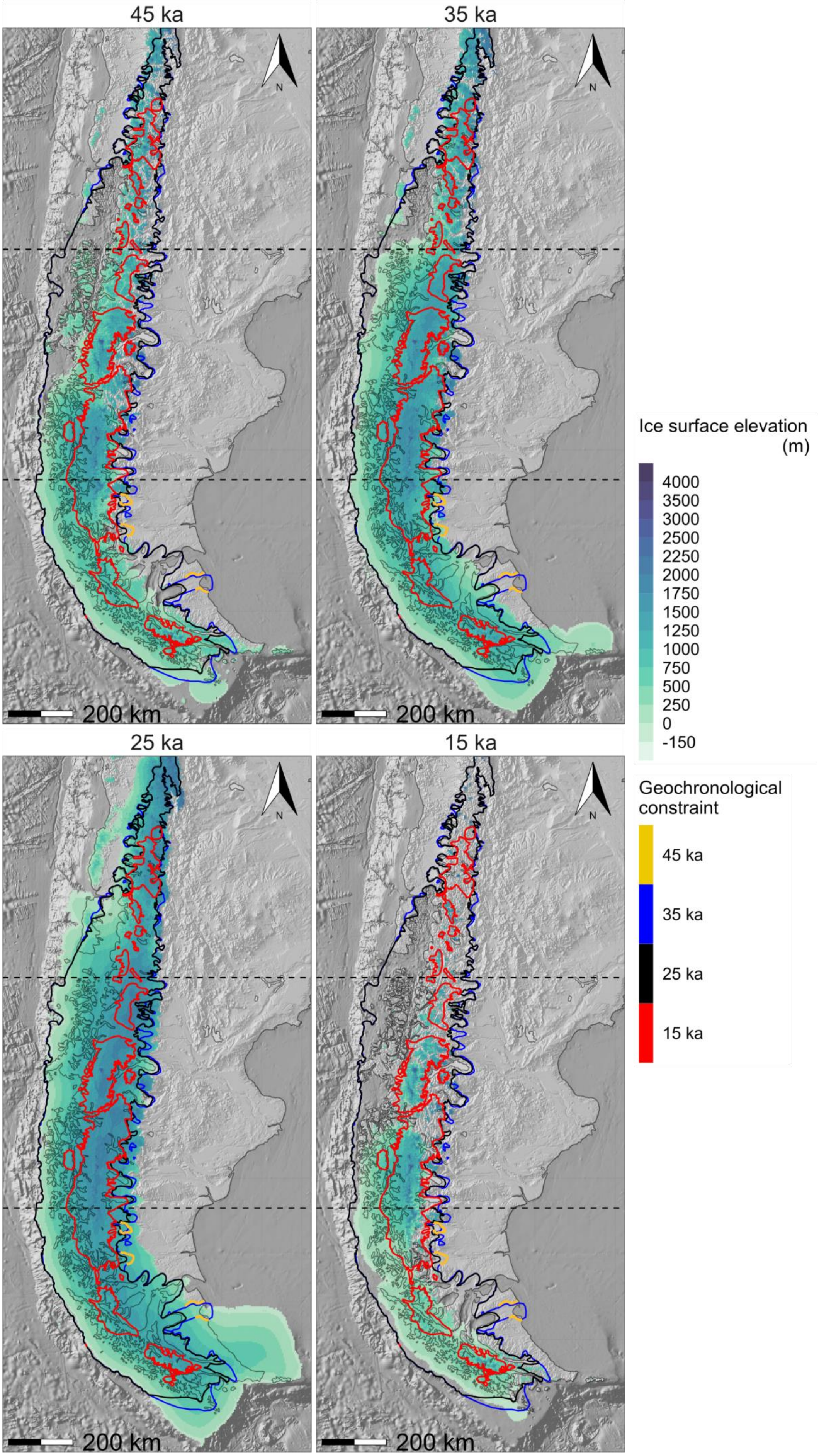

Model # 4: 'Modern precipitation' T0.75/Pp0.8

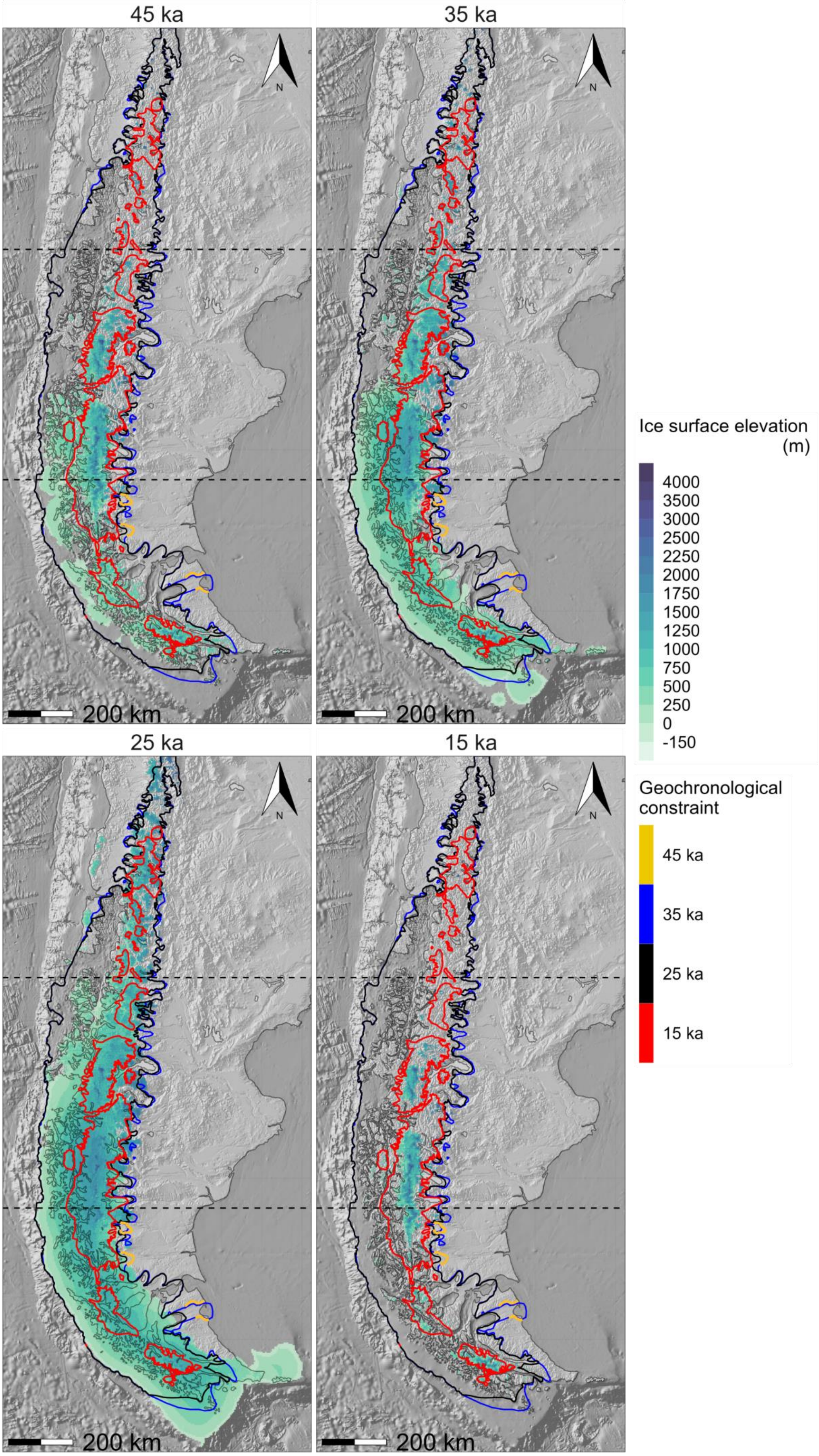

Model # 5: 'Modern precipitation' T0.75/Pp1.0

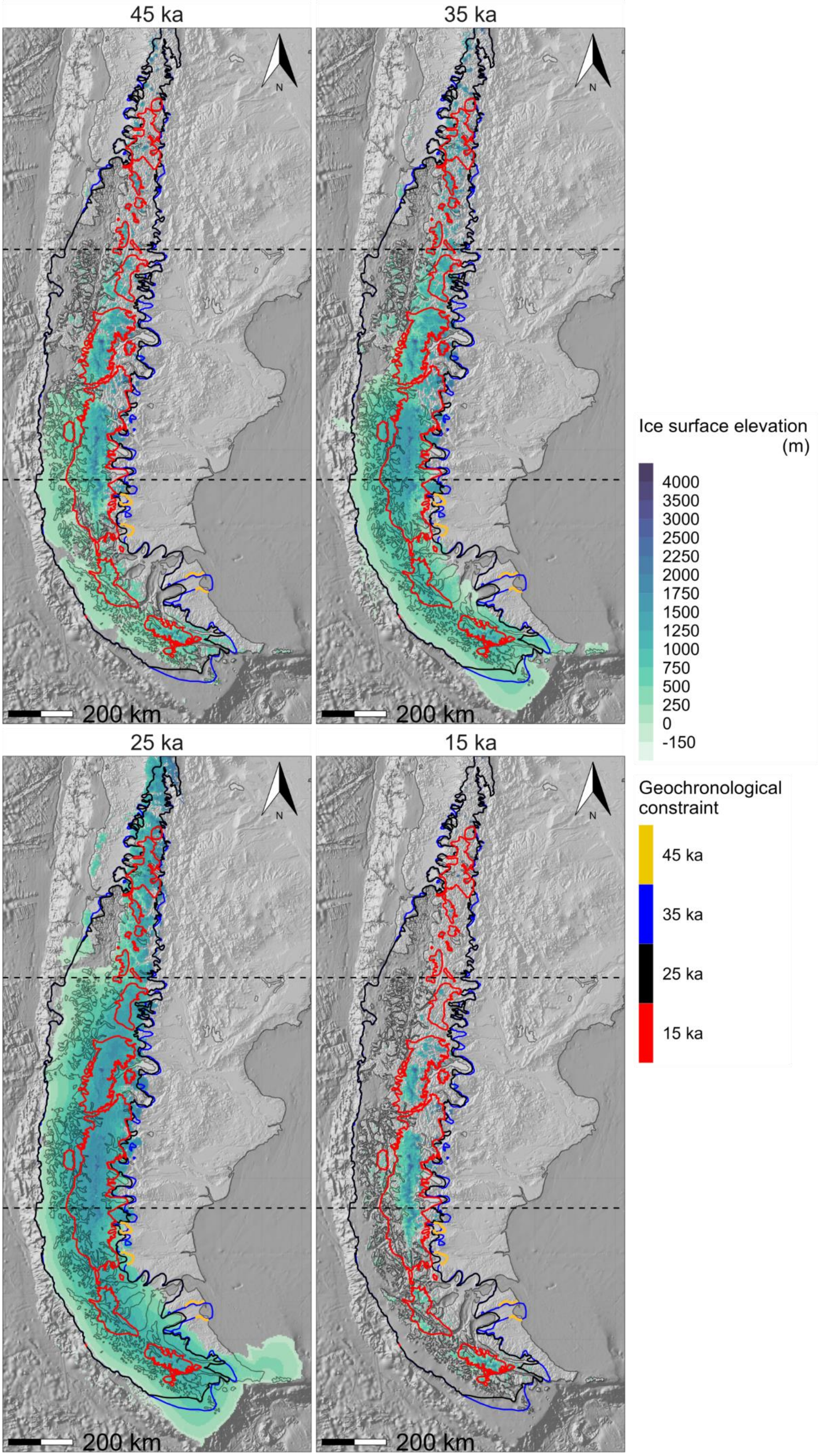

Model # 6: 'Modern precipitation' T0.75/Pp1.2

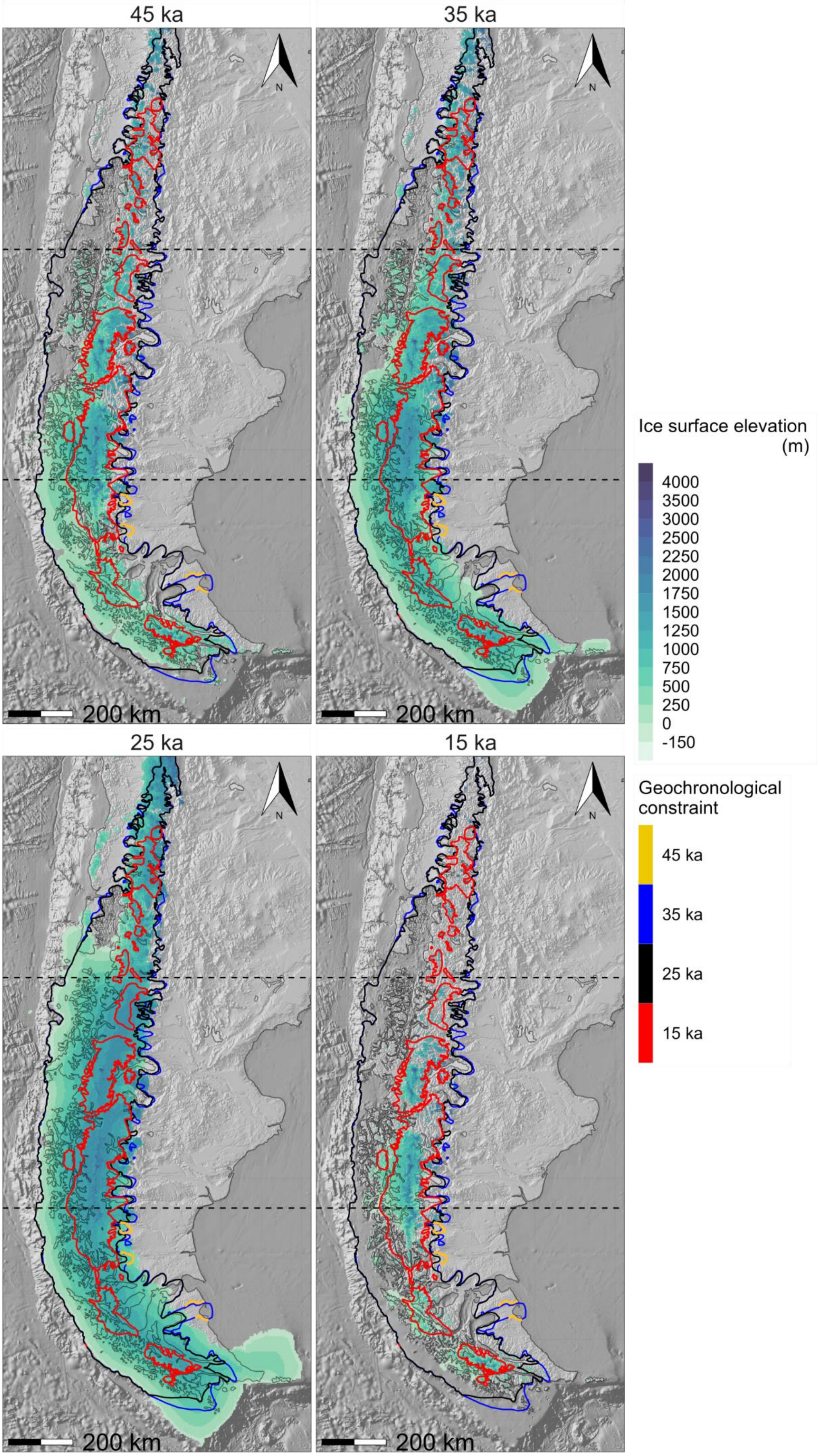

Model # 7: 'Modern precipitation' T0.65/Pp0.8

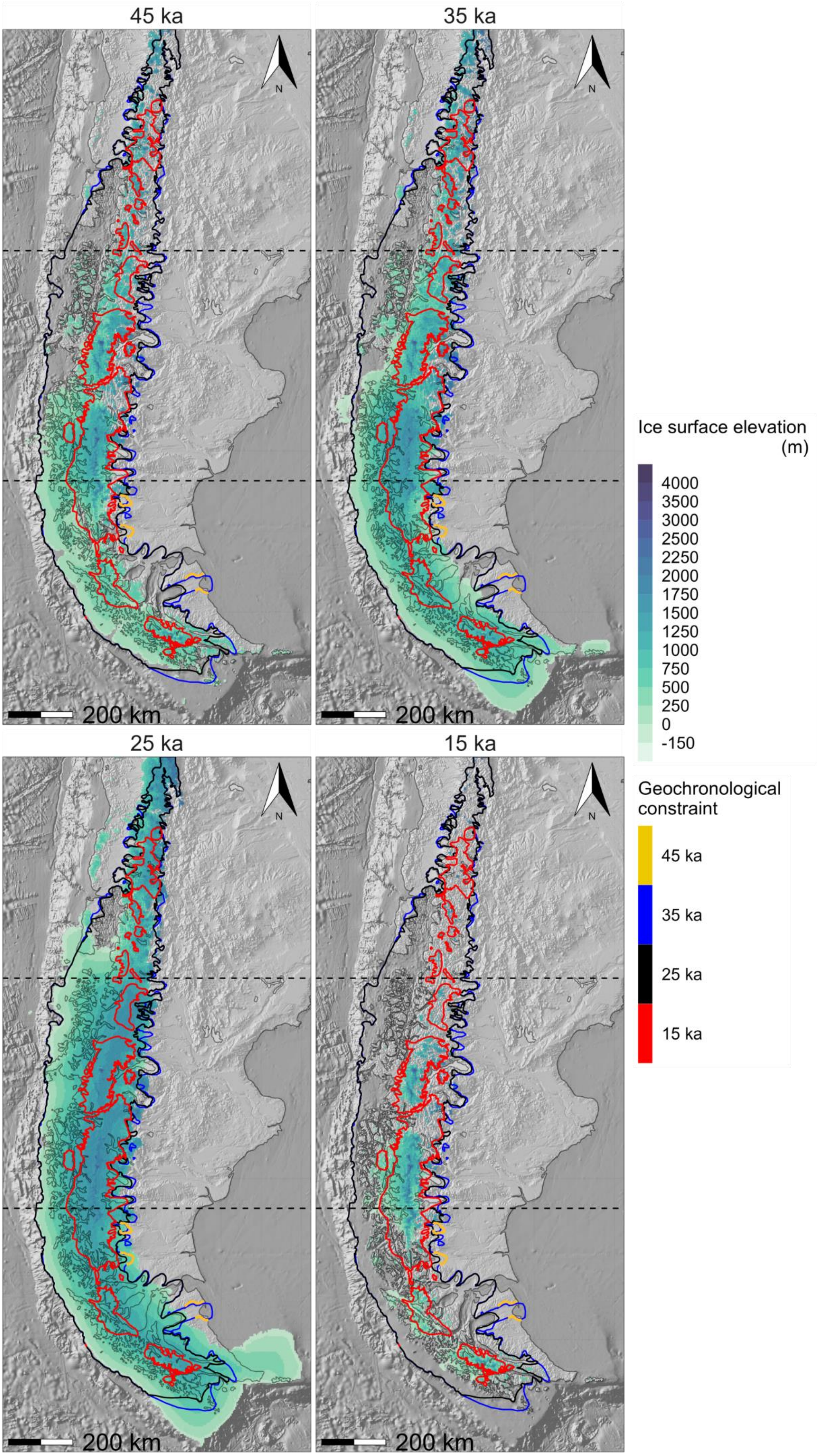

Model # 8: 'Modern precipitation' T0.65/Pp1.0

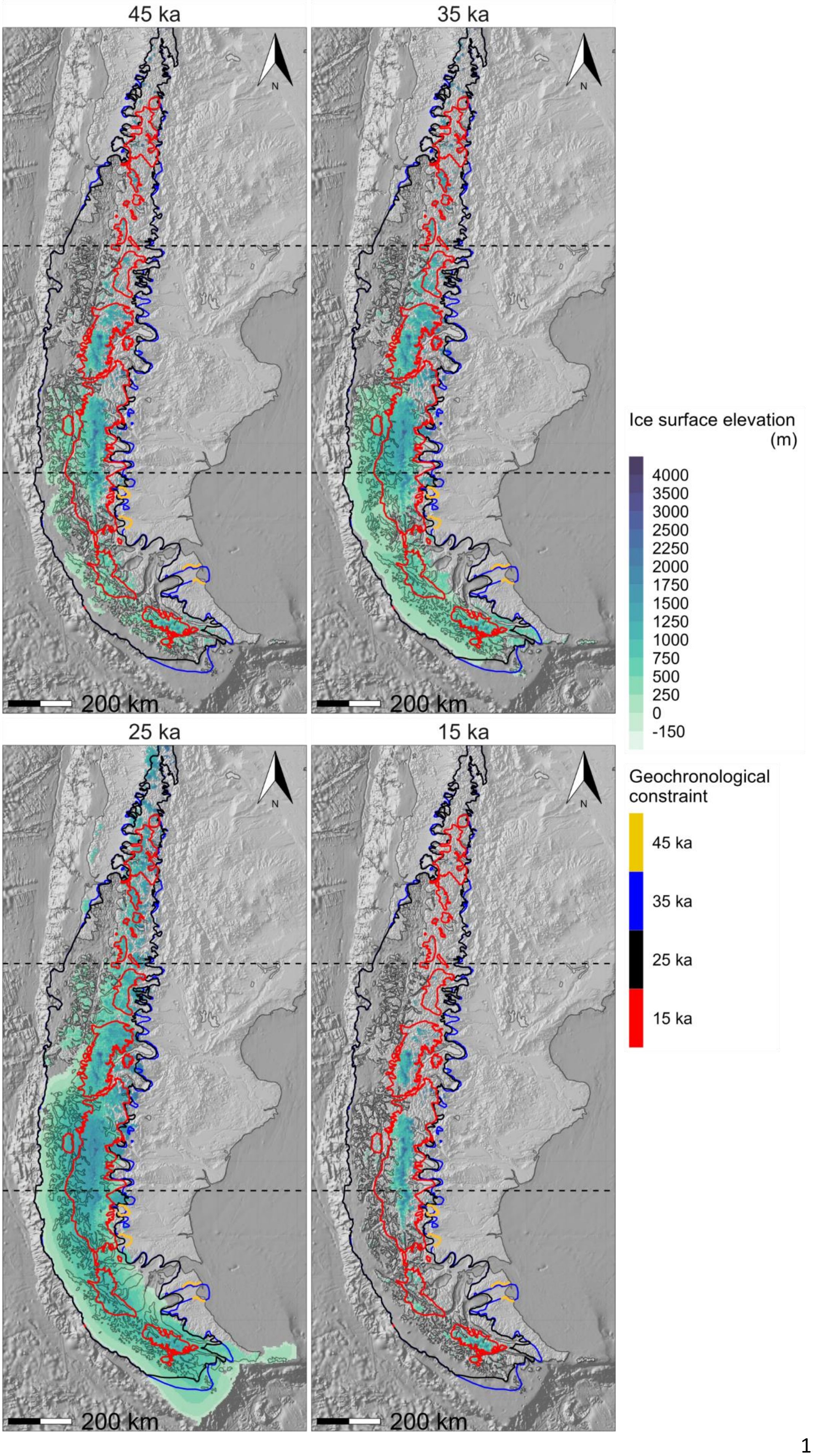

Model # 9: 'Modern precipitation' T0.65/Pp1.2

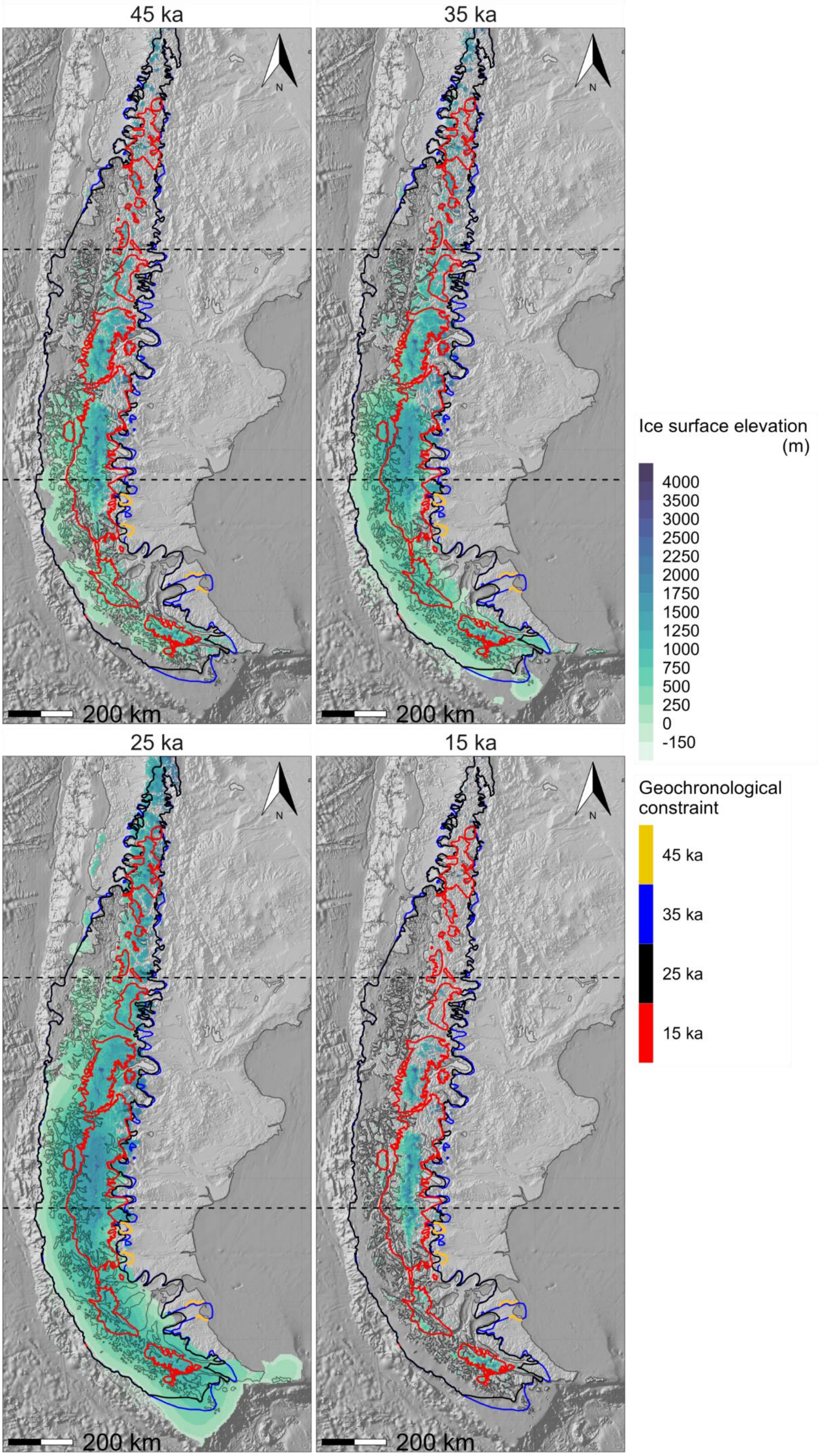
45 ka

35 ka

25 ka

15 ka

Model #10: 'Northern migration' T0.85/Pp0.8

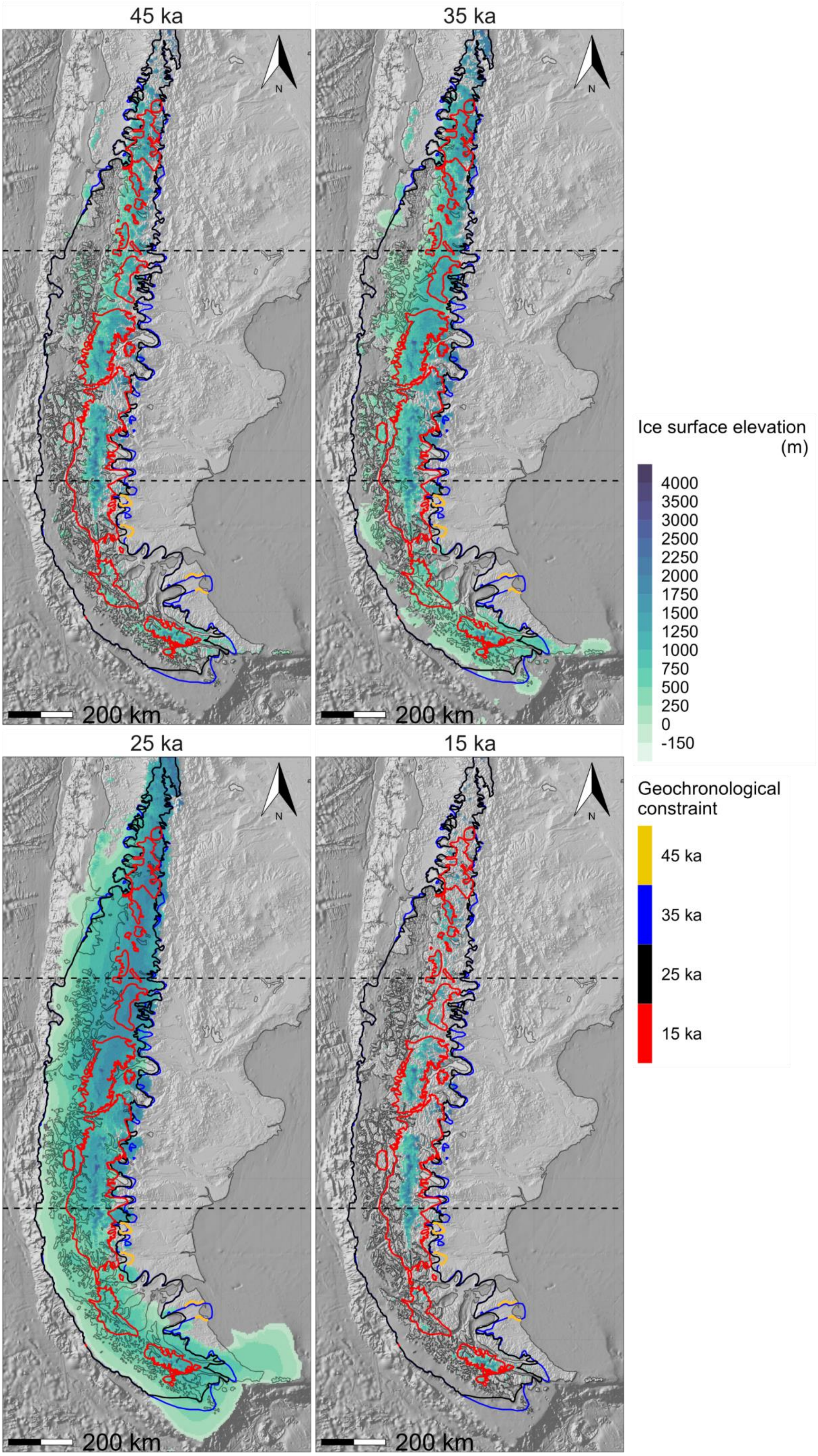

Model #11: 'Northern migration' T0.85/Pp1.0

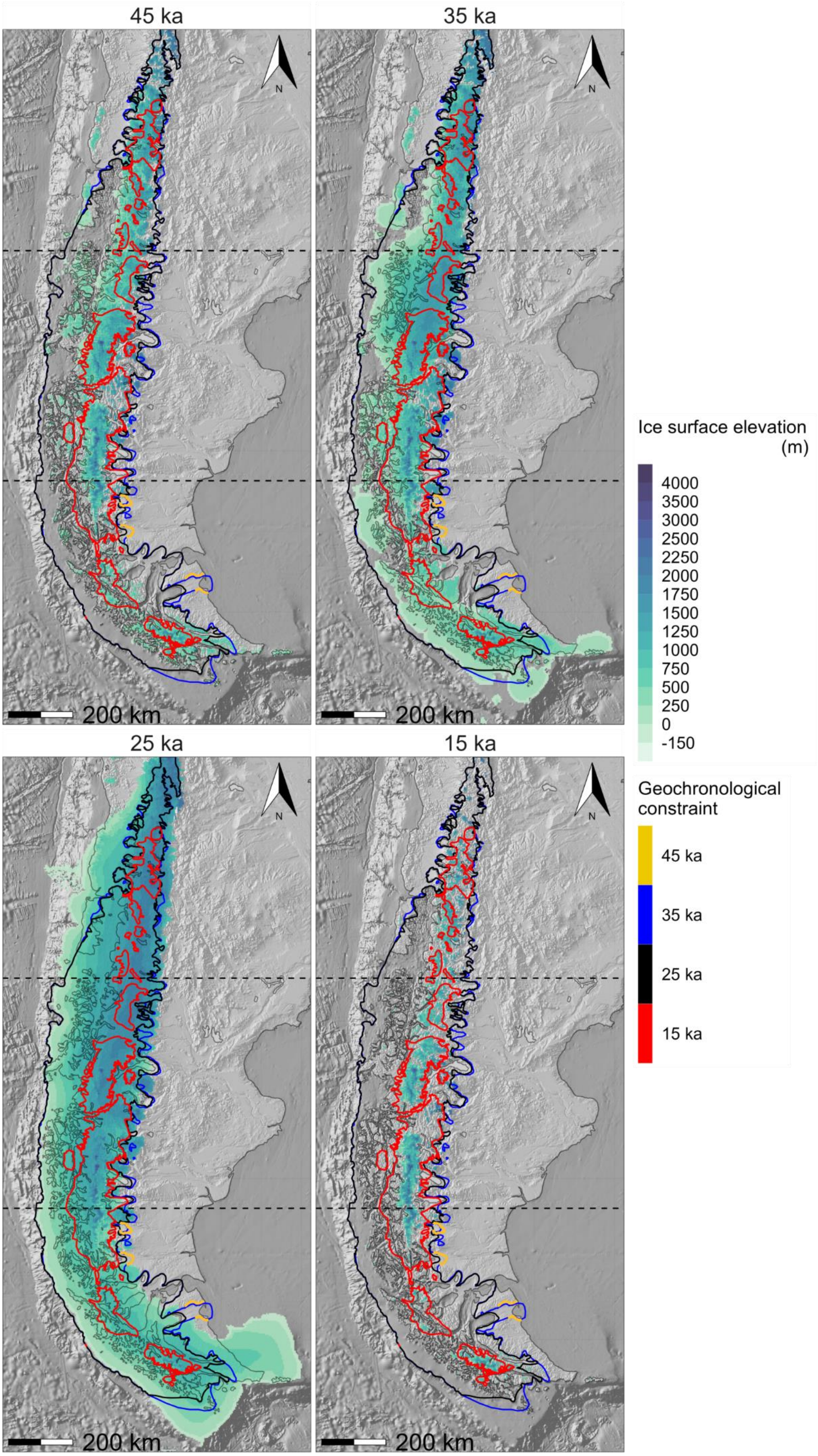

Model #12: 'Northern migration' T0.85/Pp1.2

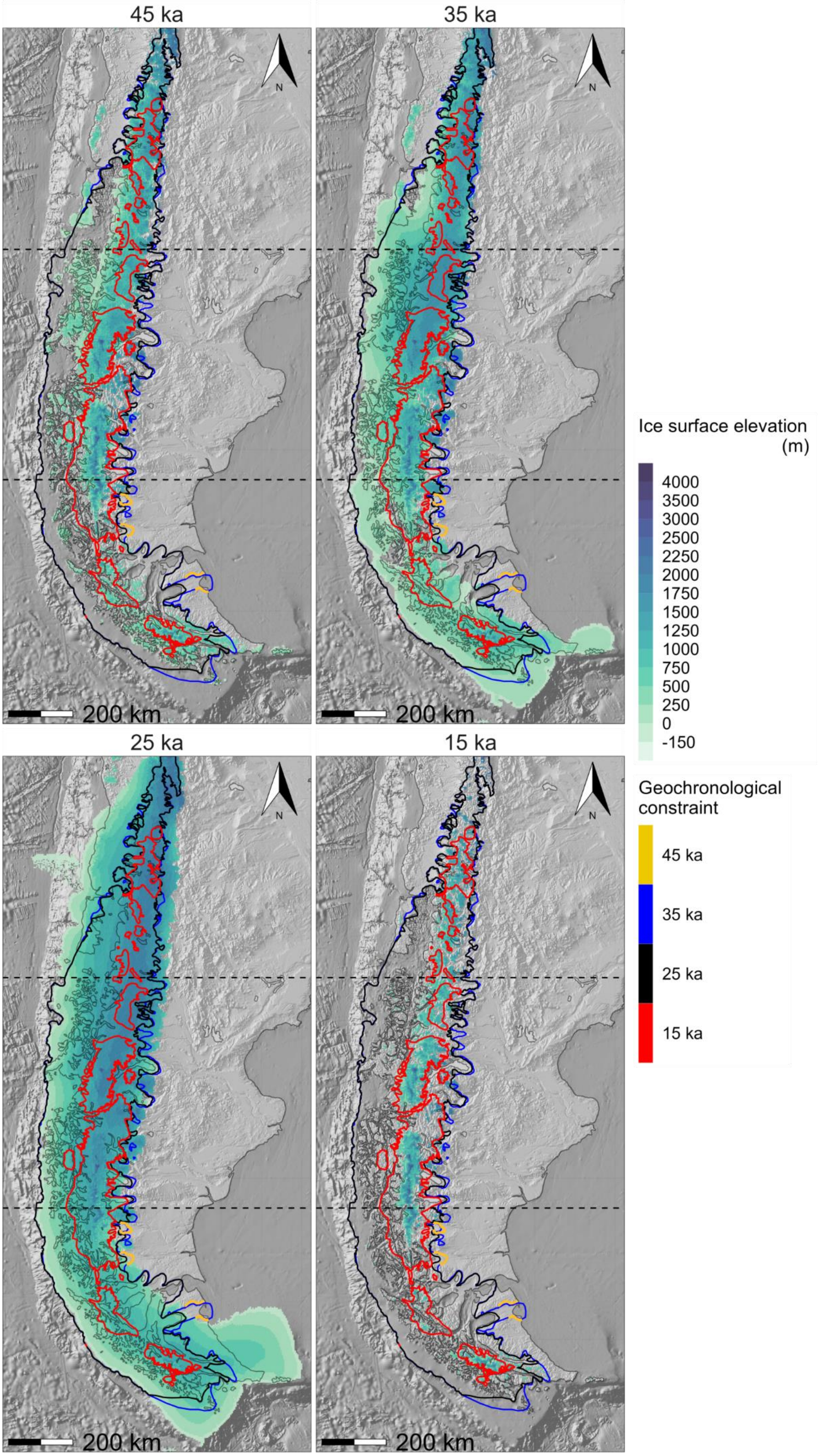

Model #13: 'Northern migration' T0.75/Pp0.8

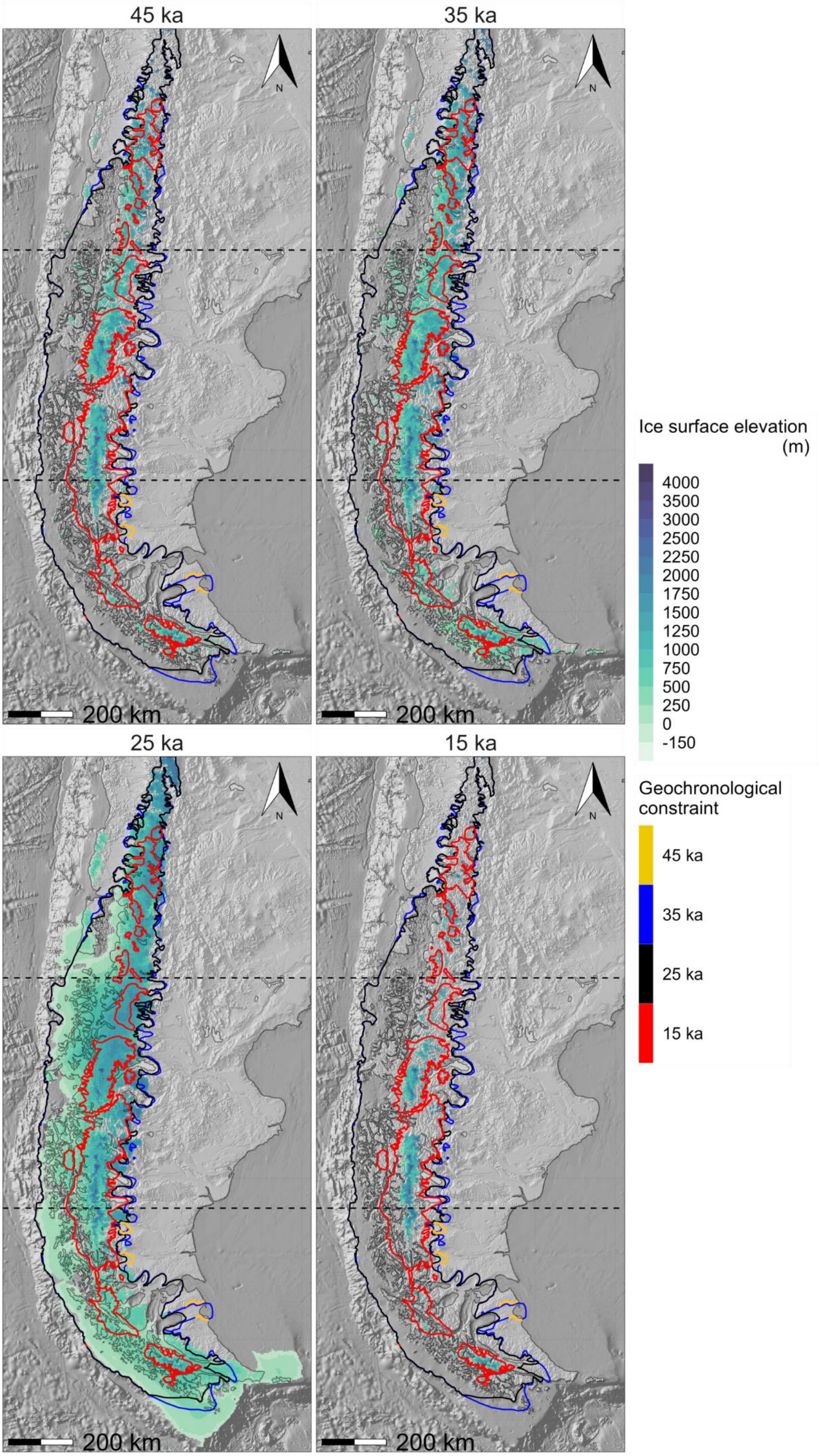

Model #14: 'Northern migration' T0.75/Pp1.0

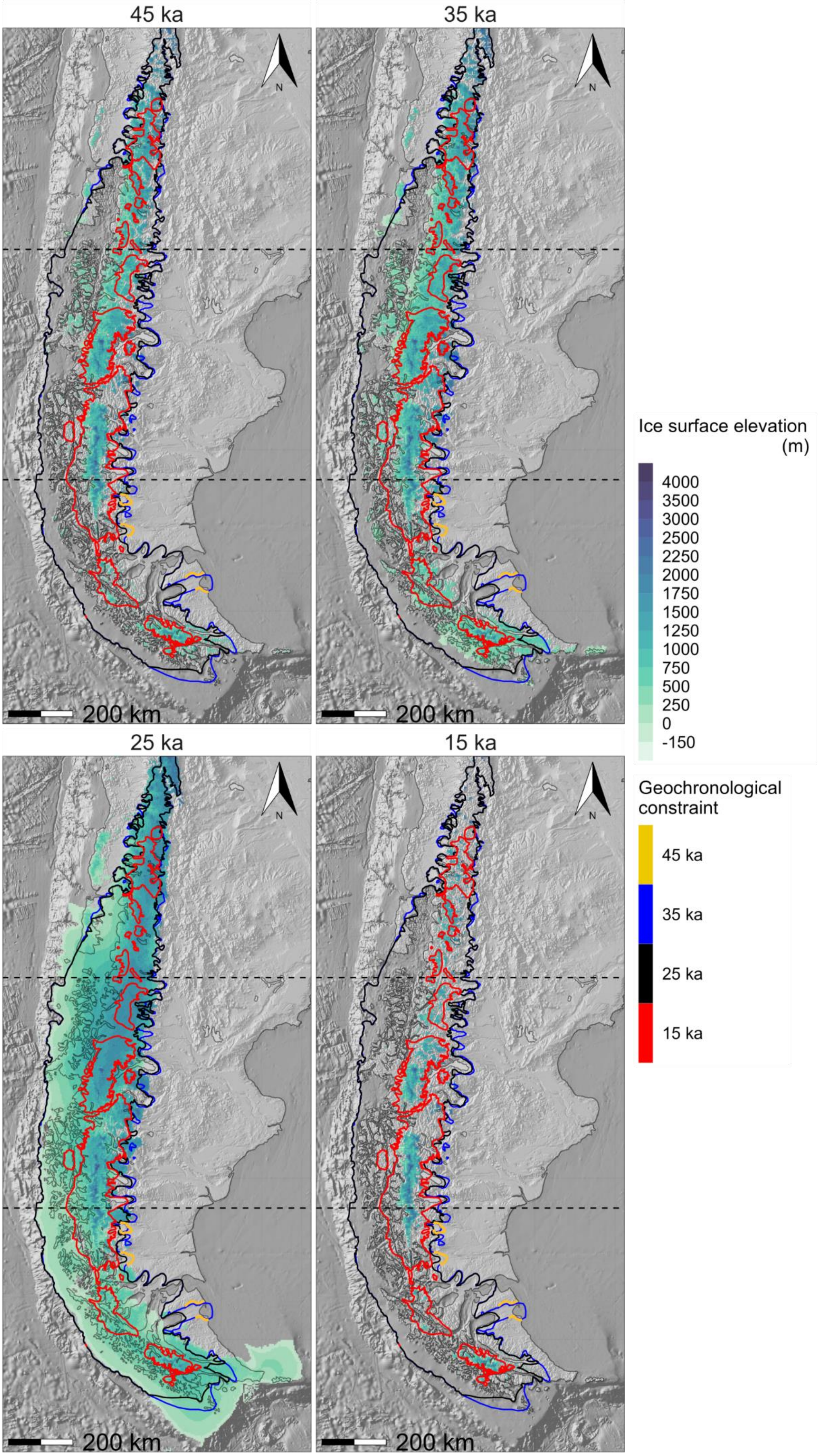

Model #15: 'Northern migration' T0.75/Pp1.2

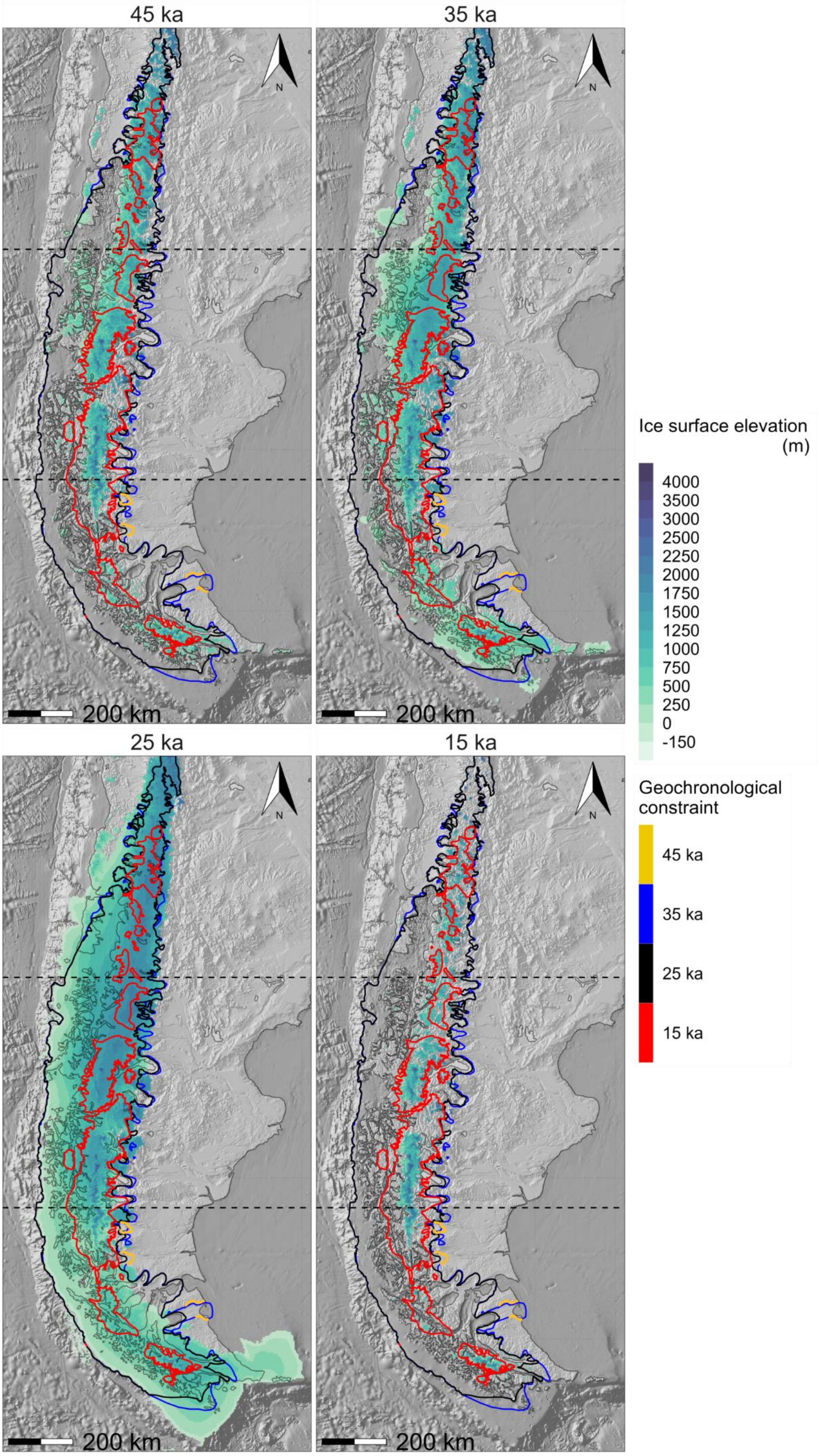

Model #16: 'Northern migration' T0.65/Pp0.8

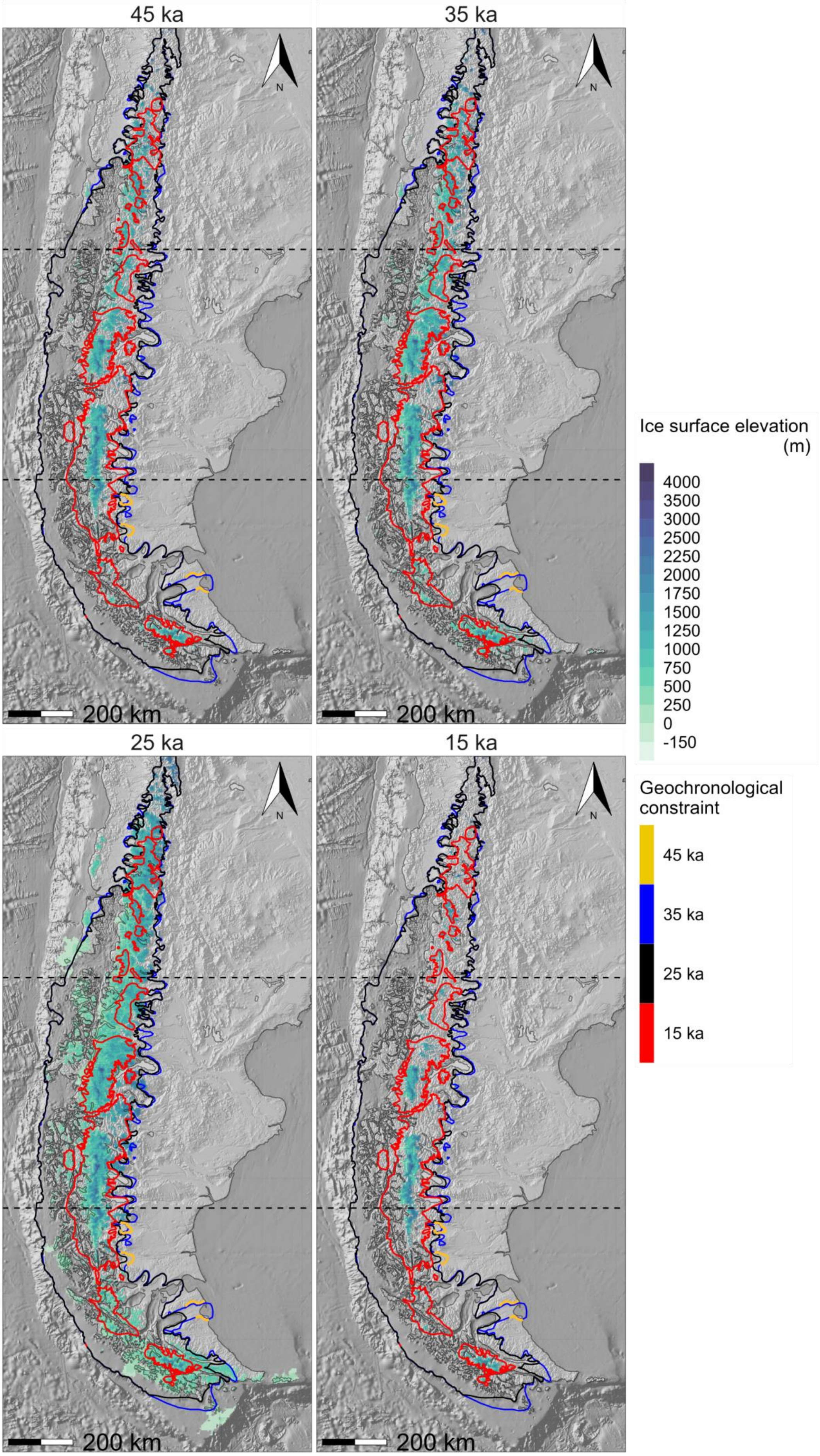

Model #17: 'Northern migration' T0.65/Pp1.0

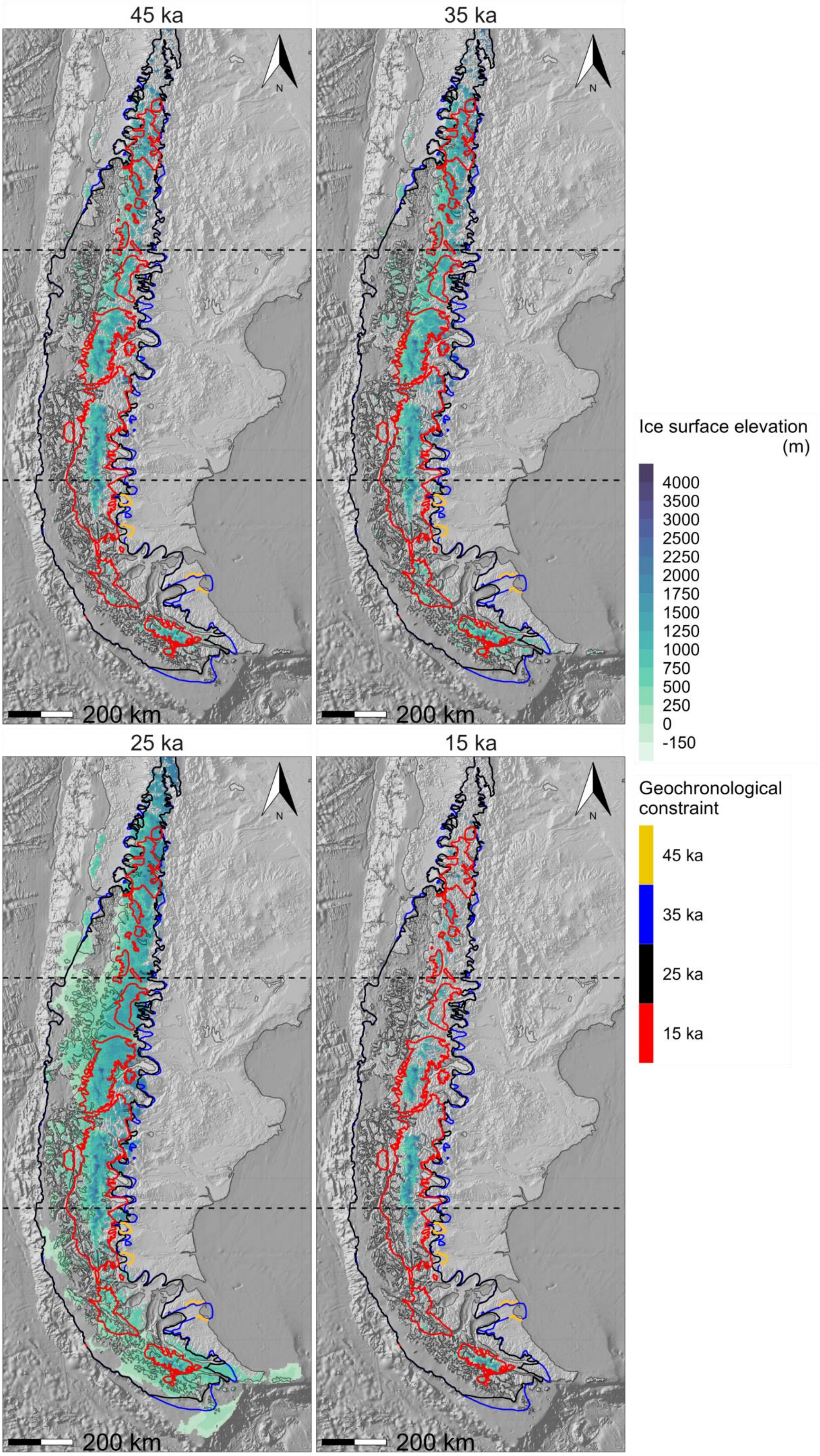

Model #18: 'Northern migration' T0.65/Pp1.2

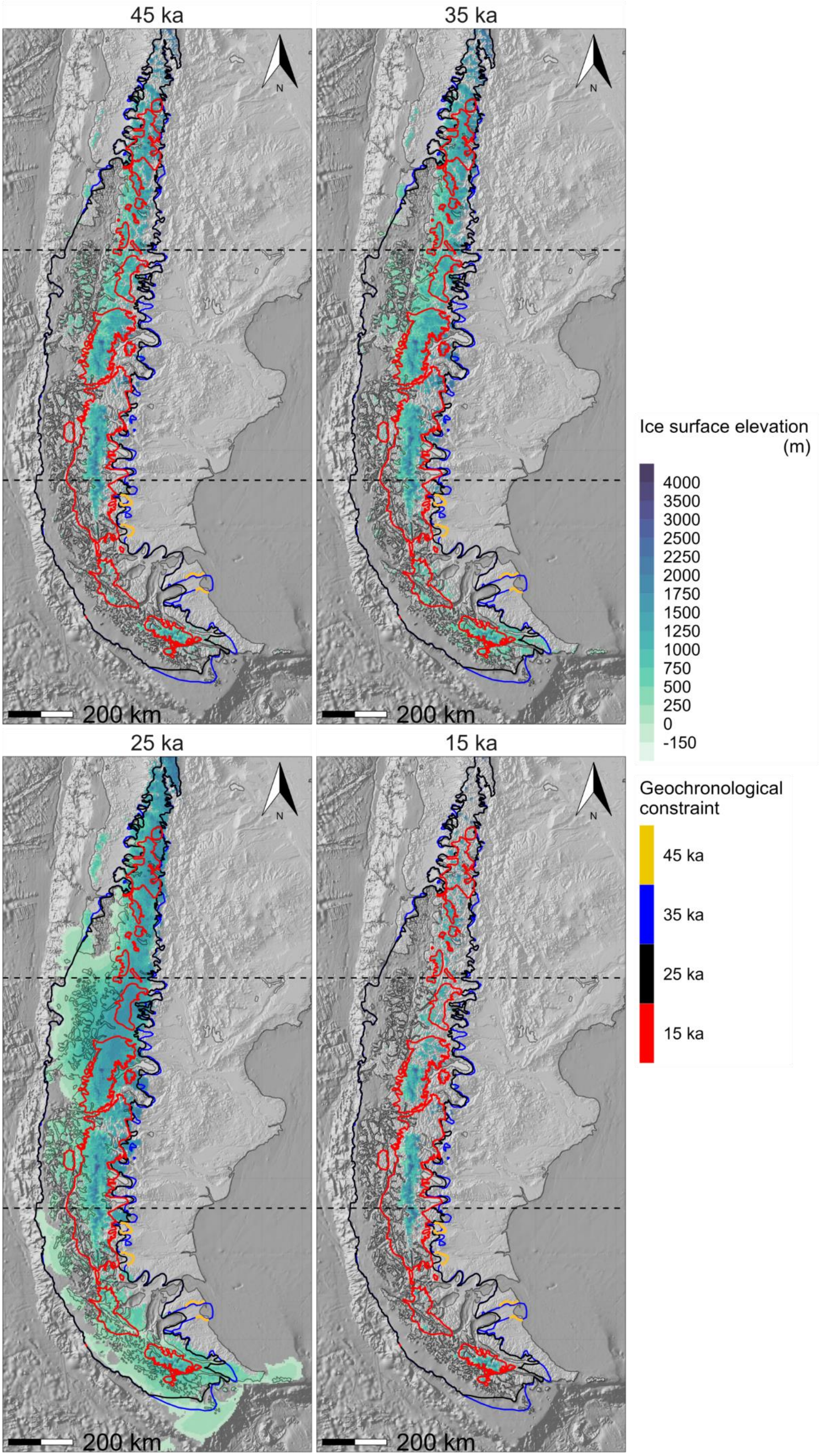

Model #19: 'Northern expansion' T0.85/Pp0.8

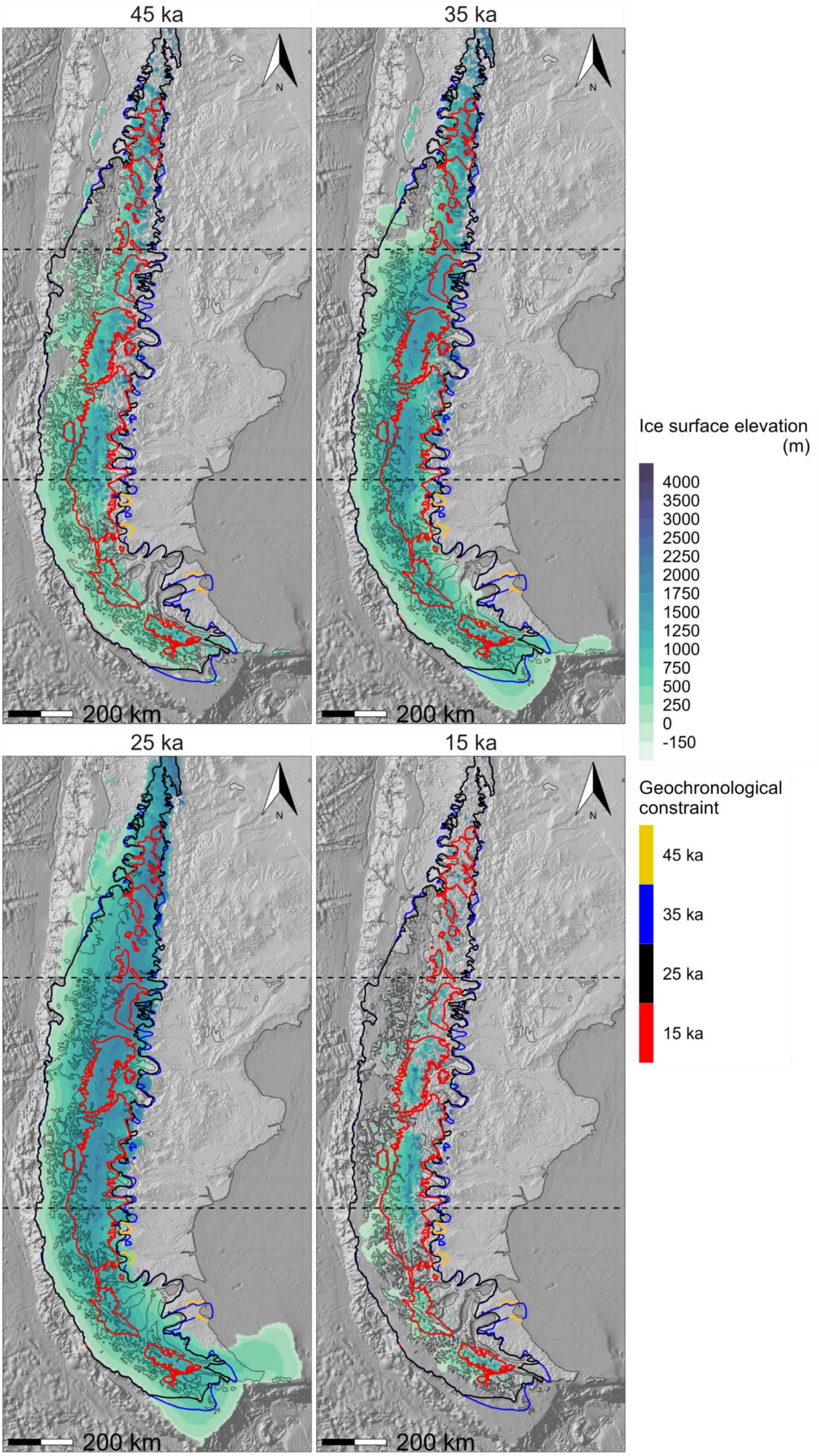

Model #20: 'Northern expansion' T0.85/Pp1.0

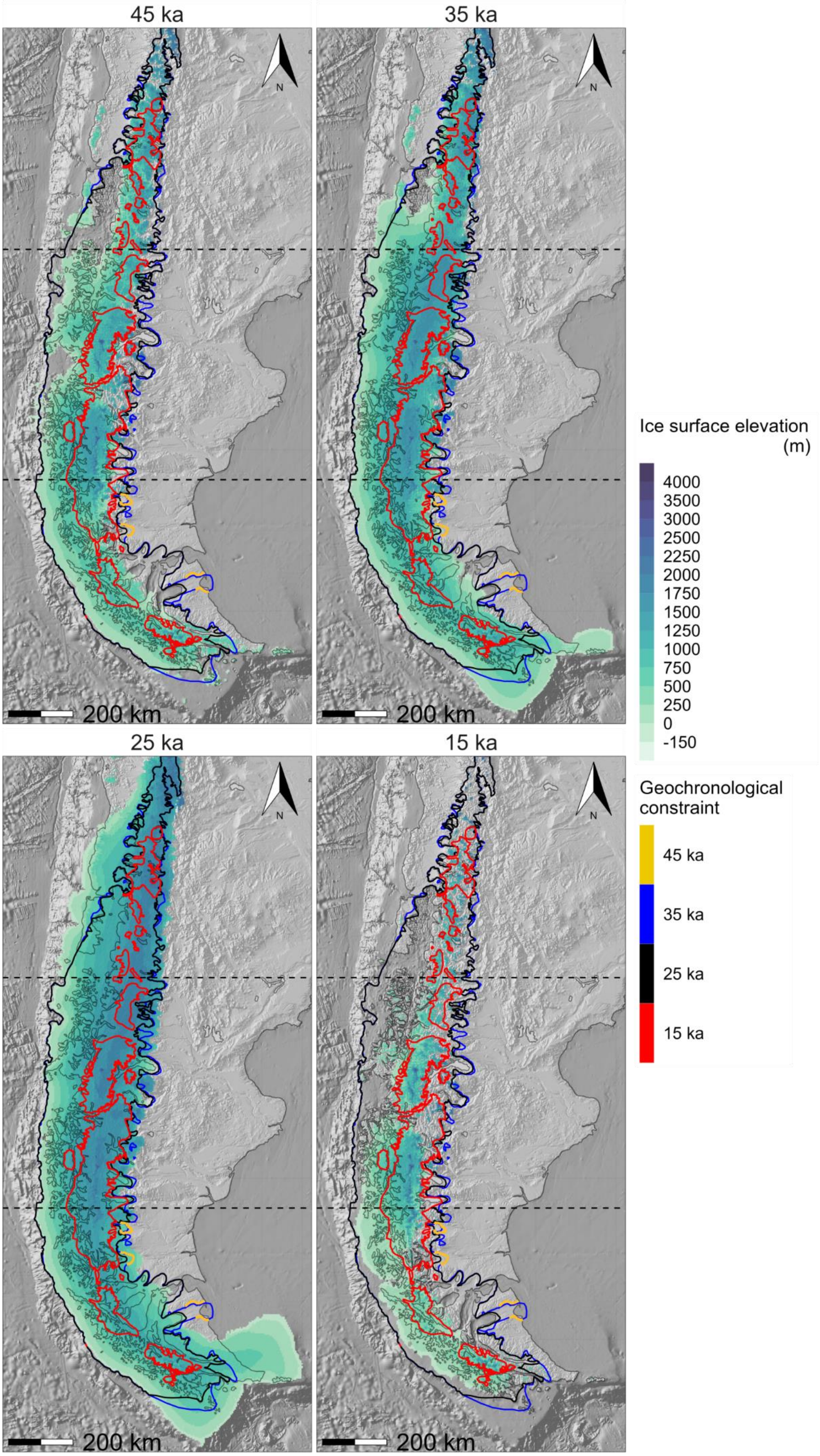

Model #21: 'Northern expansion' T0.85/Pp1.2

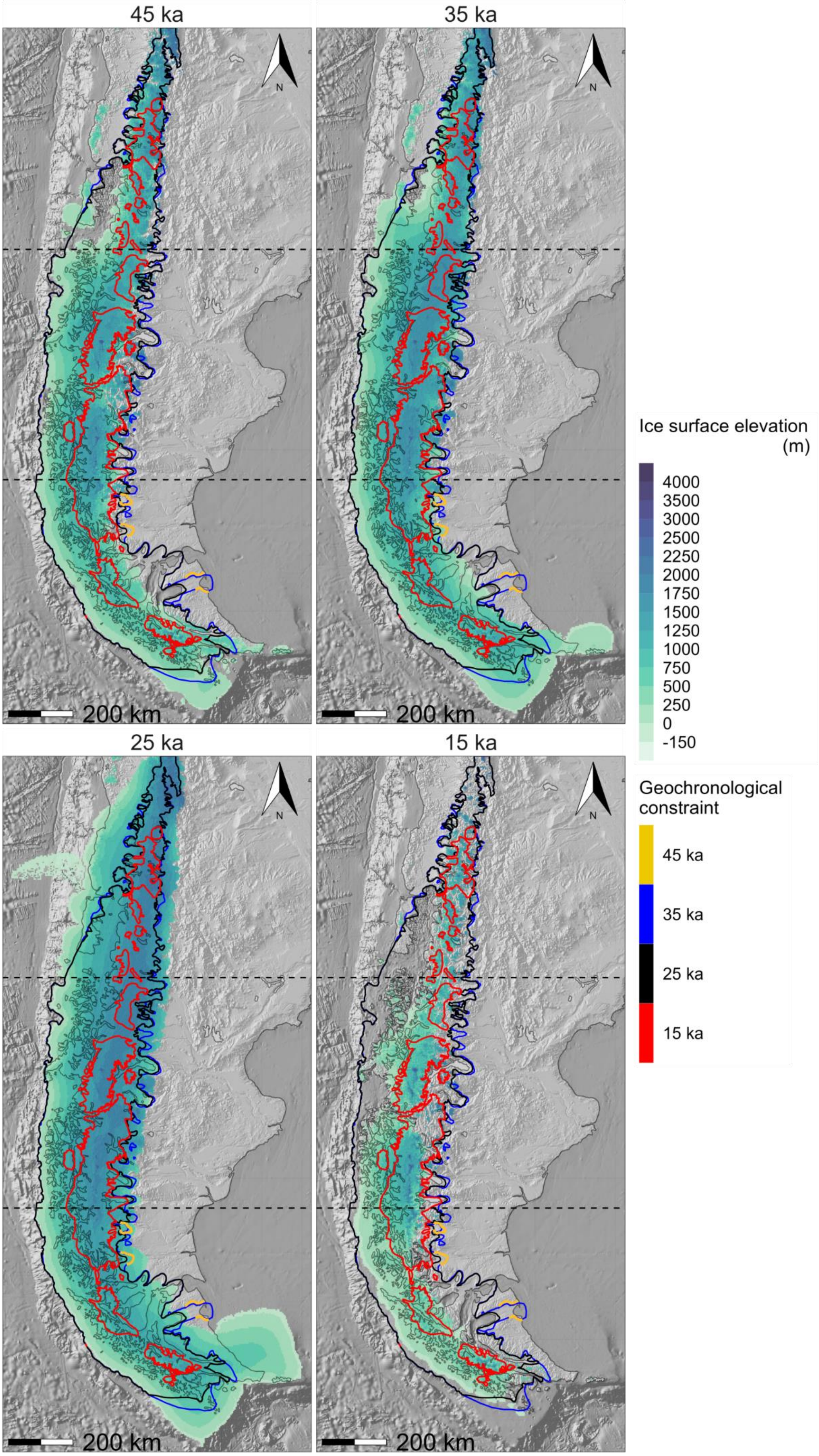

Model #22: 'Northern expansion' T0.75/Pp0.8

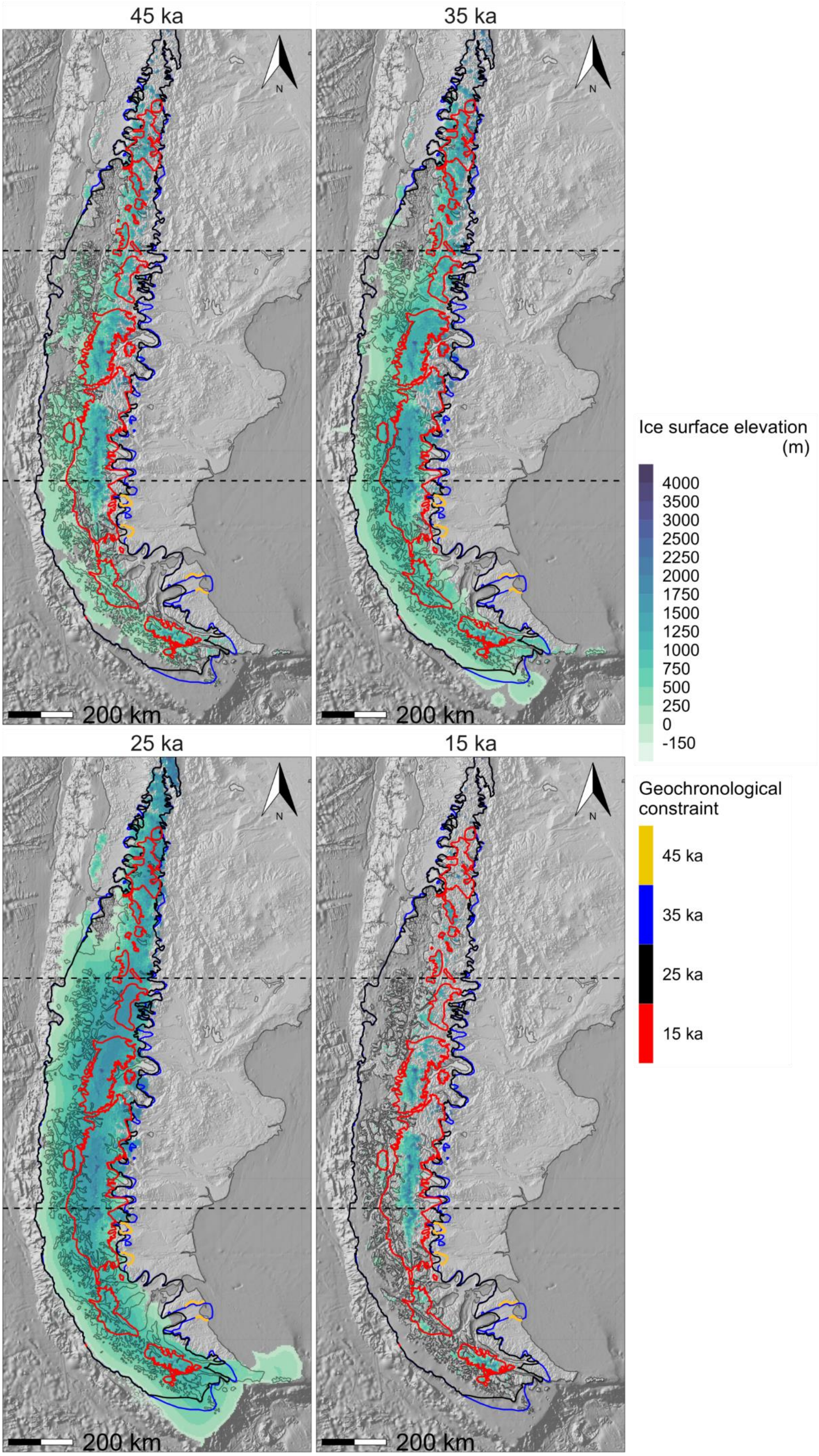

Model #23: 'Northern expansion' T0.75/Pp1.0

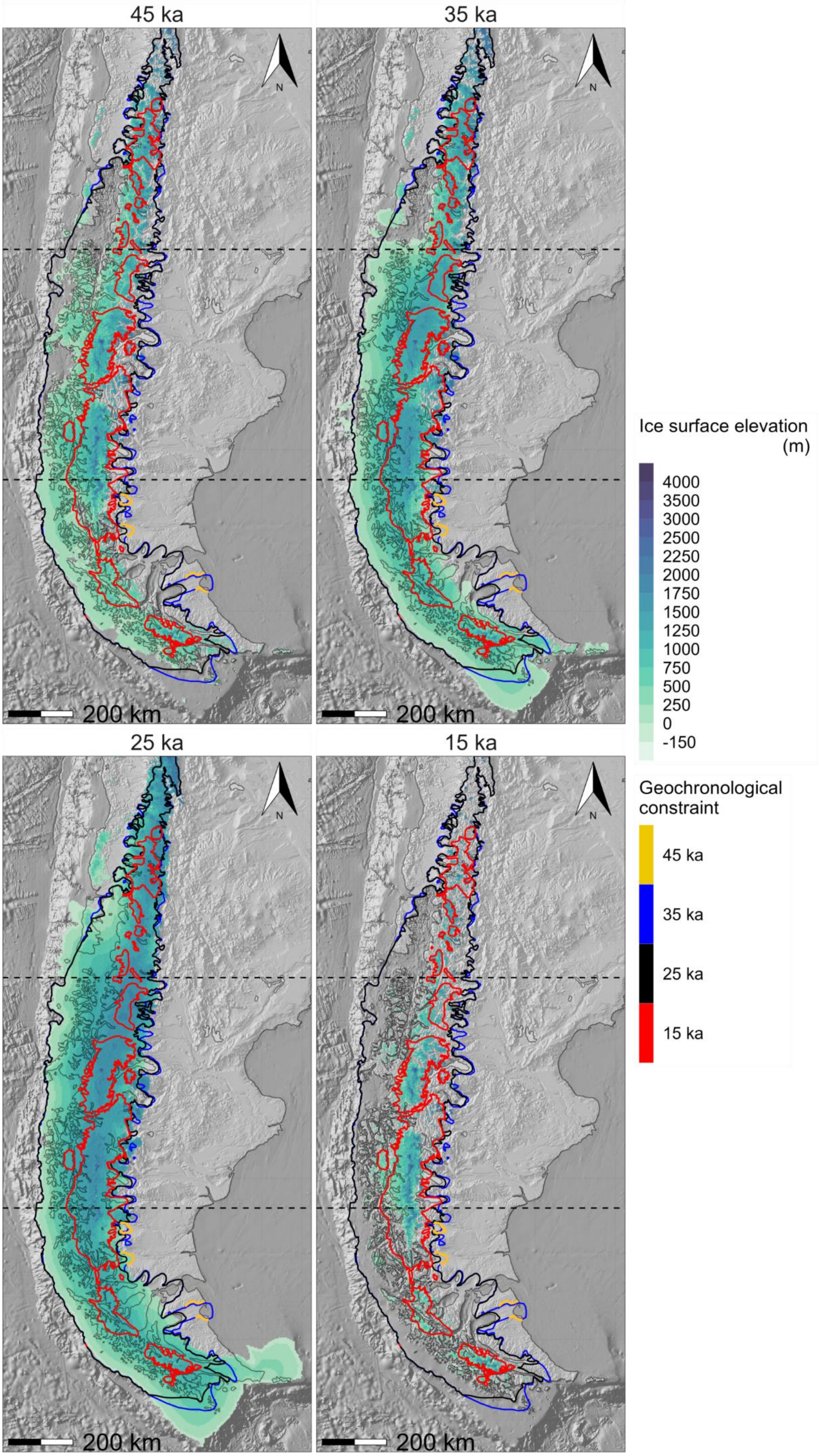

Model #24: 'Northern expansion' T0.75/Pp1.2

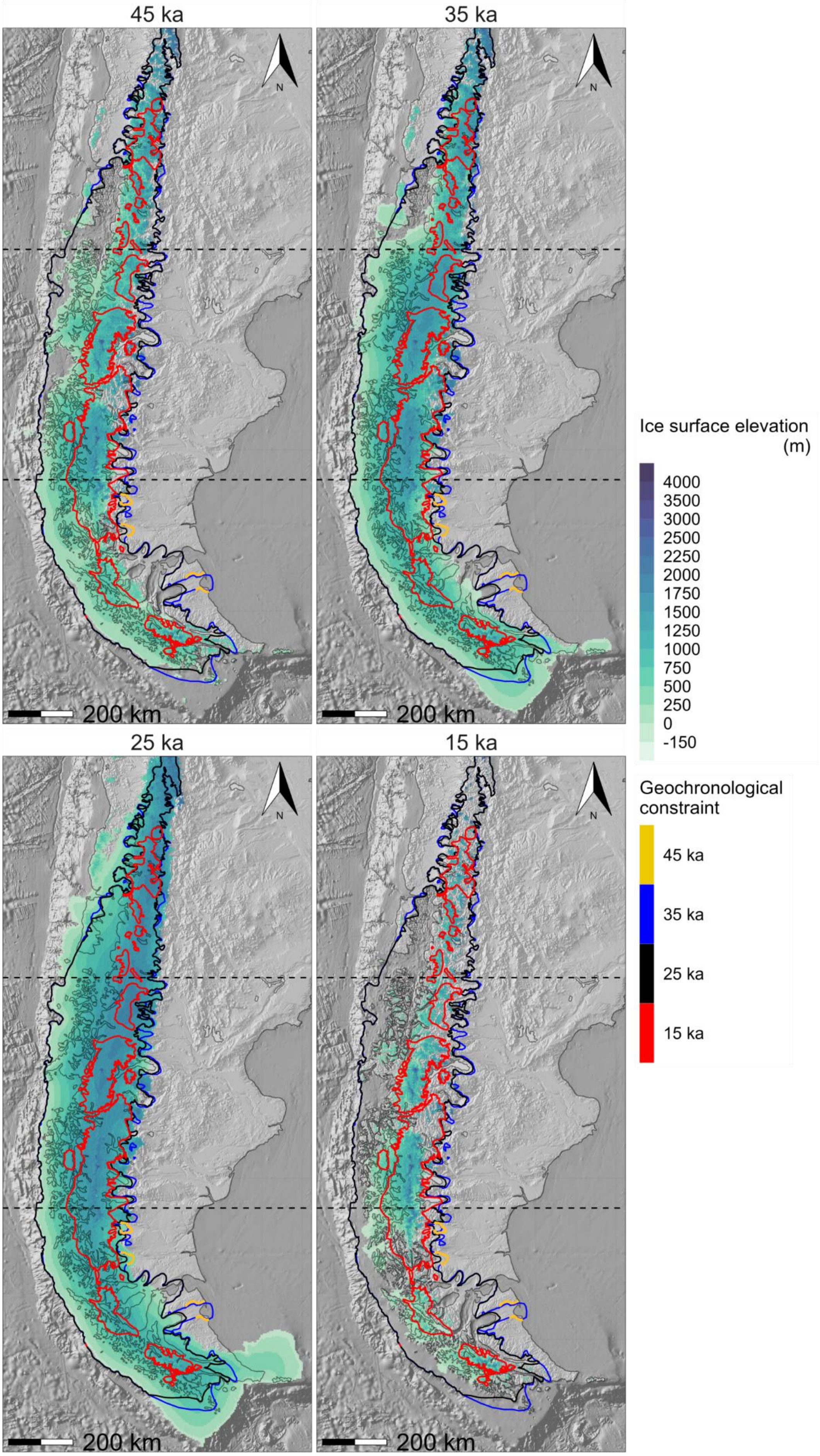

Model #25: 'Northern expansion' T0.65/Pp0.8

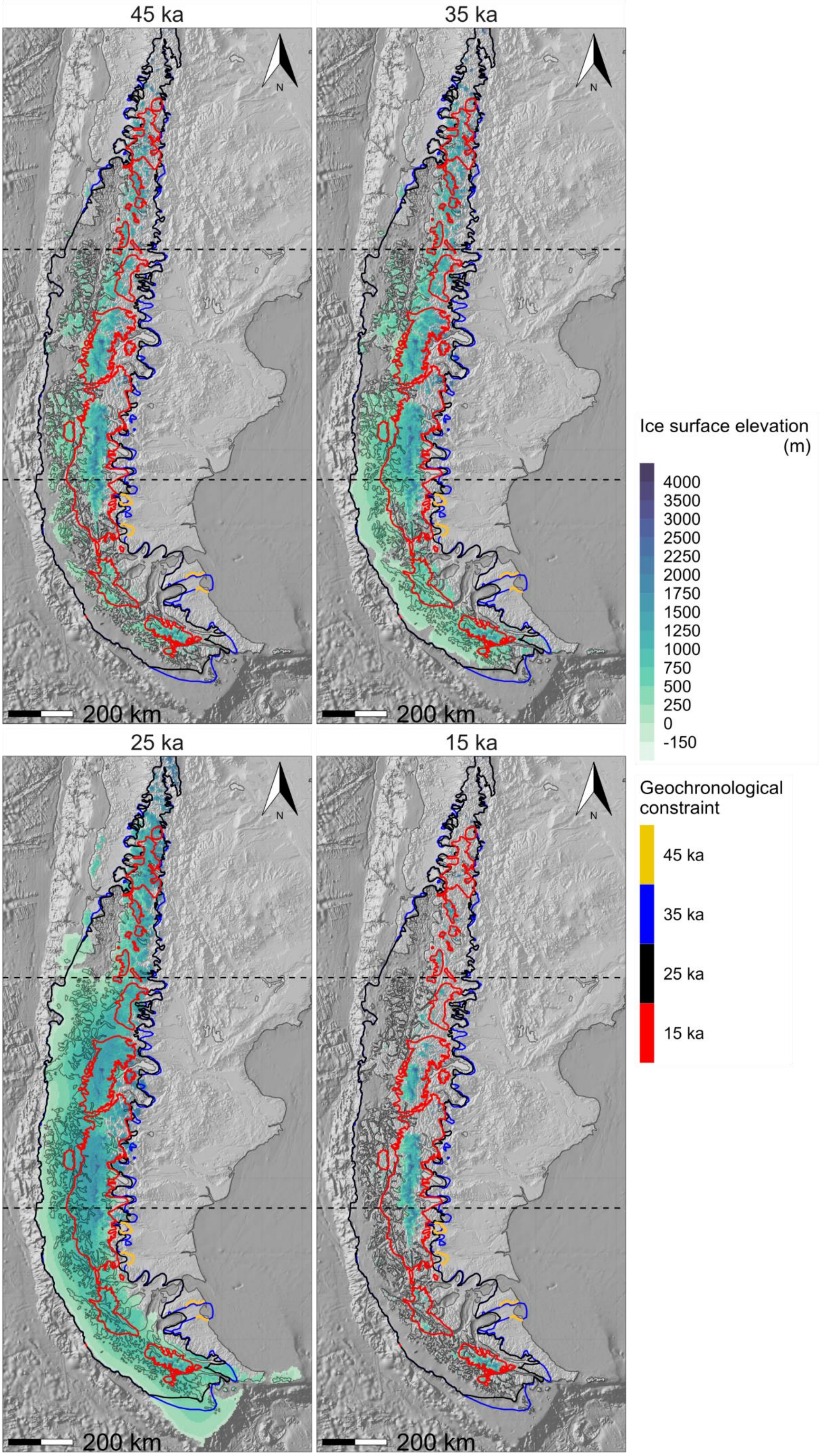

Model #26: 'Northern expansion' T0.65/Pp1.0

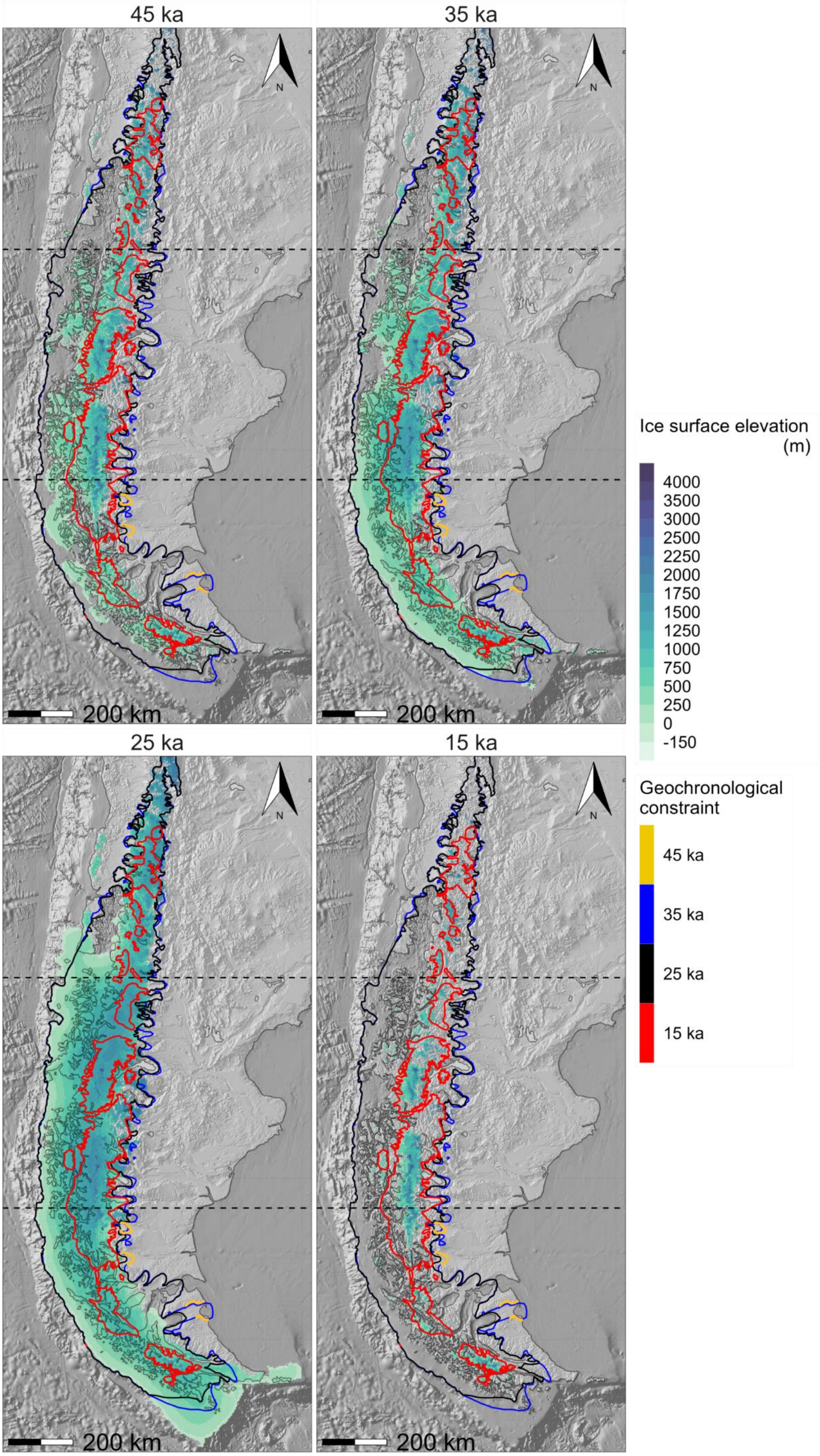

Model #27: 'Northern expansion' T0.65/Pp1.2

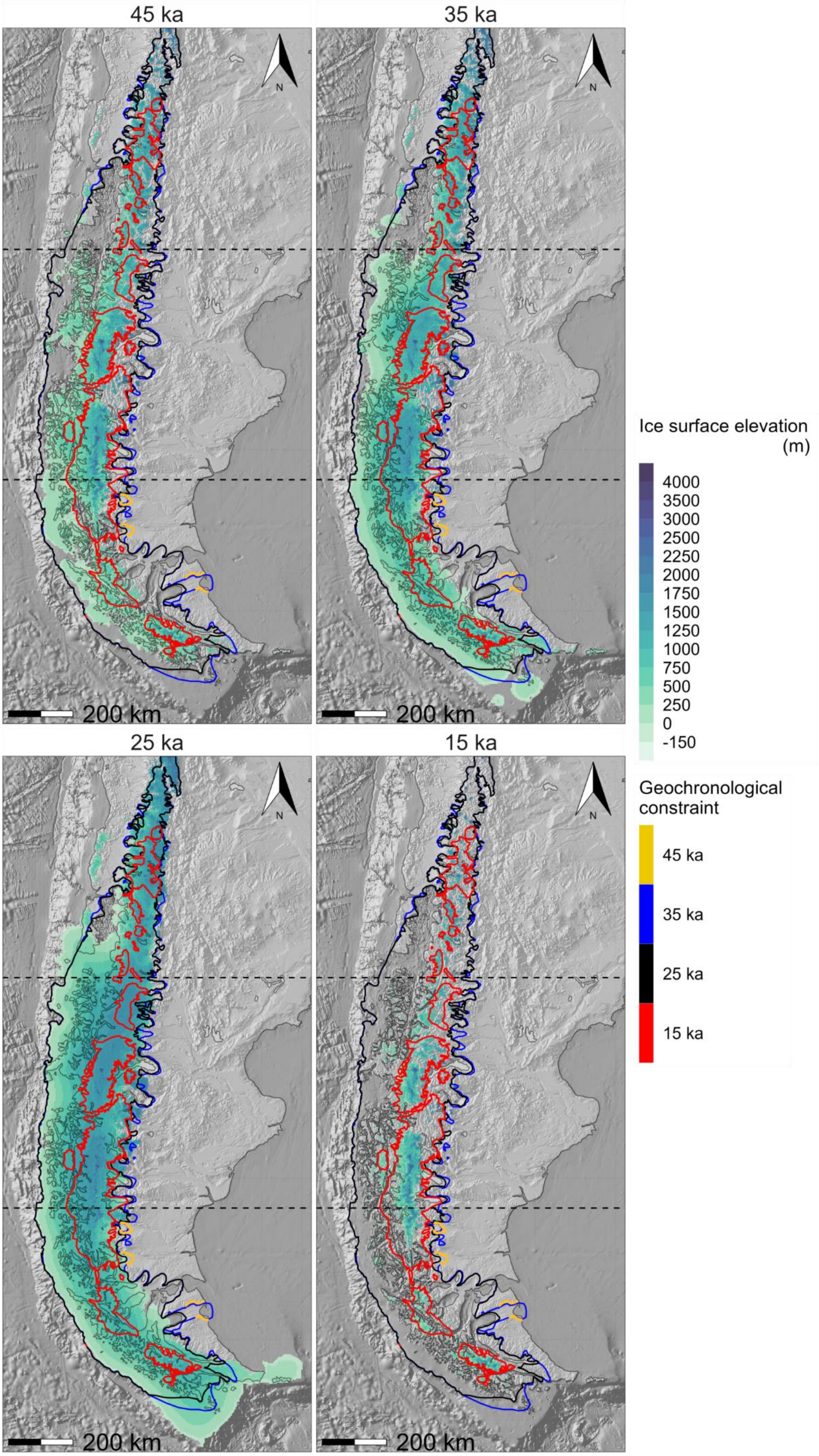

Model #28: 'Central migration' T0.85/Pp0.8

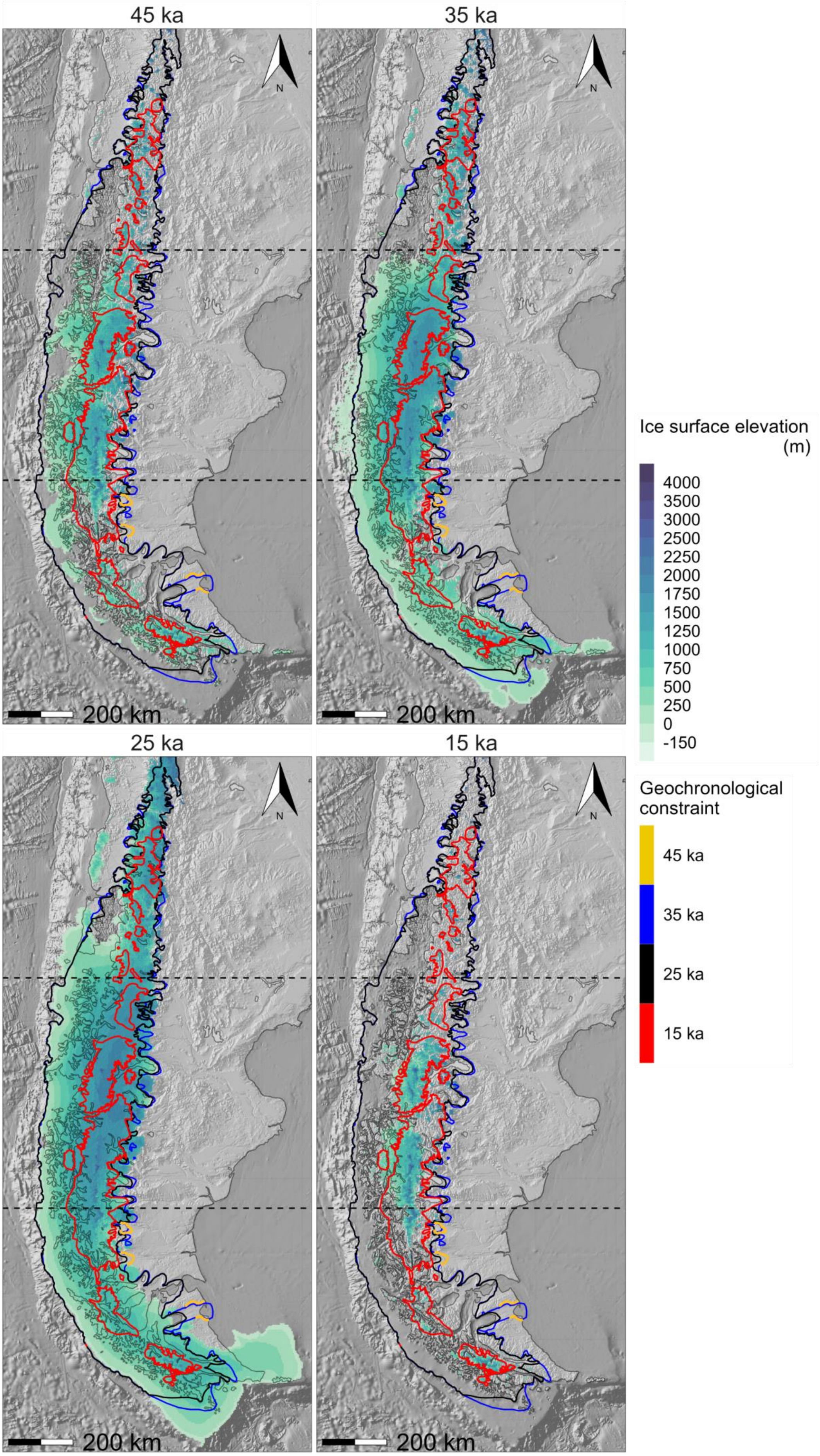

Model #29: 'Central migration' T0.85/Pp1.0

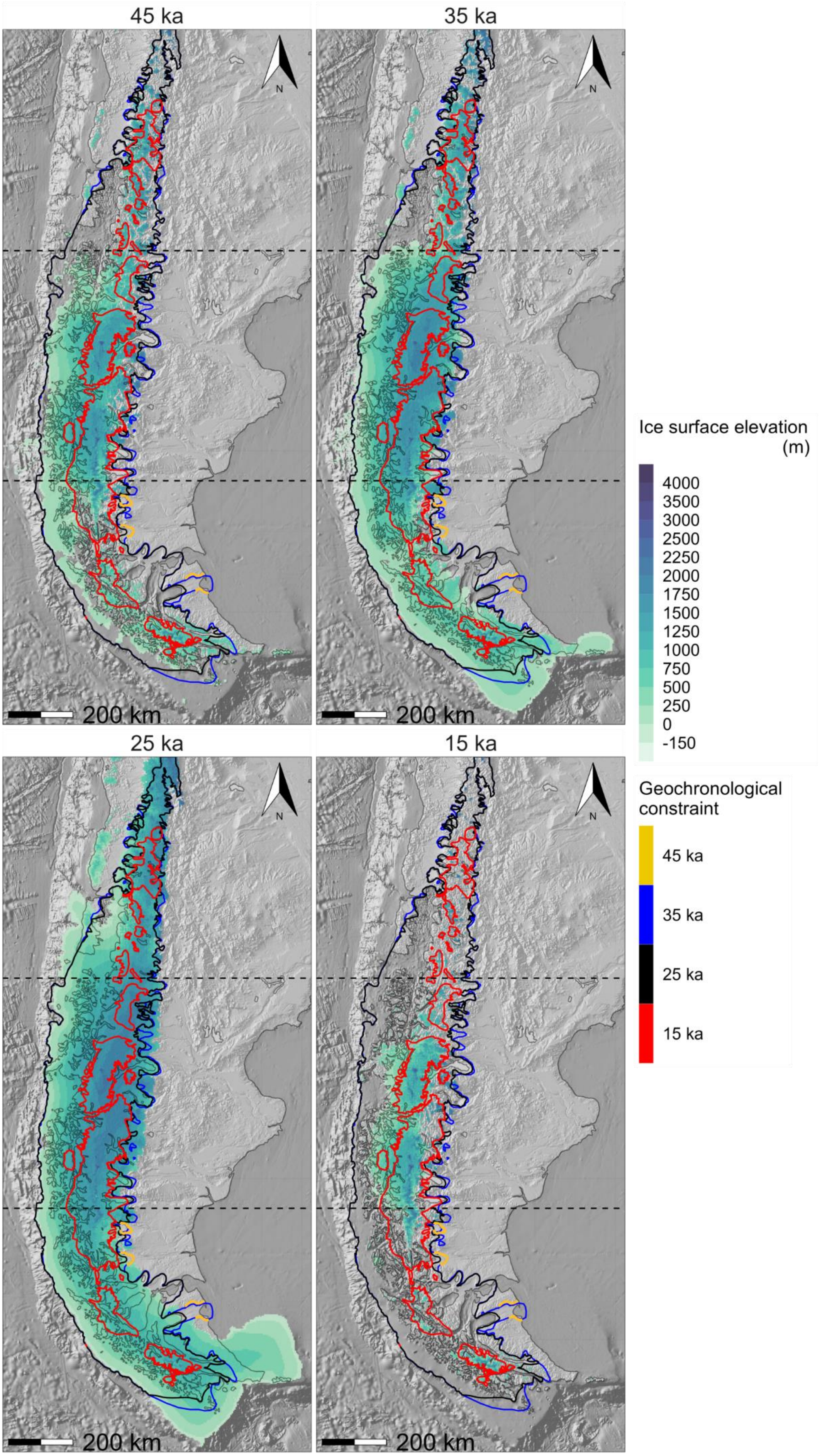

Model #30: 'Central migration' T0.85/Pp1.2

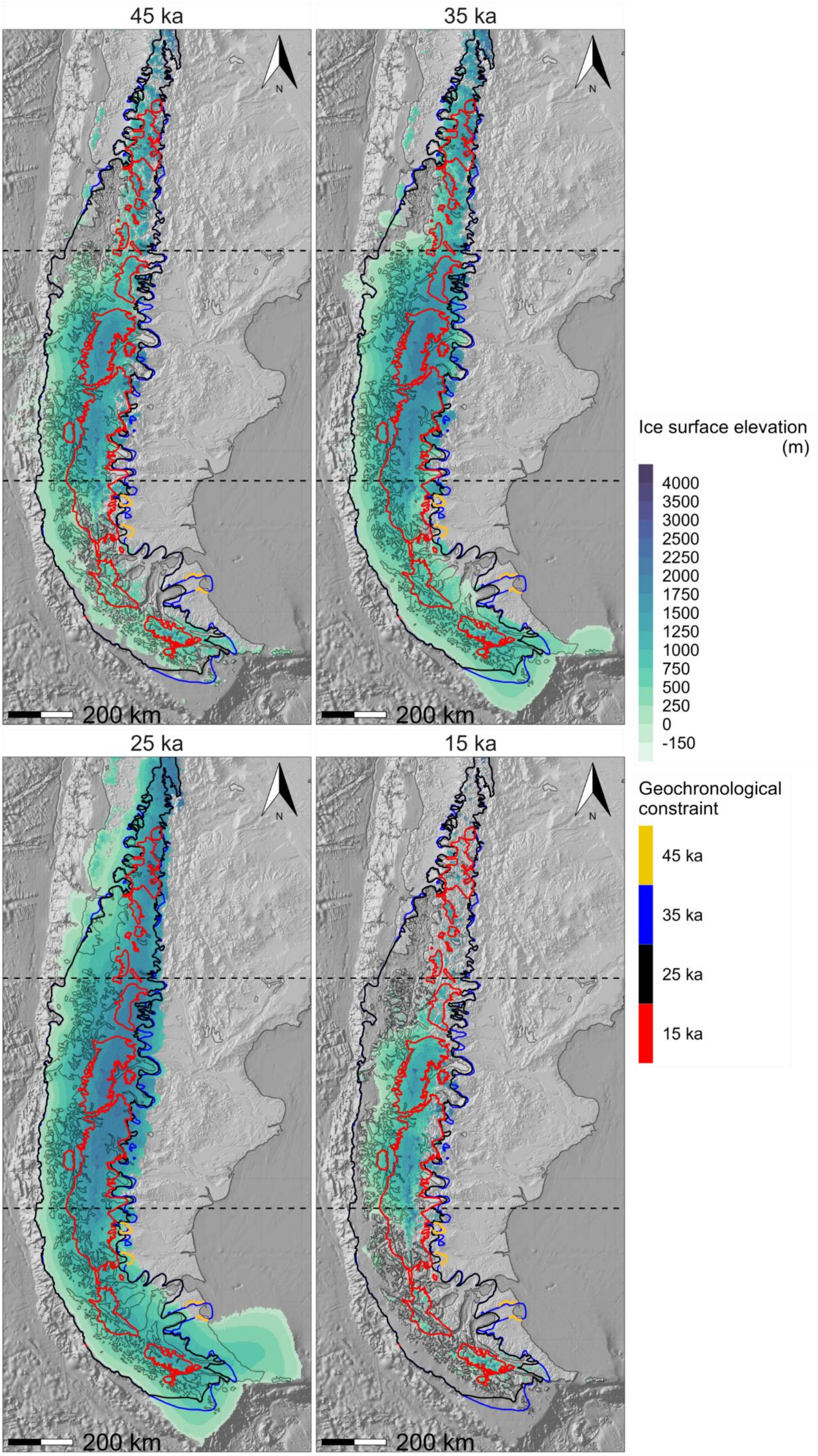

Model #31: 'Central migration' T0.75/Pp0.8

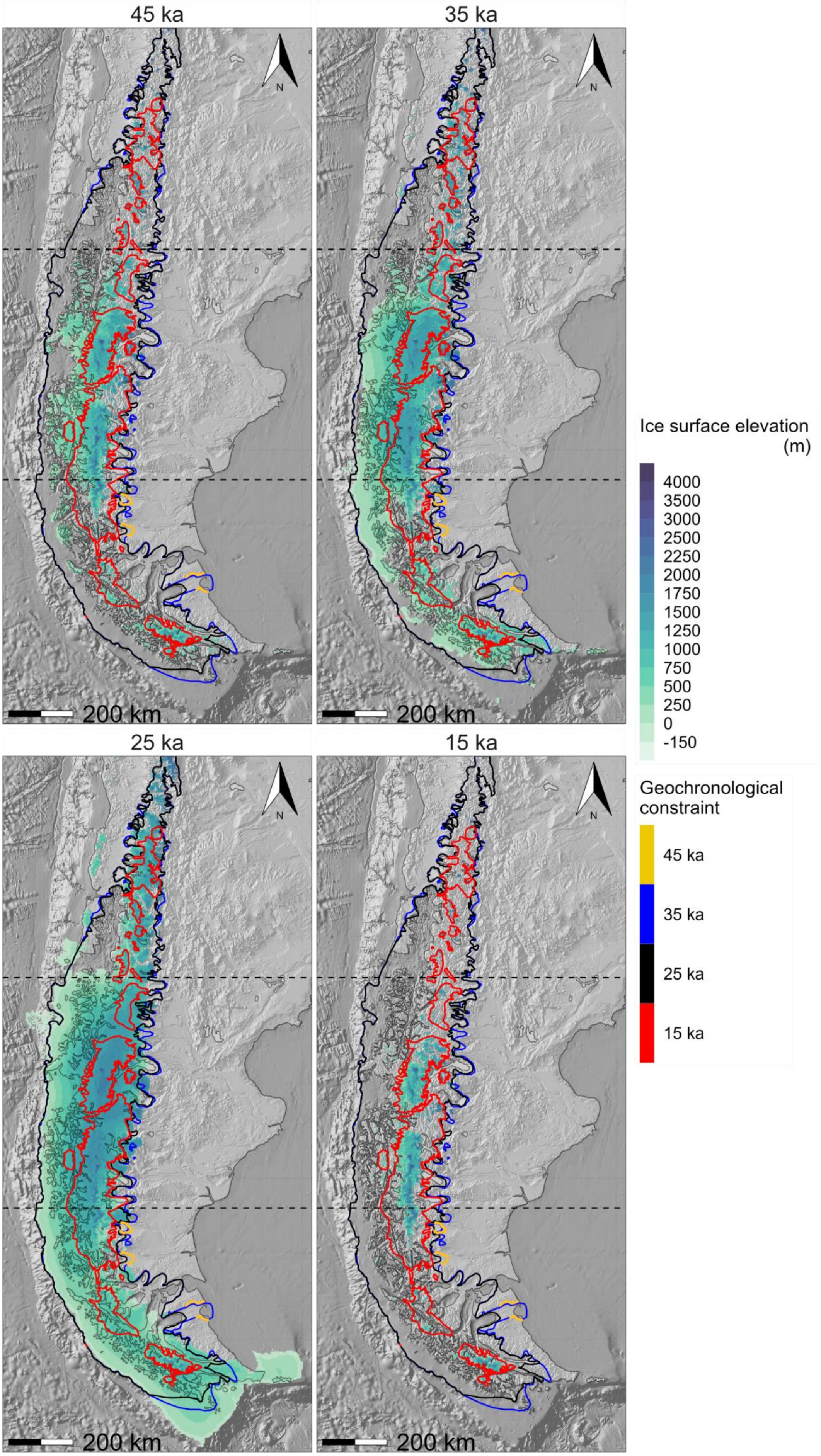

Model #32: 'Central migration' T0.75/Pp1.0

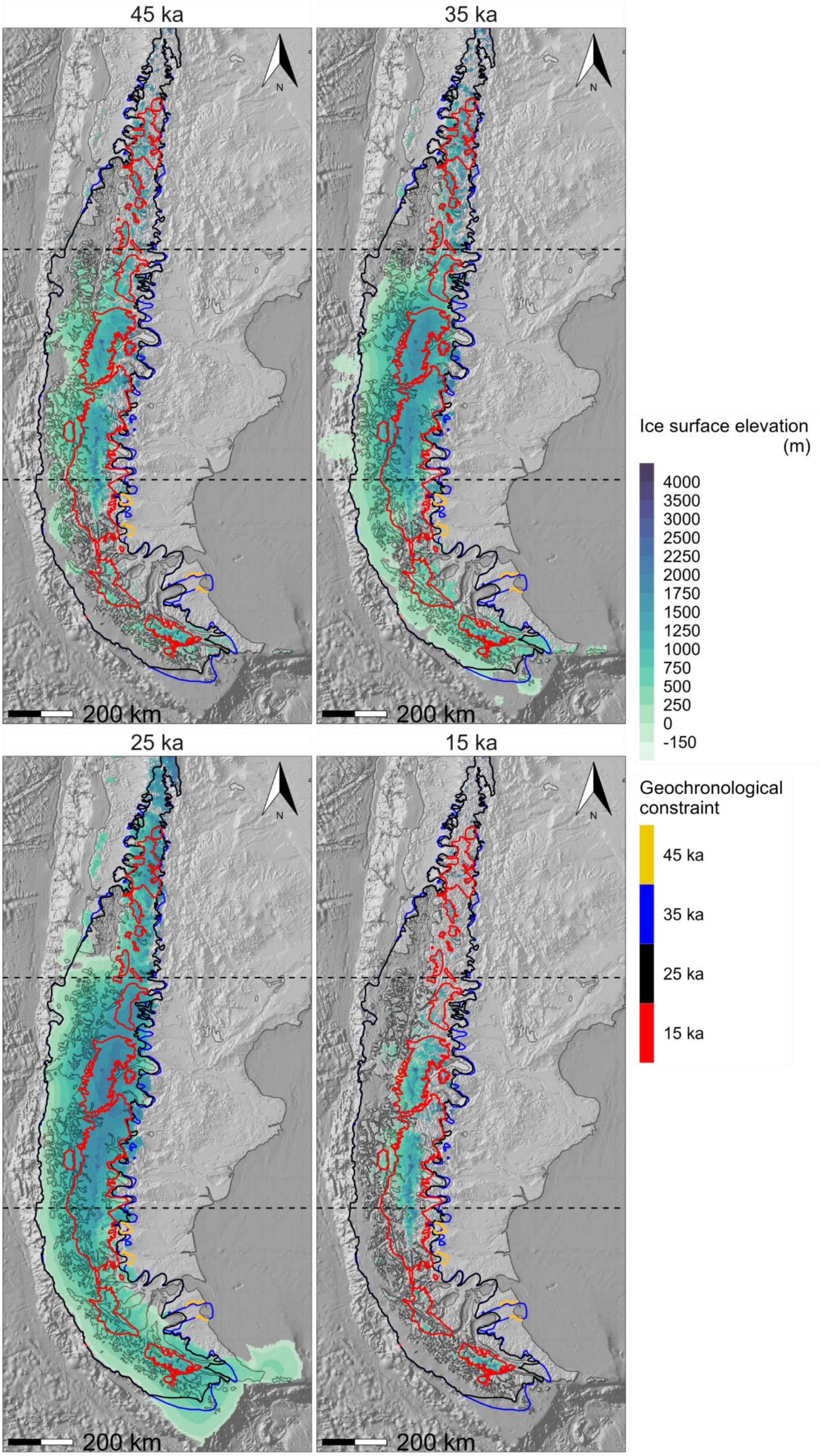

Model #33: 'Central migration' T0.75/Pp1.2

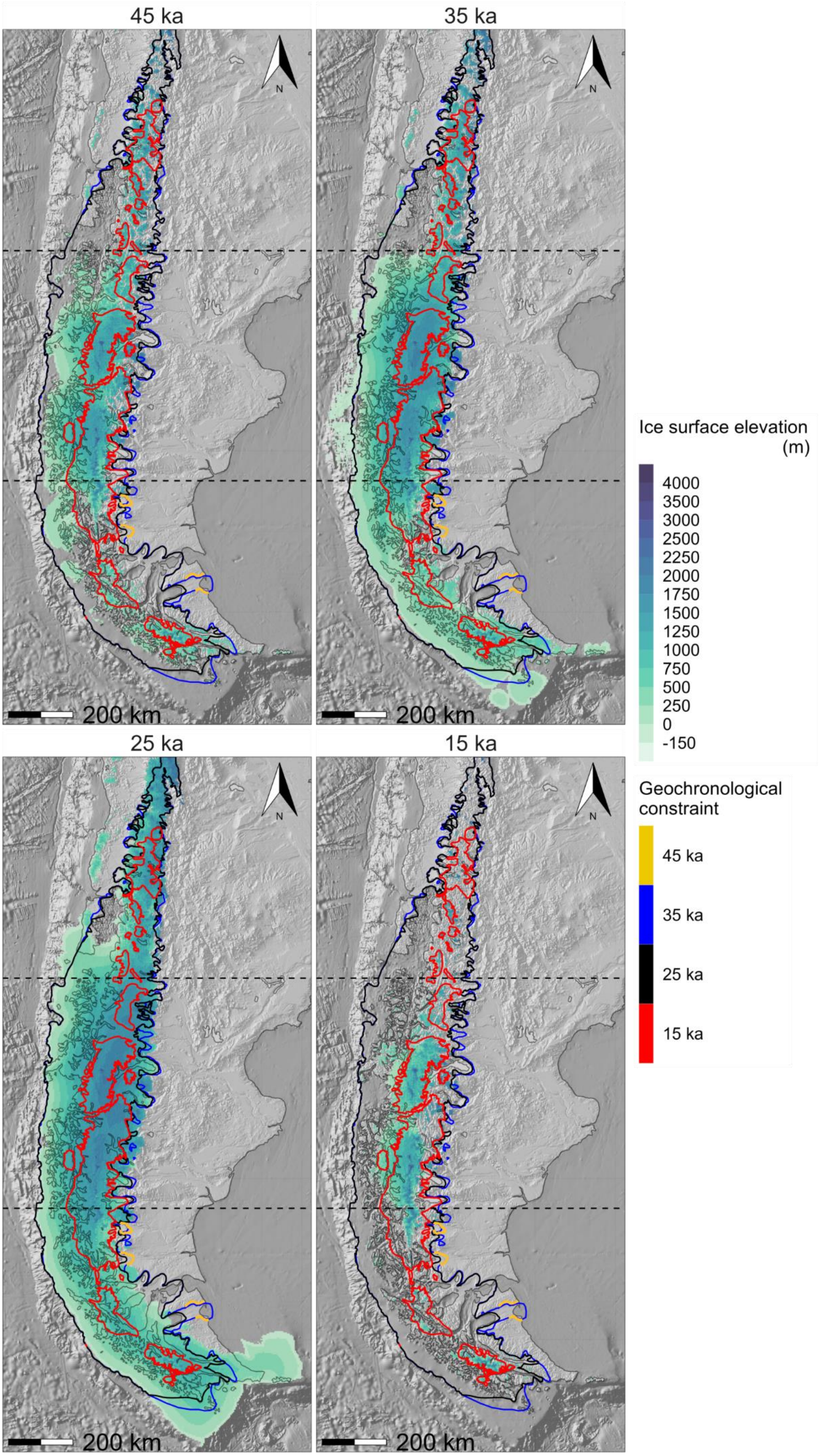

Model #34: 'Central migration' T0.65/Pp0.8

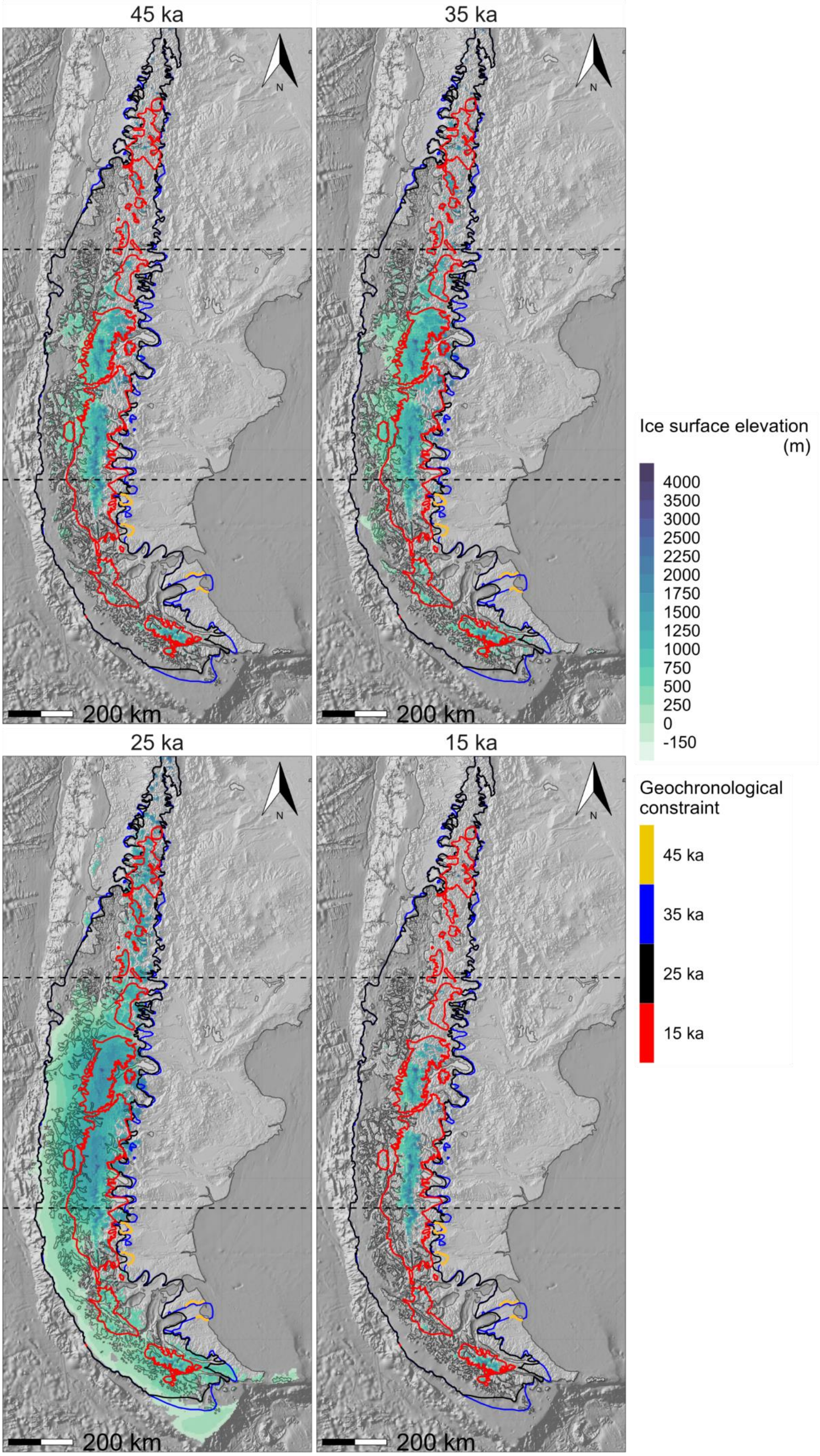

Model #35: 'Central migration' T0.65/Pp1.0

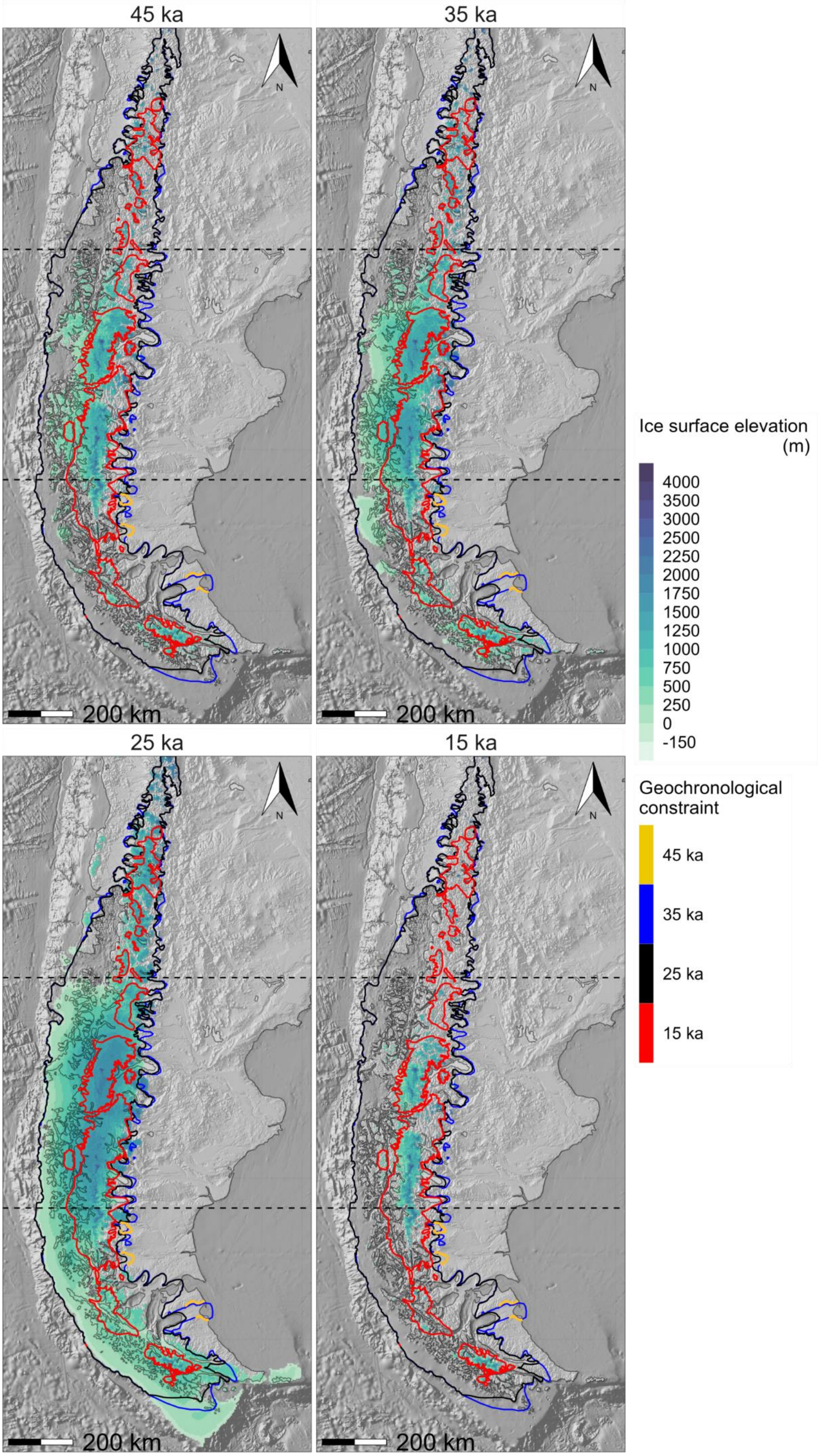

Model #36: 'Central migration' T0.65/Pp1.2

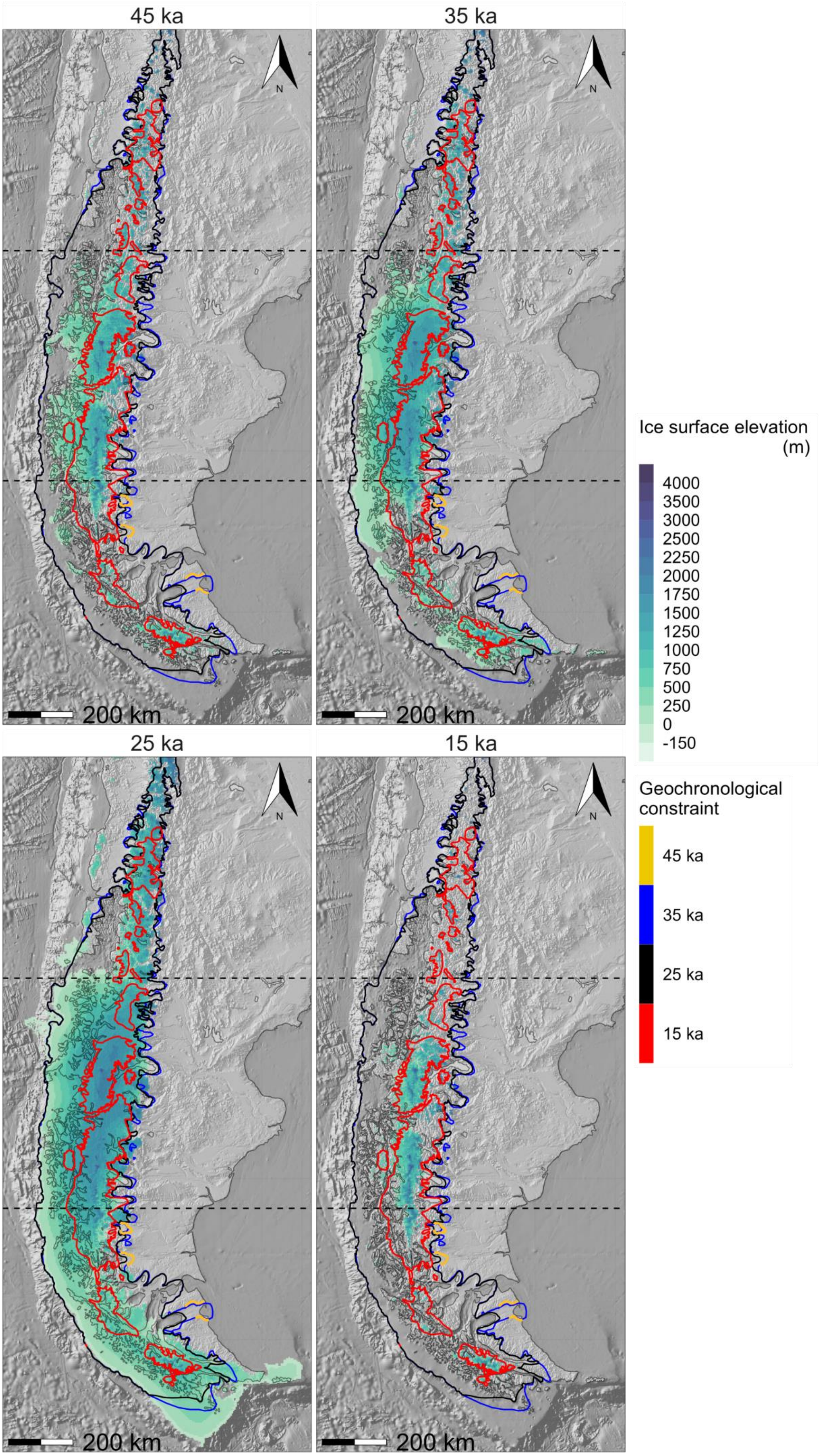

Model #37: 'Central expansion' T0.85/Pp0.8

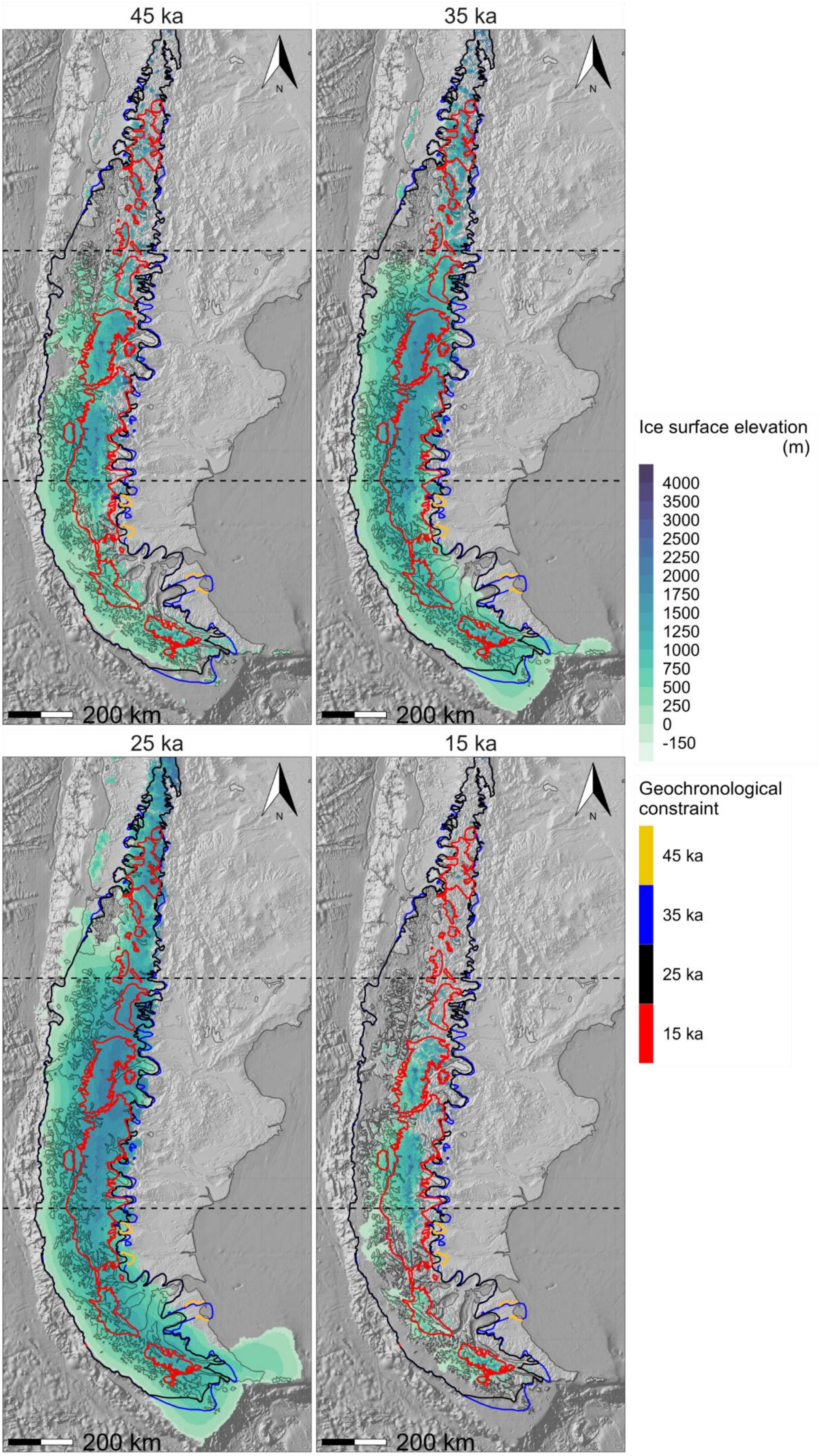

Model #38: 'Central expansion' T0.85/Pp1.0

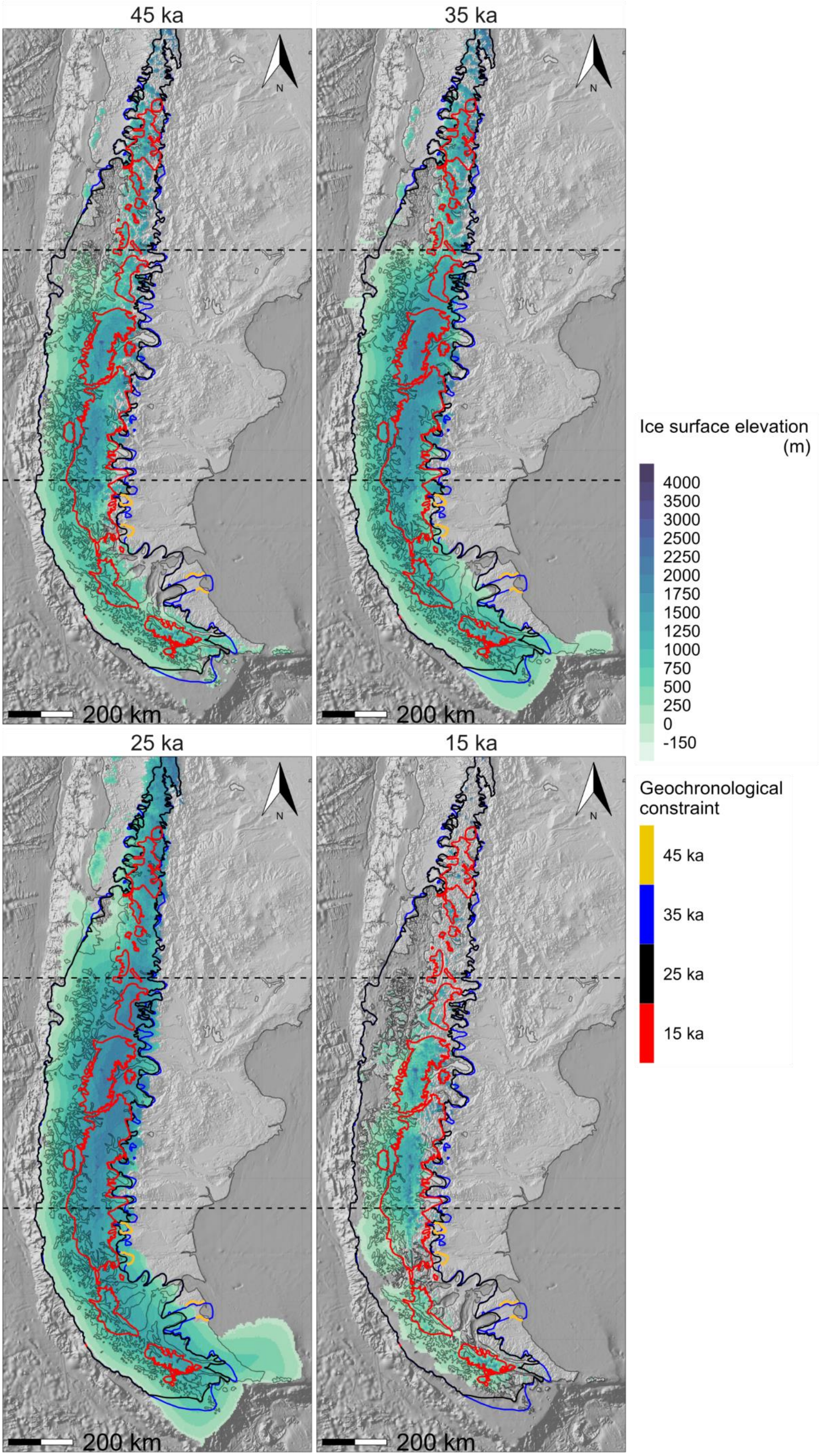

Model #39: 'Central expansion' T0.85/Pp1.2

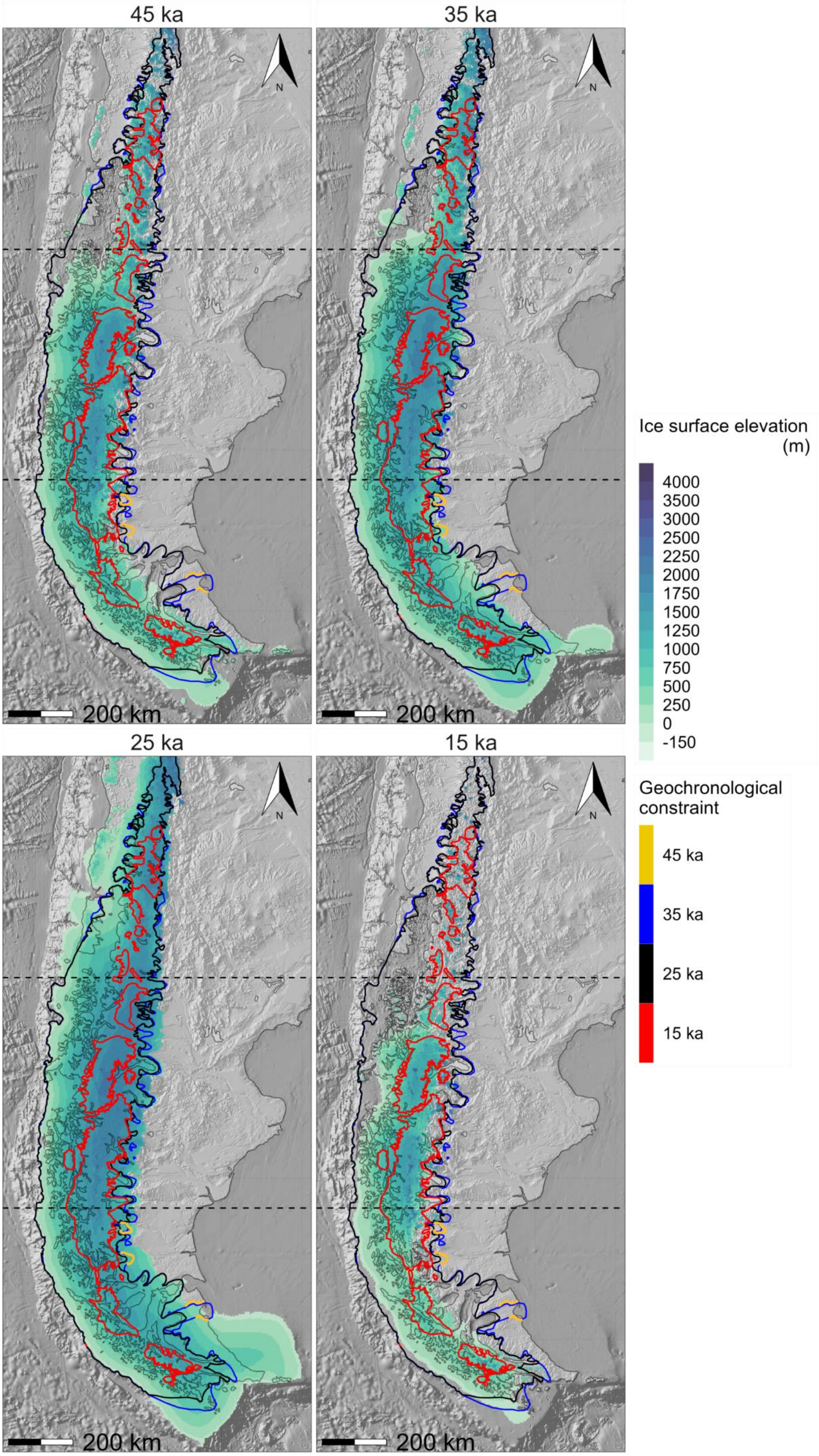

Model #40: 'Central expansion' T0.75/Pp0.8

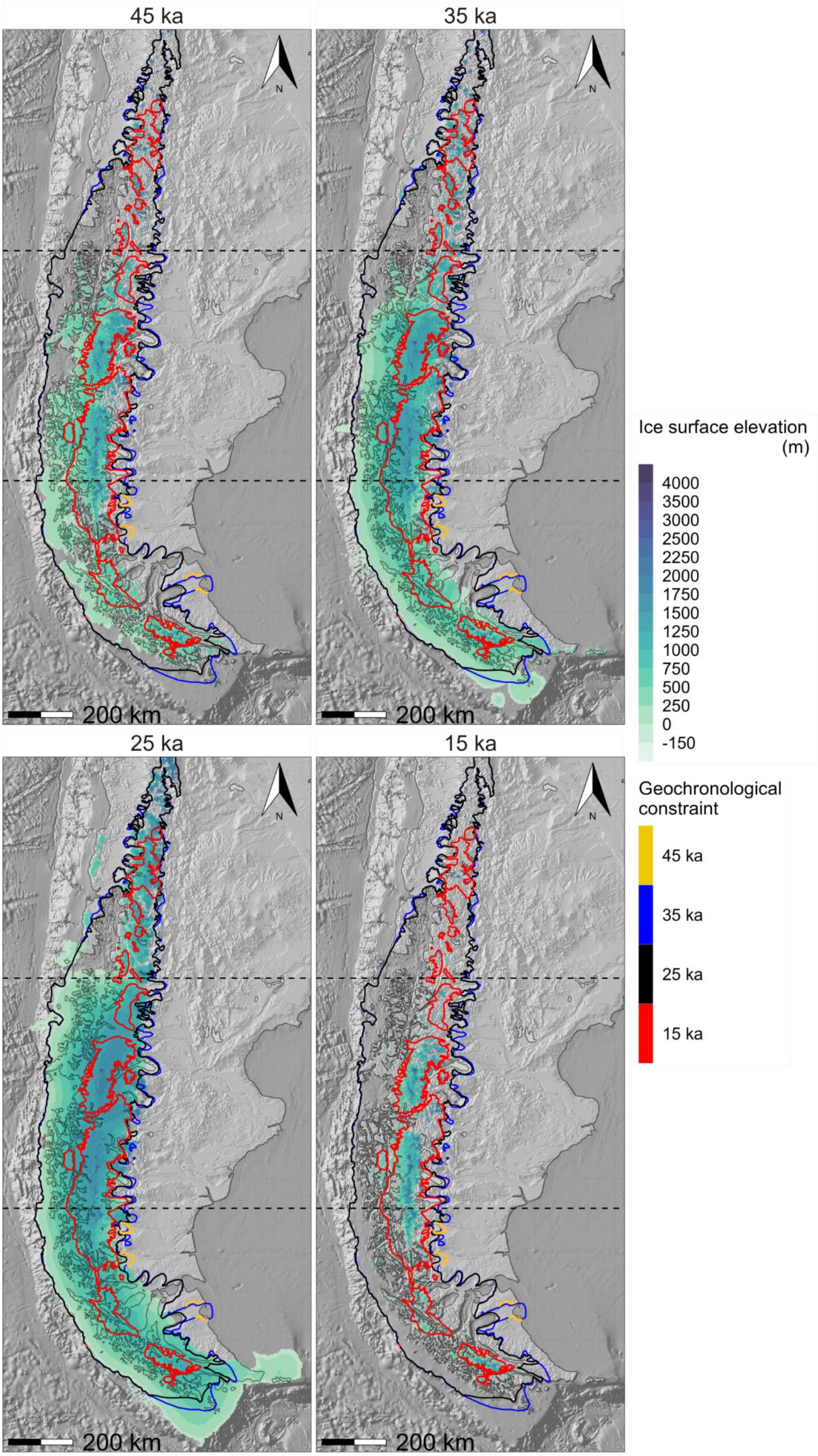

Model #41: 'Central expansion' T0.75/Pp1.0

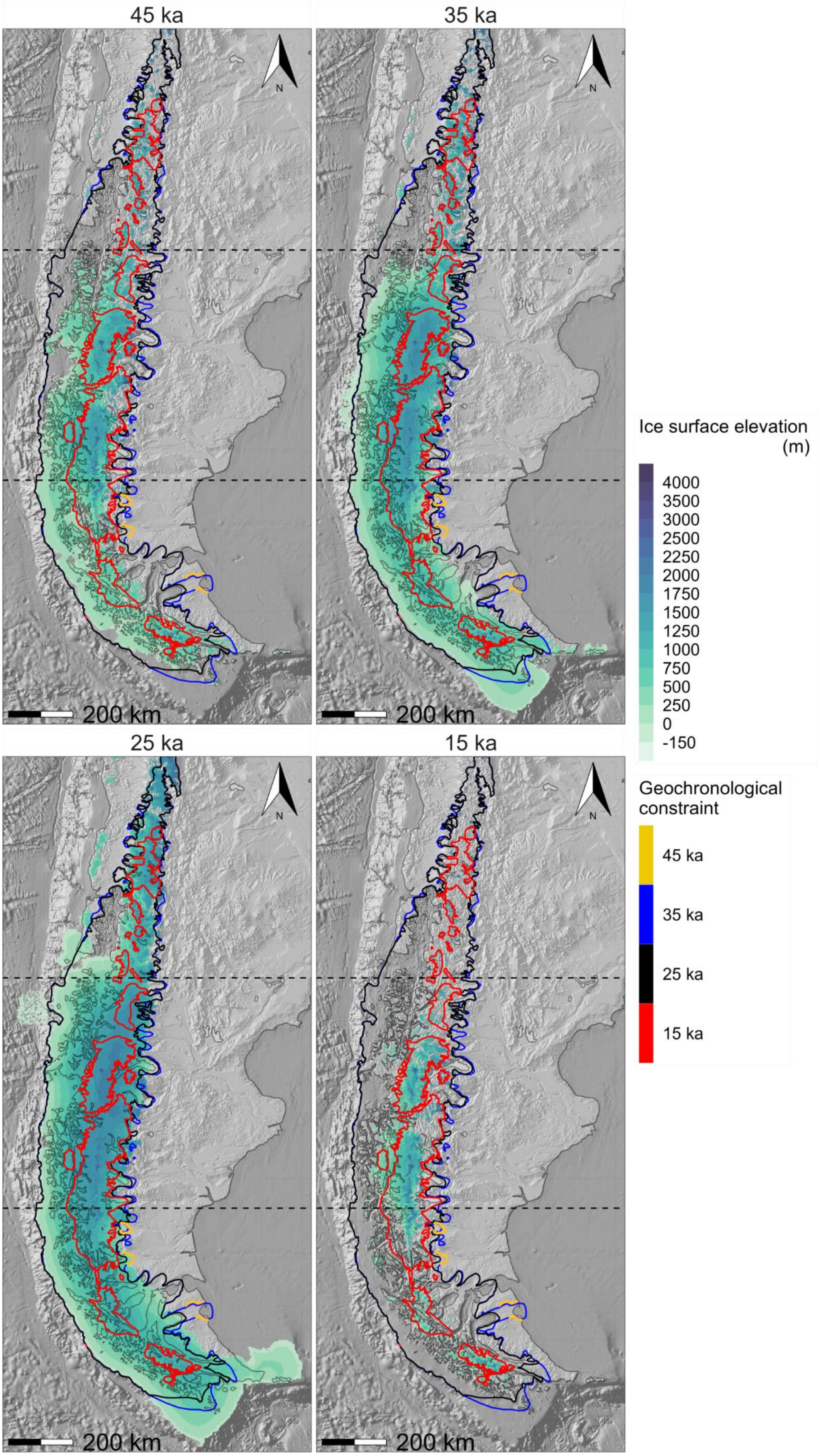

Model #42: 'Central expansion' T0.75/Pp1.2

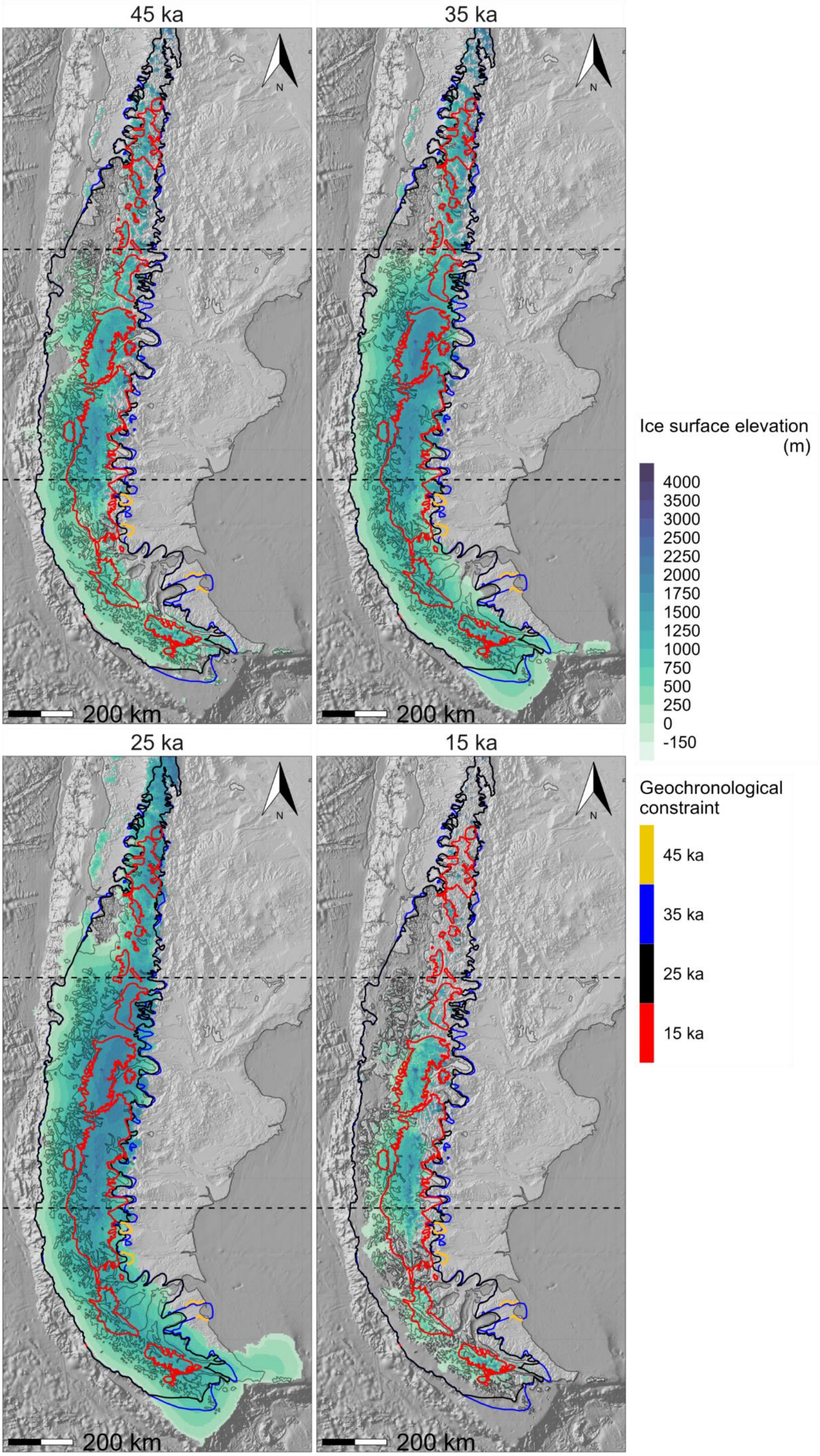
45 ka

35 ka

25 ka

15 ka

Model #43:   'Central expansion'   T0.65/Pp0.8

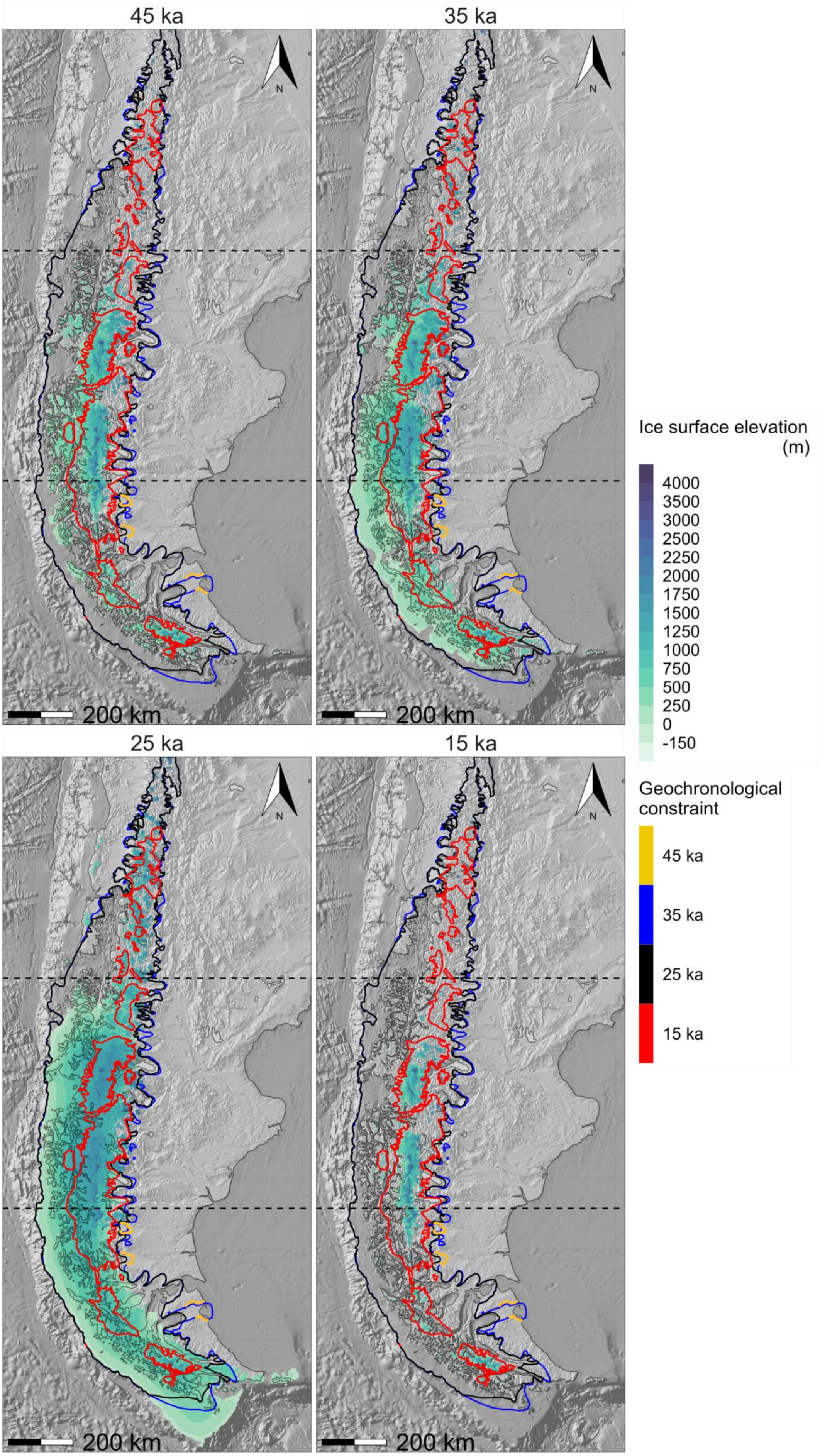

Model #44: 'Central expansion' T0.65/Pp1.0

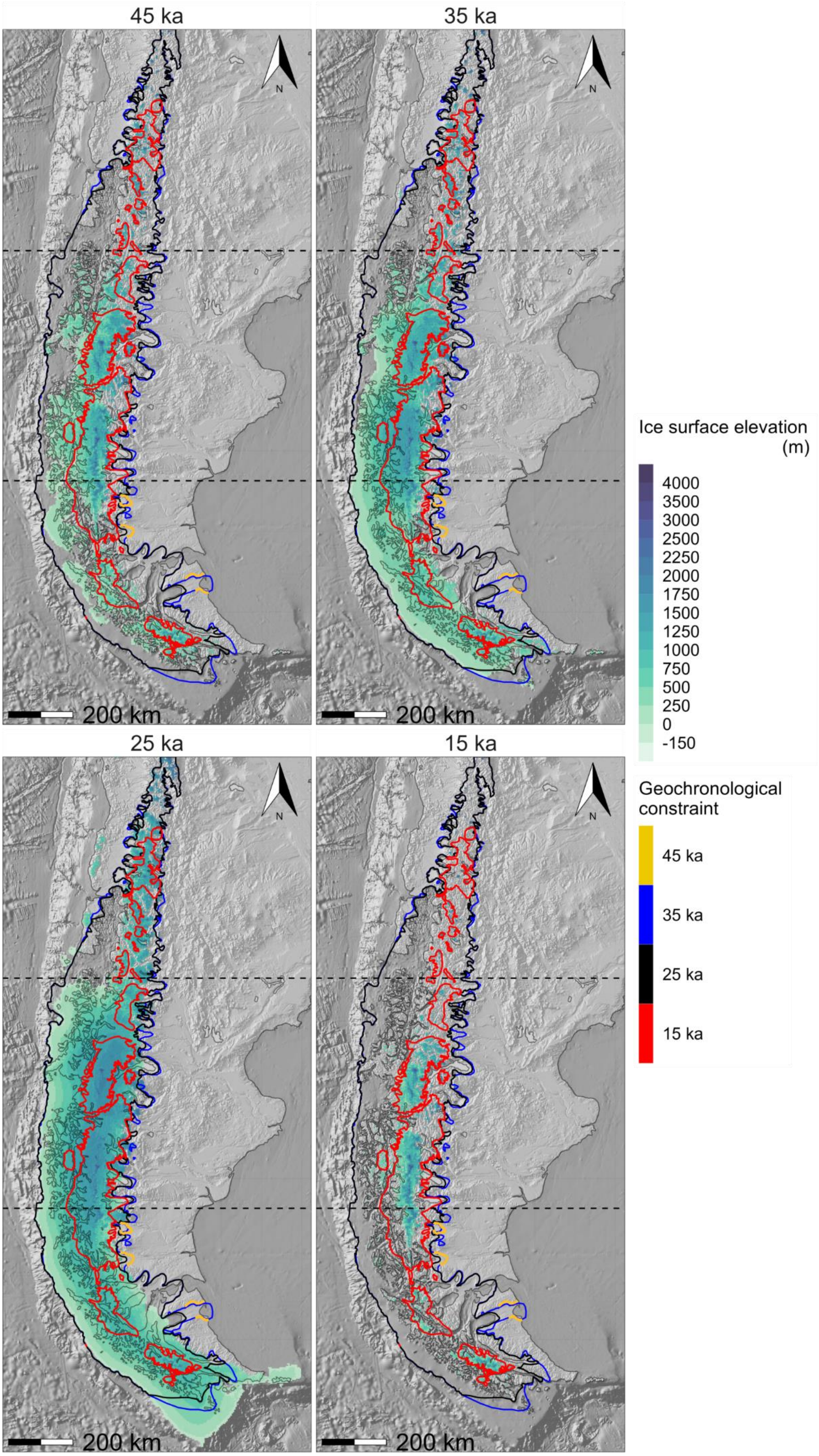

Model #45: 'Central expansion' T0.65/Pp1.2

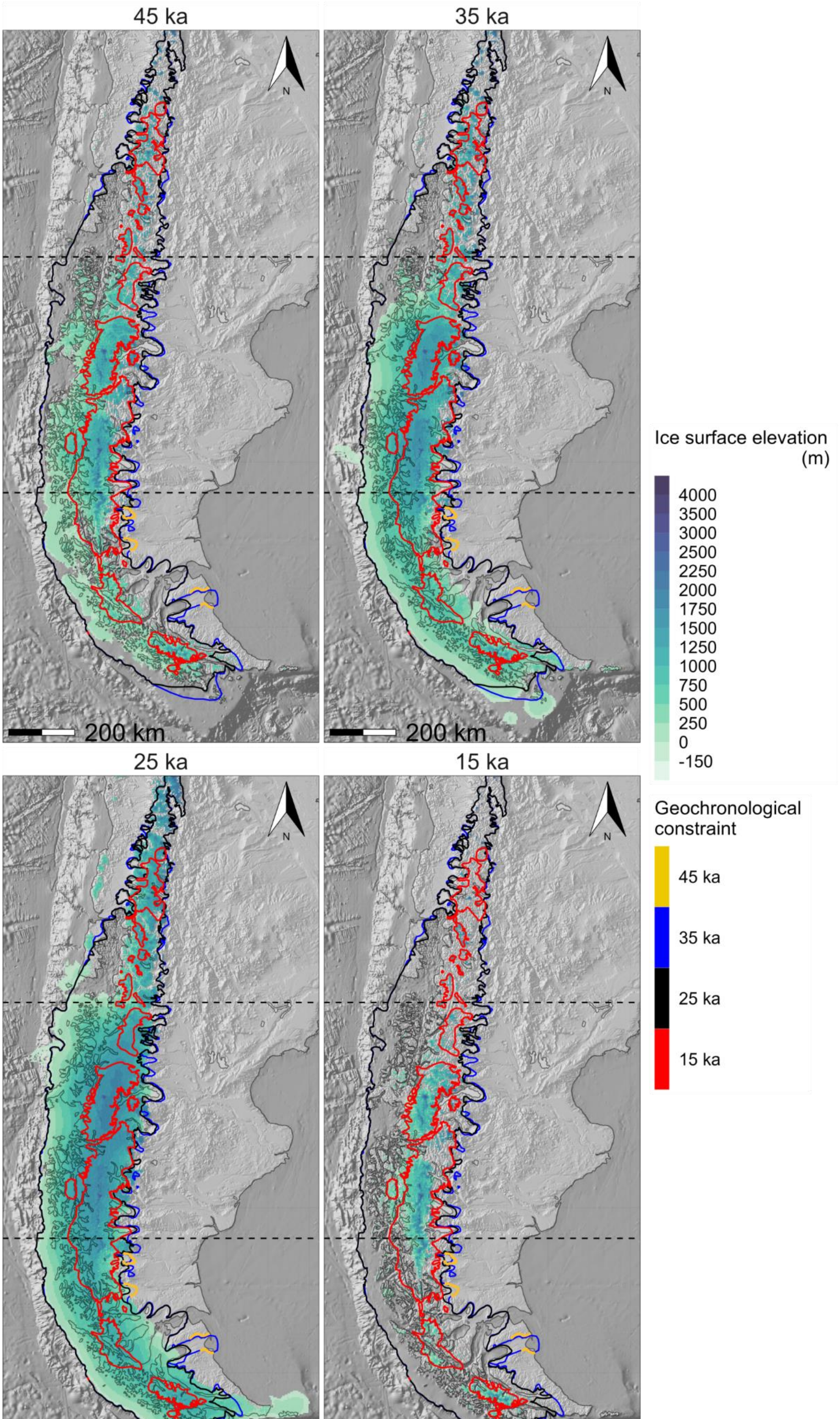

References

Albrecht, T., Winkelmann, R., & Levermann, A. (2020). Glacial-cycle simulations of the Antarctic Ice Sheet with the Parallel Ice Sheet Model (PISM)–Part 1: Boundary conditions and climatic forcing. *The Cryosphere*, *14*(2), 599-632.

Anderson, R., Ali, S., Bradtmiller, L., Nielsen, S., Fleisher, M., Anderson, B., & Burckle, L. (2009). Wind-driven upwelling in the Southern Ocean and the deglacial rise in atmospheric CO2. *science*, *323*(5920), 1443-1448.

Anderson, R. S., Dühnforth, M., Colgan, W., & Anderson, L. (2012). Far-flung moraines: Exploring the feedback of glacial erosion on the evolution of glacier length. *Geomorphology*, *179*, 269-285.

Ariztegui, D., Bianchi, M. M., Masaferro, J., Lafargue, E., & Niessen, F. (1997). Interhemispheric synchrony of Late-glacial climatic instability as recorded in proglacial Lake Mascardi, Argentina. *Journal of Quaternary Science: Published for the Quaternary Research Association*, *12*(4), 333-338.

Aschwanden, A., Aðalgeirsdóttir, G., & Khroulev, C. (2013). Hindcasting to measure ice sheet model sensitivity to initial states. *The Cryosphere*, *7*(4), 1083-1093.

Balco, G., Stone, J. O., Lifton, N. A., & Dunai, T. J. (2008). A complete and easily accessible means of calculating surface exposure ages or erosion rates from 10Be and 26Al measurements. *Quaternary Geochronology*, *3*(3), 174-195.

Balescu, S., & Lamothe, M. (1993). Thermoluminescence dating of the Holsteinian marine formation of Herzeele, northern France. *Journal of Quaternary Science*, *8*(2), 117-124.

Barr, I. D., & Lovell, H. (2014). A review of topographic controls on moraine distribution. *Geomorphology*, *226*, 44-64.

Barry, R. G., & Chorley, R. J. (2009). *Atmosphere, weather and climate*. Routledge.

Becker, P., Seguinot, J., Jouvet, G., & Funk, M. (2016). Last Glacial Maximum precipitation pattern in the Alps inferred from glacier modelling. *Geographica Helvetica*, *71*(3), 173-187.

Bell, W. (1980). Alpha dose attenuation in quartz grains for thermoluminescence dating. *Ancient Tl*, *12*(8), 4-8.

Bendle, J. M., Palmer, A. P., Thorndycraft, V. R., & Matthews, I. P. (2017). High-resolution chronology for deglaciation of the Patagonian Ice Sheet at Lago Buenos Aires (46.5 S) revealed through varve chronology and Bayesian age modelling. *Quaternary Science Reviews*, *177*, 314-339.

Benn, D. (1996). Subglacial and subaqueous processes near a glacier grounding line: sedimentological evidence from a former ice-dammed lake, Achnasheen Scotland. *Boreas*, *25*(1), 23-36.

Benn, D. I., & Clapperton, C. (2000a). Glacial sediment–landform associations and paleoclimate during the last glaciation, Strait of Magellan, Chile. *Quaternary Research*, *54*(1), 13-23.

Benn, D. I., & Clapperton, C. M. (2000b). Pleistocene glacitectonic landforms and sediments around central Magellan Strait, southernmost Chile: evidence for fast outlet glaciers with cold-based margins. *Quaternary Science Reviews*, *19*(6), 591-612.

Benn, D. I., Warren, C. R., & Mottram, R. H. (2007). Calving processes and the dynamics of calving glaciers. *Earth-Science Reviews*, *82*(3-4), 143-179.

Bennett, M. R., & Glasser, N. F. (1991). The glacial landforms of Glen Geusachan, Cairngorms: a reinterpretation. *Scottish Geographical Magazine*, *107*(2), 116-123.

Bennett, M. R., Hambrey, M. J., Huddart, D., & Glasser, N. F. (1998). Glacial thrusting & moraine-mound formation in Svalbard & Britain: The example of Coire a'Cheud-chnoic (Valley of Hundred Hills), Torridon Scotland. *Journal of Quaternary Science*, *13*(6), 17-34.

Bentley, M. (1996). The role of lakes in moraine formation, Chilean Lake District. *Earth surface processes and landforms*, *21*(6), 493-507.

Bentley, M. J., Sugden, D. E., Hulton, N. R., & McCulloch, R. (2005). The landforms and pattern of deglaciation in the Strait of Magellan and Bahía Inútil, southernmost South America. *Geografiska Annaler: series a, physical geography*, *87*(2), 313-333.

Berman, A. L., Silvestri, G. E., & Tonello, M. S. (2016). Differences between Last Glacial Maximum and present-day temperature and precipitation in southern South America. *Quaternary Science Reviews*, *150*, 221-233.

Bertrand, S., Hughen, K., Sepúlveda, J., & Pantoja, S. (2014). Late Holocene covariability of the southern westerlies and sea surface temperature in northern Chilean Patagonia. *Quaternary Science Reviews*, *105*, 195-208.

Bianchi, M. M., & Ariztegui, D. (2012). Vegetation history of the Río Manso Superior catchment area, Northern Patagonia (Argentina), since the last deglaciation. *The Holocene*, *22*(11), 1283-1295.

Blunier, T., & Brook, E. J. (2001). Timing of millennial-scale climate change in Antarctica and Greenland during the last glacial period. *science*, *291*(5501), 109-112.

Boex, J., Fogwill, C., Harrison, S., Glasser, N., Hein, A., Schnabel, C., & Xu, S. (2013). Rapid thinning of the late Pleistocene Patagonian Ice Sheet followed migration of the Southern Westerlies. *Scientific Reports*, *3*(1), 1-6.

Bøtter-Jensen, L., Andersen, C., Duller, G. A., & Murray, A. S. (2003). Developments in radiation, stimulation and observation facilities in luminescence measurements. *Radiation Measurements*, *37*(4-5), 535-541.

Braconnot, P., Harrison, S. P., Kageyama, M., Bartlein, P. J., Masson-Delmotte, V., Abe-Ouchi, A., Otto-Bliesner, B., & Zhao, Y. (2012). Evaluation of climate models using palaeoclimatic data. *Nature Climate Change*, *2*(6), 417-424.

Bravo, C., Quincey, D., Ross, A., Rivera, A., Brock, B., Miles, E., & Silva, A. (2019). Air temperature characteristics, distribution, and impact on modeled ablation for the South Patagonia Icefield. *Journal of Geophysical Research: Atmospheres*, *124*(2), 907-925.

Bueler, E. (2021). Numerical modelling of ice sheets, streams, and shelves. *Glaciers and Ice Sheets in the Climate System: The Karthaus Summer School Lecture Notes*, 185-217.

Bueler, E., & Brown, J. (2009). Shallow shelf approximation as a “sliding law” in a thermomechanically coupled ice sheet model. *Journal of Geophysical Research: Earth Surface*, *114*(F3).

Bueler, E., Lingle, C. S., & Brown, J. (2007). Fast computation of a viscoelastic deformable Earth model for ice-sheet simulations. *Annals of Glaciology*, *46*, 97-105.

Caldenius, C. C. Z. (1932). Las Glaciaciones Cuaternarias en la Patagonia y Tierra del Fuego: Una investigación regional, estratigráfica y geocronológica.—Una comparación con la escala geocronológica sueca. *Geografiska Annaler*, *14*(1-2), 1-164.

Caniupán, M., Lamy, F., Lange, C., Kaiser, J., Arz, H., Kilian, R., Baeza Urrea, O., Aracena, C., Hebbeln, D., & Kissel, C. (2011). Millennial-scale sea surface temperature and Patagonian Ice Sheet changes off southernmost Chile (53 S) over the past~ 60 kyr. *Paleoceanography*, *26*(3), 1-10.

Carrivick, J. L., Davies, B. J., James, W. H., Quincey, D. J., & Glasser, N. F. (2016). Distributed ice thickness and glacier volume in southern South America. *Global and Planetary Change*, *146*, 122-132.

Chadwick, M., Crosta, X., Esper, O., Thöle, L., & Kohfeld, K. E. (2022). Compilation of Southern Ocean sea-ice records covering the last glacial-interglacial cycle (12–130 ka). *Climate of the Past*, *18*(8), 1815-1829.

Chandler, B. M., Evans, D. J., Chandler, S. J., Ewertowski, M. W., Lovell, H., Roberts, D. H., Schaefer, M., & Tomczyk, A. M. (2020). The glacial landsystem of Fjallsjökull, Iceland: Spatial and temporal evolution of process-form regimes at an active temperate glacier. *Geomorphology*, *361*, 107192.

Çiner, A., Sarıkaya, M. A., Yıldırım, C., Girault, I., Todisco, D., Martin, F., Borrero, L., & Fabel, D. (2022). Terrestrial cosmogenic 10Be dating of the Última Esperanza ice lobe moraines (52° S, Patagonia) indicates the global Last Glacial Maximum (LGM) extent was half of the local LGM. *Geomorphology*, *414*, 108381.

Clapperton, C. (1993). *Quaternary geology and geomorphology of South America*.

Clapperton, C. M., Sugden, D. E., Kaufman, D. S., & McCulloch, R. D. (1995). The last glaciation in central Magellan Strait, southernmost Chile. *Quaternary Research*, *44*(2), 133-148.

Clark, C. D., Ely, J. C., Hindmarsh, R. C., Bradley, S., Ignéczi, A., Fabel, D., Ó Cofaigh, C., Chiverrell, R. C., Scourse, J., & Benetti, S. (2022). Growth and retreat of the last British–Irish Ice Sheet, 31 000 to 15 000 years ago: the BRITICE-CHRONO reconstruction. *Boreas*, *51*(4), 699-758.

Clark, P. U., Dyke, A. S., Shakun, J. D., Carlson, A. E., Clark, J., Wohlfarth, B., Mitrovica, J. X., Hostetler, S. W., & McCabe, A. M. (2009). The last glacial maximum. *science*, *325*(5941), 710-714.

Cogez, A., Herman, F., Pelt, É., Reuschlé, T., Morvan, G., Darvill, C. M., Norton, K. P., Christl, M., Märki, L., & Chabaux, F. (2018). U–Th and 10 Be constraints on sediment recycling in proglacial settings, Lago Buenos Aires, Patagonia. *Earth Surface Dynamics*, *6*(1), 121-140.

Cogley, J. G., Arendt, A., Bauder, A., Braithwaite, R., Hock, R., Jansson, P., Kaser, G., Moller, M., Nicholson, L., & Rasmussen, L. (2010). Glossary of glacier mass balance and related terms.

Coronato, A., Martinez, O., & Rabassa, J. (2004). Glaciations in Argentine Patagonia, southern South America. *Developments in quaternary sciences*, *2*, 49-67.

Cuffey, K., & Paterson, W. (2010). *The physics of glaciers, Fourth Edition, Elsevier, Burlington, USA* (Vol. 2989).

Darvill, C. M., Bentley, M. J., Stokes, C. R., Hein, A. S., & Rodés, Á. (2015). Extensive MIS 3 glaciation in southernmost Patagonia revealed by cosmogenic nuclide dating of outwash sediments. *Earth and Planetary Science Letters*, *429*, 157-169.

Darvill, C. M., Bentley, M. J., Stokes, C. R., & Shulmeister, J. (2016). The timing and cause of glacial advances in the southern mid-latitudes during the last glacial cycle based on a synthesis of exposure ages from Patagonia and New Zealand. *Quaternary Science Reviews*, *149*, 200-214.

Darvill, C. M., Stokes, C. R., Bentley, M. J., Evans, D. J., & Lovell, H. (2017). Dynamics of former ice lobes of the southernmost Patagonian Ice Sheet based on a glacial landsystems approach. *Journal of Quaternary Science*, *32*(6), 857-876.

Darvill, C. M., Stokes, C. R., Bentley, M. J., & Lovell, H. (2014). A glacial geomorphological map of the southernmost ice lobes of Patagonia: the Bahía Inútil–San Sebastián, Magellan, Otway, Skyring and Río Gallegos lobes. *Journal of Maps*, *10*(3), 500-520.

DaSilva, J. L., Anderson, J. B., & Stravers, J. (1997). Seismic facies changes along a nearly continuous 24 latitudinal transect: the fjords of Chile and the northern Antarctic Peninsula. *Marine Geology*, *143*(1-4), 103-123.

Davies, B., Bendle, J., Carrivick, J., McNabb, R., McNeil, C., Pelto, M., Campbell, S., Holt, T., Ely, J., & Markle, B. (2022). Topographic controls on ice flow and recession for Juneau Icefield (Alaska/British Columbia). *Earth surface processes and landforms*, *47*(9), 2357-2390.

Davies, B., Thorndycraft, V., Fabel, D., & Martin, J. (2018). Asynchronous glacier dynamics during the Antarctic Cold Reversal in central Patagonia. *Quaternary Science Reviews*, *200*, 287-312.

Davies, B. J., Darvill, C. M., Lovell, H., Bendle, J. M., Dowdeswell, J. A., Fabel, D., García, J.-L., Geiger, A., Glasser, N. F., & Gheorghiu, D. M. (2020). The evolution of the Patagonian Ice Sheet from 35 ka to the present day (PATICE). *Earth-Science Reviews*, *204*, 103152.

De Angelis, H. (2014). Hypsometry and sensitivity of the mass balance to changes in equilibrium-line altitude: the case of the Southern Patagonia Icefield. *Journal of glaciology*, *60*(219), 14-28.

Dee, D. P., Uppala, S. M., Simmons, A. J., Berrisford, P., Poli, P., Kobayashi, S., Andrae, U., Balmaseda, M., Balsamo, G., & Bauer, d. P. (2011). The ERA-Interim reanalysis: Configuration and performance of the data assimilation system. *Quarterly Journal of the royal meteorological society*, *137*(656), 553-597.

Denton, G. H., Anderson, R. F., Toggweiler, J., Edwards, R., Schaefer, J., & Putnam, A. (2010). The last glacial termination. *science*, *328*(5986), 1652-1656.

Denton, G. H., Lowell, T., Heusser, C., Schlüchter, C., Andersen, B. G., Heusser, L. E., Moreno, P. I., & Marchant, D. R. (1999). Geomorphology, stratigraphy, and radiocarbon chronology of LlanquihueDrift in the area of the Southern Lake District, Seno Reloncaví, and Isla Grande de Chiloé, Chile. *Geografiska Annaler: series a, physical geography*, *81*(2), 167-229.

Denton, G. H., Putnam, A. E., Russell, J. L., Barrell, D. J., Schaefer, J. M., Kaplan, M. R., & Strand, P. D. (2021). The Zealandia Switch: Ice age climate shifts viewed from Southern Hemisphere moraines. *Quaternary Science Reviews*, *257*, 106771.

Dewald, A., Heinze, S., Jolie, J., Zilges, A., Dunai, T., Rethemeyer, J., Melles, M., Staubwasser, M., Kuczewski, B., & Richter, J. (2013). CologneAMS, a dedicated center for accelerator mass spectrometry in Germany. *Nuclear Instruments and Methods in Physics Research Section B: Beam Interactions with Materials and Atoms*, *294*, 18-23.

Dirección General de Aguas, Chile. http://snia.dga.cl/BNAConsultas/reportes

Douglass, D., Singer, B., Kaplan, M., Mickelson, D., & Caffee, M. (2006). Cosmogenic nuclide surface exposure dating of boulders on last-glacial and late-glacial moraines, Lago Buenos Aires, Argentina: interpretive strategies and paleoclimate implications. *Quaternary Geochronology*, *1*(1), 43-58.

Douglass, D. C., Singer, B., Ackert, R., Kaplan, M., & Caffee, M. (2007). Constraining Boulder Erosion Rates and Ages of Mid-Pleistocene Moraines. Lago Buenos Aires, Argentina. GSA Abstracts and Programs Northeastern Section, 42nd Annual Meeting,

Durcan, J. A., King, G. E., & Duller, G. A. (2015). DRAC: Dose Rate and Age Calculator for trapped charge dating. *Quaternary Geochronology*, *28*, 54-61.

Evans, D. (2003a). *Glacial landsystems* (E. DJA, Ed.). Hodder Arnold: London.

Evans, D. (2003b). Ice-marginal terrestrial landsystems: active temperate glacier margins. *Glacial landsystems*, 12-43.

Evans, D. J., & Benn, D. I. (2021). *A practical guide to the study of glacial sediments* (2nd ed.). QRA.

Evans, D. J., & England, J. (1991). High Arctic thrust block moraines. *Canadian Geographer/Le Géographe Canadien*, *35*(1), 93-97.

Evans, D. J., & Twigg, D. R. (2002). The active temperate glacial landsystem: a model based on Breiðamerkurjökull and Fjallsjökull, Iceland. *Quaternary Science Reviews*, *21*(20-22), 2143-2177.

Fausto, R. S., Ahlstrøm, A. P., Van As, D., & Steffen, K. (2011). Present-day temperature standard deviation parameterization for Greenland. *Journal of glaciology*, *57*(206), 1181-1183.

Fick, S. E., & Hijmans, R. J. (2017). WorldClim 2: new 1-km spatial resolution climate surfaces for global land areas. *International journal of climatology*, *37*(12), 4302-4315.

Fogwill, C., & Kubik, P. (2005). A glacial stage spanning the Antarctic Cold Reversal in Torres del Paine (51 S), Chile, based on preliminary cosmogenic exposure ages. *Geografiska Annaler: series a, physical geography*, *87*(2), 403-408.

Furbish, D., & Andrews, J. (1984). The use of hypsometry to indicate long-term stability and response of valley glaciers to changes in mass transfer. *Journal of glaciology*, *30*(105), 199-211.

Fürst, J. J., Farías-Barahona, D., Blindow, N., Casassa, G., Gacitúa, G., Koppes, M., Lodolo, E., Millan, R., Minowa, M., & Mouginot, J. (2024). The foundations of the Patagonian icefields. *Communications Earth & Environment*, *5*(1), 142.

Galbraith, R. F., & Laslett, G. M. (1993). Statistical models for mixed fission track ages. *Nuclear tracks and radiation measurements*, *21*(4), 459-470.

Galbraith, R. F., Roberts, R. G., Laslett, G. M., Yoshida, H., & Olley, J. M. (1999). Optical dating of single and multiple grains of quartz from Jinmium rock shelter, northern Australia: Part I, experimental design and statistical models. *Archaeometry*, *41*(2), 339-364.

García, J.-L., Hall, B. L., Kaplan, M. R., Gómez, G. A., De Pol-Holz, R., García, V. J., Schaefer, J. M., & Schwartz, R. (2020). 14C and 10Be dated Late Holocene fluctuations of Patagonian glaciers in Torres del Paine (Chile, 51° S) and connections to Antarctic climate change. *Quaternary Science Reviews*, *246*, 106541.

García, J.-L., Hein, A. S., Binnie, S. A., Gómez, G. A., González, M. A., & Dunai, T. J. (2018). The MIS 3 maximum of the Torres del Paine and Última Esperanza ice lobes in Patagonia and the pacing of southern mountain glaciation. *Quaternary Science Reviews*, *185*, 9-26.

García, J.-L., Lüthgens, C., Vega, R. M., Rodés, Á., Hein, A., & Binnie, S. (2021). A composite 10Be, IR-50 and 14C chronology of the pre-LGM full ice extent of the western Patagonian Ice Sheet in the Isla de Chiloé, south Chile (42ºS). *E&G-Quaternary Science Journal*, *70*(1).

García, J.-L., Strelin, J. A., Vega, R. M., Hall, B. L., & Stern, C. R. (2015). Deglacial ice-marginal glaciolacustrine environments and structural moraine building in Torres del Paine, Chilean southern Patagonia. *Andean Geology*, *42*(2), 190-212.

García, J. L. (2012). Late Pleistocene ice fluctuations and glacial geomorphology of the Archipiélago de Chiloé, southern Chile. *Geografiska Annaler: series a, physical geography*, *94*(4), 459-479.

Garreaud, R. (2009). The Andes climate and weather. *Advances in Geosciences*, *22*, 3-11.

Garreaud, R., Lopez, P., Minvielle, M., & Rojas, M. (2013). Large-scale control on the Patagonian climate. *Journal of Climate*, *26*(1), 215-230.

Glasser, N., & Jansson, K. (2008). The glacial map of southern South America. *Journal of Maps*, *4*(1), 175-196.

Glasser, N. F., & Ghiglione, M. C. (2009). Structural, tectonic and glaciological controls on the evolution of fjord landscapes. *Geomorphology*, *105*(3-4), 291-302.

Glasser, N. F., & Hambrey, M. J. (2002). Sedimentary facies and landform genesis at a temperate outlet glacier: Soler Glacier, North Patagonian Icefield. *Sedimentology*, *49*(1), 43-64.

Glasser, N. F., Harrison, S., Jansson, K. N., Anderson, K., & Cowley, A. (2011). Global sea-level contribution from the Patagonian Icefields since the Little Ice Age maximum. *Nature Geoscience*, *4*(5), 303-307.

Glasser, N. F., Harrison, S., Schnabel, C., Fabel, D., & Jansson, K. N. (2012). Younger Dryas and early Holocene age glacier advances in Patagonia. *Quaternary Science Reviews*, *58*, 7-17.

Glasser, N. F., Jansson, K. N., Duller, G. A., Singarayer, J., Holloway, M., & Harrison, S. (2016). Glacial lake drainage in Patagonia (13-8 kyr) and response of the adjacent Pacific Ocean. *Scientific Reports*, *6*(1), 21064.

Glasser, N. F., Jansson, K. N., Harrison, S., & Kleman, J. (2008). The glacial geomorphology and Pleistocene history of South America between 38 S and 56 S. *Quaternary Science Reviews*, *27*(3-4), 365-390.

Glasser, N. S., & Hambrey, M. J. (2003). Ice-marginal terrestrial landsystems: Svalbard polythermal glaciers. *glacial landsystems. Arnold, London*, *228*, 258.

Golledge, N. R., Fogwill, C. J., Mackintosh, A. N., & Buckley, K. M. (2012a). Dynamics of the last glacial maximum Antarctic ice-sheet and its response to ocean forcing. *Proceedings of the National Academy of Sciences*, *109*(40), 16052-16056.

Golledge, N. R., Mackintosh, A. N., Anderson, B. M., Buckley, K. M., Doughty, A. M., Barrell, D. J., Denton, G. H., Vandergoes, M. J., Andersen, B. G., & Schaefer, J. M. (2012b). Last Glacial Maximum climate in New Zealand inferred from a modelled Southern Alps icefield. *Quaternary Science Reviews*, *46*, 30-45.

Goutorbe, B., Poort, J., Lucazeau, F., & Raillard, S. (2011). Global heat flow trends resolved from multiple geological and geophysical proxies. *Geophysical Journal International*, *187*(3), 1405-1419.

Gowan, E. J., Hinck, S., Niu, L., Clason, C., & Lohmann, G. (2023). The impact of spatially varying ice sheet basal conditions on sliding at glacial time scales. *Journal of glaciology*, *69*(276), 1056-1070.

Griggs, J. A., & Bamber, J. (2011). Antarctic ice-shelf thickness from satellite radar altimetry. *Journal of glaciology*, *57*(203), 485-498.

Guérin, G., Mercier, N., & Adamiec, G. (2011). Dose-rate conversion factors: update. *Ancient TI*, *29*(1), 5-8.

Guérin, G., Mercier, N., Nathan, R., Adamiec, G., & Lefrais, Y. (2012). On the use of the infinite matrix assumption and associated concepts: a critical review. *Radiation Measurements*, *47*(9), 778-785.

Hagemann, J. R., Lamy, F., Arz, H. W., Lembke-Jene, L., Auderset, A., Harada, N., Ho, S. L., Iwasaki, S., Kaiser, J., & Lange, C. B. (2024). A marine record of Patagonian ice sheet changes over the past 140,000 years. *Proceedings of the National Academy of Sciences*, *121*(12), e2302983121.

Hajdas, I., Bonani, G., Moreno, P. I., & Ariztegui, D. (2003). Precise radiocarbon dating of Late-Glacial cooling in mid-latitude South America. *Quaternary Research*, *59*(1), 70-78.

Hall, B., Lowell, T., Bromley, G., Denton, G., & Putnam, A. (2019). Holocene glacier fluctuations on the northern flank of Cordillera Darwin, southernmost South America. *Quaternary Science Reviews*, *222*, 105904.

Hall, B. L., Denton, G., Lowell, T., Bromley, G., & Putnam, A. (2017). Retreat of the Cordillera Darwin icefield during the Termination I. *Cuadernos de investigación geográfica/Geographical Research Letters*(43), 751-766.

Hall, B. L., Porter, C. T., Denton, G. H., Lowell, T. V., & Bromley, G. R. (2013). Extensive recession of Cordillera Darwin glaciers in southernmost South America during Heinrich stadial 1. *Quaternary Science Reviews*, *62*, 49-55.

Hambrey, M. J., Huddart, D., Bennett, M. R., & Glasser, N. F. (1997). Genesis of 'hummocky moraines' by thrusting in glacier ice: evidence from Svalbard and Britain. *Journal of the Geological Society*, *154*(4), 623-632.

Hancock, G. S., Anderson, R. S., Chadwick, O. A., & Finkel, R. C. (1999). Dating fluvial terraces with 10Be and 26Al profiles: Application to the Wind River, Wyoming. *Geomorphology*, *27*(1-2), 41-60.

Hein, A. S. (2009). Quaternary Glaciations in the Lago Pueyrredon Valley, Argentina.

Hein, A. S., Dunai, T. J., Hulton, N. R., & Xu, S. (2011). Exposure dating outwash gravels to determine the age of the greatest Patagonian glaciations. *Geology*, *39*(2), 103-106.

Hein, A. S., Hulton, N. R., Dunai, T. J., Schnabel, C., Kaplan, M. R., Naylor, M., & Xu, S. (2009). Middle Pleistocene glaciation in Patagonia dated by cosmogenic-nuclide measurements on outwash gravels. *Earth and Planetary Science Letters*, *286*(1-2), 184-197.

Hein, A. S., Hulton, N. R., Dunai, T. J., Sugden, D. E., Kaplan, M. R., & Xu, S. (2010). The chronology of the Last Glacial Maximum and deglacial events in central Argentine Patagonia. *Quaternary Science Reviews*, *29*(9-10), 1212-1227.

Heusser, C. J., Lowell, T. V., & Heusser, L. E. (2000). Pollen sequence from the Chilean Lake District during the Llanquihue glaciation in marine oxygen isotope stages 4–2. *Journal of Quaternary Science: Published for the Quaternary Research Association*, *15*(2), 115-125.

Heusser, C. J., Lowell, T. V., Heusser, L. E., Hauser, A., Andersen, B. G., & Denton, G. H. (1996). Full-glacial—late-glacial palaeoclimate of the Southern Andes: evidence from pollen, beetle and glacial records. *Journal of Quaternary Science: Published for the Quaternary Research Association*, *11*(3), 173-184.

Heusser, L., Heusser, C., Kleczkowski, A., & Crowhurst, S. (1999). A 50,000-yr pollen record from Chile of South American millennial-scale climate instability during the last glaciation. *Quaternary Research*, *52*(2), 154-158.

Heusser, L., Heusser, C., Mix, A., & McManus, J. (2006). Chilean and Southeast Pacific paleoclimate variations during the last glacial cycle: directly correlated pollen and δ18O records from ODP Site 1234. *Quaternary Science Reviews*, *25*(23-24), 3404-3415.

Hobbs, J. E., Lindesay, J., & Bridgman, H. A. (1998). Climates of the southern continents: present, past, and future. *(No Title)*.

Hock, R. (2003). Temperature index melt modelling in mountain areas. *Journal of hydrology*, *282*(1-4), 104-115.

Hodgson, D. A., Roberts, S. J., Izagirre, E., Perren, B. B., De Vleeschouwer, F., Davies, S. J., Bishop, T., McCulloch, R. D., & Aravena, J.-C. (2023). Southern limit of the Patagonian Ice Sheet. *Quaternary Science Reviews*, *321*, 108346.

Hogg, A. G., Heaton, T. J., Hua, Q., Palmer, J. G., Turney, C. S., Southon, J., Bayliss, A., Blackwell, P. G., Boswijk, G., & Ramsey, C. B. (2020). SHCal20 Southern Hemisphere calibration, 0–55,000 years cal BP. *Radiocarbon*, *62*(4), 759-778.

Hubbard, A., Hein, A. S., Kaplan, M. R., Hulton, N. R., & Glasser, N. (2005). A modelling reconstruction of the last glacial maximum ice sheet and its deglaciation in the vicinity of the Northern Patagonian Icefield, South America. *Geografiska Annaler: series a, physical geography*, *87*(2), 375-391.

Hulton, N., Sugden, D., Payne, A., & Clapperton, C. (1994). Glacier modeling and the climate of Patagonia during the Last Glacial Maximum. *Quaternary Research*, *42*(1), 1-19.

Hulton, N. R., Purves, R., McCulloch, R., Sugden, D. E., & Bentley, M. J. (2002). The last glacial maximum and deglaciation in southern South America. *Quaternary Science Reviews*, *21*(1-3), 233-241.

Huntley, D. J., & Lamothe, M. (2001). Ubiquity of anomalous fading in K-feldspars and the measurement and correction for it in optical dating. *Canadian Journal of Earth Sciences*, *38*(7), 1093-1106.

Johnson, M., & Clayton, L. (2003). Supraglacial landsystems in lowland terrain. *glacial landsystems. Arnold, London*, *228*, 258.

Jones, R., Small, D., Cahill, N., Bentley, M., & Whitehouse, P. (2019). iceTEA: tools for plotting and analysing cosmogenic-nuclide surface-exposure data from former ice margins. *Quaternary Geochronology*, *51*, 72-86.

Jouzel, J., Masson-Delmotte, V., Cattani, O., Dreyfus, G., Falourd, S., Hoffmann, G., Minster, B., Nouet, J., Barnola, J.-M., & Chappellaz, J. (2007). Orbital and millennial Antarctic climate variability over the past 800,000 years. *science*, *317*(5839), 793-796.

Kaiser, J., Lamy, F., & Hebbeln, D. (2005). A 70-kyr sea surface temperature record off southern Chile (Ocean Drilling Program Site 1233). *Paleoceanography*, *20*(4), 1-15.

Kang, S. M., Seager, R., Frierson, D. M., & Liu, X. (2015). Croll revisited: Why is the northern hemisphere warmer than the southern hemisphere? *Climate Dynamics*, *44*, 1457-1472.

Kaplan, M., Fogwill, C., Sugden, D., Hulton, N., Kubik, P., & Freeman, S. (2008). Southern Patagonian glacial chronology for the Last Glacial period and implications for Southern Ocean climate. *Quaternary Science Reviews*, *27*(3-4), 284-294.

Kaplan, M. R., Ackert Jr, R. P., Singer, B. S., Douglass, D. C., & Kurz, M. D. (2004). Cosmogenic nuclide chronology of millennial-scale glacial advances during O-isotope stage 2 in Patagonia. *Geological Society of America Bulletin*, *116*(3-4), 308-321.

Kaplan, M. R., Douglass, D. C., Singer, B. S., Ackert, R. P., & Caffee, M. W. (2005). Cosmogenic nuclide chronology of pre-last glacial maximum moraines at Lago Buenos Aires, 46 S, Argentina. *Quaternary Research*, *63*(3), 301-315.

Kaplan, M. R., Hein, A. S., Hubbard, A., & Lax, S. M. (2009). Can glacial erosion limit the extent of glaciation? *Geomorphology*, *103*(2), 172-179.

Kaplan, M. R., Strelin, J. A., Schaefer, J. M., Denton, G. H., Finkel, R. C., Schwartz, R., Putnam, A. E., Vandergoes, M. J., Goehring, B. M., & Travis, S. G. (2011). In-situ cosmogenic 10Be production rate at Lago Argentino, Patagonia: implications for late-glacial climate chronology. *Earth and Planetary Science Letters*, *309*(1-2), 21-32.

Kilian, R., Baeza, O., Breuer, S., Ríos, F., Arz, H., Lamy, F., Wirtz, J., Baque, D., Korf, P., & Kremer, K. (2013). Late Glacial and Holocene Paleogeographical and Paleoecological Evolution of the Seno Skyring and Otway Fjord Systems in the Magellan Region. *Anales del Instituto de la Patagonia*, *41*(2), 5-26.

Kilian, R., Schneider, C., Koch, J., Fesq-Martin, M., Biester, H., Casassa, G., Arévalo, M., Wendt, G., Baeza, O., & Behrmann, J. (2007). Palaeoecological constraints on late Glacial and Holocene ice retreat in the Southern Andes (53 S). *Global and Planetary Change*, *59*(1-4), 49-66.

Kohfeld, K. E., Graham, R. M., De Boer, A. M., Sime, L. C., Wolff, E. W., Le Quéré, C., & Bopp, L. (2013). Southern Hemisphere westerly wind changes during the Last Glacial Maximum: paleo-data synthesis. *Quaternary Science Reviews*, *68*, 76-95.

Kolb, T., & Fuchs, M. (2018). Luminescence dating of pre-Eemian (pre-MIS 5e) fluvial terraces in Northern Bavaria (Germany)–Benefits and limitations of applying a pIRIR225-approach. *Geomorphology*, *321*, 16-32.

Lal, D. (1991). Cosmic ray labeling of erosion surfaces: in situ nuclide production rates and erosion models. *Earth and Planetary Science Letters*, *104*(2-4), 424-439.

Lambeck, K., Rouby, H., Purcell, A., Sun, Y., & Sambridge, M. (2014). Sea level and global ice volumes from the Last Glacial Maximum to the Holocene. *Proceedings of the National Academy of Sciences*, *111*(43), 15296-15303.

Lamy, F., Kaiser, J., Arz, H. W., Hebbeln, D., Ninnemann, U., Timm, O., Timmermann, A., & Toggweiler, J. R. (2007). Modulation of the bipolar seesaw in the Southeast Pacific during Termination 1. *Earth and Planetary Science Letters*, *259*(3-4), 400-413.

Lamy, F., Kaiser, J., Ninnemann, U., Hebbeln, D., Arz, H. W., & Stoner, J. (2004). Antarctic timing of surface water changes off Chile and Patagonian ice sheet response. *science*, *304*(5679), 1959-1962.

Lamy, F., Kilian, R., Arz, H. W., Francois, J.-P., Kaiser, J., Prange, M., & Steinke, T. (2010). Holocene changes in the position and intensity of the southern westerly wind belt. *Nature Geoscience*, *3*(10), 695-699.

Leger, T. P., Hein, A. S., Bingham, R. G., Rodés, Á., Fabel, D., & Smedley, R. K. (2021). Geomorphology and 10Be chronology of the Last Glacial Maximum and deglaciation in northeastern Patagonia, 43° S-71° W. *Quaternary Science Reviews*, *272*, 107194.

Leger, T. P., Hein, A. S., Goldberg, D., Schimmelpfennig, I., Van Wyk de Vries, M. S., Bingham, R. G., & Team, A. (2021). Northeastern Patagonian glacier advances (43° S) reflect northward migration of the Southern Westerlies towards the end of the last glaciation. *Frontiers in Earth Science*, *9*, 751987.

Leger, T. P., Hein, A. S., Rodés, Á., Bingham, R. G., Schimmelpfennig, I., Fabel, D., Tapia, P., & Team, A. (2023). A cosmogenic nuclide-derived chronology of pre-Last Glacial Cycle glaciations during MIS 8 and MIS 6 in northern Patagonia. *Climate of the Past*, *19*(1), 35-59.

Lemieux-Dudon, B., Blayo, E., Petit, J.-R., Waelbroeck, C., Svensson, A., Ritz, C., Barnola, J.-M., Narcisi, B. M., & Parrenin, F. (2010). Consistent dating for Antarctic and Greenland ice cores. *Quaternary Science Reviews*, *29*(1-2), 8-20.

Lingle, C. S., & Clark, J. A. (1985). A numerical model of interactions between a marine ice sheet and the solid earth: Application to a West Antarctic ice stream. *Journal of Geophysical Research: Oceans*, *90*(C1), 1100-1114.

Lira, M.-P., García, J.-L., Bentley, M. J., Jamieson, S. S., Darvill, C. M., Hein, A. S., Fernández, H., Rodés, Á., Fabel, D., & Smedley, R. K. (2022). The Last Glacial Maximum and Deglacial History of the Seno Skyring Ice Lobe (52° S), Southern Patagonia. *Frontiers in Earth Science*, *10*, 892316.

Lovell, H., Stokes, C. R., & Bentley, M. J. (2011). A glacial geomorphological map of the Seno Skyring-Seno Otway-Strait of Magellan region, southernmost Patagonia. *Journal of Maps*, *7*(1), 318-339.

Lovell, H., Stokes, C. R., Bentley, M. J., & Benn, D. I. (2012). Evidence for rapid ice flow and proglacial lake evolution around the central Strait of Magellan region, southernmost Patagonia. *Journal of Quaternary Science*, *27*(6), 625-638.

Manger, G. (1963). *Porosity and Bulk Density of Sedimentary Rocks. Geological Survey Bulletin, 1144-E*.

Mark, H. F., Wiens, D. A., Ivins, E. R., Richter, A., Ben Mansour, W., Magnani, M. B., Marderwald, E., Adaros, R., & Barrientos, S. (2022). Lithospheric erosion in the Patagonian slab window, and implications for glacial isostasy. *Geophysical Research Letters*, *49*(2), e2021GL096863.

Martin, J., Davies, B. J., Jones, R., & Thorndycraft, V. (2022). Modelled sensitivity of Monte San Lorenzo ice cap, Patagonian Andes, to past and present climate. *Frontiers in Earth Science*, *10*, 831631.

Martin, M. A., Winkelmann, R., Haseloff, M., Albrecht, T., Bueler, E., Khroulev, C., & Levermann, A. (2011). The Potsdam parallel ice sheet model (PISM-PIK)–Part 2: dynamic equilibrium simulation of the Antarctic ice sheet. *The Cryosphere*, *5*(3), 727-740.

Mashiotta, T. A., Lea, D. W., & Spero, H. J. (1999). Glacial–interglacial changes in Subantarctic sea surface temperature and δ18O-water using foraminiferal Mg. *Earth and Planetary Science Letters*, *170*(4), 417-432.

McCulloch, R., Bentley, M. J., Purves, R. S., Hulton, N. R., Sugden, D. E., & Clapperton, C. M. (2000). Climatic inferences from glacial and palaeoecological evidence at the last glacial termination, southern South America. *Journal of Quaternary Science: Published for the Quaternary Research Association*, *15*(4), 409-417.

McCulloch, R., Bentley, M. J., Tipping, R., & Clapperton, C. M. (2005a). Evidence for late-glacial ice dammed lakes in the Central strait of Magellan and Bahia Inutil, Southernmost South America. *Geografiska Annaler: series a, physical geography*, *87*(2), 335-362.

McCulloch, R., Fogwill, C., Sugden, D. E., Bentley, M. J., & Kubik, P. (2005b). Chronology of the last glaciation in central Strait of Magellan and Bahía Inútil, southernmost South America. *Geografiska Annaler: series a, physical geography*, *87*(2), 289-312.

Mcculloch, R. D., & Bentley, M. J. (1998). Late glacial ice advances in the Strait of Magellan, southern Chile. *Quaternary Science Reviews*, *17*(8), 775-787.

McCulloch, R. D., Blaikie, J., Jacob, B., Mansilla, C. A., Morello, F., De Pol-Holz, R., San Román, M., Tisdall, E., & Torres, J. (2020). Late glacial and Holocene climate variability, southernmost Patagonia. *Quaternary Science Reviews*, *229*, 106131.

Mcgrath, D., Sass, L., O'Neel, S., Arendt, A., & Kienholz, C. (2017). Hypsometric control on glacier mass balance sensitivity in Alaska and northwest Canada. *Earth's Future*, *5*(3), 324-336.

Meglioli, A. (1992). *Glacial geology and chronology of southernmost Patagonia and Tierra del Fuego, Argentina and Chile* Lehigh University]. Bethlehem, Pa.

Mendelová, M., Hein, A. S., Rodés, Á., & Xu, S. (2020). Extensive mountain glaciation in central Patagonia during Marine Isotope Stage 5. *Quaternary Science Reviews*, *227*, 105996.

Mercer, J. H. (1970). Variations of some Patagonian glaciers since the Late-Glacial; II. *American Journal of Science*, *269*(1), 1-25.

Millan, R., Rignot, E., Rivera, A., Martineau, V., Mouginot, J., Zamora, R., Uribe, J., Lenzano, G., De Fleurian, B., & Li, X. (2019). Ice thickness and bed elevation of the Northern and Southern Patagonian Icefields. *Geophysical Research Letters*, *46*(12), 6626-6635.

Möller, M., Schneider, C., & Kilian, R. (2007). Glacier change and climate forcing in recent decades at Gran Campo Nevado, southernmost Patagonia. *Annals of Glaciology*, *46*, 136-144.

Möller, P., Hjort, C., Björck, S., Rabassa, J., & Ponce, J. F. (2010). Late Quaternary glaciation history of Isla de los Estados, southeasternmost South America. *Quaternary Research*, *73*(3), 521-534.

Moreno, P. I. (2020). Timing and structure of vegetation, fire, and climate changes on the Pacific slope of northwestern Patagonia since the last glacial termination. *Quaternary Science Reviews*, *238*, 106328.

Moreno, P. I., Denton, G. H., Moreno, H., Lowell, T. V., Putnam, A. E., & Kaplan, M. R. (2015). Radiocarbon chronology of the last glacial maximum and its termination in northwestern Patagonia. *Quaternary Science Reviews*, *122*, 233-249.

Moreno, P. I., Jacobson Jr, G. L., Lowell, T. V., & Denton, G. H. (2001). Interhemispheric climate links revealed by a late-glacial cooling episode in southern Chile. *Nature*, *409*(6822), 804-808.

Moreno, P. I., Lowell, T. V., Jacobson Jr, G. L., & Denton, G. H. (1999). Abrupt vegetation and climate changes during the last glacial maximumand last termination in the chilean lake district: a case study from canal de la puntilla (41 s). *Geografiska Annaler: series a, physical geography*, *81*(2), 285-311.

Muir, R., Eaves, S., Vargo, L., Anderson, B., Mackintosh, A., Sagredo, E., & Soteres, R. (2023). Late glacial climate evolution in the Patagonian Andes (44–47° S) from alpine glacier modelling. *Quaternary Science Reviews*, *305*, 108035.

Murray, A. S., & Wintle, A. G. (2000). Luminescence dating of quartz using an improved single-aliquot regenerative-dose protocol. *Radiation Measurements*, *32*(1), 57-73.

Nesje, A. (1992). Topographical effects on the equilibrium-line altitude on glaciers. *GeoJournal*, *27*(4), 383-391.

Nishiizumi, K., Imamura, M., Caffee, M. W., Southon, J. R., Finkel, R. C., & McAninch, J. (2007). Absolute calibration of 10Be AMS standards. *Nuclear Instruments and Methods in Physics Research Section B: Beam Interactions with Materials and Atoms*, *258*(2), 403-413.

Pattyn, F., Schoof, C., Perichon, L., Hindmarsh, R., Bueler, E., De Fleurian, B., Durand, G., Gagliardini, O., Gladstone, R., & Goldberg, D. (2012). Results of the marine ice sheet model intercomparison project, MISMIP. *The Cryosphere Discussions*, *6*(1), 267-308.

Pedro, J. B., Bostock, H. C., Bitz, C. M., He, F., Vandergoes, M. J., Steig, E. J., Chase, B. M., Krause, C. E., Rasmussen, S. O., & Markle, B. R. (2016). The spatial extent and dynamics of the Antarctic Cold Reversal. *Nature Geoscience*, *9*(1), 51-55.

Peltier, C., Kaplan, M. R., Birkel, S. D., Soteres, R. L., Sagredo, E. A., Aravena, J. C., Araos, J., Moreno, P. I., Schwartz, R., & Schaefer, J. M. (2021). The large MIS 4 and long MIS 2 glacier maxima on the southern tip of South America. *Quaternary Science Reviews*, *262*, 106858.

Peltier, C., Kaplan, M. R., Sagredo, E. A., Moreno, P. I., Araos, J., Birkel, S. D., Villa-Martínez, R., Schwartz, R., Reynhout, S. A., & Schaefer, J. M. (2023). The last two glacial cycles in central Patagonia: A precise record from the Ñirehuao glacier lobe. *Quaternary Science Reviews*, *304*, 107873.

Pittard, M., Roberts, J., Galton-Fenzi, B., & Watson, C. (2016). Sensitivity of the Lambert-Amery glacial system to geothermal heat flux. *Annals of Glaciology*, *57*(73), 56-68.

Prescott, J. R., & Hutton, J. T. (1994). Cosmic ray and gamma ray dosimetry for TL and ESR. *International Journal of Radiation Applications and Instrumentation. Part D. Nuclear Tracks and Radiation Measurements*, *14*(1-2), 223-227.

Quade, J., & Kaplan, M. R. (2017). Lake-level stratigraphy and geochronology revisited at Lago (Lake) Cardiel, Argentina, and changes in the Southern Hemispheric Westerlies over the last 25 ka. *Quaternary Science Reviews*, *177*, 173-188.

Quik, C., Van der Velde, Y., Harkema, T., Van der Plicht, H., Quik, J., Van Beek, R., & Wallinga, J. (2021). Using legacy data to reconstruct the past? Rescue, rigour and reuse in peatland geochronology. *Earth surface processes and landforms*, *46*(13), 2607-2631.

Rabassa, J. (2008). Late cenozoic glaciations in Patagonia and Tierra del Fuego. *Developments in quaternary sciences*, *11*, 151-204.

Ritz, C. (1997). Eismint intercomparison experiment: comparison of existing Greenland models. *Laboratoire de Glaciologie et de Géophysique de l'Environnement, Saint Martin d'Hères, France*, *105*.

Roberts, H. M. (2012). Testing Post-IR IRSL protocols for minimising fading in feldspars, using Alaskan loess with independent chronological control. *Radiation Measurements*, *47*(9), 716-724.

Rodés, Á., Pallàs, R., Braucher, R., Moreno, X., Masana, E., & Bourlés, D. L. (2011). Effect of density uncertainties in cosmogenic 10Be depth-profiles: dating a cemented Pleistocene alluvial fan (Carboneras Fault, SE Iberia). *Quaternary Geochronology*, *6*(2), 186-194.

Rodés, Á., Pallàs, R., Ortuño, M., García-Melendez, E., & Masana, E. (2014). Combining surface exposure dating and burial dating from paired cosmogenic depth profiles. Example of El Límite alluvial fan in Huércal-Overa basin (SE Iberia). *Quaternary Geochronology*, *19*, 127-134.

Rogozhina, I., & Rau, D. (2014). Vital role of daily temperature variability in surface mass balance parameterizations of the Greenland Ice Sheet. *The Cryosphere*, *8*(2), 575-585.

Rojas, M., Moreno, P., Kageyama, M., Crucifix, M., Hewitt, C., Abe-Ouchi, A., Ohgaito, R., Brady, E. C., & Hope, P. (2009). The Southern Westerlies during the last glacial maximum in PMIP2 simulations. *Climate Dynamics*, *32*(4), 525-548.

Ruppel, M., Väliranta, M., Virtanen, T., & Korhola, A. (2013). Postglacial spatiotemporal peatland initiation and lateral expansion dynamics in North America and northern Europe. *The Holocene*, *23*(11), 1596-1606.

Sagredo, E., Moreno, P., Villa-Martínez, R., Kaplan, M., Kubik, P., & Stern, C. (2011). Fluctuations of the Última Esperanza ice lobe (52 S), Chilean Patagonia, during the last glacial maximum and termination 1. *Geomorphology*, *125*(1), 92-108.

Sagredo, E. A., Kaplan, M. R., Araya, P. S., Lowell, T. V., Aravena, J. C., Moreno, P. I., Kelly, M. A., & Schaefer, J. M. (2018). Trans-pacific glacial response to the Antarctic Cold Reversal in the southern mid-latitudes. *Quaternary Science Reviews*, *188*, 160-166.

Schäbitz, F., Wille, M., Francois, J.-P., Haberzettl, T., Quintana, F., Mayr, C., Lücke, A., Ohlendorf, C., Mancini, V., & Paez, M. M. (2013). Reconstruction of palaeoprecipitation based on pollen transfer functions–the record of the last 16 ka from Laguna Potrok Aike, southern Patagonia. *Quaternary Science Reviews*, *71*, 175-190.

Schneider, C., Kilian, R., & Glaser, M. (2007). Energy balance in the ablation zone during the summer season at the Gran Campo Nevado Ice Cap in the Southern Andes. *Global and Planetary Change*, *59*(1-4), 175-188.

Schoof, C. (2007). Ice sheet grounding line dynamics: Steady states, stability, and hysteresis. *Journal of Geophysical Research: Earth Surface*, *112*(F3).

Seguinot, J. (2013). Spatial and seasonal effects of temperature variability in a positive degree-day glacier surface mass-balance model. *Journal of glaciology*, *59*(218), 1202-1204.

Seguinot, J., Ivy-Ochs, S., Jouvet, G., Huss, M., Funk, M., & Preusser, F. (2018). Modelling last glacial cycle ice dynamics in the Alps. *The Cryosphere*, *12*(10), 3265-3285.

Seguinot, J., & Rogozhina, I. (2014). Daily temperature variability predetermined by thermal conditions over ice-sheet surfaces. *Journal of glaciology*, *60*(221), 603-605.

Seguinot, J., Rogozhina, I., Stroeven, A. P., Margold, M., & Kleman, J. (2016). Numerical simulations of the Cordilleran ice sheet through the last glacial cycle. *The Cryosphere*, *10*(2), 639-664.

Sigfúsdóttir, T., Benediktsson, Í. Ö., & Phillips, E. (2018). Active retreat of a Late Weichselian marine-terminating glacier: an example from Melasveit, western Iceland. *Boreas*, *47*(3), 813-836.

Singer, B. S., Ackert Jr, R. P., & Guillou, H. (2004). 40Ar/39Ar and K-Ar chronology of Pleistocene glaciations in Patagonia. *Geological Society of America Bulletin*, *116*(3-4), 434-450.

Smedley, R., Buylaert, J.-P., & Újvári, G. (2019). Comparing the accuracy and precision of luminescence ages for partially-bleached sediments using single grains of K-feldspar and quartz. *Quaternary Geochronology*, *53*, 101007.

Smedley, R., Chiverrell, R., Burke, M., Duller, G., Thomas, G., Clarke, C., & Scourse, J. (2017). Internal dynamics condition millennial-scale oscillations of a retreating ice stream margin. *Geology*, *45*, 787-790.

Smedley, R., & Duller, G. (2013). Optimising the reproducibility of measurements of the post-IR IRSL signal from single-grains of K-feldspar for dating. *Ancient Tl*, *31*(2), 49-58.

Smedley, R., Duller, G., Pearce, N., & Roberts, H. (2012). Determining the K-content of single-grains of feldspar for luminescence dating. *Radiation Measurements*, *47*(9), 790-796.

Smedley, R., Glasser, N., & Duller, G. (2016). Luminescence dating of glacial advances at Lago Buenos Aires (~ 46 S), Patagonia. *Quaternary Science Reviews*, *134*, 59-73.

Smedley, R., & Pearce, N. (2016). Internal U, Th and Rb concentrations of alkali-feldspar grains: Implications for luminescence dating. *Quaternary Geochronology*, *35*, 16-25.

Solgaard, A. M., Reeh, N., Japsen, P., & Nielsen, T. (2011). Snapshots of the Greenland ice sheet configuration in the Pliocene to early Pleistocene. *Journal of glaciology*, *57*(205), 871-880.

Spencer, C. J., Yakymchuk, C., & Ghaznavi, M. (2017). Visualising data distributions with kernel density estimation and reduced chi-squared statistic. *Geoscience Frontiers*, *8*(6), 1247-1252.

Stern, C. R., Moreno, P. I., Villa-Martínez, R., Sagredo, E. A., Prieto, A., & Labarca, R. (2011). Evolution of ice-dammed proglacial lakes in Última Esperanza, Chile: implications from the late-glacial R1 eruption of Reclús volcano, Andean Austral Volcanic Zone. *Andean Geology*, *38*(1), 82-97.

Stone, J. O. (2000). Air pressure and cosmogenic isotope production. *Journal of Geophysical Research: Solid Earth*, *105*(B10), 23753-23759.

Stuiver, M., Reimer, P., & Reimer, R. (2021). CALIB 8.2 [WWW program] at http://calib.org. In: Accessed.

Sugden, D. E., Bentley, M. J., Fogwill, C., Hulton, N., McCulloch, R., & Purves, R. (2005). Late-glacial glacier events in southernmost south america: a blend of ‘northern’and'southern’hemispheric climatic signals? *Geografiska Annaler: series a, physical geography*, *87*(2), 273-288.

Sugden, D. E., Hulton, N. R., & Purves, R. S. (2002). Modelling the inception of the Patagonian icesheet. *Quaternary International*, *95*, 55-64.

Sugden, D. E., McCulloch, R. D., Bory, A. J.-M., & Hein, A. S. (2009). Influence of Patagonian glaciers on Antarctic dust deposition during the last glacial period. *Nature Geoscience*, *2*(4), 281-285.

Taylor, K. E., Stouffer, R. J., & Meehl, G. A. (2012). An overview of CMIP5 and the experiment design. *Bulletin of the American meteorological Society*, *93*(4), 485-498.

Thomsen, K. J., Murray, A. S., Jain, M., & Bøtter-Jensen, L. (2008). Laboratory fading rates of various luminescence signals from feldspar-rich sediment extracts. *Radiation Measurements*, *43*(9-10), 1474-1486.

Thorndycraft, V. R., Bendle, J. M., Benito, G., Davies, B. J., Sancho, C., Palmer, A. P., Fabel, D., Medialdea, A., & Martin, J. R. (2019). Glacial lake evolution and Atlantic-Pacific drainage reversals during deglaciation of the Patagonian Ice Sheet. *Quaternary Science Reviews*, *203*, 102-127.

Toggweiler, J. R., Russell, J. L., & Carson, S. R. (2006). Midlatitude westerlies, atmospheric CO2, and climate change during the ice ages. *Paleoceanography*, *21*(2).

Ton-That, T., Singer, B., Mörner, N., & Rabassa, J. (1999). Datación por el método 40Ar/39Ar de lavas basálticas y geología del Cenozoico Superior en la región del Lago Buenos Aires, provincia de Santa Cruz, Argentina. *Revista de la Asociación Geológica Argentina*, *54*(4), 333-352.

Trauerstein, M., Lowick, S. E., Preusser, F., & Schlunegger, F. (2014). Small aliquot and single grain IRSL and post-IR IRSL dating of fluvial and alluvial sediments from the Pativilca valley, Peru. *Quaternary Geochronology*, *22*, 163-174.

Troch, M., Bertrand, S., Lange, C. B., Cárdenas, P., Arz, H., Pantoja-Gutiérrez, S., De Pol-Holz, R., & Kilian, R. (2022). Glacial isostatic adjustment near the center of the former Patagonian Ice Sheet (48° S) during the last 16.5 kyr. *Quaternary Science Reviews*, *277*, 107346.

Tuhkanen, S., Kuokka, I., Hyvönen, J., Stenroos, S., & Niemelä, J. (1989-1990). Tierra del Fuego as a target for biogeographical research in the past and present. *Anales del Instituto de la Patagonia Serie Ciencias Naturales*, *19*(2), 1-107.

Turner, K., Fogwill, C., McCulloch, R., & Sugden, D. E. (2005). Deglaciation of the eastern flank of the North Patagonian Icefield and associated continental-scale lake diversions. *Geografiska Annaler: series a, physical geography*, *87*(2), 363-374.

Uppala, S. M., Kållberg, P., Simmons, A. J., Andrae, U., Bechtold, V. D. C., Fiorino, M., Gibson, J., Haseler, J., Hernandez, A., & Kelly, G. (2005). The ERA-40 re-analysis. *Quarterly Journal of the Royal Meteorological Society: A journal of the atmospheric sciences, applied meteorology and physical oceanography*, *131*(612), 2961-3012.

Van der Veen, C. (2002). Calving glaciers. *Progress in Physical Geography*, *26*(1), 96-122.

Van der Veen, C. (1996). Tidewater calving. *Journal of glaciology*, *42*(141), 375-385.

Villagran, C. (1990). Glacial climates and their effects on the history of the vegetation of Chile: a synthesis based on palynological evidence from Isla de Chiloé. *Review of Palaeobotany and Palynology*, *65*(1-4), 17-24.

Warren, C. R., & Sugden, D. E. (1993). The Patagonian icefields: a glaciological review. *Arctic and Alpine Research*, *25*(4), 316-331.

Weidemann, S. S., Sauter, T., Kilian, R., Steger, D., Butorovic, N., & Schneider, C. (2018). A 17-year record of meteorological observations across the Gran Campo Nevado ice cap in southern Patagonia, Chile, related to synoptic weather types and climate modes. *Frontiers in Earth Science*, *6*, 53.

Wendt, I., & Carl, C. (1991). The statistical distribution of the mean squared weighted deviation. *Chemical Geology: Isotope Geoscience Section*, *86*(4), 275-285.

Winkelmann, R., Martin, M. A., Haseloff, M., Albrecht, T., Bueler, E., Khroulev, C., & Levermann, A. (2011). The Potsdam parallel ice sheet model (PISM-PIK)–Part 1: Model description. *The Cryosphere*, *5*(3), 715-726.

Wolff, I. W., Glasser, N. F., Harrison, S., Wood, J. L., & Hubbard, A. (2023). A steady-state model reconstruction of the patagonian ice sheet during the last glacial maximum. *Quaternary Science Advances*, *12*, 100103.

Yan, Q., Owen, L. A., Zhang, Z., Jiang, N., & Zhang, R. (2020). Deciphering the evolution and forcing mechanisms of glaciation over the Himalayan-Tibetan orogen during the past 20,000 years. *Earth and Planetary Science Letters*, *541*, 116295.

Yan, Q., Wei, T., & Zhang, Z. (2022). Modeling the climate sensitivity of Patagonian glaciers and their responses to climatic change during the global last glacial maximum. *Quaternary Science Reviews*, *288*, 107582.

Yokoyama, Y., Esat, T. M., Thompson, W. G., Thomas, A. L., Webster, J. M., Miyairi, Y., Sawada, C., Aze, T., Matsuzaki, H., & Okuno, J. i. (2018). Rapid glaciation and a two-step sea level plunge into the Last Glacial Maximum. *Nature*, *559*(7715), 603-607.

Zech, R., Zech, J., Kull, C., Kubik, P. W., & Veit, H. (2011). Early last glacial maximum in the southern Central Andes reveals northward shift of the westerlies at~ 39 ka. *Climate of the Past*, *7*(1), 41-46.

Zolitschka, B., Anselmetti, F., Ariztegui, D., Corbella, H., Francus, P., Lücke, A., Maidana, N. I., Ohlendorf, C., Schäbitz, F., & Wastegård, S. (2013). Environment and climate of the last 51,000 years–new insights from the Potrok Aike maar lake Sediment Archive Drilling prOject (PASADO). *Quaternary Science Reviews*, *71*, 1-12.

Zolitschka, B., Francus, P., Ojala, A. E., & Schimmelmann, A. (2015). Varves in lake sediments–a review. *Quaternary Science Reviews*, *117*, 1-41.